Acknowledgement

Firstly, I would like to express my sincere gratitude to my supervisor Prof. Vincent Ji for his continuous support in my research and daily life. It was so lucky to meet such a person who is willing to share his valuable scientific knowledge and life experience.

I would like to thank Prof. Jean-Luc Grosseau-Poussard, Prof. Benoît Panicaud, Dr. Gang Ji, Dr. Aurélien Debelle and Prof. Clotilde Berdin, who are the committee members of my PhD defense. It is my honor to have them in the committee. Many thanks go to Prof. Benoît Panicaud and Prof. Jean-Luc Grosseau-Poussard, who carefully reviewed and improved my manuscript. As well, I would like to thank Dr. Aurélien Debelle for consisting on following my working progress each year and his valuable advices.

I am also grateful to my (ex)-colleagues in SP2M, Ing. Jérémy Forté for his guidance of XRD operation, Ing. Patrick Ribort and Dr. Céline Byl for their assistance in SEM characterization, Dr. Diana Dragoé for her help of XPS analysis and Dr. Ning Li for sharing his skills on TGA and in-situ deflection measurements. Besides, I would like to thank the former internship students who ever took part in this work. They are Youcheng Zhang, Xingguo Wang, Jianting Zhao, Yajie Zhao and Hexin Wang. Many thanks to my dear friends Chengyi Dan, Jing Tian, Yiting Wang, Yitao Wang and Lu Jin for sharing much unforgettable happiness. Last but not least, thank all the colleagues in SP2M who have built a comfortable working environment. I wouldn’t accomplish my goal without their support and respect.

Finally, I thank my parents and my husband for their love.

Table of contents

ACKNOWLEDGEMENT ..... **I**

TABLE OF CONTENTS ..... **III**

LIST OF TABLES ..... **IX**

LIST OF FIGURES ..... **XI**

CHAPTER 1 GENERAL INTRODUCTION **3**

1.1 PROBLEM STATEMENT 3

1.2 OBJECTIVES 5

1.3 THESIS ORGANIZATION 5

1.4 REFERENCE 7

CHAPTER 2 BIBLIOGRAPHY **11**

2.1 AUSTENITIC STAINLESS STEEL 11

2.2 BASIC THEORIES OF OXIDATION 14

2.2.1 Phase equilibria *15*

2.2.1.1 Chemical potential & condition of equilibrium 15

2.2.1.2 Standard free energy of formation versus temperature 17

2.2.1.3 Isothermal phase diagram for ternary system 18

2.2.2 Mass transport *19*

2.2.2.1 Diffusion with point defects in the oxide scale 20

2.2.2.2 Simplified diffusion model & Wagner's theory 21

2.2.2.3 Kirkendall effect at MO/M interface 22

2.2.2.4 Oxidation rate equations 24

2.3 DEVELOPMENT OF OXIDE SCALES 25

2.3.1 Oxide Phases *25*

2.3.2 Oxidation kinetics *26*

2.3.3 Oxidation mechanisms in dry atmosphere *27*

2.3.3.1 Defects in the main oxidation products 27

2.3.3.2 Diffusion related 29

2.3.3.3 Oxidation induced phase transformation 32

2.3.4 Breakaway oxidation *33*

2.3.5 Effects of water vapor 34

2.3.5.1 Defects 34

2.3.5.2 Morphology 35

2.3.5.3 Dissociation mechanism 37

2.3.5.4 Water promoted void formation 39

2.3.5.5 Volatilization 41

2.3.5.6 Growth kinetics 42

2.3.5.7 Mechanical aspects 43

2.4 MECHANICAL BEHAVIORS OF OXIDE SCALES 44

2.4.1 Stress generation 44

2.4.1.1 Intrinsic growth stresses 45

2.4.1.2 Thermally induced stresses 49

2.4.2 Stress release 50

2.4.2.1 Viscoplastic Deformation 50

2.4.2.2 Damage & self-healing 51

2.4.3 Residual stress 53

2.4.3.1 Types of residual stress 53

2.4.3.2 Residual stress measurement 54

2.4.3.3 Residual stress in oxide scales 55

2.5 SUMMARY 56

2.6 REFERENCE 57

CHAPTER 3 MATERIALS AND METHODS 73

3.1 SAMPLE PREPARATION 73

3.1.1 Basic observation in advance 73

3.1.2 Sample preparation for thermogravimetric analysis 75

3.1.3 Cross section preparation for microscopic characterization after oxidation 75

3.1.4 Sample preparation for growth stress determination by in-situ deflection 75

3.2 THERMOGRAVIMETRIC ANALYSIS (TGA) 76

3.3 FIELD EMISSION SCANNING ELECTRON MICROSCOPY (FESEM) 78

3.4 X-RAY PHOTOELECTRON SPECTROSCOPY (XPS) 79

3.5 GRAZING INCIDENCE X-RAY DIFFRACTION (GIXRD) 82

3.5.1 Phase identification and quantification *84*

3.5.2 Residual stress measurement *86*

3.6 DEFLECTION EXPERIMENT 91

3.7 REFERENCE 93

***CHAPTER 4 OXIDATION OF AISI 316L SS – THERMOCHEMICAL ASPECT* 97**

4.1 OXIDATION IN DRY AIR 97

4.1.1 Kinetics *97*

4.1.2 Morphology and microstructure *100*

4.1.2.1 Surface 100

4.1.2.2 Cross-section 103

4.1.3 Phases *105*

4.1.4 Discussion *108*

4.1.4.1 Inward growth vs outward growth 108

4.1.4.2 Oxide composition 109

4.1.4.3 Phase transformation at higher temperatures 110

4.1.4.4 Proposed growth mechanisms in dry air 111

4.2 OXIDATION IN HUMID AIR 113

4.2.1 Kinetics *113*

4.2.2 Morphology and microstructure *116*

4.2.2.1 Surface 116

4.2.2.2 Cross-section 120

4.2.3 Phases *124*

4.2.4 XPS Depth profile *128*

4.2.5 Discussion *133*

4.2.5.1 Oxidation kinetics 133

4.2.5.2 Grain size 137

4.2.5.3 Internal oxidation 138

4.2.5.4 Martensitic phase transformation 139

4.2.5.5 Oxide composition and proposed growth mechanisms in humid air 140

4.3 SUMMARY 141

4.4 REFERENCE 143

CHAPTER 5 OXIDATION OF AISI 316L SS - THERMOMECHANICAL ASPECT 149

5.1 GROWTH STRESS 149

5.1.1 Deflection results *151*

5.1.2 Elastic analysis *153*

5.1.3 About creep analysis *155*

5.2 THERMAL STRESS 158

5.3 RESIDUAL STRESS 162

5.3.1 In dry air *162*

5.3.2 In humid air *166*

5.4 DISCUSSION 175

5.4.1 Deformation *175*

5.4.2 Damages *176*

5.4.2.1 Under tension 177

5.4.2.2 Under compression 178

5.4.3 Temperature and humidity dependences of residual stress *182*

5.5 SUMMARY 183

5.6 REFERENCE 186

CHAPTER 6 COMPREHENSIVE ANALYSES OF OXIDATION MECHANISM 191

6.1 TENSILE STRESS ENHANCED OXYGEN INWARD DIFFUSION 191

6.2 SELF-HEALING OF OXIDE SCALES 193

6.3 CHEMICAL DEPENDENCE OF STRESSES 196

6.3.1 Fe_3O_4 ..... *196*

6.3.2 FeO *197*

6.4 BREAKAWAY OXIDATION 198

6.4.1 Morphology and microstructure *198*

6.4.2 Internal stresses *202*

6.4.3 Breakaway oxidation of AISI 316L in humid air *205*

6.5 SUMMARY 206

6.5.1 Combined actions of water vapor and stress *206*

6.5.2 Proposed oxidation mechanism *207*

6.5.2.1 In dry air 207

6.5.2.2 In humid air 207

6.6 REFERENCE 209

***CHAPTER 7 CONCLUSIONS AND PERSPECTIVES* 215**

7.1 CONCLUSIONS 215

7.2 PERSPECTIVES 216

***APPENDIX 1 AN APPROXIMATE CALCULATION OF OXIDE SCALE THICKNESS* 221**

***APPENDIX 2 RELEVANT PARAMETERS CALCULATIONS FOR XRD* 225**

APP. 2.1 X-RAY LINEAR ABSORPTION COEFFICIENT CALCULATION 225

App. 2.1.1 For a compound *225*

App. 2.1.2 For an oxide scale *225*

APP. 2.2 X-RAY PENETRATION DEPTH CALCULATION 225

App. 2.2.1 For phase analysis *225*

App. 2.2.2 For stress analysis *227*

APP. 2.3 DETERMINATION OF X-RAY IRRADIATED AREA 229

REFERENCE 230

***APPENDIX 3 QUANTITATIVE COMPOSITIONAL DEPTH PROFILING OF XPS* 231**

APP. 3.1 DEFINITION OF DEPTH RESOLUTION IN THIS WORK 231

APP. 3.2 APPROXIMATIVE CONVERSION OF SPUTTERING TIME TO SPUTTERED DEPTH 232

REFERENCE 233

***APPENDIX 4 RIETVELD REFINEMENT* 235**

***APPENDIX 5 ELASTIC MODULI CALCULATION OF SOLID SOLUTION CONFIRMED BY DFT SIMULATION* 239**

REFERENCE 240

List of tables

Table 2.1 Relevant parameters for AISI 316L SS *14*

Table 2.2 Oxidation parabolic constant values (chromia growth in air) *26*

Table 2.3 Comparison of oxygen, chromium, iron and manganese diffusion velocities in chromia film formed on various substrates [Sabioni et al., 2005, Sabioni et al., 2007, Sabioni et al., 2012c, Sabioni et al., 2013, Sabioni et al., 2015] *31*

Table 2.4 Comparison of chromium, iron and manganese diffusion velocities in $MnCr_2O_4$ film [Gilewicz-Wolter et al., 2005] *31*

Table 2.5 Oxidation parabolic constant values (chromium oxide growth) *42*

Table 3.1 Chemical composition of AISI 316L stainless steel *74*

Table 3.2 Elastic constants (at room temperature) of bulk oxides used in this study *90*

Table 4.1 kp calculated for the oxidation of AISI 316L SS in dry air at the given temperatures *99*

Table 4.2 kp ($g^2cm^{-4}s^{-1}$) calculated for the oxidation of AISI 316L SS in wet air at the given temperatures matching the results shown in Figure 4.2 and Figure 4.18 ..... *115*

Table 4.3 Elemental compositions of the points in Figure 4.20.a-2 (wt.%) *117*

Table 4.4 Mass-transfer parameters correlated *134*

Table 4.5 Mass loss rates of $CrO_2(OH)_2$ under different humidity *135*

Table 5.1 Stabilized In-plane growth stresses (GPa) of oxide scales for AISI 316L oxidized between 700˚C and 900˚C in the air with different humidity (elastic analysis) *154*

Table 5.2 Thermal expansion coefficients of selected oxides *158*

Table 5.3 Thermal expansion coefficients and thermal stresses evaluated *159*

Table 5.4 Comparison of the residual stress calculated by the thermal and growth stress and determined by XRD method (in the corundum-type oxide scales) *165*

Table 5.5 Surface fracture energy and fracture toughness for selected oxides at room temperature [Robertson et al., 1990] *181*

Table 6.1 Element constituents of oxide surface with and without spalling (wt.%) *199*

Table 6.2 Elemental analyses corresponding different regions marked in Figure 6.4 (wt.%) *200*

Table App. 1.1 Thicknesses of oxide scales formed under different conditions *227*

Table App. 2.1 MACs of atoms correlated in this thesis [Bryan, 1993] *229*

Table App. 2.2 MACs of compounds calculated *229*

Table App. 2.3 X-ray penetration depths (μm) for phase identification *230*

Table App. 2.4 Average X-ray penetration depths (μm) for stress determination in corundum-type oxide scales *232*

Table App. 4.1 Summary of refinement goodness for the oxide scales formed at 700˚C.....*240*

Table App. 4.2 Summary of refinement goodness for the oxide scales formed at 800˚C.....*241*

Table App. 4.3 Summary of refinement goodness for the oxide scales formed at 900˚C.....*242*

List of figures

Figure 1.1 Photographs of corrosion in industries from [Feedwater] (a) and [CETEC] (b) ····· *3*

Figure 2.1 A diagram illustrating a part of austenitic stainless steels in AISI grades with their respective alloying additions and principle applications [(SSINA) et al., 2014] ····· *13*

Figure 2.2 Ellingham diagram illustrating the standard free energies of formation for certain oxides plotted versus temperature, coupled with corresponding equilibrium $pO2$, $H2H2O$ ratio and $COCO2$ ratio [DerSilberspiegel, 2016] ····· *18*

Figure 2.3 Isothermal phase Diagrams of the Fe-Cr-O System at: 700°C (a); 800°C (b) [Oum et al., 2016] ····· *19*

Figure 2.4 Schematic of cross section showing the interfaces ····· *20*

Figure 2.5 A diagram of scale formation according to Wagner's model [Birks et al., 2006] ····· *22*

Figure 2.6 Schematics of vacancy transport and sinking operation associated with metal oxidation: (a) Vacancy clustering at polycrystalline metal/oxide interface; (b) vacancy absorption at nano-twinned metal/oxide interface [Huang et al., 2018] ····· *23*

Figure 2.7 SEM & EDX characterizations for verifying two-layer oxide structure of oxide scale formed at different temperatures: 800˚C, inner Cr_2O_3 and outer $(Mn, Cr)_3O_4$ (a) [Yang et al., 2004]; 600˚C, outermost grains $(Mn, Cr)_3O_4$ and outer Cr-Fe oxides (b) [Nezakat et al., 2016] ····· *26*

Figure 2.8 Kröger-Vink diagram where intrinsic electron equilibrium predominates, showing a defect structure situation in chromia containing chromium and oxygen vacancies and interstitials [Arve Holt, 1994a] ····· *28*

Figure 2.9 Kröger-Vink diagram showing the MO (M=Mg as an example) solubility as a function of oxygen activity with oxygen vacancies and electron holes considered [Arve Holt, 1994b] ····· *29*

Figure 2.10 Schematic explaining the mechanism of martensite phase transformation along grain boundaries: proposed flow diagram (a); EBSD and EDS mappings of martensite layers (b) [La Fontaine et al., 2014] ····· *33*

Figure 2.11 Kröger-Vink diagram showing the effect of water vapor on oxygen and metal vacancy defect concentrations versus partial oxygen pressure [Chandra-ambhorn et al., 2019] ····· *35*

Figure 2.12 Selected typical cross-sectional characterizations of oxide scales in the conditions marked in the upper highlight boxes, deriving respectively from [Kim et al., 2015] (Left); [Ehlers et al., 2006] (Right): TEM micrograph (Left-a); Overall 3-D atom elemental maps and stratified schematics showing chosen tips interested at grain boundary (Left-b), 2 μm away from grain boundary (Left-c) and 4 μm away from grain boundary (Left-c); reconstruction of individual element or oxide corresponding to those three tips (Left-e); schematic of oxide layer constitute (Left-f); SEM micrograph in dry gas (Right-a) and in wet gas (Right-b); schematic of oxide scale distribution in wet gas (Right-c). ····· *36*

Figure 2.13 Schematic of dissociation mechanism for the oxidation of Fe-Cr alloy in water vapor at high temperatures [Fujii et al., 1964] ····· *37*

Figure 2.14 Schematic showing oxygen transfer across a scale void carried by water molecular [Othman et al., 2009a] ····· *38*

Figure 2.15 Diagram illustrating water-vapor-promoted alloy oxidation: in-situ TEM micrographs showing nickel oxide growth in O_2 and H_2O with corresponding schematics (a) (a-1 and a-3: in O2; a-2 and a-4: in H_2O); formation process of vacancy and vacancy cluster (b) (b-2: schematic showing in atomic scale water promoted vacancy generation and vacancy clustering; b-1 DFT calculation result showing the vacancy formation energy difference without and with H; b-3: DFT calculation results showing vacancy pair formation energy without and with H as well as related energy difference); DFT calculation results showing diffusion barriers without and with H (c) [Luo et al., 2018] ····· *40*

Figure 2.16 Logarithm of partial pressure of Cr oxide and oxyhydroxide vapor species above Cr_2O_3 (s) as a function of temperature ($pH2o = 0.1$ atm, $pO2 = 0.1$ atm) [Ebbinghaus, 1993] ····· *41*

Figure 2.17 Improved Pilling-Bedworth model illustrating the oxide intrusion at M/MO interface created by anion inward diffusion [Evans, 1983] ····· *46*

Figure 2.18 Micrograph of wrinkled alumina surface (a); schematic of the dislocation climb model proposed by Clarke (b): A lateral growth strain generates at A with a Burgers vector parallel to the M/MO interface, while no lateral strain forms at B where the Burgers vector is perpendicular to the interface [Clarke, 2003] ····· *48*

Figure 2.19 Deformation map for chromia at the grain size of 1μm [Schütze, 1990] ····· *51*

Figure 2.20 Schematic of oxide damaging mechanisms: in tension (a); in compression (b) [Evans, 1988] ····· *52*

Figure 2.21 Schematic showing the buckling of chromia formed at 1200˚C in Ar-20%O_2 and its self-healing behaviors [Dorcheh et al., 2018] ····· *53*

Figure 2.22 Residual stress distribution over several grains of a polycrystalline material showing three types of residua stresses [Epp, 2016] ····· *54*

Figure 2.23 Spatial resolution and penetration of measuring residual stresses for different methods [Kypris et al., 2013] ····· *55*

Figure 3.1 Metallographic microstructures of AISI 316L stainless steel from different views: (a) RD-TD; (b) RD-ND; (c) TD-ND. ····· *74*

Figure 3.2 The flow diagram of the sample preparation for in-situ growth stress determination ····· *76*

Figure 3.3 Hypothetical mass-gain versus time curve for an oxidation reaction [Birks et al., 2006] ····· *77*

Figure 3.4 An overview of SETARAM TGA 92-16.18 apparatus schematic: (a) the furnace body; (b) the circulating cooling unit (LAUDA UKT 600); (c) the controller (CS 32); (d) the vapor generator ····· *77*

Figure 3.5 A schematic of SEM [Inkson, 2016] ····· *79*

Figure 3.6 Schematic description of related energy flow in XPS of solid surfaces [Hofmann, 2012] ····· *80*

Figure 3.7 A schematic of XPS using a monochromatized X-ray source. [Vickerman et al., 2011] ····· *81*

Figure 3.8 Diffraction with respect to the Bragg's law ····· *83*

Figure 3.9 PANalytical X'Pert PRO MRD system ····· *84*

Figure 3.10 Optical path schematics for (a) phase identification (b) residual stress measurement with the five motorized movements of the sample stage shown ····· *86*

Figure 3.11 The stress components (a) and the geometry correlated to residual stress determination (b) ····· *87*

Figure 3.12 Photography of the setup for in-situ growth stress determination [Huntz et al., 2007] (a) and schematic of the oxidation growth stress induced bending (b) ····· *91*

Figure 4.1 Mass gain curves of AISI 316L SS oxidized at 700˚C, 800˚C and 900˚C for 96 hours in dry air ····· *98*

Figure 4.2 Linear relationship between $\Delta MS2$ and time showing the parabolic rate law obeyed for the oxidation of AISI 316L SS at 700˚C, 800˚C and 900˚C for 96 hours in dry air ····· *98*

Figure 4.3 Plots of ln(kp) as a function of (1000/T) from this work and other studies for calculating the oxidation activation energies of Cr_2O_3 formation on various substrates (Ref.1: [Dorcheh et al., 2018], Ref.2: [Karczewski et al., 2019],Ref.3: [Huntz et al., 2007], Ref.4: [Perez et al., 2000], Ref.5: [Wei et al., 2018]) ····· *99*

Figure 4.4 SEM images illustrating the oxide surface morphology development versus the oxidation time and temperature: 6 hours (a) and 72 hours (b) at 700˚C; 6 hours (c) and 72 hours (d) at 800˚C; 6 hours (e) and 72 hours (f) at 900˚C, where “2” marked is the local enlargement of "1" marked ····· *100*

Figure 4.5 EDX quantitative elemental analysis of oxide surface as a function of oxidation time at 700 ˚C, 800 ˚C and 900˚C in dry air: O (a); Cr (b); Fe (c); Mn (d) ····· *101*

Figure 4.6 SEM image with eight lines measured (a) and plot profile of line i (b) showing the grain size determination process ····· *102*

Figure 4.7 Size development of oxide grains on the oxide surface for AISI 316L SS oxidized at 700˚C, 800˚C and 900˚C in dry air based on the ex-situ SEM observations ····· *102*

Figure 4.8 SEM images and EDS mapping of oxide scale oxidized at 700˚C for 96 hours in dry air: surface (a); cross-section (b); O mapping (c); Cr mapping (d); Ni mapping (e); Fe mapping (f); Mn mapping (g) ····· *104*

Figure 4.9 SEM images and EDS mapping of oxide scale oxidized at 800˚C for 96 hours in dry air: surface (a); cross-section (b); O mapping (c); Cr mapping (d); Ni mapping (e); Fe mapping (f); Mn mapping (g) ····· *104*

Figure 4.10 SEM images and EDS mapping of oxide scale oxidized at 900˚C for 96 hours in dry air: surface (a); cross-section (b); O mapping (c); Cr mapping (d); Ni mapping (e); Fe mapping (f); Mn mapping (g) ····· *105*

Figure 4.11 EDX line scan analysis of oxide cross-section after oxidation at 900˚C for 96 hours in dry air: SEM image (a) and corresponding line scan analysis (b) ····· *105*

Figure 4.12 Rietveld refinement of diffracted pattern for AISI 316L SS oxidized at 900˚C for 6 hours in dry air: analyzing graphic (a) and difference plot (b) ····· *106*

Figure 4.13 GIXRD patterns of the oxide scales after oxidation for different durations in dry air at 700 ˚C (a), 800 ˚C (b) and 900 ˚C (c) and corresponding quantitative phase composition analyses with respect to different X-ray penetration depths: 330 - 380 nm (d); 1.03 – 1.50 μm (e); 1.81 – 3.25 μm (f) ····· *107*

Figure 4.14 Calculated Mn-Cr-O phase diagrams: isothermal, 800°C (a); isobaric, air (b) [Jung, 2006] ····· *109*

Figure 4.15 In-situ XRD monitoring the martensitic phase transformation for AISI 316L oxidized at 900˚C for 24 hours in dry air ····· *110*

Figure 4.16 Schematic presentation of AISI 316L SS oxidized at 700˚C (a), 800˚C (b) and 900˚C (c) in dry air ····· *112*

Figure 4.17 Mass gain curves of AISI 316L SS oxidized at 700˚C, 800˚C and 900˚C for 96 and 6 hours in humid air: 96 hours (a) and 6 hours (b) at 700˚C; 96 hours (c) and 6 hours (d) at 800˚C; 96 hours (e) and 6 hours (f) at 900˚C ····· *114*

Figure 4.18 Linear relationship between $\Delta MS2$ and time showing the parabolic rate law obeyed for the oxidation of AISI 316L SS at 700˚C, 800˚C and 900˚C for 24 hours in humid air (exception: the initial 10 hours before breakaway oxidation considered for the oxidation at 900˚C in 8% water vapor containing air): air containing 1% water vapor (a); air containing 2% water vapor (b); air containing 4% water vapor (c); air containing 8% water vapor ····· *115*

Figure 4.19 Plots of ln (kp) as a function of (1000/T) for the oxidation activation energies of AISI 316L SS oxidized between 700˚C and 900˚C in the air with different water vapor contents ····· *116*

Figure 4.20 SEM images illustrating the oxide surface morphology development after 72 hour oxidation versus the temperature and humidity: at 700˚C in the air with 1% (a), 2% (b), 4% (c) and 8% (d) water vapor; at 800˚C in the air with 1% (e), 2% (f), 4% (g) and 8% (h) water vapor; at 900˚C in the air with 1% (i), 2% (j), 4% (k) and 8% (l) water vapor, where “2” marked is the local enlargement of "1" marked and Roman numerals represent different oxidation zones on the same specimen ····· *118*

Figure 4.21 EDX quantitative elemental analyses of oxide surface as a function of oxidation time in the air with different water vapor contents (0, 1, 2, 4 and 8%) at different temperatures: 700˚C (a); 800˚C (b) and 900˚C (c) ····· *119*

Figure 4.22 SEM images and EDS mapping of oxide scale grown at 700˚C for 96 hours in 1% water vapor containing air: surface (a); cross-section (b); O mapping (c); Cr mapping (d); Ni mapping (e); Fe mapping (f); Mn mapping (g) ····· *121*

Figure 4.23 SEM images and EDS mapping of oxide scale grown at 700˚C for 96 hours in 2% water vapor containing air: surface (a); cross-section (b); O mapping (c); Cr mapping (d); Ni mapping (e); Fe mapping (f); Mn mapping (g) ····· *121*

Figure 4.24 SEM images and EDS mapping of oxide scale grown at 700˚C for 96 hours in 4% water vapor containing air: surface (a); cross-section (b); O mapping (c); Cr mapping (d); Ni mapping (e); Fe mapping (f); Mn mapping (g) ····· *121*

Figure 4.25 SEM images and EDS mapping of oxide scale grown at 800˚C for 96 hours in 1% water vapor containing air: surface (a); cross-section (b); O mapping (c); Cr mapping (d); Ni mapping (e); Fe mapping (f); Mn mapping (g) ····· *122*

Figure 4.26 SEM images and EDS mapping of oxide scale grown at 800˚C for 96 hours in 2% water vapor containing air: surface (a); cross-section (b); O mapping (c); Cr mapping (d); Ni mapping (e); Fe mapping (f); Mn mapping (g) ····· *122*

Figure 4.27 SEM images and EDS mapping of oxide scale grown at 800˚C for 96 hours in 4% water vapor containing air: surface (a); cross-section (b); O mapping (c); Cr mapping (d); Ni mapping (e); Fe mapping (f); Mn mapping (g) ····· *123*

Figure 4.28 SEM images and EDS mapping of oxide scale grown at 900˚C for 96 hours in 1% water vapor containing air: surface (a); cross-section (b); O mapping (c); Cr mapping (d); Ni mapping (e); Fe mapping (f); Mn mapping (g); Si mapping (h) *124*

Figure 4.29 SEM images and EDS mapping of oxide scale grown at 900˚C for 96 hours in 2% water vapor containing air: surface (a); cross-section (b); O mapping (c); Cr mapping (d); Ni mapping (e); Fe mapping (f); Mn mapping (g) *124*

Figure 4.30 SEM images and EDS mapping of oxide scale grown at 900˚C for 96 hours in 4% water vapor containing air: surface (a); cross-section (b); O mapping (c); Cr mapping (d); Ni mapping (e); Fe mapping (f); Mn mapping (g) *124*

Figure 4.31 GIXRD patterns of the oxide scales after short and long time oxidation at different temperatures in the air with different water vapor contents at: 700˚C for 6 hours (a) and 96 hours (b); 800˚C for 6 hours (c) and 96 hours (d); 900˚C for 6 hours (e) and 96 hours (f) *125*

Figure 4.32 Quantitative phase composition analyses of oxide scales as a function of oxidation time and water vapor contents, obtained under different X-ray penetration depths: 300 - 330 nm (a-1), 1.00 – 1.07 μm (a-2) and 1.78 – 2.06 μm (a-3) at 700˚C; 310 - 380 nm (b-1) and 1.02 – 1.27 μm (a-2) at 800˚C; 370 - 400 nm (c-1), 1.16 – 1.53 μm (c-2) and 2.70 – 3.25 μm (c-3) at 900˚C *126*

Figure 4.33 XPS survey spectra obtained at different etch time of AISI 316L SS oxidized at 800˚C for 24 hours in dry air *129*

Figure 4.34 XPS depth profiles of the oxide scales formed at 700˚C in the air with 0% (a), 2% (b) and 8% (c) water vapor and 800˚C in the air with 0% (d), 2% (e) and 8% (f) water vapor *130*

Figure 4.35 XPS spectra of O 1s peak versus the etch time where the front one is from the surface before etching (a) and schematic presentation of O 1s peak fitting for the pattern obtained after 29463-second etching (b) for AISI 316L SS oxidized at 800˚C for 24 hours in dry air *132*

Figure 4.36 XPS depth profiles of O^{2-} and OH^{-} for AISI 316L SS oxidized at 700˚C in the air with 0% (a), 2% (b) and 8% (c) water vapor and 800˚C in the air with 0% (d), 2% (e) and 8% (f) water vapor *133*

Figure 4.37 The measured mass gains (a-c) and true mass gains with volatile mass compensated (d-f) for AISI 316L SS oxidized between 700˚C and 900˚C in humid air for 96 hours (before breakaway oxidation) *136*

Figure 4.38 Sizes of grains on the oxide surface as a function of water content for the oxidation at 700˚C (a), 800˚C (b) and 900˚C (c) for different durations *137*

Figure 4.39 In-situ XRD monitoring the martensitic phase transformation for AISI 316L after oxidation at 700˚C for 96 hours in the 4% water containing air *139*

Figure 4.40 Schematic presentation of AISI 316L SS oxidized at 700˚C (a), 800˚C and 900˚C (c) in humid air *141*

Figure 5.1 Raw data of deflection experiment in different atmospheres at 700˚C (a), 800˚C (b) and 900˚C (c) with corresponding results after deflections in argon subtracted (d-f) *150*

Figure 5.2 Deflection results during isothermal oxidation at 700˚C (a), 800˚C (b) and 900˚C (c) in the air with different water vapor contents *152*

Figure 5.3 Elastic analysis of growth stress evolution for short-term oxidation of AISI 316L SS between 700˚C and 900˚C in the air with different humidity ····· *155*

Figure 5.4 Imaginary system for determining the stresses in the oxide and substrate: the oxide neutral axis outside the oxide (a); the oxide neutral axis inside the oxide (b) [J. G. Zhao, 1984, Evans, 1995] ····· *156*

Figure 5.5 Residual stresses in the oxide scales formed in dry air as a function of oxidation time: in corundum-type oxides (a); in spinel-type oxides (b) ····· *163*

Figure 5.6 Residual stress evolution in the corundum oxide scales formed at 700˚C in the air with different water vapor contents ····· *167*

Figure 5.7 Residual stress evolution in the corundum oxide scales formed at 800˚C in the air with different water vapor contents ····· *171*

Figure 5.8 Residual stress evolution in the spinel oxide scales formed at 800˚C in the air with different water vapor contents ····· *171*

Figure 5.9 Residual stress evolution in the corundum oxide scales formed at 900˚C in the air with different water vapor contents ····· *174*

Figure 5.10 Residual stress evolution in the spinel oxide scales formed at 900˚C in the air with different water vapor contents ····· *174*

Figure 5.11 Schematic of the stress distribution at a wavy M/MO interface [A. G. Evans, 1983] ····· *176*

Figure 5.12 Buckling presentation for AISI 316L SS oxidized at 700˚C for 48 hours in the air with 4% water vapor ····· *179*

Figure 5.13 Schematic presentation of buckling process ····· *180*

Figure 6.1 Schematic presentation of self-healing process for AISI 316L SS after buckling: initiation (a); buckling (b) and diffusion within the interfacial void (c); cracking (d) and healing (e); corresponding SEM observation for the specimen after 48-hour oxidation at 700˚C in the 4% water containing air (f) ····· *194*

Figure 6.2 SEM/EDX observation of the oxide scale formed at 800˚C for 96 hours in the air with 2% water vapor: image showing the X-ray penetration depth for residual stress determination (a); the enlarged region interested in the discussion (b) and corresponding EDX element mappings (c-e) ····· *196*

Figure 6.3 SEM images of oxide surface after breakaway oxidation at 800˚C in the air with 8% water vapor for 72 hours ····· *199*

Figure 6.4 Optical observations (a-1, b-1, b-2 and c-1) and SEM images (a-2, 3, 4 and c-2, 3, 4) of oxide surface after breakaway oxidation at 900˚C in the air with 8% water vapor for 96 hours ····· *200*

Figure 6.5 SEM image and EDS mapping of oxide scale grown at 900˚C for 24 hours in 8% water vapor containing air: cross-section (a); O mapping (b); Cr mapping (c); Ni mapping (d); Fe mapping (e); Mn mapping (f) ····· *201*

Figure 6.6 Gradient of residual stresses in the corundum-type oxide scales formed at 900˚C in the air with different water contents: 96-hour and 72-hour oxidation in the air with 0% and 1% water vapor (a); 72-hour oxidation in the air with 8% water vapor ····· *202*

Figure App. 1.1 Thickness determination of oxide scale: SEM image of oxide scale after 96-hour oxidation at 900˚C in the 2% H_2O containing air (a); corresponding oxide scale contour extracted (b) *226*

Figure App. 2.1 Residual stress measurement geometry showing the related angles in the systems of specimen (S), laboratory (L) and instrument (I) for constant penetration depth determination: the relation between the sample and instrument coordinate systems (a); the relation between the specimen surface and diffracted plane coordinate systems *232*

Figure App. 3.1 Schematic broadening of the iron profile at a sharp interface and definition of the depth resolution, Δz (20-80%) in this thesis. For a Gaussian resolution function, $\Delta z=2\sigma$, with σ=the standard deviation. *236*

Figure App. 5.1 Mixing enthalpy of ternary $(Fe, Cr)_2O_3$ calculated by cluster expansion *243*

Figure App. 5.2 Voigt-Reuss-Hill average of $(Fe, Cr)_2O_3$ solid solution elastic moduli (E, G & ν), calculated by density functional theory *244*

CHAPTER

1

General Introduction

Contents

CHAPTER 1 GENERAL INTRODUCTION **3**

1.1 PROBLEM STATEMENT 3

1.2 OBJECTIVES 5

1.3 THESIS ORGANIZATION 5

1.4 REFERENCE 7

Chapter 1 General introduction

1.1 Problem statement

Steels are one of the most important engineering and construction materials in the world, which are widely used in our lives, such as building structures, engine components, rails, platforms and pipelines of energy sector, the steel packaging and household appliances etc. They are produced and consumed annually in extraordinary quantities. In 2018, the world crude steel production reached 1808.6 million tons, and the global steel demand forecasted will reach 1,735 million tons in 2019 [*WorldsteelAssociation, 2019*]. As structural materials, steels are welcomed due to both excellent mechanical properties and low price, but the relatively low corrosion resistance is their biggest disadvantage.

Scientists have noticed the corrosion issues in emerging technologies and emphasized the significant economic impact of corrosion cost [*Fürbeth et al., 2009*]. As the most important engineering materials, the focus on the corrosion problems of steels, is of great importance. Among the general corrosion issues for steels, high temperature oxidation is a common one, which is of interest in this work. In some chemical industries, steels in use at high temperatures are inevitably exposed to an oxidized environment which can influence or even destroy functions of the components (see Figure 1.1).

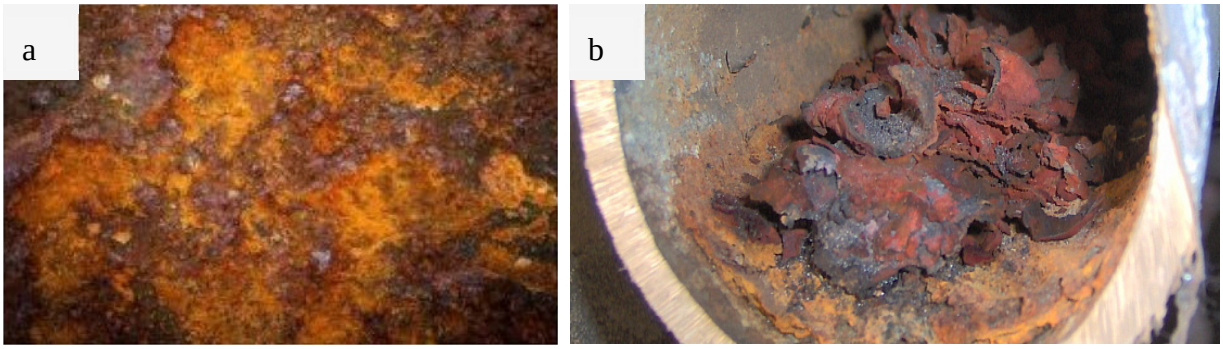

*Figure 1.1 Photographs of corrosion in industries from [*Feedwater*] (a) and [*CETEC*] (b)*

Oxidation is normally considered as a process that includes two reactants, i.e., metal and corrosive environment. The process can be perceived of as happening in three stages [*Young, 2016*]. Firstly, all superficial reactive constituents of steel contacting a hot corrosive gas are possible to react each other simultaneously. Afterwards, selective oxidation occurs where some less thermodynamically stable compounds are substituted by more stable ones, so as to locally approach a state of quasi-equilibrium. At this stage, the chemical constituents and morphology of oxide scales almost keep unchanging versus time, which can be regarded as a “steady state”. Finally, under both chemical and mechanical attacks, the system cannot hold such a “steady

state". Breakaway oxidation and incurable damages of oxide scale will make all reactive metallic components exhausted in a final breakdown stage.

During service of steels at high temperatures, one or several of the constituent metallic elements form particular compounds. Among which some can play key roles in protecting metals, e.g. chromium oxide or aluminum oxide, while others may aggravate corrosion damages, e.g. iron-rich oxides [*Robertson, 1991*]. The lifetime of steels depends on how long the protective layer will maintain. In other words, the transformation of the second stage to the third, which determines the lifetime of components, is of pronounced significance for high temperature oxidation research. However, the commencement of the third stage varies with a wide range of conditions, leading to the difficulty of being predicted [*Wood, 1961*]. Within the existing knowledge framework, the second quasi-equilibrium stage which directly determines the third one is relatively easy to be investigated. Thus, many researchers have carried out vast laboratory examples of the second stage and been trying to find the appropriate oxidation mechanisms to explain.

For commonly used Cr-containing stainless steels, a protective fine layer of chromium oxide not only lowers the oxidation rate but also has natural techniques to self-healing when ruptured or broken, which is the crucial function in the application at high temperatures [*Schütze, 1997*]. Once such protective scale is gone, the body steel will be depleted significantly and rapidly in a short time, leading to material failure. Therefore, scientists have been working on the factors that may influence the protective properties, such as the content of Cr in steels [*Evans et al., 1980, Ani et al., 2009*], reaction temperature [*Betz et al., 1974, R. Y. Chen, 2003*], corrosive atmosphere [*Robertson, 1991, Nešić, 2007*] and mechanical behaviors of oxide layer [*Hancock et al., 1974, Evans, 1995, Schütze, 2016*] etc. In general, their investigations center on two subjects, i.e., oxidation kinetics and oxidation mechanisms. The latter topic is quite attractive due to its complexity.

In recent years, one of the research hotspots of high temperature oxidation is to investigate the oxidation mechanisms in more complicated environment in order to simulate the real situation in industries. The effects of water vapor on oxidation cannot be ignored because humidity is present more or less in every reactive environment where steels are used at high temperatures and it really challenges the oxidation mechanisms summarized in the early years [*Saunders et al., 2008*]. Moreover, the entry points of research are not confined in thermal-chemical field. It has been accepted for several decades that the internal stress generation and relief during the oxidation impact the growth mechanism and adhesion of oxide scales. More advanced

characterization techniques and more thorough theories provide a good chance for perfecting oxidation mechanisms considered under thermal-chemical-mechanical conditions.

In this work, a frequently used austenitic stainless steel, AISI 316L, is chosen as the research object; the motivation is to investigate the effects of water vapor (0-8 vol.%) on oxidation at high temperatures (700-900°C) from the view of internal stress in oxide scales. This research mainly focuses on the quasi-equilibrium stage, i.e. the oxidation stage before breakdown.

1.2 Objectives

To interpret the effects of water vapor on the oxidation behavior of AISI 316L stainless steel (AISI 316L SS) at high temperature, the following objectives will be accomplished.

Initially, the chemical composition distribution, morphology and microstructure of oxide scales will be visibly characterized relying on a series of techniques. Referring to the existing oxidation mechanisms, oxidation schematics versus the humidity in air will be proposed.

Subsequently, the growth stress and residual stress in oxide scales will be prudently determined with the in-situ deflection method and X-ray diffraction technique respectively. Some discussions related to internal stress (oxide growth stress, residual stress and thermal stress) will be conducted based on the above results and related theories: the influence of temperature, morphology reflected deformation behaviors, the roles of grain boundaries and micro-cracks, water vapor promoted void formation and oxide scale breakdown etc.

Finally, two oxidation mechanisms considered under thermal-chemical-mechanical conditions matching with the humidity in air will be constructively summarized.

1.3 Thesis organization

This thesis includes seven chapters in total:

Chapter one provides a general introduction of this work, where the research background, objectives and dissertation structure are presented.

Chapter two sums up previous and existing studies mainly from two separated parts, as high temperature oxidation of stainless steel is a convoluted issue concerning a multidisciplinary field. In the first part, some basic theories related to thermodynamics, kinetics, physical metallurgy etc. are introduced to better comprehend the reaction kinetics, phase constitutions and their transformations, oxide morphology and mechanical properties. Besides, a review of oxide growth mechanisms and water vapor effects reported by others is given in favor of understanding the results in this study. In the second part, some essential knowledge and

practical examples of internal stresses developed in oxide scales are given, offering a foundation to study oxidation mechanisms in more complicated environments.

Chapter three presents relevant characterization techniques employed in this thesis such as TGA for in-situ monitor of oxide mass gain, FESEM&EDX for chemical constituent and morphology characterization, XPS for elemental and compounds depth profile, the most important GIXRD for phase identification and residual stress determination as well as the in-situ deflection method for oxide growth stress determination.

Chapter four to six is the main part of this dissertation. Chapter four presents the results from a series of characterization techniques, including oxide mass gain versus time, oxide scale surface and cross section morphology with their chemical component analysis, depth profile of oxide layers and phase identification of oxidation products with quantification by refinement. Based on the above, schematics of oxidation are proposed respectively corresponding to different temperatures and humidity. Chapter five calculates the residual stresses in the oxide scales developed under different humidity, and offers the results of in-situ growth stress determination under related conditions. The relationship between residual stress evolution and several factors (temperature, humidity, oxide morphology and microstructure) are discussed. Causes of final breakdown stage are analyzed. Chapter six suggests two oxidation mechanisms established on the comprehensive consideration of the two former sections. The whole analysis process is done within the framework of thermal-chemical-mechanical conditions.

Chapter seven makes conclusions of this work and suggests further and complementary research works on this topic.

1.4 Reference

[Ani et al., 2009] ANI, M. H. B., KODAMA, T., UEDA, M., KAWAMURA, K. & MARUYAMA, T. 2009. The Effect of Water Vapor on High Temperature Oxidation of Fe-Cr Alloys at 1073 K. *Materials Transactions,* 50**,** 2656-2663.

[Betz et al., 1974] BETZ, G., WEHNER, G., TOTH, L. & JOSHI, A. 1974. Composition-vs-depth profiles obtained with Auger electron spectroscopy of air-oxidized stainless-steel surfaces. *Journal of Applied Physics,* 45**,** 5312-5316.

[CETEC] CETEC. *Corrosion of pipes* [Online]. Available: *https://www.cetec.com.au/images/CorrosionIM000915pipe-960.jpg* [Accessed].

[Evans et al., 1980] EVANS, H., HILTON, D., HOLM, R. & WEBSTER, S. 1980. The development of localized pits during stainless steel oxidation. *Oxidation of Metals,* 14**,** 235-247.

[Evans, 1995] EVANS, H. E. 1995. Stress effects in high temperature oxidation of metals. *International Materials Reviews,* 40**,** 1-40.

[Feedwater] FEEDWATER. *Cooling water corrosion* [Online]. Available: *https://feedwater.co.uk/wp-content/uploads/2014/06/shutterstock_131967242-500x333.jpg* [Accessed].

[Fürbeth et al., 2009] FÜRBETH, W. & SCHÜTZE, M. 2009. Progress in corrosion protection as a requirement for technical progress. *Materials and corrosion,* 60**,** 481-494.

[Hancock et al., 1974] HANCOCK, P. & HURST, R. 1974. The mechanical properties and breakdown of surface oxide films at elevated temperatures. *Advances in corrosion science and technology.* Springer.

[Nešić, 2007] NEŠIĆ, S. 2007. Key issues related to modelling of internal corrosion of oil and gas pipelines–A review. *Corrosion science,* 49**,** 4308-4338.

[R. Y. Chen, 2003] R. Y. CHEN, W. Y. D. Y. 2003. Review of the High-Temperature Oxidation of Iron and Carbon Steels in Air or Oxygen. *Oxidation of Metals,* 59**,** 433-468.

[Robertson, 1991] ROBERTSON, J. 1991. The mechanism of high temperature aqueous corrosion of stainless steels. *Corros. Sci,* 32**,** 443-465.

[Saunders et al., 2008] SAUNDERS, S. R. J., MONTEIRO, M. & RIZZO, F. 2008. The oxidation behaviour of metals and alloys at high temperatures in atmospheres containing water vapour: A review. *Progress in Materials Science,* 53**,** 775-837.

[Schütze, 1997] SCHÜTZE, M. 1997. *Protective oxide scales and their breakdown,* Wiley.

[Schütze, 2016] SCHÜTZE, M. 2016. Stress effects in high temperature oxidation.

[Wood, 1961] WOOD, G. C. 1961. The oxidation of iron-chromium alloys and stainless steels at high temperatures. *Corrosion Science,* 2.

[WorldsteelAssociation, 2019] WORLDSTEELASSOCIATION. 2019. *2019 PRESS RELEASES* [Online]. Available: *https://www.worldsteel.org/media-centre/press-releases/2019.html* [Accessed].

[Young, 2016] YOUNG, D. J. 2016. *High temperature oxidation and corrosion of metals,* Elsevier.

CHAPTER

2

Bibliography

Contents

CHAPTER 2 BIBLIOGRAPHY **11**

2.1 AUSTENITIC STAINLESS STEEL 11

2.2 BASIC THEORIES OF OXIDATION 14

2.2.1 Phase equilibria *15*

2.2.1.1 Chemical potential & condition of equilibrium 15

2.2.1.2 Standard free energy of formation versus temperature 17

2.2.1.3 Isothermal phase diagram for ternary system 18

2.2.2 Mass transport *19*

2.2.2.1 Diffusion with point defects in the oxide scale 20

2.2.2.2 Simplified diffusion model & Wagner's theory 21

2.2.2.3 Kirkendall effect at MO/M interface 22

2.2.2.4 Oxidation rate equations 24

2.3 DEVELOPMENT OF OXIDE SCALES 25

2.3.1 Oxide Phases *25*

2.3.2 Oxidation kinetics *26*

2.3.3 Oxidation mechanisms in dry atmosphere *27*

2.3.3.1 Defects in the main oxidation products 27

2.3.3.2 Diffusion related 29

2.3.3.3 Oxidation induced phase transformation 32

2.3.4 Breakaway oxidation *33*

2.3.5 Effects of water vapor *34*

2.3.5.1 Defects 34

2.3.5.2 Morphology 35

2.3.5.3 Dissociation mechanism 37

2.3.5.4 Water promoted void formation 39

2.3.5.5 Volatilization 41

2.3.5.6 Growth kinetics 42

2.3.5.7 Mechanical aspects 43

2.4 MECHANICAL BEHAVIORS OF OXIDE SCALES 44

2.4.1 Stress generation *44*

2.4.1.1 Intrinsic growth stresses 45

2.4.1.2 Thermally induced stresses 49

2.4.2 Stress release *50*

2.4.2.1 Viscoplastic Deformation 50

2.4.2.2 Damage & self-healing 51

2.4.3 Residual stress *53*

2.4.3.1 Types of residual stress 53

2.4.3.2 Residual stress measurement 54

2.4.3.3 Residual stress in oxide scales 55

2.5 SUMMARY 56

2.6 REFERENCE 57

Chapter 2 Bibliography

Austenitic stainless steels are a group of diverse grades designed for specific applications in both daily life (e.g., home appliances, construction structures, vehicles etc.) and industry (e.g., petrochemical and chemical, pulp and paper, food processing, energy industry etc.). Mastering the metallurgical parameters of each grade is the premise to better utilize their superior properties in various service environments. Generally, the properties refer to the processability, mechanical properties at high temperature and corrosion resistance. Austenitic stainless steels are possible to resist the exterior erosion at high temperature thanks to a thin, dense, adherent and self-repair oxide film on the surface. However, large amounts of thermal, chemical and mechanical attacks dramatically influence the formation and preservation of such protective thin film, consequently lead to a rapid and unpredictable material failure. In this chapter, a literature research will be done, covering a brief presentation of basic oxidation theories, a review of oxide scale formation mechanisms under different conditions and an introduction of mechanical behaviors of oxide scales concerned.

2.1 Austenitic stainless steel

What is stainless steel? The standard answer commonly accepted is: an iron-based alloy steel with at least 10.5% chromium added and maximum 1.2% C which is resistant to rust and corrosive attacks [*15510:2014, 2019*]. The development of stainless steel is time-honored and can be tracked back to 1900s when the first stainless steel was patented and manufactured. It started off in 1889 with the discovery of Riley [*Riley, 1889*] that tensile strength of mild steel could be improved owning to the addition of nickel. The rudiment of stainless steel formed initially in the study of Leon Alexandre Guillet during 1904 and 1905 [*Guillet et al., 1905*]. His research on the steel with a series of elements contained (e.g. Ni, Mn, Si, Cr, W, Mo, Sn, Ti, V, Al etc.) excited countless scientists and engineers into the field of stainless-steel exploit. He was also the initiator to explore Cr and Cr-Ni steels with martensitic, ferritic and austenitic structures, but it was a pity that he did not think about the corrosion resistance properties of these steels. In 1905, Portevin was inspired by his experimental result that steels with at least 9% Cr became anti-resistant to acid corrosion. Then he made sustained efforts to study the role of Cr in corrosion resistance to acid, and he also used some alloy products of Guillet. His achievement promoted the research on martensitic and ferritic stainless steel, among which the most essential was the original formula for AISI 430 SS, as published in 1909 [*Portevin, 1909*]. At the same time, Giesen reported his findings in regard to austenitic Cr-Ni stainless steel and steels containing 8 - 18% Cr with 0.3% C [*Giesen, 1909*]. Based on the contributions of Portevin and Giesen, the concept of modern austenitic, martensitic and ferritic stainless steels became

clear. The first patent on stainless steel manufacturing process was obtained by Monnartz and Borchers in 1910. One year later, Monnartz published a brilliant paper, where he unlocked the secret of stainlessness for the first time. He found that the formation of protective chromium oxides needed at least 10.5% Cr content and pointed out that Mo could form more stable molybdenum carbides rather than chromium carbides [*Monnartz, 1911*]. Harry Brearley, who was hailed as " Stainless Pioneer " [*Cobb, 2010*], melt the first commercial chromium steel in 1913. He was also the originator of a stainless steel cutlery industry [*Anonymous, 1915*].

When talking about the history of austenitic stainless steel, Maurer and Strauss have to be mentioned, who created a precedent of commercial austenitic stainless steel in several years after austenitic stainless steel was initially made by Guillet and Giesen. They developed a type of Cr-Ni austenitic stainless steel named V2A and further another type of Cr-Ni-Mo austenitic stainless steel named V4A at the Krupp research laboratories in 1912. V2A was the first austenitic stainless-steel patent (German patent number: 304159 [*E. Maurer, 1912*]). Compared with V2A (Fe-20Cr-7Ni), V4A had 2% Mo in addition so as to improve the corrosion resistance to acid. Moreover, in 1920 they initiated the so-called Schaeffler diagram to roughly illustrate the relationship between the alloy composition and stainless steel structure [*Strauss. B, 1920*].

Over the past one hundred years, a wide range of austenitic stainless-steel types have been exploited to satisfy various service environments. The base for the numerous stainless steels is the binary Fe-Cr system, whose properties (e.g., corrosion resistance, mechanical properties, fabricability etc.) and structure (from body centered cubic to face centered cubic) can be modified by dissolving several primary alloying elements for instance Ni, Mo, Mn etc. and some supporting ones for instance C and N. Austenitic stainless steels mainly contain 16 - 26wt.% Cr and up to 35wt.% Ni [*Rafferty, 2018*], and maintain predominate austenitic structures at all temperatures. They are the most commonly used and familiar types of stainless steels, whose market occupancy approaches 65 - 70% [*G. George, 2002*]. People choose austenitic stainless steels because of its superior corrosion resistance and abundant grades designed for multi-purposes.

Austenitic stainless steels can be classified rather loosely into three groups: common chromium-nickel (300 series), manganese-chromium-nickel-nitrogen (200 series) and specialty alloys. The so-called "300" and "200" belong to the numbering system used for stainless steel standardization. The most accepted stainless-steel numbering system is developed by the American Iron and Steel Institute (AISI). Actually in 1930s, AISI had a numbering system specifically for wrought stainless steels. However, such system could neither satisfy the ever-growing types of stainless steels nor solve the chaotic naming problem in the world's stainless

steel market [*Cobb, 2010*]. Therefore, a new numbering system to unify the designation of stainless steel was badly in need of development, i.e., the now known AISI steel grades. Figure 2.1 illustrates a part of austenitic stainless steels in AISI grades with their respective alloying additions and principle applications. AISI 316L SS is a molybdenum bearing austenitic stainless steel, whose resistance to both general corrosion, pitting and crevice corrosion is accordingly better than the most frequently used AISI 304 SS. The subscript "L" represents low carbon. This steel also shows the potential in higher creep and tensile strength at high temperature, indicating its more suitable application in high temperature techniques. Some parameters of AISI 316L SS corresponding to chemical composition, physical properties and mechanical properties are listed in Table 2.1

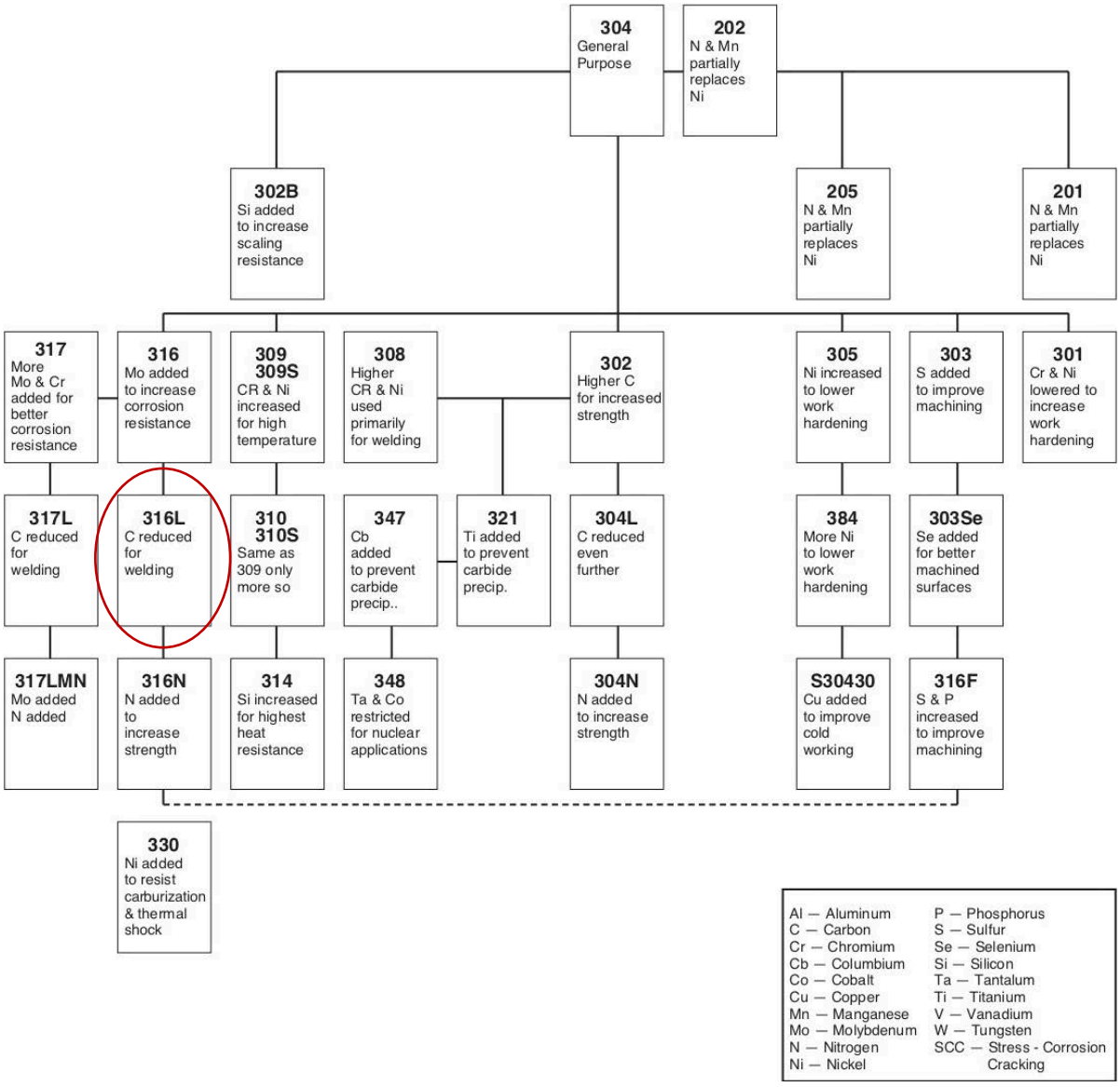

Figure 2.1 A diagram illustrating a part of austenitic stainless steels in AISI grades with their respective alloying additions and principle applications [(SSINA) et al., 2014*]*

Table 2.1 Relevant parameters for AISI 316L SS

Chemical composition (wt.%) ①									
C	Mn	P	S	Si	N	Fe	Cr	Ni	Mo
0.03 max.	2.00 max.	0.045 max.	0.03 max.	1.00 max.	0.10 max.	Bal.	16.00 – 18.00	10.00 – 14.00	2.00 – 3.00

Physical properties at room temperature				
Density (g/cm^3)	Thermal expansion coefficient (10^{-6} / °C)		Modulus of elasticity in tension	Modulus of Shear (GPa)
8.027	20°C - 100°C	16.5	200	82
	20°C - 500°C	18.2		
	20°C - 1000°C	19.5		

Mechanical properties ①				
Product form	Max. thickness (mm)	Min. 0.2% proof strength	Ultimate tensile strength (MPa)	Elongation after fracture (%)
Cold rolled strip	8	240	530 - 680	40
Hot rolled strip	13.5	220	530 - 680	40
hot rolled plate	75	220	520 - 670	45

Notes: Data with superscript ① is from [*EuroInox, 2006*] and the other without script is from [*UnitedPerformanceMetals, 2019*]

2.2 Basic theories of oxidation

As mentioned in the previous chapter, the second stage before the final breakdown stage locally approaches a state of equilibrium or quasi-equilibrium. As the basic requirements to study thermodynamics, phase equilibria, will be first introduced. Since oxidation kinetics is concerned with the particle (ions or atoms) diffusion process and interfacial chemical reaction, the fundamental knowledge of mass transport at the interface between gas/metal, metal/oxide, oxide/oxide will also be introduced. It should be noted here that this work will mainly consider the diffusion process within the oxide scale. Since oxides are usually ionic compounds, the diffusion of ions across the oxide scale will be primarily presented in this part.

2.2.1 Phase equilibria

2.2.1.1 Chemical potential & condition of equilibrium

It has been accepted that the second thermodynamic law is the effective criterion of whether or not an oxidation reaction can happen. An oxidation reaction can be assumed as:

$$\mathrm{M} + 1/2\,\mathrm{O}_2 = \mathrm{MO}. \tag{2.1}$$

For a system at a state of thermodynamic equilibrium, the stability of which can be described by the total Gibbs free energy G [*Callen et al., 1960*], written as:

$$G = H - TS = U + pV - TS, \tag{2.2}$$

where H, S, U denote the enthalpy, entropy and internal energy of the system respectively; V, T , p the volume, temperature and pressure respectively. For a closed system of multiphase, each phase can be regarded as an open system. If mass transfer occurs due to chemical reactions, the differential of internal energy can be expressed as:

$$dU = TdS - pdV + \sum_i \mu_i dn_i, \tag{2.3}$$

where n_i is the number of moles of component i; the item $\sum_i \mu_i dn_i$ is used to explain the compositional change in the whole system. Now the partial derivative of internal energy with respect to n_i is given by:

$$(\partial U/\partial\, n_i)_{T,p,n_{j\neq i}} = \mu_i, \tag{2.4}$$

where one of the most important concepts in thermodynamics [*Gibbs, 1961*], chemical potential μ_i is defined. Incorporating Equation (2.2) and Equation (2.3) both written in the form of derivative, produces:

$$dG = Vdp - SdT + \sum_i \mu_i dn_i. \tag{2.5}$$

For an isothermal, isobaric system, the reaction of Equation (2.1) is spontaneously conducted if $dG < 0$; it is thermodynamically impossible if $dG > 0$; the system is at equilibrium if $dG = 0$.

From Equation (2.5), it can be found that the partial differential of G in relation to n_i:

$$(\partial G/\partial\, n_i)_{T,p,n_{j\neq i}} = \mu_i, \tag{2.6}$$

gives another common expression of chemical potential, in other words, the chemical potential means the contribution to the free energy of the whole system with increasing one mole of component i at a state of constant temperature, pressure and other components unchanged.

Considering an equilibrium state of an isothermal, isobaric system, Equation (2.5) can be integrated to:

$$G = \sum_i \mu_i n_i = 0, \tag{2.7}$$

which is the so-called Gibbs equation and the condition for chemical equilibrium [*Young, 2016*].

Generally, the following relation for any reaction is true due to mass conservation:

$$\sum_i v_i M_i = 0, \tag{2.8}$$

where v_i is the stoichiometric coefficients with negative for reactants and positive for products; M_i the molar mass of component i. The extent of chemical reaction ξ is introduced as an intermediate variable:

$$dn_1/v_1 = dn_2/v_2 \cdots = dn_m/v_m = d\xi, \tag{2.9}$$

so, Equation (2.5) can be expanded and expressed as:

$$\begin{aligned} dG &= Vdp - SdT + \mu_1 dn_1 + \cdots \mu_m dn_m \\ &= Vdp - SdT + (v_1\mu_1 + \cdots v_m\mu_m)d\xi. \end{aligned} \tag{2.10}$$

According to Equation (2.10), the partial differential of G in relation to ξ can be written as:

$$(\partial G/\partial \xi)_{T,p} = \sum_i v_i \mu_i. \tag{2.11}$$

Under the condition of chemical equilibrium described by Equation (2.7), a particular form of Gibbs Equation is given by:

$$\sum_i v_i \mu_i = 0, \tag{2.12}$$

Utilizing Equation (2.5) and Equation (2.6) to component A in the isothermal and fixed constituent system, yields:

$$\partial \mu_A/\partial p = V_A, \tag{2.13}$$

where V_A is the partial molar volume. Importing the ideal gas equation, produces:

$$V_A = V/(\sum_i n_i) = N_A RT/p_A, \tag{2.14}$$

where $N_A = n_A/\sum_i n_i$ is the mole fraction. Equation (2.13) is accordingly written in the derivative form combining with Equation (2.14) as:

$$d\mu_A = (N_A RT/p_A)dp, \tag{2.15}$$

which leads to:

$$d\mu = RT(dp_A/p_A). \tag{2.16}$$

In an isothermal system with a given constituent, employing the Dalton's law of partial pressures for the ideal gas mixtures, yields $p_A/p = N_A$ and $dp_A = N_A dp$. Equation (2.16) is then integrated to:

$$\mu = \mu^\circ + RT\ln(p_A/p_A^\circ), \tag{2.17}$$

where the superscript ∘ means the standard state.

For the oxidation reaction described as Equation (2.1), when it satisfies Equation (2.8) and the metal and its oxides are regarded as pure and immiscible solids, the following relation can be obtained under the condition of chemical equilibrium given by Equation (2.12):

$$\mu_{\mathrm{MO}} - \mu_{\mathrm{M}} - (1/2)\mu_{\mathrm{O_2}}^\circ - (1/2)RT\ln p_{\mathrm{O_2}} = 0, \tag{2.18}$$

which can be rewritten as:

$$\Delta G^\circ = \mu_{\mathrm{MO}}^\circ - \mu_{\mathrm{M}}^\circ - (1/2)\mu_{\mathrm{O_2}}^\circ = (1/2)RT\ln p_{\mathrm{O_2}}, \tag{2.19}$$

where the item $RT\ln(p_A/p_A^\circ)$ in Equation (2.17) for MO and M is ignored due to the insensitivity of solids to pressure. Simultaneously, chemical equilibrium constant K_p for Equation (2.1) is given as:

$$K_p = \exp(-\Delta G^\circ/RT) = p_{\mathrm{O_2}}^{-1/2}. \tag{2.20}$$

2.2.1.2 Standard free energy of formation versus temperature

Now considering a more general oxidation reaction such as:

$$(2x/y)\mathrm{M} + \mathrm{O_2} = (2/y)\mathrm{M}_x\mathrm{O}_y, \tag{2.21}$$

of which the standard free formation energy plotted as a function of temperature can be made into the Ellingham diagram [*Ellingham, 1944*], as shown in . In the Ellingham diagram, the y-axis and x-axis represent ΔG° and temperature respectively. It is noted that all reactions are normalized to one mole of O_2 and hence $\Delta G^\circ = RT\ln p_{\mathrm{O_2}}$. The frequent usages are briefly summarized below:

- To estimate the relative ease of reduction reaction: for the reactions closer to the top of the diagram, their oxides are unstable and easily reduced; moreover, when a red line with negative slope which represents $\mathrm{C} + \mathrm{O_2} = 2\mathrm{CO}$ goes below orange lines which represent oxidation reactions, the carbon can thus reduce the oxide to metal;
- To determine the partial pressure of oxygen in equilibrium with the selected metal and its oxide at a given temperature: the method of determination is shown by the green dash line in , the process of which is first choosing a temperature interested, subsequently finding the

crossed point of the selected temperature and reaction line, then connecting this point to the "O" point at the top left, next extending this green dash line in the opposite direction up to the dark red line which represents p_{O_2}, and finally obtaining the crossed point marked as a green star which presents the equilibrium pressure of oxygen;

- To evaluate the CO/CO_2 ratio and H_2/HO_2 ratio used for reduction at a selected temperature with the similar procedure introduced above but with respect to the point "C" and "H" respectively.

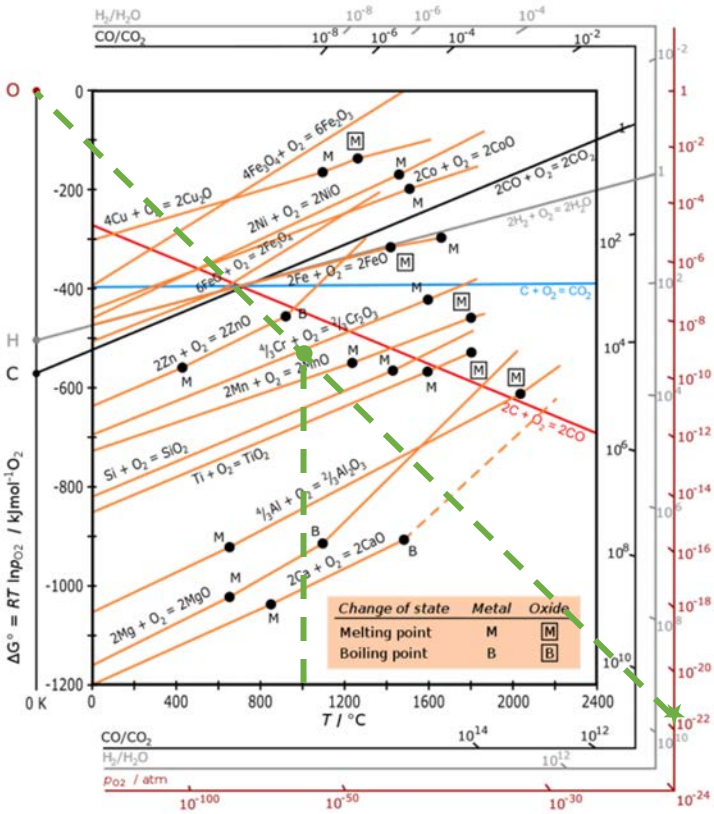

*Figure 2.2 Ellingham diagram illustrating the standard free energies of formation for certain oxides plotted versus temperature, coupled with corresponding equilibrium p_{O_2}, H_2/H_2O ratio and CO/CO_2 ratio [*DerSilberspiegel, 2016*]*

2.2.1.3 Isothermal phase diagram for ternary system

A practical issue of oxidation at high temperature is frequently concerned with one or more reactive metallic components and multiple corrosive atmospheres. Phase diagrams are able to formulate all chemical potentials of phases in a multicomponent system so as to interpret the effect of more than two variables (e.g., concentration, temperature and pressure) on the phase constituent of the system. Therefore, discussions of the phase diagram for multicomponent system at a given temperature or pressure are of great significance. Researchers have reported

many two-dimension isothermal phase diagrams corresponding to either a binary alloy with one gas such as the ternary (Fe-Cr-O, Cr-Mn-O and Fe-Mn-O) system respectively [*Oum et al., 2016, Kjellqvist et al., 2010, Kang et al., 2016*] or a mono metal with two gases [*Giggins et al., 1980, Rahmel et al., 1965b*]. The former is of more interest to this thesis.

The isothermal sections shown in Figure 2.3 imply the oxide phase constituent formed on the ferritic Fe-Cr alloy at high temperatures, i.e., iron and chromium solid solution oxide, iron-rich spinel oxide and halite oxide (FeO). It also indicates the temperature-dependence oxide growth confirmed by the highlight region, i.e., phase constituent change from halite at 800°C to spinel at 700°C.

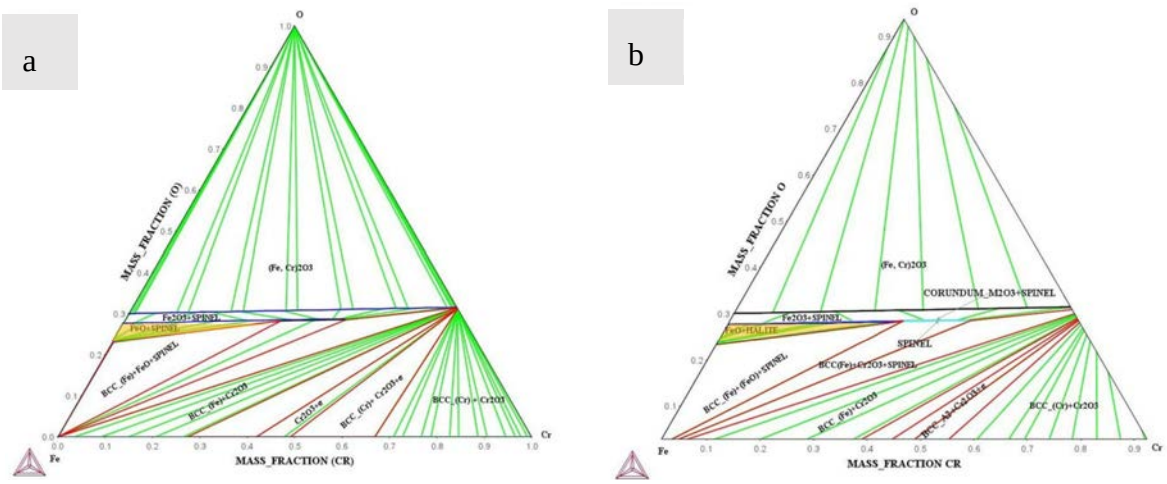

*Figure 2.3 Isothermal phase Diagrams of the Fe-Cr-O System at: 700℃ (a); 800℃ (b) [*Oum et al., 2016*]*

2.2.2 Mass transport

The classical theory describing the flux and concentration gradient is Fick's law:

$$J = -D(\partial C/\partial x), \tag{2.22}$$

where J is the diffusion flux; D the diffusion coefficient; C the concentration and x position. Equation (2.22) is usually effective for the diffusion process in one dimension in an isotropic media and it does not consider the concentration change with respect to time. In this case, the driving force of diffusion can be simply regarded as the concentration difference between two regions. But for an oxidation process where the factors such as the chemical reaction where the change of concentration versus time etc. should be considered, Equation (2.22) cannot satisfy. It is accepted from thermodynamics that any spontaneous process should follow the direction of minimization of the free energy. Five or six decades ago, researchers debated on the real driving force of diffusion, and reached a final agreement, i.e., chemical potential gradient of

atoms [*Herring et al., 1951, Stevens et al., 1971*]. Therefore, with respect to the principle of lowest free energy, the diffusion flux J can be described as:

$$J = -M_A C_A (\partial \mu_A / \partial x), \tag{2.23}$$

where M_A is the mobility of A atoms.

Considering a general oxidation reaction such as Equation (2.1), two reactants M and O_2 are separated by the oxide layer MO, hence forming two interfaces, i.e., M/MO and MO/O_2, as shown in Figure 2.4.

The sustain oxidation reaction counts on the contact of two reactants, i.e., oxygen has to penetrate the oxide layer to arrive at the MO/M interface or metal has to diffuse through the oxide layer up to the MO/O_2 interface. Therefore, the study of mass transport during oxidation plays an essential role in exploring the oxide growth mechanisms.

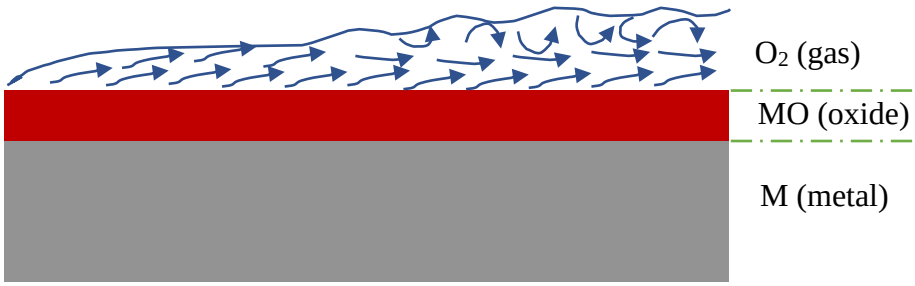

Figure 2.4 Schematic of cross section showing the interfaces

2.2.2.1 Diffusion with point defects in the oxide scale

Point defects are important for diffusion during oxidation from two aspects: the capability of mass transport in ionic oxide compounds can be viewed as “vehicles for diffusion” of reactive atoms; their equilibrium concentrations can be calculated thanks to statistical thermodynamics [*Mehrer, 2007*]. In this work, point defects in ionic crystals are of interest since oxides are usually ionic compounds in which diffusion is possibly the main rate-controlling process. The concept of point defects in ionic crystalline solids was first introduced by Frenkel in 1926 [*Frenkel, 1926*], who proposed that thermal agitation resulted in atoms transporting from their normal lattice sites to interstitial positions and leaving behind lattice vacancies. There is another defect type now known as Schottky’s type, which was first suggested by Schottky in the early 1930s [*Schottky et al., 1931*]. In the former case, the anion sublattice is perfect but the cation sublattice contains vacancies and interstitials; while in the latter case, both cation and anion sublattices contain vacancies. For high temperature oxidation, Frenkel’s and Schottky’s defect types are able to explain the stoichiometric oxides, while for those non-stoichiometric oxides,

more complicated defect type is in need. Thus, the defect types respectively described as the n-type semi-conductivity (metal excess or oxygen deficit) and p-type semi-conductivity (metal deficit or oxygen excess) were suggested in [*Metikoš-Huković et al., 1987*, *Sikora et al., 2002*, *Feng et al., 2010*] etc. Charge neutrality of these defect types are kept by assuming the anions or cations with different chemical valences such as a common oxide $Fe_{(1-x)}O$.

2.2.2.2 Simplified diffusion model & Wagner's theory

As mentioned above, the formation of a thin oxide layer leads to the separation of reactants, therefore, the reactants must penetrate through this oxide layer so as to continue the oxidation process, accompanied with chemical reactions at interfaces. The location of new oxides formed counts on the principle diffusion types, i.e., the so-called outward diffusion (cations), inward diffusion (anions) or mixed diffusion (anions and cations). Based on the previous analysis, Wagner's theory concerning the diffusion during high temperature oxidation was suggested in 1933 [*Wagner, 1933*], giving such a profound and complicated process a simple description on the premise of several assumptions:

- The rate-controlling process relies on the transport of ions or free carriers (electrons or positive holes);
- The oxide layer formed is dense and adherent;
- Thermodynamic equilibrium is locally established at the interfaces of both metal-oxide and oxide-gas;
- Thermodynamic equilibrium is locally established all over the scale with considering only chemical reaction at the interfaces;
- The ionic diffusion flux is calculated regardless of position in the oxide scale by assuming the stoichiometric oxide or near-stoichiometric oxide formation;
- The thickness of oxide scale should be larger than that of electrical double layer so as to ignore the effect of space charge;
- Oxygen solubility in the metal may be neglected.

The oxide scale formed in this work can be assumed dense and adherent. Their thicknesses vary from several dozens of nanometers to several micrometers for the stage before breakaway oxidation. Wagner's theory is thus worthy being referenced to. A figure of oxide scale formation established on Wagner's theory is illustrated in Figure 2.5. Due to the assumption that thermodynamic equilibrium is locally established at the interfaces, the activity gradients of metal and corrosive gas can be considered across the oxide scale, and simultaneously metallic

cations and oxygen anions tend to diffuse towards opposite directions across the oxide scale. An electronic field will be established during the directed movement of charged ions, hence electrons are promoted to move towards gas and finally a charge equilibrium is achieved at a particular move rate of ions and electrons.

The driving force of charged ion migration during oxidation is provided by both chemical and electrical potential gradient. Assuming a particle i (cations, anions or electrons in oxide scales) with charge Z_i carried, situates at a field with the chemical potential gradient $(\partial\mu_i/\partial x)$ and the electrical potential gradient $(\partial\phi/\partial x)$, the force that the particle i is under can be given:

$$(1/N_{AV})[(\partial\mu_i/\partial x) + Z_i F(\partial\phi/\partial x)]\ (\mathrm{J}\cdot\mathrm{particle}^{-1}\cdot\mathrm{cm}^{-1}), \tag{2.24}$$

where N_{AV} is the Avogadro's number and F the Faraday constant. Owning to the force in Equation (2.24), the mobility velocity v_i is then expressed as:

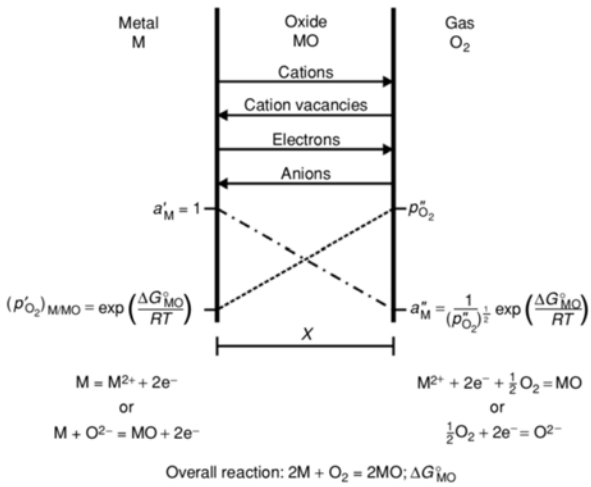

*Figure 2.5 A diagram of scale formation according to Wagner's model [*Birks et al., 2006*]*

$$v_i = (-B_i/N_{AV})[(\partial\mu_i/\partial x) + Z_i F(\partial\phi/\partial x)]\ (\mathrm{cm}\cdot\mathrm{s}^{-1}), \tag{2.25}$$

where B_i is the mobility of particle i. The flux of particles J_i is thus achieved:

$$J_i = C_i v_i = (-C_i B_i/N_{AV})[(\partial\mu_i/\partial x) + Z_i F(\partial\phi/\partial x)]\ (\mathrm{mol}\cdot\mathrm{cm}^{-2}\cdot\mathrm{s}^{-1}), \tag{2.26}$$

where C_i is the concentration of particle i.

2.2.2.3 Kirkendall effect at MO/M interface

Kirkendall effect discovered by Smigelskas and Kirkendall in 1947 [*Kirkendall et al., 1947*] and further analyzed by Darken in 1948 [*Darken, 1948*] occupies an essential position in diffusion theory of metal. It proposes the vacancy-mediated diffusion in solids: for a diffusion couple, elements with different diffusion coefficients mutually exchange by moving through

vacancies, promoting the vacancies coalesce and thus void formation near the side of faster diffusing. [*Hormadaly et al., 2012*]. In fact, Kirkendall effect is of great interest in many fields such as nanomaterials, thin films, microelectronic devices etc. as well as in relevant analyses such as stress and deformation.

For high temperature oxidation of steels, voids can be observed at the M/MO interface [*Cox et al., 1973, Gong et al., 2010*]. Kirkendall effect is one of the mechanisms to explain this phenomenon. After the initial formation of thin oxide film on the substrate surface, the oxidation subsequently relies on the outward diffusion of metallic cations and inward diffusion of oxygen anions within the oxide scale. If the diffusivity of cations in the oxide scale is larger than that of anions, vacancies may be injected into the substrate and probably condense out into voids near the interface. The difference between the diffusivities of cations and anions across the oxide scale is regarded as Kirkendall effect [*Wang et al., 2014*]. Figure 2.6 is an example that Kirkendall effect occurs at the interface of Cu/CuO_2. This work concerns the suppression of interdiffusion-induced voiding in oxidation of copper nanowires [*Huang et al., 2018*]. More atomic steps and kinks leads to a large vacancy generation rate and small nucleation threshold, whereby a fast formation of Kirkendall voids at the interface occurs (Normally, it is difficult for nanoscale materials to generate Kirkendall shift which is another form of Kirkendall effect), as shown in Figure 2.6.a. On the other hand, the twin-modified surface containing less atomic steps and kinks leads to limited vacancy generation rate. Besides, imported coherent twin boundaries (CTBs) are not effective vacancy sinks compared with incoherent twin boundaries. Due to the combination of these two effects, the shift of lattice plane (the so-called Kirkendall shift) forms at the interface instead of forming voids, as shown in Figure 2.6.b.

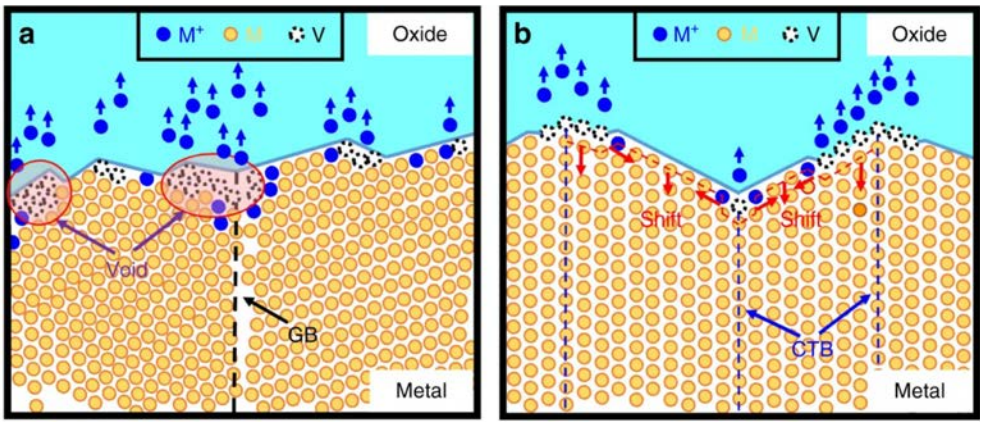

*Figure 2.6 Schematics of vacancy transport and sinking operation associated with metal oxidation: (a) Vacancy clustering at polycrystalline metal/oxide interface; (b) vacancy absorption at nano-twinned metal/oxide interface [*Huang et al., 2018*]*

2.2.2.4 Oxidation rate equations

The core issue of oxidation kinetics is the determination of oxidation rate, which might follow the parabolic, linear or logarithmic rate law depending on the rate-controlling process. In practice, oxidation rate can be calculated through the data of thermogravimetric analysis. Oxide thickness can be evaluated by mass gain if the oxide phase constituent is known.

- **Parabolic rate law**

When a compact and perfectly adhesive oxide film formed on the surface of metal, the rate-controlling process is ion diffusion within the oxide scale. Assuming all the migrated ions are cations and local thermodynamic equilibrium is established in any region, the cation diffusion flux $J_{M^{2+}}$ is thus expressed as:

$$J_{M^{2+}} = -J_{V_M} = D_{V_M}\left[\left(C''_{V_M} - C'_{V_M}\right)/x\right], \tag{2.27}$$

where J_{V_M} denotes the flux of vacancies corresponding to the migrated cations; D_{V_M} the diffusion coefficient of cation vacancies; $\left(C''_{V_M} - C'_{V_M}\right)$ the vacancy concentration difference between the oxide/gas interface and oxide/metal interface, which is constant at the state of thermodynamic equilibrium. And Equation (2.27) is rewritten accordingly as:

$$J_{M^{2+}} = (1/V_{\mathrm{ox}})(dx/dt) = D_{V_M}\left[\left(C''_{V_M} - C'_{V_M}\right)/x\right], \tag{2.28}$$

where V_{ox} is the molar volume of oxide. Oxidation rate described as oxide thickness increase is given by:

$$dx/dt = k'/x, \tag{2.29}$$

and oxidation rate constant k' is thus defined combining Equation (2.28) and (2.29):

$$k' = D_{V_M} V_{\mathrm{ox}}\left(C''_{V_M} - C'_{V_M}\right). \tag{2.30}$$

Integrating Equation (2.29) with the boundary condition x = 0, t = 0, yields the parabolic rate law:

$$x^2 = 2k't. \tag{2.31}$$

- **Linear rate law**

When the rate-controlling process is the chemical reaction at the interface of metal/oxide or gas/oxide, the thickness of oxide follows:

$$x = k''t, \tag{2.32}$$

which is the linear rate law and k'' is the linear oxidation rate constant. It is usually obeyed in two oxidation situations, i.e., a porous oxide scale facilitating oxygen to penetrate and a low pressure of corrosive atmosphere [*Zhang, 2010*].

- **Logarithmic rate law**

For the initial stage of low temperature oxidation (generally refers to less than 100 nm thickness oxide layer and less than 400°C reaction temperature), a large oxidation rate appears at first with subsequently a rapid decrease. Such oxidation obeys the logarithmic rate law, which can be described as:

$$x = k_{+}''' \log(t + t_0) + A, \tag{2.33}$$

$$1/x = B - k_{-}''' \log t, \tag{2.34}$$

where k_{+}''' and k_{-}''' are the logarithmic rate law constants corresponding to direct log law and inverse log law respectively; t and t_0 temperatures; A and B constants.

2.3 Development of oxide scales

Research on oxidation of stainless steel and related alloys at high temperature can be tracked back to the 1920s [*Wood, 1961*]. Vast practical examples concerning oxide growth kinetics and oxide products have been reported and accumulated, based on which several oxidation mechanisms have been established. In this section, the relevant investigations will be briefly presented.

2.3.1 Oxide Phases

Oxide scales usually consist of several layers with various phase compositions. The composition distribution of these layers after a long-time oxidation is closely linked to the stability of each oxide and oxygen partial pressure gradient within the scale. For austenitic stainless steels, the formation of Cr-rich oxide acts as an effective diffusion barrier against corrosive anions and other cations so as to protect the metallic substrate [*Sabioni et al., 2005*]. The oxide scale of austenitic stainless steel formed at high temperatures (500 - 900°C) was usually identified as consisting of two layers with an outer spinel-type AB_2O_4 layer (A and B usually refers Mn and Cr, sometimes one or two of Cr, Fe, Mn and Ni depending on conditions) and an inner thin and dense corundum-type layer M_2O_3 (M usually refers Cr, sometimes Fe and/or Mn contained) [*Wild, 1977, A. L. Marasco, 1991, A. Bautista, 2003, Vesel et al., 2008, Zheng et al., 2010, Cionea et al., 2016, Wonneberger et al., 2019*], as shown in Figure 2.7.

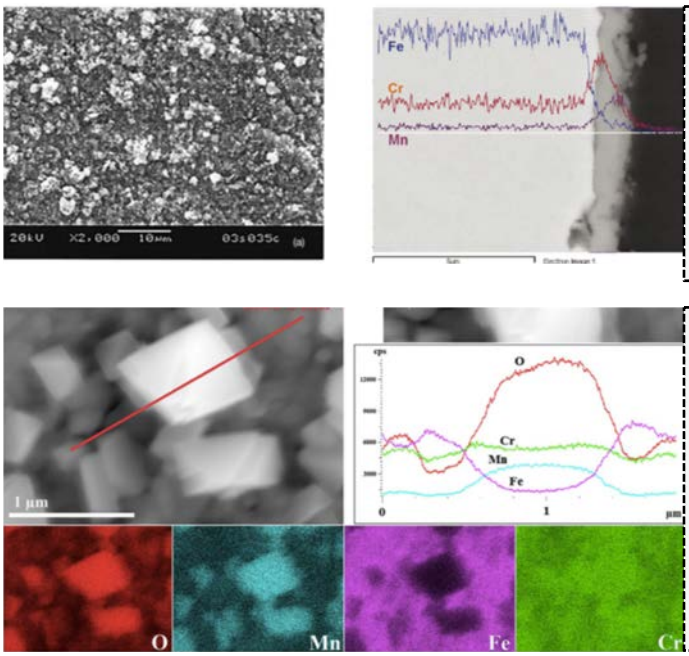

(a)

Surface (left) and cross-section (right) characterization of oxide scales formed on AISI 430 SS after oxidation at 800˚C for 300 hours in air

(b)

Surface characterization of outer oxide scale formed on AISI 316L SS after oxidation at 600˚C for 1000 hours in air

*Figure 2.7 SEM & EDX characterizations for verifying two-layer oxide structure of oxide scale formed at different temperatures: 800˚C, inner Cr_2O_3 and outer $(Mn, Cr)_3O_4$ (a) [*Yang et al., 2004*]; 600˚C, outermost grains $(Mn, Cr)_3O_4$ and outer Cr-Fe oxides (b) [*Nezakat et al., 2016*]*

2.3.2 Oxidation kinetics

Massive data in relation to oxidation kinetics has been reported for the past several decades. Table 2.2 gives an example of oxidation rate constants concerning chromia formed on various substrates in air reported in the literature.

Table 2.2 Oxidation parabolic constant values (chromia growth in air)

Substrate		Temperature (°C)	Oxidation rate constant k_p ($g^2cm^{-4}s^{-1}$)	Ref.
Pure Cr		950	2×10^{-10}	[*Dorcheh et al., 2018*]
		1050	3×10^{-10}	
		1200	9×10^{-9}	
Ferrite	AISI 430	800	3.33×10^{-14}	[*Xu et al., 2019*]
		1000	8.06×10^{-10}	
		950	5.31×10^{-12}	[*Wei et al., 2018*]
		1000	1.24×10^{-11}	

	Fe-20Cr-Mn-Mo-Nb-Ti	1050	2.06×10^{-11}	
		1100	5.51×10^{-11}	
	AISI 430L	600	2.13×10^{-16}	[*Karczewski et al., 2019*]
		700	2.41×10^{-15}	
		800	1.72×10^{-14}	
	AISI 439	850	4.0×10^{-13}	[*Huntz et al., 2007*]
		900	1.6×10^{-12}	
		950	3.0×10^{-12}	
Austenite	AISI 304	850	2.1×10^{-13}	
		900	6.9×10^{-13}	
		950	1.4×10^{-12}	
		900	3.6×10^{-13}	[*Perez et al., 2000*]
	Low Ni steel	600	5.22×10^{-14}	[*Perez et al., 2001*]
	(Fe-17Cr-11Mn-	700	2.27×10^{-13}	
	Fe-18Cr-10Ni-1Ti	1100	7.3×10^{-11}	[*Goncel et al., 1979*]
	AISI 316	1150	3.3×10^{-8}	[*Seal et al., 1994*]
	AISI 316L	900	3.92×10^{-9}	[*A. Bautista, 2003*]

Obviously, the oxidation rate constant shows sensitivity to temperature since the order of magnitude of which are the same for those normal Cr-containing steels (e.g., AISI 430, 430L, 439, 304 and 316). The properties of substrates may also have an impact probably by changing the growth mechanism.

2.3.3 Oxidation mechanisms in dry atmosphere

Oxidation mechanism can be understood roughly from the diffusion issue during a relative long-time oxidation process at high temperature. Many researchers have carried out their work from all conceivable angles, part of which are classified in this thesis and introduced in brief below.

2.3.3.1 Defects in the main oxidation products

Per Kofstad and Arve Holt et al. made a lot of efforts in regard to the defect structures of oxides such as Cr_2O_3, $Co_{(1-y)}O$, $Ni_{(1-y)}O$ etc. or oxides with impurities. Kofstad [*Kofstad et al., 1980, Kofstad, 1988*] suggested that chromia showed a p-type semiconductor behavior at its primarily used temperature and higher oxygen pressure, which was in accordance with the studies in [*Young et al., 1987, Metikoš-Huković et al., 1987*]. Young et al. found chromia showed an n-

type semiconductor behavior at low oxygen pressure [*Young et al., 1985*]. In a recent research, the defect structure of chromia has been further verified through oxidizing pure chromium under different oxygen partial pressures between 800˚C and 900˚C [*Latu-Romain et al., 2018, Parsa et al., 2018*]. The defect structure of chromia is mainly influenced by the oxygen partial pressure for the oxidation of pure chromium between 800˚C and 900˚C [*Parsa et al., 2018*]. Therefore, it can be summarized in general that: an n-type chromia grows when $p_{O_2} < 10^{-14}$ atm; a p-type chromia grows when $p_{O_2} > 10^{-12}$ atm; the most protective stoichiometric chromia grows when $5 \times 10^{-14} < p_{O_2} < 5 \times 10^{-13}$ atm. The reason of slow diffusion in chromia was explained by Kofstad, who suggested that the concentration of defects at near-stoichiometric compositions became low when intrinsic electron equilibrium was predominant, and this suggestion was confirmed by the Kröger-Vink diagram, as shown in Figure 2.8.

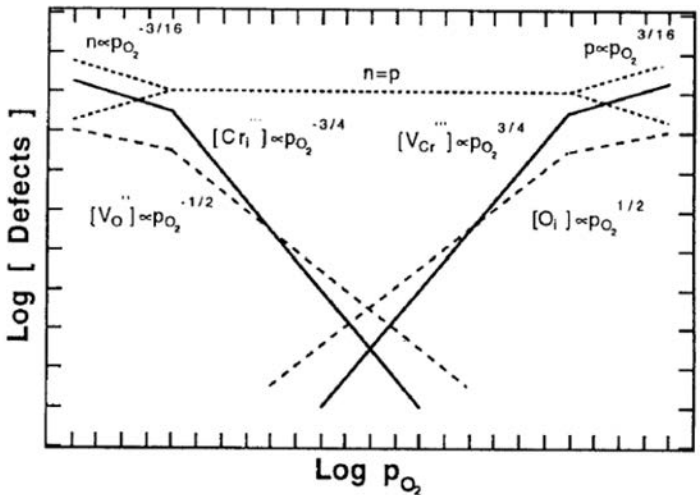

*Figure 2.8 Kröger-Vink diagram where intrinsic electron equilibrium predominates, showing a defect structure situation in chromia containing chromium and oxygen vacancies and interstitials [*Arve Holt, 1994a*]*

In his opinion [*Kofstad, 1995*], the formation of chromium vacancy and establishment of related defect equilibrium can be expressed respectively as:

$$3/4\, O_2 = 3/2\, O_2^x + V_{Cr}''' + 3h^{\cdot}, \tag{2.35}$$

$$[V_{Cr}'''] = K_{V_{Cr}} [h^{\cdot}]^{-3} p_{O_2}^{3/4}, \tag{2.36}$$

where, according to the notation system developed by Kröger and Vink [*Kröger et al., 1956*], O_2^x denotes a neutral oxygen atom; V_{Cr}''' a chromium vacancy with three negative effective charges; $h^{\cdot}$ an electron hole with a positive charge (while e' denotes an electron with a negative charge); $K_{V_{Cr}}$ the equilibrium constant for chromium vacancy; p_{O_2} the oxygen pressure.

Considering the dominant situation of intrinsic electronic equilibrium with the electroneutrality condition $[\mathrm{e}'] = [\mathrm{h}^{\cdot}] = K_{\mathrm{i}}^{1/2}$, where K_{i} is the equilibrium constant for interstitials, the concentration of chromium vacancies can accordingly be expressed as:

$$[\mathrm{V}_{\mathrm{Cr}}'''] = K_{\mathrm{V_{Cr}}} K_{\mathrm{i}}^{-3/2} p_{\mathrm{O_2}}^{3/4}, \tag{2.37}$$

from which Kofstad thought qualitatively that the concentration of point defects was inversely proportional to that of electronic defects.

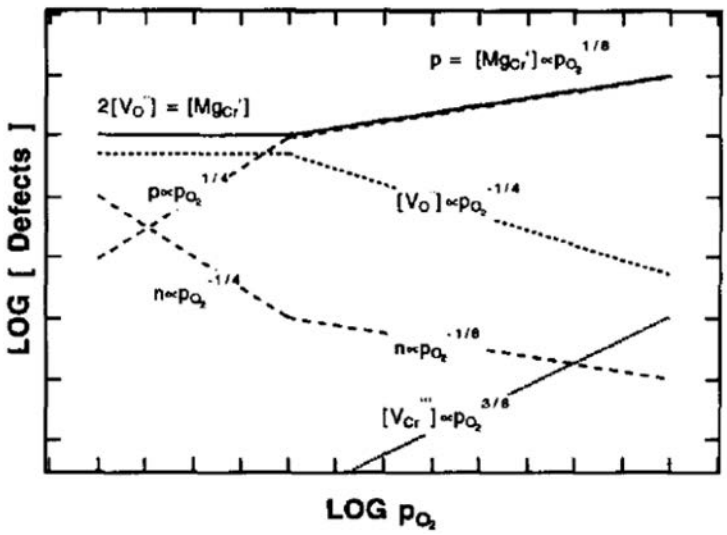

*Figure 2.9 Kröger-Vink diagram showing the MO (M=Mg as an example) solubility as a function of oxygen activity with oxygen vacancies and electron holes considered [*Arve Holt, 1994b*]*

In addition, Arve Holt studied the electrical conductivity and defect structure of Cr_2O_3 doped with MgO, providing generalized rules to other divalent metallic oxide impurities [*Arve Holt, 1994b*], as shown in Figure 2.9. Therefore, the defect structure of $MnCr_2O_4$ (Cr_2O_3 with MnO doped) can be deduced based on his general view:

in the case of oxygen vacancy compensation to dissolved MnO, the solubility of MnO was independent of oxygen partial pressure;

in the case of electron hole or chromium interstitial formation, the solubility of MnO rised with rising oxygen partial pressure.

2.3.3.2 Diffusion related

The existence of defects can promote diffusion process. In general, defects can be divided into four types matching various diffusional paths [*Paul et al., 2017*]: zero-dimension point defects such as vacancies, self-interstitials, impurities and anti-sites as the lattice diffusion path; one-dimension line defects such as dislocations and two-dimension planar defects such as surfaces,

grain boundaries and interphase boundaries as the short-circuit diffusion path; three-dimension volume defects, i.e., the assemble of the defects above such as dispersants, inclusions, voids and cracks, as the diffusion paths of micro-crack, micro-pore etc.

It has been accepted for long that diffusion through line and volume defects is faster than that through point defects. The common method to determine the effective diffusion coefficients for oxidation process with bulk and grain boundary diffusion coefficients combined has been established based on the studies of Hart and Harrison [*Hart, 1957, Harrison, 1961*]. Many researchers used this method to study the diffusivities of various reactive components within oxide scale. For instance, Tsai studied the relation between oxygen diffusion and oxidation kinetics for Ni-30Cr alloy oxidized at 900˚C in air. He confirmed that the countercurrent diffusion of oxygen and chromium jointly determined the oxide growth especially diffusion along grain boundaries [*Tsai et al., 1995*]. He also found the slowdown effect of yttrium on grain boundary diffusion [*Tsai et al., 1996*]. Sabioni investigated the diffusion of Fe, Cr, O, Mn in Cr_2O_3 layer formed at 700 – 1100˚C in air on both Ni-30Cr and Fe-15Cr alloys and AISI 304 and AISI 439 stainless steels respectively. From his systematic and comprehensive investigations, the main points can be summarized:

- Cr_2O_3 plays as a barrier against ion diffusion; iron diffusion and cationic self-diffusion are similar in chromia scale. Due to segregation phenomena, the activation energy of Fe diffusion along grain boundary becomes higher than the values for bulk diffusion [*Sabioni et al., 2005*];
- Similar results are obtained for Mn diffusion; in addition, Mn shows a good affinity with oxygen so as to easily diffuse across chromia towards to the outer surface, forming its oxides [*Sabioni et al., 2007*];
- Oxygen ion inward diffusion is predominant for chromia growth kinetics on both ferritic and austenitic stainless steels especially at high temperatures. For ferritic stainless steel oxidation, cation outward diffusion also plays a role [*Sabioni et al., 2012a, Sabioni et al., 2012b, Sabioni et al., 2012c, Sabioni et al., 2013*];
- Grain boundary diffusion is the rate-controlling process for chromia growth on Fe-15Cr alloy; the diffusivity of chromium and iron is independent of oxygen partial pressure [*Sabioni et al., 2015*].

From the work of Sabioni, a rough comparison of diffusion velocities in chromia film for various components is summarized, as seen in Table 2.3. The comparisons in the table depend

on the values of diffusion coefficients determined from the diffusion experiments (700 - 1100˚C, in air).

As mentioned in Section 0, one of the important spinel oxide layers formed on Cr-containing stainless steels at interested temperature is $MnCr_2O_4$. Some researchers investigated ion diffusivities in this film such as [*Gilewicz-Wolter et al., 2005*]. Gilewicz-Wolter proposed that bulk diffusion predominated during Mn, Cr and Fe diffusion at 800 and 900˚C, simultaneously grain boundary diffusion was also present except Mn diffusion at 900˚C. Based on his study, the diffusivity comparison of elements interested is listed in Table 2.4.

*Table 2.3 Comparison of oxygen, chromium, iron and manganese diffusion velocities in chromia film formed on various substrates [*Sabioni et al., 2005, Sabioni et al., 2007, Sabioni et al., 2012c, Sabioni et al., 2013, Sabioni et al., 2015*]*

substrate	Ni-30Cr alloy	Fe-15Cr	Ferritic & austenitic
Bulk	Mn > O > Cr > Fe	Fe > Cr > O	O > Cr
Grain boundary	Mn > Cr > O> Fe (>800˚C)		Notes:
Effective	--		$Cr_{(ferrite)} > Cr_{(austenite)}$

*Table 2.4 Comparison of chromium, iron and manganese diffusion velocities in $MnCr_2O_4$ film [*Gilewicz-Wolter et al., 2005*]*

Temperature	800˚C	900˚C
Bulk	Mn > Fe > Cr	Mn > Cr > Fe
Grain boundary	Mn > Cr > Fe	Fe > Cr

Young did a set of theoretical thermodynamics analysis of diffusion during oxidation such as the establishment of oxidation rate equations coupling with the Gibbs-Duhem equation [*D. J. Young, 1988*]. Internal oxidation happens when a reactive metallic component cannot afford continuous oxidation after it's selectively oxidized. Young reported the prediction of internal oxidation rate based on interstitial diffusion [*Young, 2012*].

In addition, a number of factors impacting the diffusion process have also been investigated. For instance, Gerland studied the effects of dislocation on oxidation of AISI 316L stainless steel at 300 and 600˚C in air. The TEM micrographs combined with other techniques of chemical analysis provided a clear comparison between before and after oxidation. He referred that dislocations affected the thickness and composition of oxide scale and inversely some unstable dislocations near subsurface were annihilated due to the flux of Cr vacancies [*M. Gerland, 2001*]. Other works concerning grain size were reported in [*Raman et al., 2009, Liu*

et al., 2015]. In Raman's work, the oxidation resistance of nanocrystalline Fe-15Cr alloy was compared with the same constituent microcrystalline. The result indicated that five times greater concentration of Cr was found in the inner oxide layer formed on nanocrystalline. Generally, grain refinement caused more grain boundaries through which more chromium could thus diffuse from the substrate. This result verified their postulation that oxidation resistance could be improved using nanocrystalline with lower Cr content. Liu's work suggested that grain refinement of Fe-13Cr-Ni alloy contributed to anion inward diffusion, leading to a quick formation of inner chromium layer, and corrosion resistance at 700˚C in air was accordingly improved. Buscail introduced the role of molybdenum in oxidation resistance of AISI 316L stainless steel [*Buscail et al., 2008*], which was similar to that of silicon [*Huntz et al., 2003, Yang et al., 2008*]. He proposed that molybdenum could act as vacancy sinks at the M/MO interface, contributing to the adherence of oxide scale, meanwhile molybdenum oxide could prevent iron in the substrate from migrating towards the surface.

2.3.3.3 Oxidation induced phase transformation

Martensitic phase transformation (from γ-austenite to α'-martensite) occurring in steel near the M/MO interface has been reported several times [*Duh et al., 1988, Duh et al., 1990, Jervis et al., 1990*]. α'-martensite formed beneath the scale during cooling process after oxidation at 1000 -1095˚C in a low oxygen pressure atmosphere [*Susan et al., 2012*] and it was often discovered along grain boundaries due to Cr depletion with martensite temperature increased [*Butler et al., 1986*]. The disappearance of α' phase completely finished after one-hour heating at 700˚C [*Guillamet et al., 1993*].

Fontaine proposed a model to explain the mechanism [*La Fontaine et al., 2014*]. From Figure 2.10.a, sensitization (A-B) appeared after heating at high temperature with easily oxidized grain boundaries formed, simultaneously leading to Cr-depletion zones beneath oxide layer (C). Martensitic phase transformation occurred in these Cr-depletion zones when the temperature decreased below martensite transformation temperature (D). If cycle oxidation considered, the existing martensite zones were easily oxidized with new Cr-depletion zones generated, subsequently new martensitic phases formed during cooling (E). A final stratified morphology was considered as the result of the repetition of process E, as seen in Figure 2.10.b.

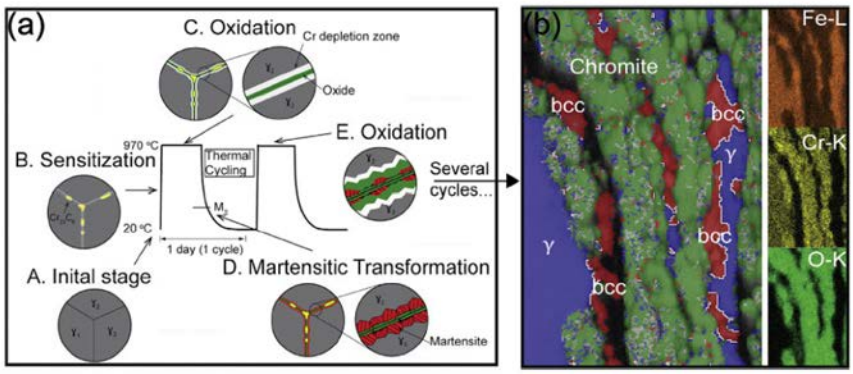

*Figure 2.10 Schematic explaining the mechanism of martensite phase transformation along grain boundaries: proposed flow diagram (a); EBSD and EDS mappings of martensite layers (b) [*La Fontaine et al., 2014*]*

Clamunger also suggested that α'-martensite could play a role of grain refinement and chromia layer formation was thus promoted above martensite zone with the inward and outward ion diffusion impeded. So, the zones without martensite were more corroded than those with martensite [*Calmunger et al., 2015*]. The improvement of Ni/Cr ratio was in favor of austenitic phase stability in Cr-depletion zones [*Calmunger et al., 2016*].

2.3.4 Breakaway oxidation

In ideal cases, a dense, intact, slow growing and protective chromia scale is expected for steels in high temperature environment. But in some cases, non-protective iron rich oxide scales suddenly grow dramatically, which is called as "breakaway oxidation". The reasons motivating the onset of breakaway oxidation have been investigated for around eighty years. Generally, they can be divided into chemical attacks and mechanical attacks [*Caplan et al., 1952*]. According to Evan, breakaway oxidation was mainly attributed to chemical attacks (Cr depletion) at higher temperature (> 1117˚) while at lower temperature both of them play a role [*Evans et al., 1999*]. According to Evans, chemical attacks mean that the protective oxide (e.g. chromia) becomes thermodynamically unstable due to the alloy composition at the MO/M interface. On the other hand, mechanical attacks mean that cracking or spalling of protective oxide scale (e.g. chromia) occurs and less-stable oxides (e.g., magnetite or iron and chromium spinel oxide) subsequently form. Col gave a comprehensive description of microstructure evolution for the breakaway oxidation of austenitic stainless steel at 850˚C in oxygen [*Col et al., 2017*]. She emphasized that Cr depletion beneath the oxide after long-time oxidation caused oxide constituent and microstructure conversion, i.e., chromia transformed to Fe-Cr spinel, subsequently to a two-layer oxide nodule consisting of inner Fe-Cr spinel (Fe-Ni metallic compounds contained) and outer Fe-rich oxide, then the zone of nodule extended laterally until

the neighboring grain boundaries and continuously consumed Cr supplied from grain boundaries. Finally the inner reaction zone stopped at where chromia scale or a new surface defect existed. Habib found that AISI 316 stainless steel had higher breakaway oxidation resistance at 1100˚C in air than another austenitic AISI 304 stainless steel [*Habib et al., 2011*]. In addition, some factors have been investigated, such as alloyed sulphur (MnS inclusion) which aggravates Cr locally depleted by trapping Cr in the shape of Cr-Mn oxysulfide in the subscale of steels [*Pascal et al., 2015*]; surface finish which influences the initial microstructure of oxide scales (ground surface: a homogeneous oxide layer; polished surface: preferred oxide islands) [*Green et al., 2014*].

2.3.5 Effects of water vapor

A great deal of information concerning high temperature oxidation of stainless steel in aqueous environment has been reported since more attention was given to the influence of water vapor [*Robertson, 1991, Stellwag, 1998*]. A series of related questions were proposed during the international workshop on high-temperature corrosion in 1996 [*Douglass et al., 1996*], where discussions about hydrogen defects and diffusion paths of oxidant were dominated. Corresponding comments were given but definite answers still need further research. This section will introduce some focuses and their recent progresses.

2.3.5.1 Defects

Water plays various roles in high temperature chemical reactions since water can be as a reactant, product and catalyst [*Akiya et al., 2002*]. For high temperature oxidation, water vapor can modify the defect structures of oxides, and thus impacts the essential mass transport, simultaneously with new oxidation mechanisms proposed. The remarkable achievement of Kofstad shows that the main defects of oxides during high temperature oxidation are oxygen vacancies at low oxygen pressure or metal vacancies at high oxygen pressure [*Kofstad, 1988, Kofstad, 1989, Kofstad, 1995*]. Researchers also studied the protonic defects on high temperature oxidation such as [*Norby et al., 1997, Norby Truls, 2004*] since the proton $H^{\cdot}$ was generally accepted as the transport species in the presence of water vapor [*Iwahara et al., 1982, Norby et al., 1986*]. Protons usually rotate around their host oxygen ions with quite low activation energy, and thus temporary hydrogen bonds form with nearby oxygens rather than jump directly into the sublattices of oxygen [*Norby Truls, 2004*]. Norby also divided oxygen partial pressure into three regimes, i.e., low p_{O_2} ($[e'] = 2[V_O^{\cdot\cdot}]$), intermediate p_{O_2} ($[e'] = [H_i^{\cdot}]$), and high p_{O_2} ($3[V_M'''] = [H_i^{\cdot}]$), so as to respectively discuss the concentration of M_2O_3-type oxide defects as a function of oxygen partial pressure [*Norby, 1993*]. Based on the work of Norby, Chandra-Ambhorn proposed a Kröger-Vink diagram showing the effect of water vapor

on oxygen and metal vacancy defect concentrations as a function of partial oxygen pressure [*Chandra-ambhorn et al., 2019*], as illustrated in Figure 2.11.

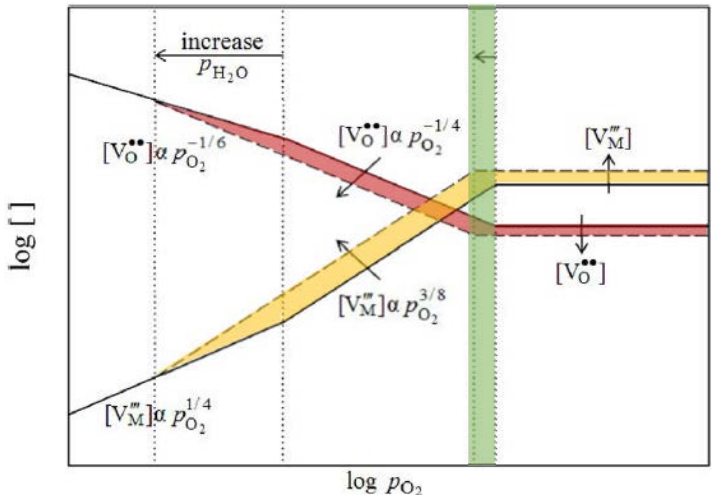

*Figure 2.11 Kröger-Vink diagram showing the effect of water vapor on oxygen and metal vacancy defect concentrations versus partial oxygen pressure [*Chandra-ambhorn et al., 2019*]*

For M_2O_3-type oxide, which is the main oxidation product formed on Fe-15.7Cr-8.5Mn at 700˚C in O_2 containing 9vol.% water, the effects of water vapor on defect structure can be attributed to the increase of metal vacancy concentration (yellow highlight) and corresponding decrease of oxygen vacancy concentration (red highlight) at high and intermediate partial oxygen pressure, as well as the expansion of the region (green highlight) where metal vacancy is the predominant defect.

Holt also studied the defect structure of impurity doped Cr_2O_3 (spinel structure: $MO{\bullet}Cr_2O_3$) in aqueous environment [*Arve Holt, 1994b*], suggesting the electroneutrality condition as:

$$[H_i^{\cdot}] + 2[V_O^{\cdot\cdot}] = [M_{Cr}'], \tag{2.38}$$

where M_{Cr}' represents that lower valent impurities (M^{2+}) constituent the defects in Cr matrix with effective negative charges, which are compensated by protonic defects and oxygen vacancies at reduced oxygen activity.

2.3.5.2 Morphology

The morphology of oxide microstructure is of primary significance in almost any reports concerning high temperature oxidation of steels. Two representative cross-sectional observations of steels oxidized at 600 – 700˚C with and without water vapor for different oxidation durations are illustrated in Figure 2.12, indicating the influence of water vapor on

microstructures of oxide scales formed on steels with consideration of early stage and long-time oxidation.

Left: *30-min* oxidation of Fe-18Cr-9Ni-3Cu austenitic stainless steel at 700˚C in air with 20% water vapor

Right: *100-hour* oxidation of Fe-9Cr ferritic steel at 650˚C in N_2-1%O_2-x%H_2O (x = 0 or 2 - 7)

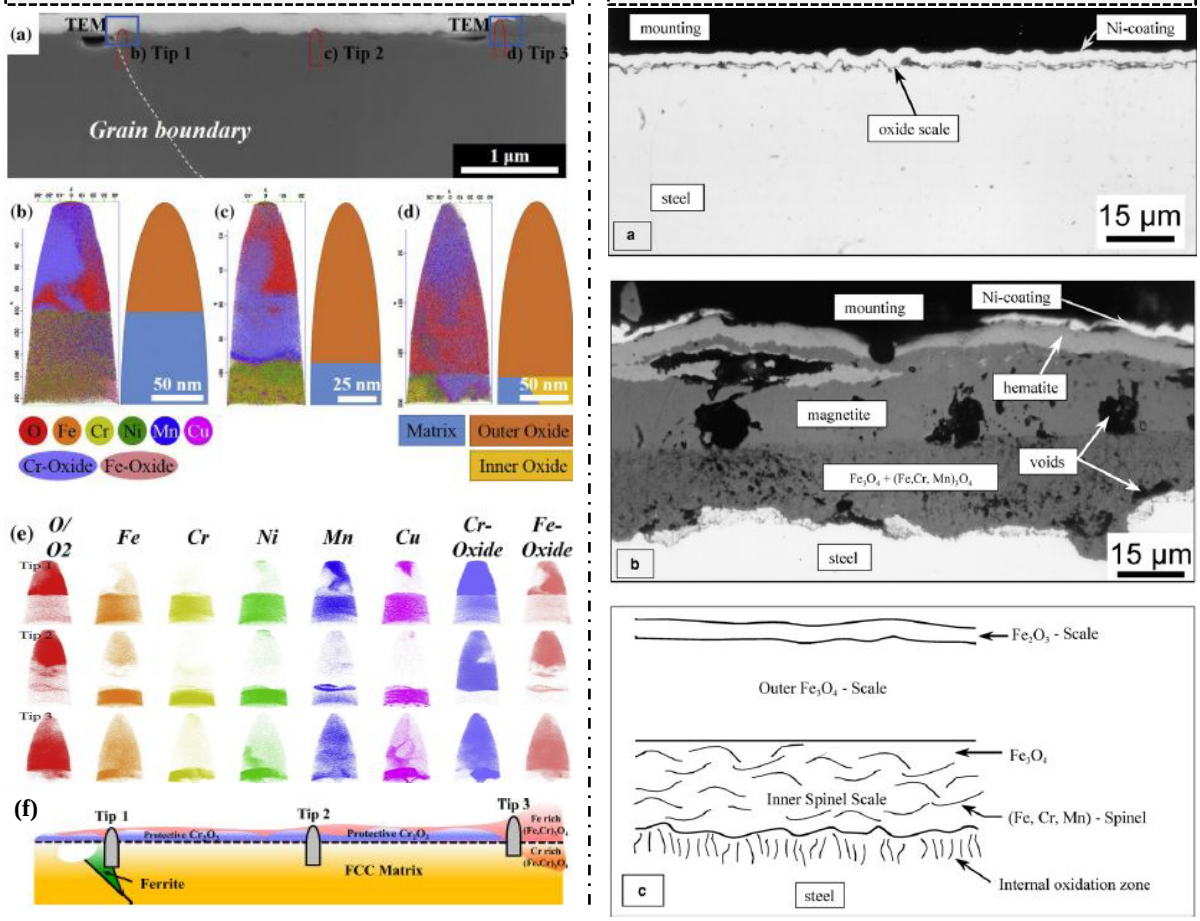

*Figure 2.12 Selected typical cross-sectional characterizations of oxide scales in the conditions marked in the upper highlight boxes, deriving respectively from [*Kim et al., 2015*] (Left); [*Ehlers et al., 2006*] (Right): TEM micrograph (Left-a); Overall 3-D atom elemental maps and stratified schematics showing chosen tips interested at grain boundary (Left-b), 2 μm away from grain boundary (Left-c) and 4 μm away from grain boundary (Left-c); reconstruction of individual element or oxide corresponding to those three tips (Left-e); schematic of oxide layer constitute (Left-f); SEM micrograph in dry gas (Right-a) and in wet gas (Right-b); schematic of oxide scale distribution in wet gas (Right-c).*

Some general conclusions can be qualitative obtained even though the components of substrate and contents of water vapor are different for these two representative examples. It shows that, overall, significant microstructural difference cannot be recognized between early stage

oxidation in wet air and long-time oxidation in dry gas. But for long-time oxidation, water vapor promotes oxide scale thickening dramatically, great numbers of voids forming and separation between inner and outer oxide layer occurring [*Ehlers et al., 2006*]. In particular, for early stage oxidation, the role of grain boundary cannot be neglected, which is reflected in water enhanced Kirkendall voids at MO/M interface and diffusion dependence oxide layer distribution related to water [*Kim et al., 2015*]. Oxidation products in the presence of water vapor cannot be determined only from these two examples due to the difficulty of reactive condition normalization for numerous experiments. However, they can be as a reference when the oxide constituent in this work is analyzed using the combination of SEM/EDX, XRD and XPS techniques.

2.3.5.3 Dissociation mechanism

The mechanism of H_2O transport in oxide scale had been not well explained and established until Fujii proposed a dissociated process [*Fujii et al., 1963*] for the oxidation of Fe-Cr alloy in $0.1H_2O$-0.9Ar at 700 - 1000˚C. He further introduced such a dissociation mechanism in detail [*Fujii et al., 1964*], which was schematically described in Figure 2.13.

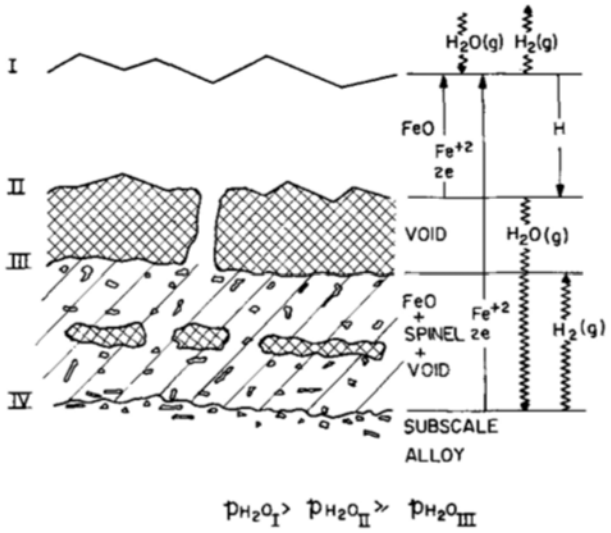

*Figure 2.13 Schematic of dissociation mechanism for the oxidation of Fe-Cr alloy in water vapor at high temperatures [*Fujii et al., 1964*]*

The key point is to understand how water transport accomplished within the hole so as to support the sustained growth of both inner and outer oxide scales. According to the views in [*Fujii et al., 1964*], it can be summarized with respect to Kröger-Vink notation [*Kröger et al., 1956*]:

- At gas/MO interface, water vapor in the exterior atmosphere has to be adsorbed to the surface of oxide with various defects, then the adsorbed H_2O decomposed to adsorbed H_2

through chemical reaction, and thus adsorbed H_2 either desorbs into the atmosphere or forms two protonic defects, expressed as:

$$H_2O(ads) \rightarrow H_2(ads) + O_O^x + V_{Fe}'' + 2h^{\cdot}, \tag{2.39}$$

$$H_2(ads) \leftrightarrow H^{\cdot}, \tag{2.40}$$

$$H_2(ads) \leftrightarrow H_2(g); \tag{2.41}$$

- The reactions similar to Equations (2.39) - (2.41) also happen at inner interface marked as III.
- At the interface marked as II, hydrogen generated from the above two interfacial reactions (either protonic defects or hydrogen) first becomes adsorbed hydrogen, and subsequently facilitates the transport of oxygen by regenerating H_2O, by:

$$2H^{\cdot} \leftrightarrow H_2(ads), \tag{2.42}$$

$$H_2(g) \leftrightarrow H_2(ads), \tag{2.43}$$

$$H_2(ads) + O_O^x + V_{Fe}'' + 2h^{\cdot} \rightarrow H_2O(ads), \tag{2.44}$$

$$H_2O(ads) \leftrightarrow H_2O(g); \tag{2.45}$$

A small composition change accordingly occurs in the inner spinel oxide, as:

$$FeCr_2O_4 + 4FeO \rightarrow 2CrFe_2O_4 + Fe_i^{\cdot\cdot} + 2e'. \tag{2.46}$$

At the same time, Rahmel and Tobolski suggested that water transport across voids in the scale was attributed to an oxidation/reduction ($H_2 \leftrightarrow H_2O$) mechanism [*Rahmel et al., 1965a*], which was schematically displayed in [*Othman et al., 2009a*], as shown in Figure 2.14.

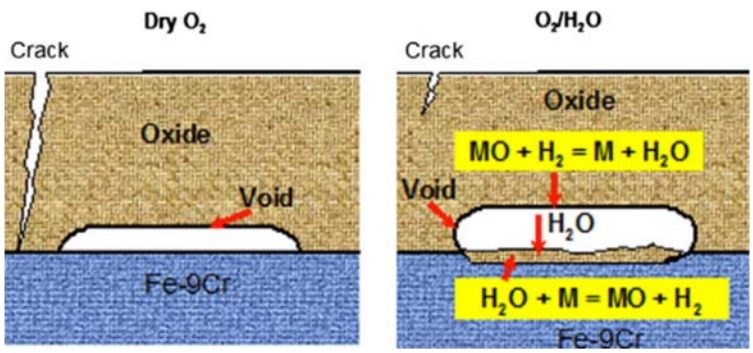

*Figure 2.14 Schematic showing oxygen transfer across a scale void carried by water molecular [*Othman et al., 2009a*]*

The dissociation mechanism has been demonstrated by more and more evidences thanks to the hydrogen penetration profiling techniques. Normally these techniques can be divided into two

groups, i.e., the in-situ hydrogen permeation experiment and commonly used ex-situ analysis after oxidation in humid environment. An in-situ hydrogen permeation experiment for ferritic steel boiler in a steam and air dual environment implied that the dissociation mechanism accounted for the increased oxidation rate at air side. [*Nakagawa et al., 2003*]. Ex-situ analysis mainly includes thermal desorption spectroscopy to determine the presence or absence of hydrogen [*Yamauchi et al., 2006*], glow discharge spectrometry to show hydrogen ingress track [*Hänsel et al., 2010, Dumerval et al., 2014*] and D_2O isotropic tracer method cooperated with secondary ion mass spectrometry [*Brady et al., 2011, Ardigo et al., 2012, Hänsel et al., 2010*]. All results confirm a fact that water vapor changes the oxidation mechanism by a dissociation mechanism, and simultaneously provide more information. Hydrogen is often detected at the M/MO interface and even in the sublattice of underlying substrate [*Brady et al., 2011, Dumerval et al., 2014*]. Brady also suggested that few hydrogen detected in austenitic stainless steel after oxidation in air containing 10% D_2O at 800 ˚C was attributed to two possibilities, i.e., large hydrogen solubility of FCC structure and thus lack of hydrogen detected in oxide scale as well as the effects of Mn and Si correlated to the formation of spinel and SiO_2 [*Brady et al., 2011*]. Dumerval proposed that the oxide growth of AISI 316L stainless steel in PWR primary water depended on anion inward diffusion, and oxygen and hydrogen were not coupled in a single molecule during the penetration process [*Dumerval et al., 2014*]. However, the growth of spinel oxide, $MnCr_2O_4$, cannot be assisted by the hydrogen containing oxygen at low oxygen partial pressure, so the dissociation mechanism is not efficient in this case [*Hänsel et al., 2010*]. Moreover, some simulations have been done to verify this mechanism, such as the chemical molecular dynamics approach in [*Das et al., 2009*].

2.3.5.4 Water promoted void formation

As mentioned in the previous section, a great number of voids forms at the M/MO interface and within the oxide scale in presence of water vapor, and simultaneously the dissociation mechanism established on the existence of voids facilitates faster scaling rates. Luo, Su and Yan demonstrated the role of water vapor in void formation and concomitant diffusion process by combing advanced in-situ TEM observations and DFT first principles calculations [*Luo et al., 2018*], the main results of which are shown in Figure 2.15. In dry and wet environment, NiO grew following the layer by layer mechanism. No vacancies were observed in the oxide formed in O_2, while, the evolution from vacancy generation and movement to annihilation (marked by yellow arrows) was found in the scale formed in H_2O. The presence of protonic defects facilitated to decrease the formation energy of vacancy (ΔE = -2.83 eV) and vacancy cluster ((ΔE = -0.7 eV) in the oxide scale, and at the same time to reduce the Ni diffusion barrier

(from 1.44 eV to 0.48 eV). Therefore, water vapor enhances void (the final shape of vacancy clusters) formation as well as metallic cation diffusion whereby it promoted oxide growth.

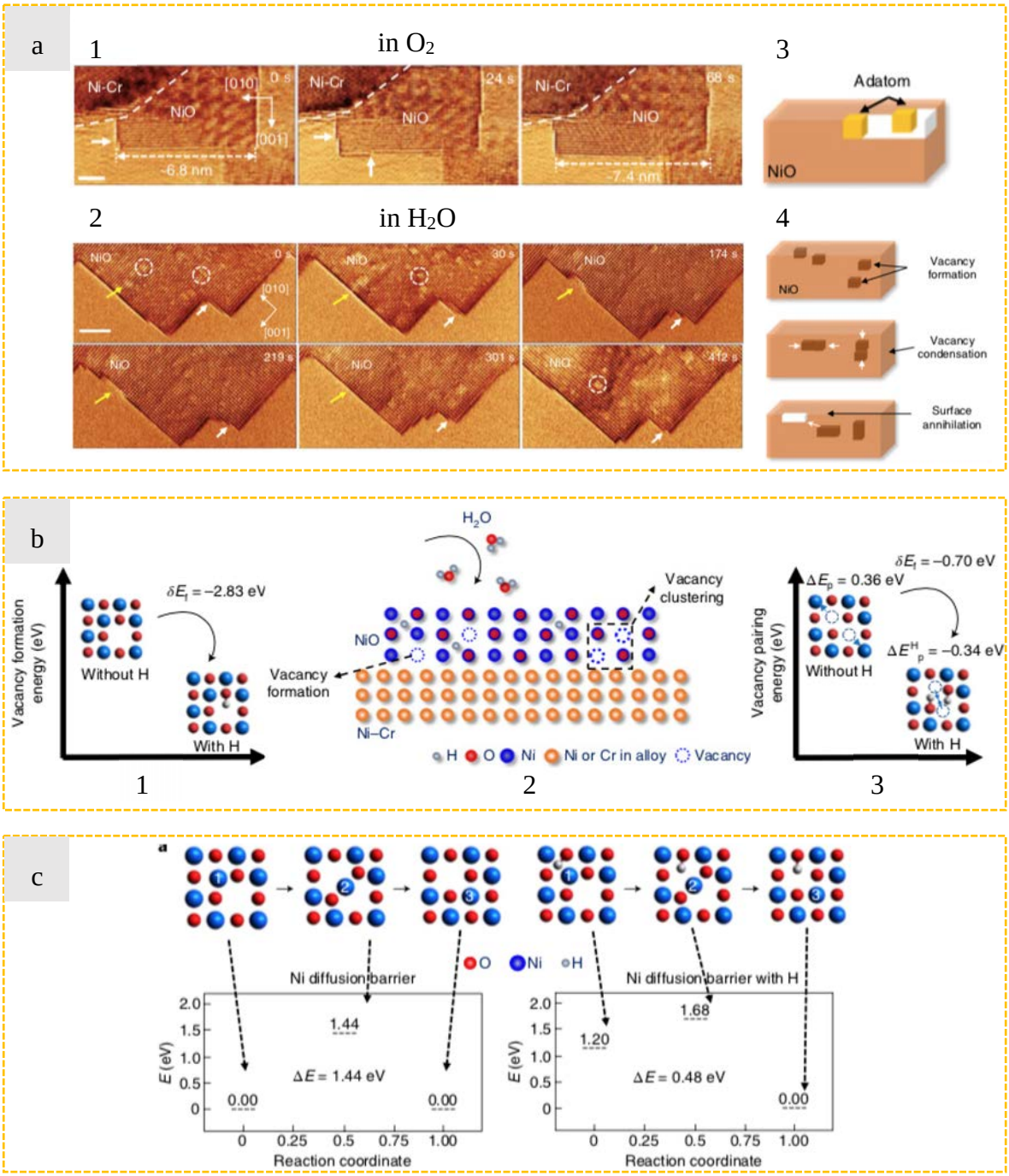

Figure 2.15 Diagram illustrating water-vapor-promoted alloy oxidation: in-situ TEM micrographs showing nickel oxide growth in O_2 and H_2O with corresponding schematics (a) (a-1 and a-3: in O2; a-2 and a-4: in H_2O); formation process of vacancy and vacancy cluster (b) (b-2: schematic showing in atomic scale water promoted vacancy generation and vacancy clustering; b-1 DFT calculation result showing the vacancy formation energy difference without and with H; b-3: DFT calculation results showing vacancy pair formation energy

*without and with H as well as related energy difference); DFT calculation results showing diffusion barriers without and with H (c) [*Luo et al., 2018*]*

2.3.5.5 Volatilization

A great deal of thermogravimetric analysis about mass loss has been published in regard to the oxidation of chromia forming steel at high temperature in presence of water vapor such as [*Asteman et al., 1999*]. The mass loss is mainly attributed to the evaporation of oxide promoted by water vapor or high temperature. In the case of stainless steel, this volatile is primarily supposed to be Cr-rich oxide or oxyhydroxide. Some researchers calculated the stabilities of Cr-containing volatiles under various conditions [*Ebbinghaus, 1993, Beverskog et al., 1997, Opila et al., 2007*], and reached a consensus that $CrO_2(OH)_2$ is the main product at moderate temperatures (500 – 900˚C) while CrO_3 at higher temperatures, as shown in Figure 2.16.

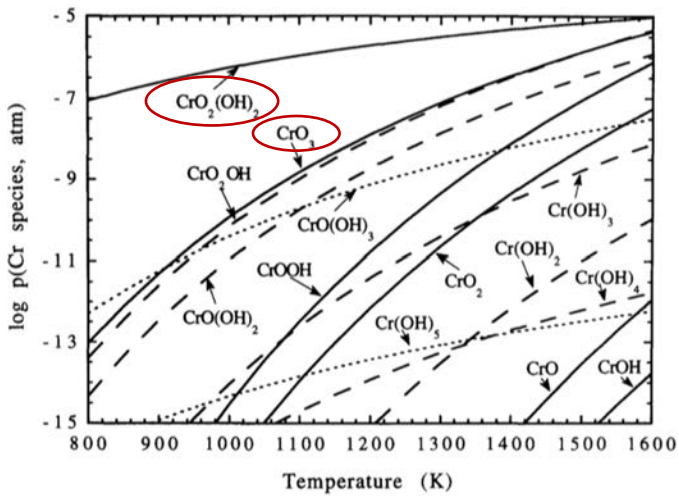

*Figure 2.16 Logarithm of partial pressure of Cr oxide and oxyhydroxide vapor species above Cr_2O_3 (s) as a function of temperature ($p_{H_2O} = 0.1$ atm, $p_{O_2} = 0.1$ atm) [*Ebbinghaus, 1993*]*

In recent years, a denuder accessory coated with Na_2CO_3 inside and equipped at the gas outlet has been gradually employed to estimate the mass loss caused by $CrO_2(OH)_2$ [*Sachitanand et al., 2013, Falk-Windisch et al., 2015, Pour-Ali et al., 2019*], where the chemical reaction is:

$$CrO_2(OH)_2(g) + Na_2CO_3(s) \rightarrow Na_2CrO_4(s) + H_2O(g) + CO_2(g). \qquad (2.47)$$

In addition, Asteman carried out a series of investigations about the effects of gas flow rate on Cr evaporation during steel oxidation at 500 – 800˚C in O_2 without and with (10% and 40%) water vapor [*Asteman et al., 2000, H. Asteman, 2002a, H. Asteman, 2002b*]. He summarized that oxidation rate showed gas flow rate dependence due to the diffusion-controlled evaporation process, and consequently local spallation of protective oxide scale occurred rapidly at highest temperature with fastest gas flow.

2.3.5.6 Growth kinetics

Similar to Section 2.3.2, some parabolic rate constants are listed in Table 2.5, indicating the difference between the dry and wet atmospheres.

Table 2.5 Oxidation parabolic constant values (chromium oxide growth)

Substrate	Temperature (˚C)	Atmosphere	k_p ($g^2cm^{-4}s^{-1}$)	Ref.
Ferritic Fe-17Cr alloy	700	Ar+20%O_2	1.5×10^{-14}	[*Othman et al., 2009b*]
		Ar+20%O_2+5%H_2O	2.0×10^{-13}	
		Ar+5%O_2+20%H_2O	3.5×10^{-13}	
		Ar+10%H_2+5%H_2O	2.5×10^{-13}	
Ferritic AISI 439	900	Air	1.6×10^{-12}	[*Huntz et al., 2007*]
		Air+8%H_2O	1.8×10^{-12}	
		Ar/H_2+H_2O	1.5×10^{-12}	
Austenitic AISI 304	900	Air	$6{,}9 \times 10^{-13}$	
		Air+8%H_2O	6.5×10^{-13}	
		Ar/H_2+H_2O	3.2×10^{-13}	
Austenitic AISI 316L	800	Air	4.8×10^{-14}	[*Buscail et al., 2015*]
		Air+10%H_2O	3.5×10^{-14}	
	900	Air	5.8×10^{-14}	
		Air+10%H_2O	2.6×10^{-13}	

All mentioned above indicates that water vapor can promote the oxidation scaling rate. However, the parabolic rate constants in Table 2.5 seem not to absolutely support this viewpoint. The decrease of rate constant can ascribe to the evaporation of Cr, as demonstrated in [*Buscail et al., 2015*]. Before talking about the effects of water vapor, it is necessary to distinguish between two cases, i.e., O_2-poor and O_2-rich circumstances [*Jonsson et al., 2013*]. In the O_2-poor condition, the predominant oxidant is water, the concentration of which necessarily impacts both the oxidation kinetics and thermodynamics. In the O_2-rich condition, on the contrary, the dominant oxidant is oxygen, the absorption of which on the scale surface is not expected to be influenced by water vapor. Hansel once proposed that the effects of water vapor could be neglectable at high oxygen partial pressure and only visible with oxygen partial pressure relatively reduced. This was reflected in the modification of oxide defects, oxidation rate and morphology [*M. Hansel, 2003*]. But a general law cannot be obtained simply relying

on these rate constants. Water vapor changes the defect structure of oxide scale (see Section 2.3.5.1) and oxygen partial pressure gradient within the oxide scale formed on steels, and thus impacts the diffusion kinetics. Besides, water vapor causes volatiles, observed intuitively in mass gain curves, and influences the accuracy of kinetics calculation. Therefore, for kinetics study of stainless-steel oxidation, a specific analysis should be made according to specific circumstance.

2.3.5.7 Mechanical aspects

The reports focusing on the influence of water vapor on mechanical behaviors in oxide scales are rare. The corrosion fatigue cracks prefers initiating and propagating in presence of water vapor for 316LN SS oxidized respectively in 320˚C water and dry air [*Wu et al., 2015*]. Wu found that water lowered the mechanical properties of oxide scales as well as promoted the formation of more complex oxide distribution. Xiao investigated the residual stresses in oxide scales formed on Inconel 600 at 600 – 900 ˚C in dry and wet air, finding that compressive residual stresses increased with increasing humidity [*Xiao et al., 2013*]. He also inferred that this change mainly ascribed to the growth stress affected by water vapor. Further analyses concerning the related phenomena have been tried, which will be introduced in two parts.

On fracture

That water reduces the resistance to fracture has been demonstrated in SiO_2 thin films [*McElhaney et al., 2004*]. However, Yamauchi measured the values of Vickers hardness for oxide scales formed on AISI 900˚C in N_2-3%O_2, N_2-2.4%O_2-19.7H_2O and N_2-19.7H_2O respectively, indicating that water vapor lowered the Vickers hardness and thus increase the brittleness of chromium oxide [*Yamauchi et al., 2006*]. He proposed that the water vapor induced mechanical property degradation of chromium oxide was lack of evidence. Galerie suggested that iron nucleated at the initiation of chromia scale fracture, thus the breakdown of chromia layer ascribed to the further iron oxide fast growth promoted by water [*Galerie et al., 2014*]. He interpreted this mechanism from both views of thermodynamics and kinetics respectively, that the stability of hematite could be satisfied in the void at M/MO interface whereby nodule of iron oxide gradually formed; hematite showed a good affinity with water because its more acidic property, thus preferred forming nodules at the crack tip or in an interfacial void compared with chromia. Othman proposed that the stored strain energy in chromia might be greater than that required for cracking or locally spalling when the thickness of oxide became large enough; the thickening rate of chromia could be increased in the presence of water vapor during the isothermal oxidation process. These could qualitatively explain that mechanical damages (cracking or spalling) of chromia occurred earlier in wet air than in dry

air for Fe-xCr (x= 12 - 20) alloy oxidized between 600˚C and 700˚C. [*Othman et al., 2010*]. Yuan agreed that hydrogen derived from water played a detrimental role in the integrity of chromia scale because it enhance the buckling and cracking [*Yuan et al., 2016*]. According to him, hydrogen permeated into the void at M/MO interface, resulting in a hydrogen trap and raising the pressure within the void gradually, thus promoted buckling formation. Scale cracking occurred when the stress reached the critical one.

On scale adhesion

Chandra-ambhorn thought that water vapor contributes to the connection between the scale and substrate [*Chandra-Ambhorn et al., 2007*], based on the results of tensile tests under SEM for oxide scales formed on ferritic stainless steels at 800˚C. He found that a lower spallation ratio occurred in presence of water vapor. The similar results with the same approach was also achieved in his later report in regard to the oxide scales formed on Fe-15.7Cr-8.5Mn austenitic stainless steel at 700˚C in oxygen and oxygen with 9% water [*Chandra-ambhorn et al., 2019*].

2.4 Mechanical behaviors of oxide scales

When steels are exposed to corrosive atmosphere at high temperature, oxide scales are gradually subject to mechanical stresses caused by various factors, simultaneously accompanied with stress releases. After high temperature oxidation, part of stress may still remain in oxide scales without external loading, known as residual stress. It is of great significance to study the stress state in oxide scales due to its decisive role in affecting lifetime of component. From a technical point of view, the onset of breakaway oxidation means the end of the service for a component. As mentioned above, at moderated temperatures, not only chemical attacks determine the breakaway oxidation of steels but also mechanical attacks too. Therefore, the study of oxidation behaviors of steels at high temperatures should consider the oxidation process and mechanical stress together, which are coupled together. This section will briefly present the possible causes of stress generation and release during oxidation and the role of residual stresses, as well as the damage process of oxide scales.

2.4.1 Stress generation

The origins of stress in oxide scales have been discussed and summarized in some excellent review articles such as [*Stringer, 1970*], [*Hancock et al., 1974*], [*Evans, 1995*], [*Schütze, 1997*] etc. According to the recent report of Schüze [*Schütze, 2016*], stresses during oxidation usually involves intrinsic growth stresses, thermally induced stresses, geometrically induced stresses (e.g., curved substrate surface) and external stresses (e.g., constraints in structures), where the previous two are primarily considered in this thesis.

2.4.1.1 Intrinsic growth stresses

Several models for intrinsic growth stresses of oxide scales formed on alloys at high temperatures has been proposed for the past fifty years, including Pilling-Bedworth ratio, epitaxial relationship between oxide and metal, compositional changes in either the alloy or oxide, vacancy condensation, recrystallisation, lateral growth of new oxide within the oxide scale, which will be briefly introduced in this part.

Pilling-Bedworth model

Pilling-Bedworth model is the oldest one to interpret the stress in the oxide [*Bedworth et al., 1923*]. When an oxide forms at M/MO interface, the volume change for alloy can be expressed with PBR (Pilling-Bedworth ratio) as [*Xu et al., 2000*]:

$$\mathrm{PBR}_{\mathrm{alloy}} = \frac{\text{volume of a mole of } \mathrm{B}_x\mathrm{O}_y}{\text{volume of } x \text{ moles of B in alloy}}, \tag{2.48}$$

if $\mathrm{PBR}_{\mathrm{alloy}} > 1$, the stress yielded is compressive, while if $\mathrm{PBR}_{\mathrm{alloy}} > 1$, the stress is tensile. The strain in the oxide can then be evaluated based on PBR, given by [*Bernstein, 1991*]:

$$\varepsilon_{\mathrm{ox}} = \omega\left[(\mathrm{PBR})^{1/3} - 1\right], \tag{2.49}$$

where ω is a factor concerning the possible stress-reducing processes.

Pilling-Bedworth model has been well used in the case that anion inward diffusion is predominant, however, many oxide formations are mainly supported by cation outward diffusion or both. For instance, Rhines and Wolf suggested that NiO formed on surfaces where nickel and oxygen fluxes contacted [*Rhines et al., 1970*]. They further proposed that the correlated stresses were the results of the strain mismatches at grain boundaries perpendicular to various interfaces. After that, Evans modified the Pilling-Bedworth model, by regarding the grain boundary as a short circuit diffusion path for oxygen migration to M/MO interface [*Evans, 1983*]. Consequently, the Pilling-Bedworth model can be employed at these interfaces where oxide intrusion forms by oxygen inward transport along grain boundaries, as shown in Figure 2.17.

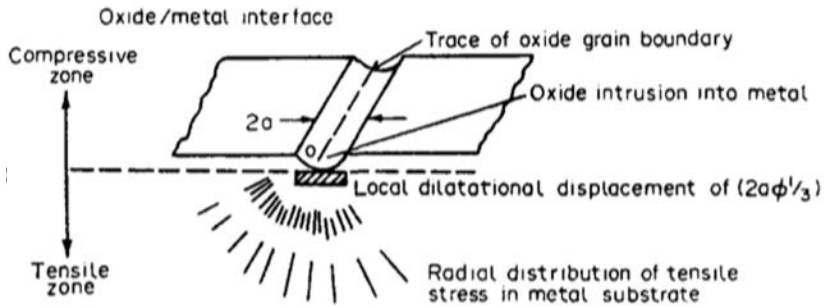

*Figure 2.17 Improved Pilling-Bedworth model illustrating the oxide intrusion at M/MO interface created by anion inward diffusion [*Evans, 1983*]*

Epitaxial stress

The lattice mismatch between the metal and oxide causes epitaxial stresses. Normally, this stress appears at M/MO interface with the maximum value and decreases to zero at the oxide surface. It shows the film thickness dependence, for instance, the influence of epitaxial stress on distortion becomes less with increasing the Cu_2O film thickness [*Borie et al., 1962*]. Epitaxial stress is especially active for thin film at low temperature [*Hancock et al., 1974*], and thus it will not be considered in this thesis.

Compositional change induced stress

Growth stress can be induced due to the compositional changes in either the alloy or oxide. Selective oxidation can create a reacting metallic component depletion zone within the subscale of alloy, modifying the lattice constant thus giving rise to stress [*Birks et al., 2006*]. Stress also appears in the oxide with a wide stoichiometry range such as FeO [*Stringer, 1970*]. Howes proposed that the initial tensile stress in $(Cr, Fe)_2O_3$ and subsequent compressive stress were attributed to increasing Cr and the transition from $(Cr, Fe)_2O_3$ to $(Fe, Cr)_3O_4$ respectively [*Howes et al., 1969*].

Vacancy related stress

The effect of vacancy on growth stress has been controversial. The oxide growth relying on cation outward diffusion usually accompanies with a vacancy inward diffusion flux, and thus stress develops with a vacancy concentration gradient formed within the oxide [*Stringer, 1970*]. Moreover, vacancies at M/MO interface may be annihilated, but those which are not completely annihilated may migrate along interface, thus form voids as a result of the mismatch between metal and oxide [*Howes et al., 1969*]. Vacancies can also migrate into metal and condense to nucleate voids along grain boundaries. This process may cause stress due to the shrinkage of metal, such as the growth stress for nickel oxidation. Meanwhile such a void is beneficial to the

creep of substrate, which is known as a stress relief process [*Stott et al., 1994*]. Another recent mechanism related to the Kirkendall effect in the alloy indicates that tensile stress in the substrate near the M/MO interface accounts for the formation of interfacial voids. Due to selective oxidation, different metallic components diffuse in opposite directions at different rates in the alloy. Such nonreciprocal diffusion and the interfacial process induce stress in the alloy, having a close relation to the oxidation mechanism [*Suo et al., 2003*].

Recrystallisation induced stress

Jaenicke suggested that the recrystallisation process contributed to stress generation for the oxidation of copper (e.g., total growth stress for Cu_2O is around 1.17 GPa; oxidation condition: 300˚C, in oxygen with $p_{O_2} = 0.18$ atm, 600 nm in thickness) [*Jaenicke et al., 1958, Jaenicke et al., 1964*]. It is more likely, however, to be a result of stress relief. For instance, during the oxidation of a grain-refined AISI 430 stainless steel at 1250˚C, Fe containing nodules start nucleation when grain boundaries of alloy migrate accompanied with stress released [*Horibe et al., 1975*]. In this work, recrystallisation induced stresses will not be analyzed in detail because of the limited techniques applied.

Lateral oxide growth stress

Among various stress contributors for the oxidation on a flat substrate, Schütze affirmed the most essential factor was the lateral growth when new oxide formed within the oxide scale [*Schütze, 1997*]. The defect structure study of Atkinson implied that stress could be generated when new oxide grew along grain boundaries perpendicular to the surface [*Atkinson, 1982*]. Srolowitz once gave a formula to calculate such stress σ_{ox} in the lateral direction based on elastic mechanics:

$$\sigma_{\mathrm{ox}} = (4G_{\mathrm{ox}}d_i')/[2\delta(1-2v_{\mathrm{ox}})], \tag{2.50}$$

where G_{ox} and v_{ox} are the shear modulus and Poisson's ratio of the oxide; d_i' the conceivable thickness for the new oxide formed on the oxide grains; δ the oxide grain size. Equation (2.50) requires $d \gg \delta$, where d is the thickness of the surface scale [*Srolovitz et al., 1984*]. Similarly, Stott further inferred that stresses might be derived from the intersections between perpendicular grain boundaries and M/MO interface, which was in accordance with the improved Pilling-Bedworth model [*Evans, 1983*] and the observation of Rhines and Wolf [*Rhines et al., 1970*]. The value in the study of Stott is that it describes the microscopic spatial stress field and its time evolution on the premise that oxidation counts on the grain boundary diffusion [*Stott et al., 1994*]. From the experimental aspect, for instance, the wrinkled surface of alumina has been reported as a response to the stress accumulation caused by lateral oxide

growth [*Huntz et al., 1994, V. K. Tolpygo, 1998, Clarke, 2003*], as seen in Figure 2.18.a. Recently, a model conceptually describing the lateral growth strain rate has been proposed by Clarke, with consideration of geometric structures instead of defect structures, which is suitable for those oxides grown through grain boundary diffusion [*Clarke, 2003*]. A small part of the countercurrent migrating Al and O ions are trapped at dislocation cores, activating the dislocation climb. The lateral growth strain is discussed in two cases, i.e., at the dislocation core with a Burgers vector parallel to the M/MO interface (point A in Figure 2.18.b) and at the other with a Burgers vector normal to the M/MO interface (point B in Figure 2.18.b). And only the former case contributes to the lateral growth strain because in the latter case, a rigid body displacement perpendicular to the M/MO interface will appear rather than lateral growth strain.

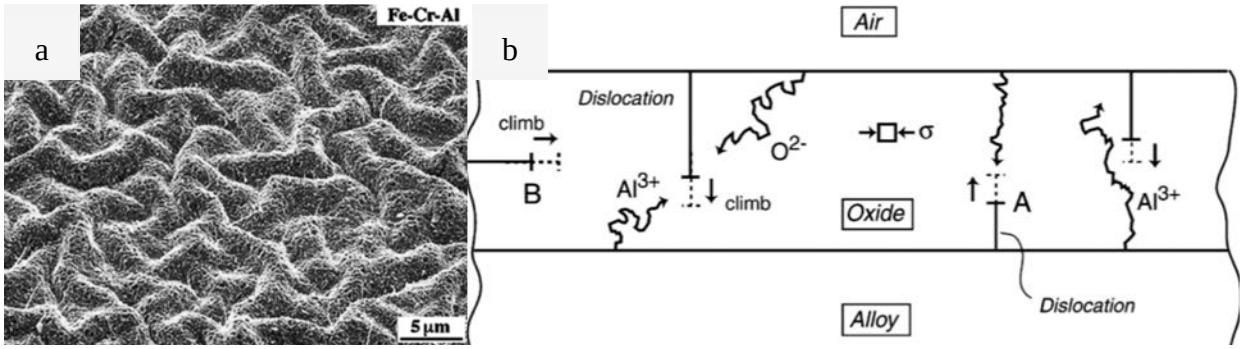

*Figure 2.18 Micrograph of wrinkled alumina surface (a); schematic of the dislocation climb model proposed by Clarke (b): A lateral growth strain generates at A with a Burgers vector parallel to the M/MO interface, while no lateral strain forms at B where the Burgers vector is perpendicular to the interface [*Clarke, 2003*]*

The proposal of Clarke gives a linear relation between the lateral growth strain rate $\dot{\varepsilon}_{\mathrm{ox}}$ and oxide thickening rate $\dot{h}_{\mathrm{ox}}$ assuming no stress releases:

$$\dot{\varepsilon}_{\mathrm{ox}} = \left[(A\theta' R')/\left(ab\bar{\xi}\right)\right]\dot{h}_{\mathrm{ox}} \tag{2.51}$$

where A is the cross-section for a diffusing cation to attach to the dislocation core; θ' the misorientation angle between grain boundary and surface; R' the ratio of the outward cation flux to the inward oxygen flux; a the average distance between traps; b the Burgers vector of the dislocation; $\bar{\xi}$ the average thickness of grain boundaries. His proposal has been successfully applied in modelling [*Panicaud et al., 2006, Panicaud et al., 2008*].

2.4.1.2 Thermally induced stresses

When an oxidized alloy is cooled from high temperature, stress generates at the M/MO interface. The so-called thermal stress ascribes to the different thermal expansion coefficients between the alloy and oxide.

The relation between the in-plane stress in the oxide σ_{ox} generated during cooling process is proposed [*Timoshenko, 1925, Tien et al., 1975*] as:

$$\sigma_{\mathrm{ox}} = [-E_{\mathrm{ox}}\Delta T(\alpha_{\mathrm{m}} - \alpha_{\mathrm{ox}})]/[(E_{\mathrm{ox}}/E_{\mathrm{m}})(d_{\mathrm{ox}}/d_{\mathrm{m}})(1 - v_{\mathrm{m}}) + (1 - v_{\mathrm{ox}})], \quad (2.52)$$

where E_{ox} and E_{m} are the elastic moduli of the oxide and the alloy respectively; α_{ox} and α_{m} the thermal expansion coefficients of the oxide and the alloy respectively; d_{ox} and d_{m} the thicknesses of the oxide scale and the alloy substrate respectively; v_{ox} and v_{m} the Poisson's ratios of the oxide and the alloy respectively; ΔT the temperature difference. For systems with rather thin oxide scale and relatively thick substrate, which share similar Poisson's ratios, Equation (2.52) can thus be simplified to:

$$\sigma_{\mathrm{ox}} = [-E_{\mathrm{ox}}\Delta T(\alpha_{\mathrm{m}} - \alpha_{\mathrm{ox}})]/(1 - v), \quad (2.53)$$

where v is the Poisson's ratio assuming $v_{\mathrm{ox}} \approx v_{\mathrm{m}} = v$.

Lin and Stout also took into the temperature dependences of Young's moduli and thermal expansion coefficients of the oxide and alloy, and improved accordingly the expression of Tien, in the integral form of these two variables as a function of the temperature [*Stout et al., 1989*]. For multilayer oxide scales, Metcalfe and Manning developed an expression to calculate the thermal stress in the layer i of n layers [*Metcalfe et al., 1966*], as:

$$\sigma_i = \Delta T[E_i/(1 - v_i)][(\bar{\alpha} - \alpha_i)/(1 - \alpha_i\Delta T)], \quad (2.54)$$

where E_i, $\alpha_i$and v_i are the elastic modulus, thermal expansion coefficient and Poisson's ratio of i oxide; $\bar{\alpha}$ the average thermal expansion coefficient of the joint oxide scale, given by:

$$\bar{\alpha} = \{\textstyle\sum_i^n (d_i E_i \alpha_i)/[(1 - v_i)(1 - \alpha_i\Delta T)]\}/\{\sum_i^n (d_i E_i)/[(1 - v_i)(1 - \alpha_i\Delta T)]\}, \quad (2.55)$$

where d_i is the thickness of Oxide i. It should be noted that Equations (2.52) - (2.55) are based on linear elastic behaviors of the oxide and alloy, irrespective of any possible plastic deformation. The work of Barnes has taken into account only the creep of substrate with the oxide scale (e.g., chromia) deforming elastically, and regarded creep as a mechanism of stress relaxation [*john J. Barnes, 1989*]. According to him, cooling process causes a compressive stress in the film (with relatively high melting point and a low thermal expansion coefficient), hence tensile stress in the substrate (with a relatively high thermal expansion coefficient).

Moreover, the plastic deformation in the alloy probably leads to net tensile stresses in the oxide scales.

2.4.2 Stress release

The recent study of stress release in α-Cr_2O_3 oxide thin films indicates that grain boundary sliding, intra-film cracking and delamination are mainly responsible for the stress relief [*Guerain et al., 2017*]. The above three stress release mechanisms (the grain boundary sliding, intra-film cracking and delamination) indicate the complexity of stress relaxation during oxidation. To minimize the stored elastic energy, stress can release through either deformation without damages or with damages (cracking, detachment, spalling etc.)

2.4.2.1 Viscoplastic Deformation

To solve the stress issue of oxidation, the model which only considers the linear elastic behaviors is not enough, since the metal substrate at high temperature can easily deform plastically. Besides, the plastic deformation of oxide is not neglectable, indicated by some evidences such as those mentioned previously. This part will thus briefly introduce the plastic behaviors of oxides.

It has been accepted that a plastic deformation for a polycrystalline material should be activated at least five independent dislocation slip systems [*Von Mises, 1923*]. While for most oxides, the number of primary slip systems is far from the required one, for instance, two for alumina ((0001) and $\langle 11\bar{2}0\rangle$) [*Hancock et al., 1974*]. These oxides prefer forming cracks rather than the plastic deformation caused by dislocation glide. However, the secondary slip systems may take place with increasing temperature whereby dislocation glide becomes possible [*Evans et al., 1976*]. It can be deduced that low temperature plastic deformation has less significance for oxides. The creep behaviors at high temperature are thus likely to predominate, including dislocation creep, dynamic recrystallisation and diffusion creep. Normally diffusion creep is recognized in two cases, i.e., Nabarro-Herring creep (lattice diffusion) and Coble creep (grain boundary diffusion) [*Schütze, 1990*]. For the simple uniaxial tension, the relationship between the principal stress σ (principal strain rate $\dot{\varepsilon}$) and shear stress τ (shear strain rate $\dot{\gamma}$) can be expressed as [*Ashby, 1972*]:

$$\sigma = \tau/\sqrt{3} \tag{2.56}$$

$$\dot{\gamma} = \dot{\varepsilon}/\sqrt{3}, \tag{2.57}$$

Based on the above two basic equations as well as some other creep model equations reported in [*Frost et al., 1982*], Ashby proposed the deformation maps of several oxides to explain their

deformation mechanisms at a given temperature with a corresponding shear stress, such as chromia, as illustrated in Figure 2.19.

Three zones highlighted with distinct colors can be seen as well as two sets of lines being circled. The blue zone shows the low temperature plasticity mainly ascribes to the dislocation glide; the orange zone corresponds to the power law creep due to the combination of dislocation glide and climb; the green zone agrees to the diffusional flow, suggesting the stress leads to a diffusive flux through either lattice (Nabarro-Herring creep) or grain boundary (Coble creep), where the strain rate depends on the grain size. The lines in red or purple circles correspond to a series of critical stresses of crack occurrence calculated from the oxidation experiments for two chromia-forming alloys.

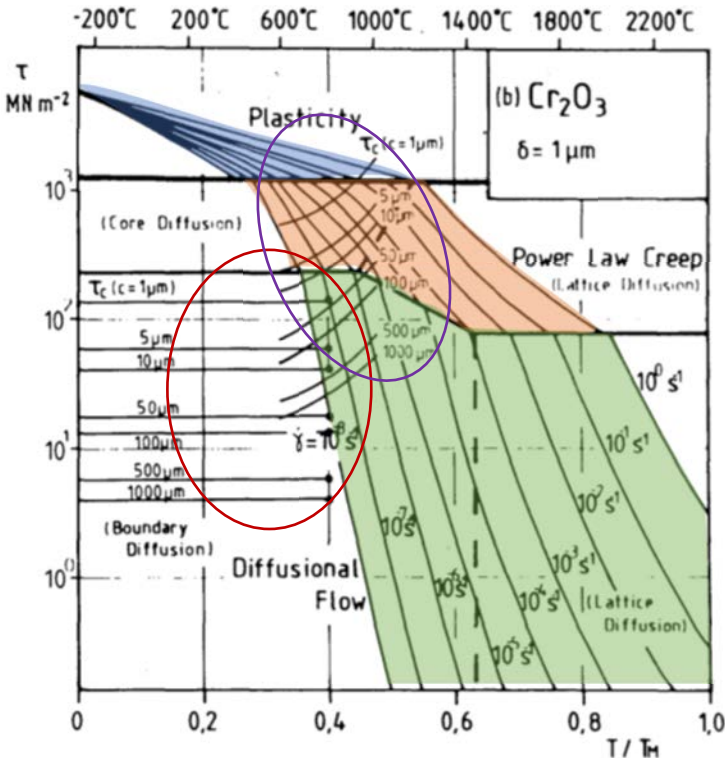

*Figure 2.19 Deformation map for chromia at the grain size of 1 μm [*Schütze, 1990*]*

2.4.2.2 Damage & self-healing

Evans has proposed qualitatively several possible damaging mechanisms of oxide scales corresponding to the cases of compression and tension respectively [*Evans, 1988*]. He described the processes in detail from the initial crack to the ultimate spallation, where two failure routes were applicable for the oxide layer under compressive stress, illustrated in Figure 2.20.

When the oxide scale is subject to tensile stress, a crack is likely to grow first, subsequently the stresses near the separated surfaces caused by the crack gradually release. More cracks are possible to form if the layer is subject to tensile stress. The zone between two through-scale

cracks can be damaged by the shear stress along the MO/M interface, leading to a final exfoliation. When the oxide scale is subject to compressive stress, two possibilities exist corresponding to the weak oxide/strong interface (Route I) and strong oxide/ weak interface (Route II) respectively. In Route I, shear stress promotes the formation of cracks within the oxide scale followed by debonding of the zone between two cracks. New surfaces generated through spalling appears, leading to stress relaxation and the displacement of oxides along the stress direction. In Route II, shear stresses perpendicular the interface motivate the interface separation. Then buckling is likely to form upon the decohesion zone whereby cracks generate along the interface to promote more serious debonding. The final spalling ascribes to the formation of cracks within the buckling oxide scale.

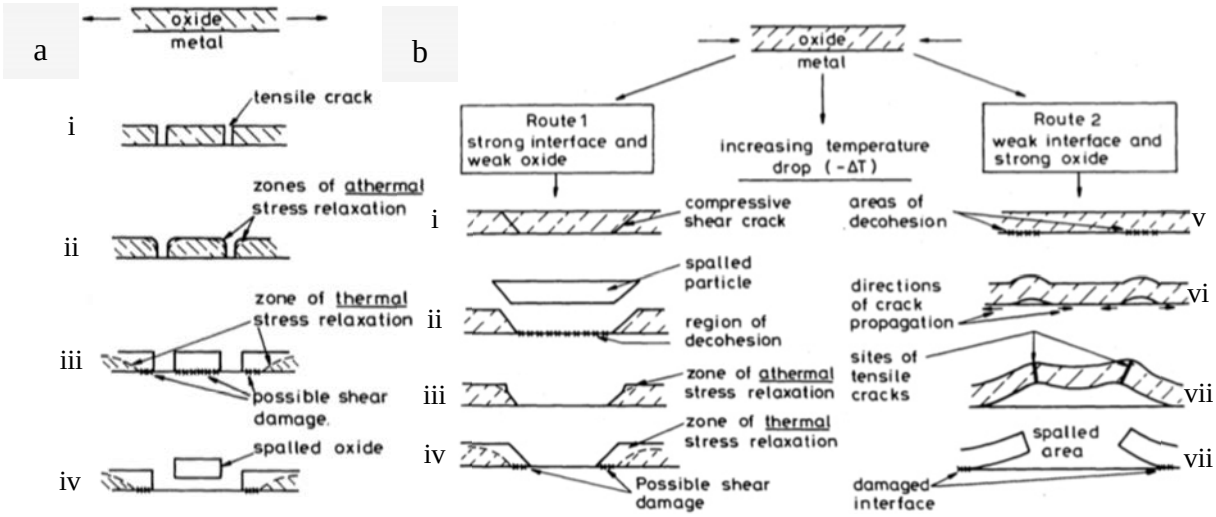

Figure 2.20 Schematic of oxide damaging mechanisms: in tension (a); in compression (b) [Evans, 1988]

The spallation resistance can be improved with increasing initial Cr content in the substrate [*Otsuka, 2005, Yang et al., 2013*], due to the sufficient supply of protective metallic elements for the self-healing process.

Now consider two extreme situations of scale self-healing process, i.e., the oxide scale grows only by metallic cation outward diffusion and the oxide scale grows only by oxygen anion inward diffusion [*Schütze, 1997*]. In the former case, the crack within the oxide scale can be gradually close up by new oxides generation from both sides and the base of the crack. In the latter case, oxygen can diffuse into the inner part of the oxide scale or even the substrate through the crack, while the original crack still remains. In reality, these two extreme healing processes are expected to coexist because the oxide growth through entire inward diffusion of oxygen or entire outward diffusion of metallic rarely happens. Figure 2.21 illustrates the healing process

of chromia formed on the pure chromium at 1200˚C in Ar-20%O_2 after cracking and local debonding [*Dorcheh et al., 2018*]. According to Dorcheh, cracks can be healed by new oxide growing on the sides of the crack and at its base (through chromium ion outward diffusion) as well as at the tip of the crack (through oxygen inward diffusion).

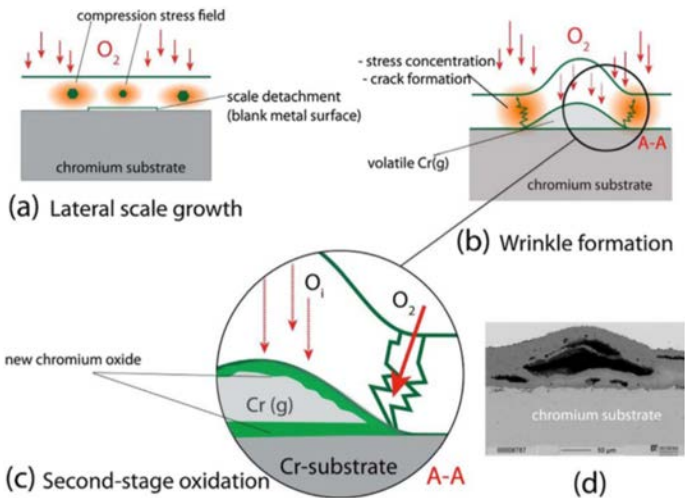

*Figure 2.21 Schematic showing the buckling of chromia formed at 1200˚C in Ar-20%O_2 and its self-healing behaviors [*Dorcheh et al., 2018*]*

2.4.3 Residual stress

Oxide scales without any applied external loadings at room temperature can still be subject to internal stress. This stress self-equilibrated between the oxide scale and substrate is the so-called residual stress, which is simply regarded as the sum of the growth stress and thermal stress.

2.4.3.1 Types of residual stress

It is recognized that residual stresses can be divided into three groups depending on the scope of action [*Macherauch et al., 1973*]. As illustrated in Figure 2.22, the first type residual stress σ^{I} varies over all crystallites and phases within the considered volume, as it is called the macro residual stress and represents an average stress state of the whole. The second type residual stress σ^{II} and the third type residual stress σ^{III}, in contrast, are the micro residual stresses. The former acts between the grains and crystallites of the same or different phases, hence it is called homogeneous micro-stress. The latter varies locally within the grain, known as inhomogeneous micro-stress [*Withers et al., 2001*].

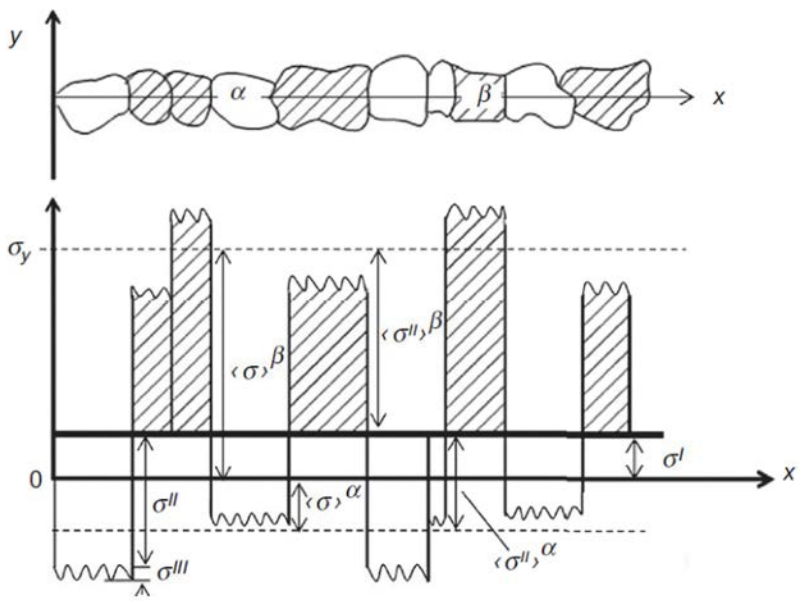

*Figure 2.22 Residual stress distribution over several grains of a polycrystalline material showing three types of residua stresses [*Epp, 2016*]*

2.4.3.2 Residual stress measurement

The methods for measuring residual stress in either industrial field or laboratory have plenty of options, normally can be divided into destructive and non-destructive methods. For instance, X-ray diffraction [*Prevey, 1986*, *Welzel et al., 2005*, *Chollet et al., 2017*], neutron diffraction [*Hutchings et al., 2005*], Raman spectrum [*Ager III et al., 1993*], nanoindentation [*Lee et al., 2003*], metal magnetic memory test [*Wilson et al., 2007*], ultrasonic method [*Crecraft, 1967*], thermoelastic method [*Wong et al., 1988*], birefringence method [*Weng et al., 2009*], scanning electron acoustic microscopy [*Cantrell et al., 1990*] and curvature method [*Zhao et al., 2002*] are the basic methods of non-destructive measurements. While hole-drilling, ring coring, deep hole drilling, splitting, sectioning, layer removal and contouring are the typical methods of destructive measurements [*Schajer, 2013*]. In recent years, some advanced techniques combined with these classical methods provide new insights into the residual stress measurement as well as algorithms, for instance, the focused ion beam (FIB) cooperated with hole drilling [*Winiarski et al., 2012*] or layer removal [*Treml et al., 2016*] enables the depth profile determination of residual stresses in the monolayer or multi-layer materials with enhanced spatial resolution. Figure 2.23 shows a summary in regard to the penetration and spatial resolution of various residual stress measurement methods [*Kypris et al., 2013*]. To determine residual stress in the oxide scales, this work chooses X-ray diffraction due to the required penetration depth satisfied by grazing incidence as well as its highest precision (~20 MPa).

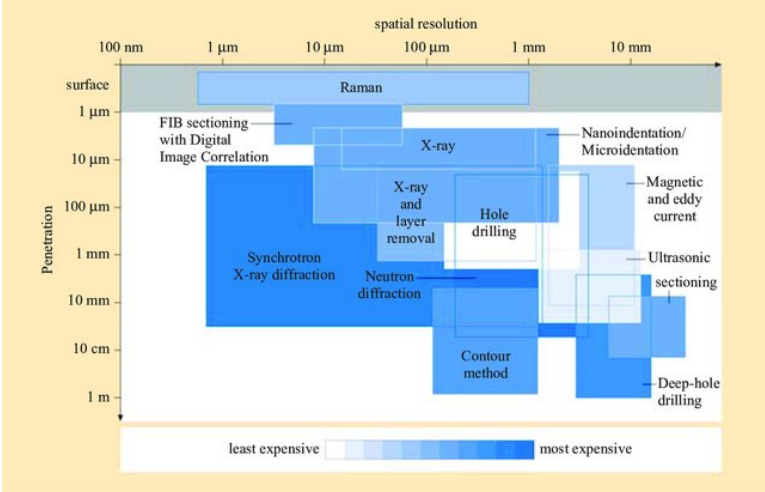

*Figure 2.23 Spatial resolution and penetration of measuring residual stresses for different methods [*Kypris et al., 2013*]*

2.4.3.3 Residual stress in oxide scales

Relatively few reports have been published concerning directly the residual stresses in the oxide scales for the past thirty years. The Haynes 230 (Ni-Cr alloy) oxidized is subject to tensile stresses in the substrate and compressive stresses in the oxide scale, as reported in [*Tung et al., 2012*]. While for the similar Ni-Cr alloy, compressive stress in the substrate was found. Zhao proposed that the internal oxidation, creep behavior of the substrate and Cr concentration gradient might account for the compressive residual stresses [*Zhao et al., 1986*]. Most of the residual stress in chromia formed on pure chromium and Ni-30Cr alloy at 900˚C originates from the thermal stress [*Stout et al., 1989*], which has been verified in theoretical analysis [*Huntz, 1995*]. However, Galerie suggested that for the ferritic stainless steel oxidized at 900˚C, the growth stress had more significance [*Galerie et al., 2004*]. Residual stress relaxes with increasing the oxidation time during the oxidation of Fe-22Cr-4.8Al-0.3Y alloy at the temperature above 1000˚C. However, in the initial one hour, relaxation did not happen because chemical reaction was the rate controlling factor [*Tolpygo et al., 1998*]. At the same time, residual stress in chromia gradually accumulates with the scale thicken [*Bernard et al., 2002*] but will release through such as surface undulation and spallation [*Liu et al., 2011*]. The temperature dependence has also been indicated in these two studies that lower residual stresses remain after higher temperature oxidation. Moreover, the residual stress gradient has been discovered and analyzed within the oxide scales such as [*Chen et al., 2011*]. Chen investigated the residual stress gradient within the zirconia films deposited (by metal-organic chemical vapor deposition) on (1 0 0) silicon single crystals by changing the X-ray penetration depths. He found that tensile residual stress acted on the region near the surface and it decreased quickly

as the X-ray penetrating depth increases; the stresses acting in the deeper region became compressive. He proposed that the origin of residual stress could be the combination effect of the growth stress during film deposition and the thermal stress during film cooling. In regard to the influence of stress on oxide growth, higher compressive residual stress concentration in proximity of grain boundaries enhances the intergranular oxide penetration since its concomitant biaxial tensile promotes the oxide growth deeper into the substrate [*Bertali et al., 2016*].

2.5 Summary

The literature research has been done centering around the oxidation mechanisms of steels at high temperature in this chapter. To investigate the coupling influence of thermal-chemical-mechanical conditions, it is of importance to know the existing knowledge in regard to mechanical behaviors of oxide scales in addition to thermochemical studies related to the oxidation. It is known that the oxide constituents are determined by not only the chemical stability of each component but also the mass transport process. The latter usually attracts more attention because it is closely related to the oxidation kinetics and mechanisms. This section responds to the following: the common oxide composition distribution; correlated growth kinetics; the defect structure of main oxidation products; diffusion of different elements; martensitic phase transformation related to the element depletion; the causes of breakaway oxidation; the origins of oxidation stress; the main forms of stress relaxation and residual stresses in the oxide scales. Referring to water vapor, it influences the oxidation mechanisms, in essence through changing the defect structures. Water vapor promotes vacancies to generate and coalesce, and thus forms a dissociation transport mechanism. Simultaneously, water vapor leads to the evaporation of protective component, impacting the oxide composition and other aspects such as diffusion process and mechanical properties. In the case of the oxide scale failure, it also starts from the defects. Hence, a chance is available to connect water vapor with damage mechanisms, which might be a complex and formidable task.

2.6 Reference

[15510:2014, 2019] 15510:2014, I. 2019. Stainless steels — Chemial compostion.

[(SSINA) et al., 2014] (SSINA), S. S. I. O. T. U. S., (SSINA), S. S. I. O. N. A., (NDI), N. D. I. & (AISI), A. I. S. I. 2014. *Design Guidelines for the Selection and Use of Stainless Steel*, Specialty Steel Industry of the United States.

[A. Bautista, 2003] A. BAUTISTA, F. V., M.CAMPOS, M. E. RABANAL AND J. M. TORRALBA 2003. Oxidation Behavior at 900°C of Austenitic, Ferritic, and Duplex Stainless Steel Manufactured By Powder Metallurgy. *Oxidation of Metals,* 59**,** 373-393.

[A. L. Marasco, 1991] A. L. MARASCO, D. J. Y. 1991. The oxidation of Iron-Chromium-Manganese alloys at 900°C. *Oxidation of Metals,* 36**,** 157-174.

[Ager III et al., 1993] AGER III, J. W. & DRORY, M. D. 1993. Quantitative measurement of residual biaxial stress by Raman spectroscopy in diamond grown on a Ti alloy by chemical vapor deposition. *Physical Review B,* 48**,** 2601.

[Akiya et al., 2002] AKIYA, N. & SAVAGE, P. E. 2002. Roles of water for chemical reactions in high-temperature water. *Chemical reviews,* 102**,** 2725-2750.

[Anonymous, 1915] Anonymous. 1915. A Non-rusting Steel.; Sheffield Invention Especially Good for Table Cutlery. *New York Times,* 31 January p.7.

[Ardigo et al., 2012] ARDIGO, M. R., POPA, I., CHEVALIER, S., WEBER, S., HEINTZ, O. & VILASI, M. 2012. Effect of Water Vapor on the Oxidation Mechanisms of a Commercial Stainless Steel for Interconnect Application in High Temperature Water Vapor Electrolysis. *Oxidation of Metals,* 79**,** 495-505.

[Arve Holt, 1994a] ARVE HOLT, P. K. 1994a. Electrical conductivity and defect structure of Cr2O3. I. High temperatures (>~1000°C). *Solid State Ionics,* 69**,** 127-136.

[Arve Holt, 1994b] ARVE HOLT, P. K. 1994b. Electrical conductivity and defect structure of Cr2O3. II. Reduced temperatures (<~1000°C). *Solid State Ionics,* 69**,** 137-143.

[Ashby, 1972] ASHBY, M. F. 1972. A first report on deformation-mechanism maps. *Acta Metallurgica,* 20**,** 887-897.

[Asteman et al., 1999] ASTEMAN, H., SVENSSON, J.-E., JOHANSSON, L.-G. & NORELL, M. 1999. Indication of chromium oxide hydroxide evaporation during oxidation of 304L at 873 K in the presence of 10% water vapor. *Oxidation of Metals,* 52**,** 95-111.

[Asteman et al., 2000] ASTEMAN, H., SVENSSON, J.-E., NORELL, M. & JOHANSSON, L.-G. 2000. Influence of water vapor and flow rate on the high-temperature oxidation of 304L; effect of chromium oxide hydroxide evaporation. *Oxidation of metals,* 54**,** 11-26.

[Atkinson, 1982] ATKINSON, A. 1982. Conditions for the formation of new oxide within oxide films growing on metals. *Corros. Sci,* 22**,** 347-357.

[Bedworth et al., 1923] BEDWORTH, R. & PILLING, N. 1923. The oxidation of metals at high temperatures. *J Inst Met,* 29**,** 529-582.

[Bernard et al., 2002] BERNARD, O., AMIRI, G., HAUT, C., FELTZ, B., HUNTZ, A. & ANDRIEUX, M. 2002. Mechanical and microstructural characterisation of oxide films damage. *Materials Science and Engineering: A,* 335**,** 32-42.

[Bernstein, 1991] BERNSTEIN, H. 1991. A model for the oxide growth stress and its effect on the creep of metals. *Metallurgical transactions A,* 18**,** 975-986.

[Bertali et al., 2016] BERTALI, G., SCENINI, F. & BURKE, M. G. 2016. The effect of residual stress on the Preferential Intergranular Oxidation of Alloy 600. *Corrosion Science,* 111**,** 494-507.

[Beverskog et al., 1997] BEVERSKOG, B. & PUIGDOMENECH, I. 1997. Revised pourbaix diagrams for chromium at 25–300 C. *Corrosion Science,* 39**,** 43-57.

[Birks et al., 2006] BIRKS, N., MEIER, G. H. & PETTIT, F. S. 2006. *Introduction to the high temperature oxidation of metals,* Cambridge University Press.

[Borie et al., 1962] BORIE, B., SPARKS JR, C. & CATHCART, J. 1962. Epitaxially induced strains in Cu2O films on copper single crystals—I X-ray diffraction effects. *Acta metallurgica,* 10**,** 691-697.

[Brady et al., 2011] BRADY, M. P., FAYEK, M., KEISER, J. R., MEYER, H. M., MORE, K. L., ANOVITZ, L. M., WESOLOWSKI, D. J. & COLE, D. R. 2011. Wet oxidation of stainless steels: New insights into hydrogen ingress. *Corrosion Science,* 53**,** 1633-1638.

[Buscail et al., 2008] BUSCAIL, H., MESSKI, S. E., RIFFARD, F., PERRIER, S., CUEFF, R., CAUDRON, E. & ISSARTEL, C. 2008. Characterization of the oxides formed at 1000°C on the AISI 316L stainless steel—Role of molybdenum. *Materials Chemistry and Physics,* 111**,** 491-496.

[Buscail et al., 2015] BUSCAIL, H., ROLLAND, R. & PERRIER, S. 2015. Influence of water vapour on 316L oxidation at high temperature-in situ X-Ray diffraction.

[Butler et al., 1986] BUTLER, E. & BURKE, M. 1986. Chromium depletion and martensite formation at grain boundaries in sensitised austenitic stainless steel. *Acta Metallurgica,* 34**,** 557-570.

[Callen et al., 1960] CALLEN, H. B. & KESTIN, J. 1960. An Introduction to the Physical Theories of Equilibrium Thermostatics and Irreversible Thermodynamics. American Society of Mechanical Engineers Digital Collection.

[Calmunger et al., 2015] CALMUNGER, M., ERIKSSON, R., CHAI, G., JOHANSSON, S. & MOVERARE, J. J. 2015. Surface phase transformation in austenitic stainless steel induced by cyclic oxidation in humidified air. *Corrosion Science,* 100**,** 524-534.

[Calmunger et al., 2016] CALMUNGER, M., ERIKSSON, R., CHAI, G. C., JOHANSSON, S., HÖGBERG, J. & MOVERARE, J. 2016. Local Surface Phase Stability during Cyclic Oxidation Process. *Materials Science Forum,* 879**,** 855-860.

[Cantrell et al., 1990] CANTRELL, J. H., QIAN, M., RAVICHANDRAN, M. & KNOWLES, K. 1990. Scanning electron acoustic microscopy of indentation-induced cracks and residual stresses in ceramics. *Applied physics letters,* 57**,** 1870-1872.

[Caplan et al., 1952] CAPLAN, D. & COHEN, M. 1952. High temperature oxidation of some iron-chromium alloys. *JOM,* 4**,** 1057-1057.

[Chandra-ambhorn et al., 2019] CHANDRA-AMBHORN, S., SARANYACHOT, P. & THUBLAOR, T. 2019. High temperature oxidation behaviour of Fe–15.7 wt.% Cr–8.5 wt.% Mn in oxygen without and with water vapour at 700 ºC. *Corrosion Science,* 148**,** 39-47.

[Chandra-Ambhorn et al., 2007] CHANDRA-AMBHORN, S., WOUTERS, Y., ANTONI, L., TOSCAN, F. & GALERIE, A. 2007. Adhesion of oxide scales grown on ferritic stainless steels in solid oxide fuel cells temperature and atmosphere conditions. *Journal of Power Sources,* 171**,** 688-695.

[Chen et al., 2011] CHEN, Z., PRUD'HOMME, N., WANG, B. & JI, V. 2011. Residual stress gradient analysis with GIXRD on ZrO2 thin films deposited by MOCVD. *Surface and Coatings Technology,* 206**,** 405-410.

[Chollet et al., 2017] CHOLLET, M., VALANCE, S., ABOLHASSANI, S., STEIN, G., GROLIMUND, D., MARTIN, M. & BERTSCH, J. 2017. Synchrotron X-ray diffraction investigations on strains in the oxide layer of an irradiated Zircaloy fuel cladding. *Journal of Nuclear Materials,* 488**,** 181-190.

[Cionea et al., 2016] CIONEA, C., ABAD, M. D., AUSSAT, Y., FRAZER, D., GUBSER, A. J. & HOSEMANN, P. 2016. Oxide scale formation on 316L and FeCrAl steels exposed to oxygen controlled static LBE at temperatures up to 800 °C. *Solar Energy Materials and Solar Cells,* 144**,** 235-246.

[Clarke, 2003] CLARKE, D. R. 2003. The lateral growth strain accompanying the formation of a thermally grown oxide. *Acta Materialia,* 51**,** 1393-1407.

[Cobb, 2010] COBB, H. M. 2010. *The history of stainless steel,* ASM International.

[Col et al., 2017] COL, A., PARRY, V. & PASCAL, C. 2017. Oxidation of a Fe–18Cr–8Ni austenitic stainless steel at 850°C in O2: Microstructure evolution during breakaway oxidation. *Corrosion Science,* 114**,** 17-27.

[Cox et al., 1973] COX, M., MCENANEY, B. & SCOTT, V. 1973. Vacancy condensation and void formation in duplex oxide scales on alloys. *Philosophical Magazine,* 28**,** 309-319.

[Crecraft, 1967] CRECRAFT, D. 1967. The measurement of applied and residual stresses in metals using ultrasonic waves. *Journal of Sound and Vibration,* 5**,** 173-192.

[D. J. Young, 1988] D. J. YOUNG, F. G. 1988. Thermodynamics of ionic diffusion and oxidation rate equations. *Oxidation of Metals,* 29**,** 169-185.

[Darken, 1948] DARKEN, L. S. 1948. Diffusion, mobility and their interrelation through free energy in binary metallic systems. *Trans. Aime,* 175**,** 184-201.

[Das et al., 2009] DAS, N. K., SUZUKI, K., OGAWA, K. & SHOJI, T. 2009. Early stage SCC initiation analysis of fcc Fe–Cr–Ni ternary alloy at 288°C: A quantum chemical molecular dynamics approach. *Corrosion Science,* 51**,** 908-913.

[DerSilberspiegel, 2016] DERSILBERSPIEGEL. 2016. *Ellingham Richardson-diagram* [Online]. Available: *https://commons.wikimedia.org/wiki/File:Ellingham_Richardson-diagram_english.svg* [Accessed].

[Dorcheh et al., 2018] DORCHEH, A. S., SCHÜTZE, M. & GALETZ, M. C. 2018. Factors affecting isothermal oxidation of pure chromium in air. *Corrosion Science,* 130**,** 261-269.

[Douglass et al., 1996] DOUGLASS, D., KOFSTAD, P., RAHMEL, P. & WOOD, G. 1996. International workshop on high-temperature corrosion. *Oxidation of Metals,* 45**,** 529-620.

[Duh et al., 1990] DUH, J. & WANG, C. 1990. Formation and growth morphology of oxidation-induced ferrite layer in Fe-Mn-Al-Cr-C alloys. *Journal of Materials Science,* 25**,** 2063-2070.

[Duh et al., 1988] DUH, J.-G., LEE, J. & WANG, C.-J. 1988. Microstructural development in the oxidation-induced phase transformation of Fe-Al-Cr-Mn-C alloys. *Journal of materials science,* 23**,** 2649-2660.

[Dumerval et al., 2014] DUMERVAL, M., PERRIN, S., MARCHETTI, L., TABARANT, M., JOMARD, F. & WOUTERS, Y. 2014. Hydrogen absorption associated with the

corrosion mechanism of 316L stainless steels in primary medium of Pressurized Water Reactor (PWR). *Corrosion Science,* 85**,** 251-257.

[E. Maurer, 1912] E. MAURER, B. S. 1912. Germany patent application 304159.

[Ebbinghaus, 1993] EBBINGHAUS, B. B. 1993. Thermodynamics of gas phase chromium species: the chromium oxides, the chromium oxyhydroxides, and volatility calculations in waste incineration processes. *Combustion and Flame,* 93**,** 119-137.

[Ehlers et al., 2006] EHLERS, J., YOUNG, D. J., SMAARDIJK, E. J., TYAGI, A. K., PENKALLA, H. J., SINGHEISER, L. & QUADAKKERS, W. J. 2006. Enhanced oxidation of the 9%Cr steel P91 in water vapour containing environments. *Corrosion Science,* 48**,** 3428-3454.

[Ellingham, 1944] ELLINGHAM, H. 1944. Transactions and communications. *J. Soc. Chem. Ind.(London),* 63**,** 125.

[Epp, 2016] EPP, J. 2016. X-ray diffraction (XRD) techniques for materials characterization. *In:* HÜBSCHEN, G., ALTPETER, I., TSCHUNCKY, R. & HERRMANN, H.-G. (eds.) *Materials characterization using Nondestructive Evaluation (NDE) methods.* Woodhead publishing.

[EuroInox, 2006] EUROINOX, T. 2006. *Design Manual For Structural Stainless Steel (Thrid Edition),* Oxford, The European Stainless Steel Development Association and The Steel Construction Institute.

[Evans et al., 1976] EVANS, A. G. & LANGDON, T. 1976. Structural ceramics. *Progress in Materials Science,* 21**,** 171-425.

[Evans et al., 1999] EVANS, H., DONALDSON, A. & GILMOUR, T. 1999. Mechanisms of breakaway oxidation and application to a chromia-forming steel. *Oxidation of Metals,* 52**,** 379-402.

[Evans, 1983] EVANS, H. E. 1983. The role of oxide grain boundaries in the development of growth stress during oxidation. *Corros. Sci,* 23**,** 495-506.

[Evans, 1988] EVANS, H. E. 1988. Spallation of oxide from stainless steel AGR nuclear fuel cladding: mechanisms and consequences. *Materials Science and Technology,* 4**,** 414-420.

[Evans, 1995] EVANS, H. E. 1995. Stress effects in high temperature oxidation of metals. *International Materials Reviews,* 40**,** 1-40.

[Falk-Windisch et al., 2015] FALK-WINDISCH, H., SVENSSON, J. E. & FROITZHEIM, J. 2015. The effect of temperature on chromium vaporization and oxide scale growth on interconnect steels for Solid Oxide Fuel Cells. *Journal of Power Sources,* 287**,** 25-35.

[Feng et al., 2010] FENG, Z., CHENG, X., DONG, C., XU, L. & LI, X. 2010. Passivity of 316L stainless steel in borate buffer solution studied by Mott–Schottky analysis, atomic absorption spectrometry and X-ray photoelectron spectroscopy. *Corrosion Science,* 52**,** 3646-3653.

[Frenkel, 1926] FRENKEL, J. 1926. Thermal movement in solid and liquid bodies. *Z Physik,* 53**,** 652-669.

[Frost et al., 1982] FROST, H. J. & ASHBY, M. F. 1982. *Deformation mechanism maps: the plasticity and creep of metals and ceramics,* Pergamon press.

[Fujii et al., 1963] FUJII, C. & MEUSSNER, R. 1963. Oxide Structures Produced on Iron-Chromium Alloys by a Dissociative Mechanism. *Journal of the Electrochemical Society,* 110**,** 1195-1204.

[Fujii et al., 1964] FUJII, C. & MEUSSNER, R. 1964. The Mechanism of the High-Temperature Oxidation of Iron-Chromium Alloys in Water Vapor. *Journal of the Electrochemical Society,* 111**,** 1215-1221.

[G. George, 2002] G. GEORGE, H. S. 2002. Introduction to Austenitic Stainless steel. *In:* H. S. KHATAK, B. R. (ed.) *Corrosion of Austenitic Stainless Steels - Mechanism, Mitigation and Monitoring.* England: Woodhead Publishing Limited.

[Galerie et al., 2014] GALERIE, A., HENRY, S., WOUTERS, Y., MERMOUX, M., PETIT, J. P. & ANTONI, L. 2014. Mechanisms of chromia scale failure during the course of 15–18Cr ferritic stainless steel oxidation in water vapour. *Materials at High Temperatures,* 22**,** 105-112.

[Galerie et al., 2004] GALERIE, A., TOSCAN, F., DUPEUX, M., MOUGIN, J., LUCAZEAU, G., VALOT, C., HUNTZ, A.-M. & ANTONI, L. 2004. Stress and adhesion of chromia-rich scales on ferritic stainless steels in relation with spallation. *Materials Research,* 7**,** 81-88.

[Gibbs, 1961] GIBBS, J. 1961. The Scientific papers of JW Gibbs. Thermodynamics. *New York: Dover) p,* 56**,** 65.

[Giesen, 1909] GIESEN, W. 1909. The special steels in theory and practice. *Iron and Steel Inst., Carnegie Fellowship Memoirs*.

[Giggins et al., 1980] GIGGINS, C. & PETTIT, F. 1980. Corrosion of metals and alloys in mixed gas environments at elevated temperatures. *Oxidation of Metals,* 14**,** 363-413.

[Gilewicz-Wolter et al., 2005] GILEWICZ-WOLTER, J., DUDAŁA, J., ŻUREK, Z., HOMA, M., LIS, J. & WOLTER, M. 2005. Diffusion of chromium, manganese, and iron in MnCr 2 O 4 spinel. *Journal of Phase Equilibria and Diffusion,* 26**,** 561-564.

[Goncel et al., 1979] GONCEL, O., WHITTLE, D. & STRINGER, J. 1979. The oxidation behaviour of austenitic Fe□ Cr□ Ni alloys containing dispersed phases. *Corrosion Science,* 19**,** 305-320.

[Gong et al., 2010] GONG, Y. F. & DE COOMAN, B. C. 2010. Kirkendall void formation during selective oxidation. *Metallurgical and Materials Transactions A,* 41**,** 2180-2183.

[Green et al., 2014] GREEN, G. & HIGGINSON, R. L. 2014. Oxide scale formation and morphology on austenitic stainless steel at medium annealing temperatures. *Materials at High Temperatures,* 28**,** 269-273.

[Guerain et al., 2017] GUERAIN, M., RAKOTOVAO, F., BROU, S. Y., BONNET, G., PANICAUD, B., GROSSEAU-POUSSARD, J. L. & GOUDEAU, P. 2017. Stress release in α-Cr2O3 oxide thin films formed on Ni30-Cr and Fe47-Cr alloys. *Journal of Alloys and Compounds,* 718**,** 223-230.

[Guillamet et al., 1993] GUILLAMET, R., LOPITAUX, J., HANNOYER, B. & LENGLET, M. 1993. Oxidation of stainless steels (AISI 304 and 316) at high temperature. Influence on the metallic substratum. *Le Journal de Physique IV,* 03**,** C9-349-C349-356.

[Guillet et al., 1905] GUILLET, L. & LE CHATELIER, H. 1905. *Les aciers spéciaux,* Vve Ch. Dunod.

[H. Asteman, 2002a] H. ASTEMAN, J.-E. S., L. -G. JOHANSSON 2002a. Evidence for Chromium Evaporation Influencing the Oxidation of 304L The Effect of Temperature and Flow Rate. *Oxidation of Metals,* 57**,** 193-216.

[H. Asteman, 2002b] H. ASTEMAN, J.-E. S., L. -G. JOHANSSON 2002b. Oxidation of 310 steel in H2O/O2 mixtures at 600 °C the effect of water-vapour-enhanced chromium evaporation. *Corros. Sci,* 44**,** 2635-2649.

[Habib et al., 2011] HABIB, K. A., DAMRA, M. S., SAURA, J. J., CERVERA, I. & BELLÉS, J. 2011. Breakdown and Evolution of the Protective Oxide Scales of AISI 304 and AISI 316 Stainless Steels under High-Temperature Oxidation. *International Journal of Corrosion,* 2011**,** 1-10.

[Hancock et al., 1974] HANCOCK, P. & HURST, R. 1974. The mechanical properties and breakdown of surface oxide films at elevated temperatures. *Advances in corrosion science and technology.* Springer.

[Hänsel et al., 2010] HÄNSEL, M., GARCIA-FRESNILLO, L., TOBING, S. L., BREUER, U. & SHEMET, V. 2010. Hydrogen Uptake and Hydrogen Profiles in Chromia Scales Formed on Ni25Cr(Mn) in Low pO₂ Test Gases at 1000°C. *Advances in Science and Technology,* 72**,** 59-64.

[Harrison, 1961] HARRISON, L. 1961. Influence of dislocations on diffusion kinetics in solids with particular reference to the alkali halides. *Transactions of the Faraday Society,* 57**,** 1191-1199.

[Hart, 1957] HART, E. 1957. On the role of dislocations in bulk diffusion. *Acta Metallurgica,* 5**,** 597.

[Herring et al., 1951] HERRING, C. & KINGSTON, W. 1951. The physics of powder metallurgy. *WE Kingston, Edition: McGraw Hill, New York.*

[Horibe et al., 1975] HORIBE, S. & NAKAYAMA, T. 1975. Initial formation of oxide nodules due to the grain growth of an Fe-18Cr alloy. *Corrosion Science,* 15**,** 589-590.

[Hormadaly et al., 2012] HORMADALY, J. & PRUDENZIATI, M. 2012. Materials Science concepts for printed films. *Printed Films.* Elsevier.

[Howes et al., 1969] HOWES, V. & RICHARDSON, C. 1969. The initial stresses developed during high temperature oxidation of Fe-Cr alloys. *Corrosion Science,* 9**,** 385-394.

[Huang et al., 2018] HUANG, C.-L., WENG, W.-L., LIAO, C.-N. & TU, K. 2018. Suppression of interdiffusion-induced voiding in oxidation of copper nanowires with twin-modified surface. *Nature communications,* 9**,** 340.

[Huntz et al., 2003] HUNTZ, A., BAGUE, V., BEAUPLÉ, G., HAUT, C., SÉVÉRAC, C., LECOUR, P., LONGAYGUE, X. & ROPITAL, F. 2003. Effect of silicon on the oxidation resistance of 9% Cr steels. *Applied Surface Science,* 207**,** 255-275.

[Huntz et al., 1994] HUNTZ, A. & SCHÜTZE, M. 1994. Stresses generated during oxidation sequences and high temperature fracture. *Materials at High Temperatures,* 12**,** 151-161.

[Huntz, 1995] HUNTZ, A. M. 1995. Stresses in NiO, Cr2O3 and Al2O3 oxide scales. *Materials Science and Engineering: A,* 201**,** 211-228.

[Huntz et al., 2007] HUNTZ, A. M., RECKMANN, A., HAUT, C., SÉVÉRAC, C., HERBST, M., RESENDE, F. C. T. & SABIONI, A. C. S. 2007. Oxidation of AISI 304 and AISI 439 stainless steels. *Materials Science and Engineering: A,* 447**,** 266-276.

[Hutchings et al., 2005] HUTCHINGS, M. T., WITHERS, P. J., HOLDEN, T. M. & LORENTZEN, T. 2005. *Introduction to the characterization of residual stress by neutron diffraction,* CRC press.

[Iwahara et al., 1982] IWAHARA, H., UCHIDA, H. & MAEDA, N. 1982. High temperature fuel and steam electrolysis cells using proton conductive solid electrolytes. *Journal of Power Sources,* 7**,** 293-301.

[Jaenicke et al., 1958] JAENICKE, W. & LEISTIKOW, S. 1958. Mechanical Stresses in the Formation of Oxide Layers. I. Oxidation of Copper. *Z. Physik. Chem., NF,* 15**,** 175-195.

[Jaenicke et al., 1964] JAENICKE, W., LEISTIKOW, S. & STADLER, A. 1964. Mechanical stresses during the oxidation of copper and their influence on oxidation kinetics. III. *Journal of The Electrochemical Society,* 111**,** 1031-1037.

[Jervis et al., 1990] JERVIS, T., WILLIAMSON, D., HIRVONEN, J.-P. & ZOCCO, T. 1990. Characterization of the surface oxide formed by excimer laser surface processing of AISI 304 stainless steel. *Materials Letters,* 9**,** 379-383.

[john J. Barnes, 1989] JOHN J. BARNES, J. G. G., DAVID A. SHORES 1989. A Model for Stress Generation and Relief in oxide-metal systems during a temperature change. *Oxidation of Metals,* 32**,** 449-469.

[Jonsson et al., 2013] JONSSON, T., PUJILAKSONO, B., HEIDARI, H., LIU, F., SVENSSON, J. E., HALVARSSON, M. & JOHANSSON, L. G. 2013. Oxidation of Fe–10Cr in O2 and in O2+H2O environment at 600°C: A microstructural investigation. *Corrosion Science,* 75**,** 326-336.

[Kang et al., 2016] KANG, Y.-B. & JUNG, I.-H. 2016. Thermodynamic modeling of oxide phases in the Fe–Mn–O system. *Journal of Physics and Chemistry of Solids,* 98**,** 237-246.

[Karczewski et al., 2019] KARCZEWSKI, J., BRYLEWSKI, T., MIRUSZEWSKI, T., ANDERSEN, K. B., JASINSKI, P. Z. & MOLIN, S. 2019. High-temperature kinetics study of 430L steel powder oxidized in air at 600–850 °C. *Corrosion Science,* 149**,** 100-107.

[Kim et al., 2015] KIM, J.-H., KIM, B. K., KIM, D.-I., CHOI, P.-P., RAABE, D. & YI, K.-W. 2015. The role of grain boundaries in the initial oxidation behavior of austenitic stainless steel containing alloyed Cu at 700°C for advanced thermal power plant applications. *Corrosion Science,* 96**,** 52-66.

[Kirkendall et al., 1947] KIRKENDALL, E. & SMIGELSKAS, A. 1947. Zinc diffusion in alpha brass. *Aime Trans,* 171**,** 130-142.

[Kjellqvist et al., 2010] KJELLQVIST, L. & SELLEBY, M. 2010. Thermodynamic assessment of the Cr–Mn–O system. *Journal of Alloys and Compounds,* 507**,** 84-92.

[Kofstad, 1988] KOFSTAD, P. 1988. High temperature corrosion. *Elsevier Applied Science Publishers, Crown House, Linton Road, Barking, Essex IG 11 8 JU, UK, 1988.*

[Kofstad, 1989] KOFSTAD, P. 1989. Fundamental aspects of corrosion by hot gases. *Materials Science and Engineering: A,* 120-121**,** 25-29.

[Kofstad, 1995] KOFSTAD, P. 1995. Defects and transport properties of metal oxides. *Oxidation of metals,* 44**,** 3-27.

[Kofstad et al., 1980] KOFSTAD, P. & LILLERUD, K. 1980. On high temperature oxidation of chromium II. Properties of and the oxidation mechanism of chromium. *Journal of the electrochemical society,* 127**,** 2410-2419.

[Kröger et al., 1956] KRÖGER, F. & VINK, H. 1956. Relations between the concentrations of imperfections in crystalline solids. *Solid state physics.* Elsevier.

[Kypris et al., 2013] KYPRIS, O., NLEBEDIM, I. & JILES, D. 2013. Experimental verification of the linear relationship between stress and the reciprocal of the peak Barkhausen voltage in ASTM A36 steel. *IEEE Transactions on Magnetics,* 49**,** 4148-4151.

[La Fontaine et al., 2014] LA FONTAINE, A., YEN, H.-W., TRIMBY, P., MOODY, S., MILLER, S., CHENSEE, M., RINGER, S. & CAIRNEY, J. 2014. Martensitic transformation in an intergranular corrosion area of austenitic stainless steel during thermal cycling. *Corrosion Science,* 85**,** 1-6.

[Latu-Romain et al., 2018] LATU-ROMAIN, L., PARSA, Y., OLLIVIER, M., MATHIEU, S., VILASI, M., RENOU, G., ROBAUT, F. & WOUTERS, Y. 2018. About the control of semiconducting properties of chromia: investigation using photoelectrochemistry and orientation mapping in a TEM. *Materials at High Temperatures,* 35**,** 159-167.

[Lee et al., 2003] LEE, Y.-H. & KWON, D. 2003. Measurement of residual-stress effect by nanoindentation on elastically strained (100) W. *Scripta Materialia,* 49**,** 459-465.

[Liu et al., 2015] LIU, L., YANG, Z.-G., ZHANG, C., UEDA, M., KAWAMURA, K. & MARUYAMA, T. 2015. Effect of grain size on the oxidation of Fe–13Cr–5Ni alloy at 973K in Ar–21vol%O2. *Corrosion Science,* 91**,** 195-202.

[Liu et al., 2011] LIU, W. N., SUN, X., STEPHENS, E. & KHALEEL, M. 2011. Effect of substrate thickness on oxide scale spallation for solid oxide fuel cells. *Corrosion Science,* 53**,** 2406-2412.

[Luo et al., 2018] LUO, L., SU, M., YAN, P., ZOU, L., SCHREIBER, D. K., BAER, D. R., ZHU, Z., ZHOU, G., WANG, Y., BRUEMMER, S. M., XU, Z. & WANG, C. 2018. Atomic origins of water-vapour-promoted alloy oxidation. *Nat Mater,* 17**,** 514-518.

[M. Gerland, 2001] M. GERLAND, C. V., J. MENDEZ 2001. Interaction of oxide layers with dislocations for an austenitic stainless steel. *Materials Science and Engineering: A,* A311**,** 157-161.

[M. Hansel, 2003] M. HANSEL, W. J. Q., D. J. YOUNG 2003. Role of Water Vapor in Chromia-Scale Growth at Low Oxygen Partial Pressure. *Oxidation of Metals,* 59**,** 285-301.

[Macherauch et al., 1973] MACHERAUCH, E., WOHLFAHRT, H. & WOLFSTIEG, U. 1973. Zur zweckmäßigen definition von eigenspannungen. *HTM,* 28**,** 201-211.

[McElhaney et al., 2004] MCELHANEY, K. W. & MA, Q. 2004. Investigation of moisture-assisted fracture in SiO2 films using a channel cracking technique. *Acta Materialia,* 52**,** 3621-3629.

[Mehrer, 2007] MEHRER, H. 2007. Point defects in crystals. *In:* MANUEL CARDONA, P. F., KLAUS VON KLITZING, HANS-JOACHIM QUEISSER, ROBERTO MERLIN, HORST STORMER (ed.) *Diffusion in solids — Fundamentals, Methods, Materials, Diffusion-Cotrolled Processes.* New York: Springer.

[Metcalfe et al., 1966] METCALFE, E. & MANNING, M. 1966. The Spalling of Steam Grown Oxide from Austenitic and Ferritic Alloys. *Report RDy Ly Ry.*

[Metikoš-Huković et al., 1987] METIKOŠ-HUKOVIĆ, M. & CERAJ-CERIĆ, M. 1987. p-Type and n-Type Behavior of Chromium Oxide as a Function of the Applied Potential. *Journal of the Electrochemical Society,* 134**,** 2193-2197.

[Monnartz, 1911] MONNARTZ, P. 1911. Iron-chromium alloys with special consideration of resistance to acids. *Metallurgie (Halle),* 8**,** 161-176.

[Nakagawa et al., 2003] NAKAGAWA, K., MATSUNAGA, Y. & YANAGISAWA, T. 2003. Corrosion behavior of ferritic steels on the air sides of boiler tubes in a steam/air dual environment. *Materials at high temperatures,* 20**,** 67-73.

[Nezakat et al., 2016] NEZAKAT, M., AKHIANI, H., PENTTILÄ, S. & SZPUNAR, J. 2016. Oxidation Behavior of Austenitic Stainless Steel 316L and 310S in Air and Supercritical Water. *Journal of Nuclear Engineering and Radiation Science,* 2.

[Norby, 1993] NORBY, T. 1993. Protonic defects in oxide and their possible role in high temperature oxidation. *Journal de physique. IV,* 3**,** 99-106.

[Norby et al., 1986] NORBY, T. & KOFSTAD, P. 1986. Proton and native-ion conductivities in Y2O3 at high temperatures. *Solid State Ionics,* 20**,** 169-184.

[Norby et al., 1997] NORBY, T. & LARRING, Y. 1997. Concentration and transport of protons in oxides. *Current Opinion in Solid State and Materials Science,* 2**,** 593-599.

[Norby Truls, 2004] NORBY TRULS, W. M., GLÖCKNER RONNY AND LARRING YNGVE 2004. Hydrogen in oxides. *Dalton transactions,* 19**,** 3012ß3018.

[Opila et al., 2007] OPILA, E. J., MYERS, D. L., JACOBSON, N. S., NIELSEN, I. M., JOHNSON, D. F., OLMINSKY, J. K. & ALLENDORF, M. D. 2007. Theoretical and experimental investigation of the thermochemistry of CrO2 (OH) 2 (g). *The Journal of Physical Chemistry A,* 111**,** 1971-1980.

[Othman et al., 2009a] OTHMAN, N. K., OTHMAN, N., ZHANG, J. & YOUNG, D. J. 2009a. Effects of water vapour on isothermal oxidation of chromia-forming alloys in Ar/O2 and Ar/H2 atmospheres. *Corrosion Science,* 51**,** 3039-3049.

[Othman et al., 2009b] OTHMAN, N. K., ZHANG, J. & YOUNG, D. J. 2009b. Water Vapour Effects on Fe–Cr Alloy Oxidation. *Oxidation of Metals,* 73**,** 337-352.

[Othman et al., 2010] OTHMAN, N. K., ZHANG, J. & YOUNG, D. J. 2010. Temperature and water vapour effects on the cyclic oxidation behaviour of Fe–Cr alloys. *Corrosion Science,* 52**,** 2827-2836.

[Otsuka, 2005] OTSUKA, N. 2005. Fracture behavior of steam-grown oxide scales formed on 2–12%Cr steels. *Materials at High Temperatures,* 22**,** 131-138.

[Oum et al., 2016] OUM, M., HONG, J.-E. & STEINBERGER-WILCKENS, R. Thermochemical and Kinetic Modelling of Chromium-Rich Alloys. Proc. 12th European SOFC and SOE Forum, Lucerne, 2016. 5-8.

[Panicaud et al., 2006] PANICAUD, B., GROSSEAU-POUSSARD, J. L. & DINHUT, J. F. 2006. On the growth strain origin and stress evolution prediction during oxidation of metals. *Applied Surface Science,* 252**,** 5700-5713.

[Panicaud et al., 2008] PANICAUD, B., GROSSEAU-POUSSARD, J. L. & DINHUT, J. F. 2008. General approach on the growth strain versus viscoplastic relaxation during oxidation of metals. *Computational Materials Science,* 42**,** 286-294.

[Parsa et al., 2018] PARSA, Y., LATU-ROMAIN, L., WOUTERS, Y., MATHIEU, S., PÉREZ, T. & VILASI, M. 2018. Effect of oxygen partial pressure on the semiconducting properties of thermally grown chromia on pure chromium. *Corrosion Science,* 141**,** 46-52.

[Pascal et al., 2015] PASCAL, C., PARRY, V., FEDOROVA, E., BRACCINI, M., CHEMELLE, P., MEYER, N., OQUAB, D., MONCEAU, D., WOUTERS, Y. & MANTEL, M. 2015. Breakaway oxidation of austenitic stainless steels induced by alloyed sulphur. *Corrosion Science,* 93**,** 100-108.

[Paul et al., 2017] PAUL, A. & DIVINSKI, S. 2017. *Handbook of Solid State Diffusion: Volume 1: Diffusion Fundamentals and Techniques*, Elsevier.

[Perez et al., 2001] PEREZ, F., CRISTOBAL, M., ARNAU, G., HIERRO, M. & SAURA, J. 2001. High-temperature oxidation studies of low-nickel austenitic stainless steel. Part I: isothermal oxidation. *Oxidation of metals,* 55**,** 105-118.

[Perez et al., 2000] PEREZ, F., CRISTOBAL, M., HIERRO, M., PEDRAZA, F., ARNAU, G. & MERINO, T. 2000. Effect of yttrium and erbium ion implantation on the oxidation behaviour of the AISI 304 austenitic steel. *Surface and Coatings Technology,* 126**,** 116-122.

[Portevin, 1909] PORTEVIN, A. 1909. Contribution to the study of the special ternary steels. *Iron and Steel Inst., Carnegie Fellowship Memoirs*.

[Pour-Ali et al., 2019] POUR-ALI, S., KIANI-RASHID, A.-R., BABAKHANI, A., NOROUZI, M. & VIRTANEN, S. 2019. New insights into the effects of surface nanocrystallization on the oxidation of 321 austenitic stainless steel in a humid oxygen environment at 1000 °C. *Corrosion Science,* 147**,** 231-245.

[Prevey, 1986] PREVEY, P. S. 1986. X-ray diffraction residual stress techniques. *ASM International, ASM Handbook.,* 10**,** 380-392.

[Rafferty, 2018] RAFFERTY, J. P. 2018. *Stainless steel* [Online]. Encyclopaedia Britannica. Available: *https://www.britannica.com/technology/stainless-steel#ref137957* [Accessed].

[Rahmel et al., 1965a] RAHMEL, A. & TOBOLSKI, J. 1965a. Einfluss von wasserdampf und kohlendioxyd auf die oxydation von eisen in sauerstoff bei hohen temperaturen. *Corrosion Science,* 5**,** 333-346.

[Rahmel et al., 1965b] RAHMEL, A. & TOBOLSKI, J. 1965b. The influence of water vapor and carbon dioxide on the oxidation of iron in oxygen at high temperatures. *Corros. Sci,* 5**,** 333-346.

[Raman et al., 2009] RAMAN, R. K. S. & GUPTA, R. K. 2009. Oxidation resistance of nanocrystalline vis-à-vis microcrystalline Fe–Cr alloys. *Corrosion Science,* 51**,** 316-321.

[Rhines et al., 1970] RHINES, F. & WOLF, J. 1970. The role of oxide microstructure and growth stresses in the high-temperature scaling of nickel. *Metallurgical Transactions,* 1**,** 1701-1710.

[Riley, 1889] RILEY, J. 1889. On Alloys of Nickel and Steel. *The Journal of the Iron & Steel Institute.* First Edition ed. London: E & F N Spon.

[Robertson, 1991] ROBERTSON, J. 1991. The mechanism of high temperature aqueous corrosion of stainless steels. *Corros. Sci,* 32**,** 443-465.

[Sabioni et al., 2007] SABIONI, A., HUNTZ, A., BORGES, L. & JOMARD, F. 2007. First study of manganese diffusion in Cr2O3 polycrystals and thin films by SIMS. *Philosophical Magazine,* 87**,** 1921-1937.

[Sabioni et al., 2005] SABIONI, A. C. S., HUNTZ, A. M., SILVA, F. & JOMARD, F. 2005. Diffusion of iron in Cr2O3: polycrystals and thin films. *Materials Science and Engineering: A,* 392**,** 254-261.

[Sabioni et al., 2012a] SABIONI, A. C. S., MALHEIROS, E. A., JI, V. & JOMARD, F. 2012a. Determination of Oxygen Diffusion Coefficient in Oxidation Films of the AISI 439 Ferritic Stainless Steel. *Defect and Diffusion Forum,* 323-325**,** 339-344.

[Sabioni et al., 2013] SABIONI, A. C. S., MALHEIROS, E. A., JI, V., JOMARD, F., DE ALMEIDA MACEDO, W. A. & GASTELOIS, P. L. 2013. Ion Diffusion Study in the Oxide Layers Due to Oxidation of AISI 439 Ferritic Stainless Steel. *Oxidation of Metals,* 81**,** 407-419.

[Sabioni et al., 2012b] SABIONI, A. C. S., RAMOS, R. P. B., JI, V. & JOMARD, F. 2012b. Oxygen Diffusion Study in Oxidation Films of the AISI 304 Austenitic Stainless Steel. *Defect and Diffusion Forum,* 323-325**,** 345-351.

[Sabioni et al., 2012c] SABIONI, A. C. S., RAMOS, R. P. B., JI, V., JOMARD, F., MACEDO, W. A. D. A., GASTELOIS, P. L. & TRINDADE, V. B. 2012c. About the Role of Chromium and Oxygen Ion Diffusion on the Growth Mechanism of Oxidation Films of the AISI 304 Austenitic Stainless Steel. *Oxidation of Metals,* 78**,** 211-220.

[Sabioni et al., 2015] SABIONI, A. C. S., SOUZA, J. N. V., JI, V., JOMARD, F., TRINDADE, V. B. & CARNEIRO, J. F. 2015. Study of ion diffusion in oxidation films grown on a model Fe–15%Cr alloy. *Solid State Ionics,* 276**,** 1-8.

[Sachitanand et al., 2013] SACHITANAND, R., SATTARI, M., SVENSSON, J.-E. & FROITZHEIM, J. 2013. Evaluation of the oxidation and Cr evaporation properties of selected FeCr alloys used as SOFC interconnects. *International Journal of Hydrogen Energy,* 38**,** 15328-15334.

[Schajer, 2013] SCHAJER, G. S. 2013. *Practical residual stress measurement methods,* John Wiley & Sons.

[Schottky et al., 1931] SCHOTTKY, W. & WAGNER, C. 1931. Theory of ordered mixed phases, I. *Z. Phys. Chem. B,* 11**,** 163-210.

[Schütze, 1990] SCHÜTZE, M. 1990. Plasticity of protective oxide scales. *Materials Science and Technology,* 6**,** 32-38.

[Schütze, 1997] SCHÜTZE, M. 1997. *Protective oxide scales and their breakdown,* Wiley.

[Schütze, 2016] SCHÜTZE, M. 2016. Stress effects in high temperature oxidation.

[Seal et al., 1994] SEAL, S., BOSE, S. & ROY, S. 1994. Improvement in the oxidation behavior of austenitic stainless steels by superficially applied, cerium oxide coatings. *Oxidation of Metals,* 41**,** 139-178.

[Sikora et al., 2002] SIKORA, E. & MACDONALD, D. D. 2002. Nature of the passive film on nickel. *Electrochimica Acta,* 48**,** 69-77.

[Srolovitz et al., 1984] SROLOVITZ, D. & RAMANARAYANAN, T. A. 1984. An elastic analysis of growth stresses during oxidation. *Oxidation of metals,* 22**,** 133-146.

[Stellwag, 1998] STELLWAG, B. 1998. The mechanism of oxide film formation on austenitic stainless steels in high temperature water. *Corros. Sci,* 40**,** 337-370.

[Stevens et al., 1971] STEVENS, R. & DUTTON, R. 1971. The driving force for diffusion. *Scripta Metallurgica,* 5**,** 267-271.

[Stott et al., 1994] STOTT, F. H. & ATKINSON, A. 1994. The modelling of growth stresses during high-temperature oxidation. *Materials at High Temperatures,* 12**,** 195-207.

[Stout et al., 1989] STOUT, J., SHORES, D., GOEDJEN, J. & ARMACANQUI, M. 1989. Stresses and cracking of oxide scales. *Materials Science and Engineering: A,* 120**,** 193-197.

[Strauss. B, 1920] STRAUSS. B, M. E. 1920. *Kruppsche Monatsh,* 1**,** 120.

[Stringer, 1970] STRINGER, J. 1970. Stress generation and relief in growing oxide films. *Corros. Sci,* 10**,** 513-543.

[Suo et al., 2003] SUO, Z., KUBAIR, D. V., EVANS, A. G., CLARKE, D. R. & TOLPYGO, V. K. 2003. Stresses induced in alloys by selective oxidation. *Acta Materialia,* 51**,** 959-974.

[Susan et al., 2012] SUSAN, D. F., KNOROVSKY, G., ROBINO, C., MICHAEL, J. R., RODRIGUEZ, M. A. & PERRICONE, M. J. 2012. Surface alloy depletion and martensite formation during glass to metal joining of austenitic stainless steels. *Science and Technology of Welding and Joining,* 17**,** 321-332.

[Tien et al., 1975] TIEN, J. & DAVIDSON, J. 1975. Stress effects and the oxidation of metals. *Metallurgical Society AIME, 1974) p,* 200.

[Timoshenko, 1925] TIMOSHENKO, S. 1925. Analysis of Bi-Metal Thermostats. *Journal of the Optical Society of America,* 11**,** 233-255.

[Tolpygo et al., 1998] TOLPYGO, V., DRYDEN, J. & CLARKE, D. 1998. Determination of the growth stress and strain in α-Al2O3 scales during the oxidation of Fe–22Cr–4.8 Al–0.3 Y alloy. *Acta Materialia,* 46**,** 927-937.

[Treml et al., 2016] TREML, R., KOZIC, D., ZECHNER, J., MAEDER, X., SARTORY, B., GÄNSER, H. P., SCHÖNGRUNDNER, R., MICHLER, J., BRUNNER, R. & KIENER, D. 2016. High resolution determination of local residual stress gradients in single- and multilayer thin film systems. *Acta Materialia,* 103**,** 616-623.

[Tsai et al., 1996] TSAI, S., HUNTZ, A. & DOLIN, C. 1996. Growth mechanism of Cr2O3 scales: oxygen and chromium diffusion, oxidation kinetics and effect of yttrium. *Materials Science and Engineering: A,* 212**,** 6-13.

[Tsai et al., 1995] TSAI, S., HUNTZ, A. A. & DOLIN, C. 1995. Diffusion of 18 O in massive Cr 2 O 3 and in Cr 2 O 3 scales at 900° C and its relation to the oxidation kinetics of chromia forming alloys. *Oxidation of Metals,* 43**,** 581-596.

[Tung et al., 2012] TUNG, H.-M. & STUBBINS, J. F. 2012. Incipient oxidation kinetics and residual stress of the oxide scale grown on Haynes 230 at high temperatures. *Materials Science and Engineering: A,* 538**,** 1-6.

[UnitedPerformanceMetals, 2019] UNITEDPERFORMANCEMETALS. 2019. *316 and 316L Stainless Steel Sheet, Coil & Bar - AMS 5524, 5507, UNS S31600, S31603* [Online]. Available: 316 and 316L Stainless Steel Sheet, Coil & Bar - AMS 5524, 5507, UNS S31600, S31603 [Accessed].

[V. K. Tolpygo, 1998] V. K. TOLPYGO, D. R. C. 1998. Competition between stress generation and relaxation during oxidation of an Fe-Cr-Al-Y alloy. *Oxidation of Metals,* 49**,** 187-212.

[Vesel et al., 2008] VESEL, A., MOZETIC, M., DRENIK, A., HAUPTMAN, N. & BALAT-PICHELIN, M. 2008. High temperature oxidation of stainless steel AISI316L in air plasma. *Applied Surface Science,* 255**,** 1759-1765.

[Von Mises, 1923] VON MISES, R. 1923. Über die Stabilitätsprobleme der Elastizitätstheorie. *ZAMM,* 3**,** 406-422.

[Wagner, 1933] WAGNER, C. 1933. Contribution to the theory of formation of oxidation films. *Z. Phys. Chem. B,* 21**,** 25.

[Wang et al., 2014] WANG, C.-M., GENC, A., CHENG, H., PULLAN, L., BAER, D. R. & BRUEMMER, S. M. 2014. In-Situ TEM visualization of vacancy injection and chemical partition during oxidation of Ni-Cr nanoparticles. *Scientific reports,* 4**,** 3683.

[Wei et al., 2018] WEI, L., ZHENG, J., CHEN, L. & MISRA, R. D. K. 2018. High temperature oxidation behavior of ferritic stainless steel containing W and Ce. *Corrosion Science,* 142**,** 79-92.

[Welzel et al., 2005] WELZEL, U., LIGOT, J., LAMPARTER, P., VERMEULEN, A. & MITTEMEIJER, E. 2005. Stress analysis of polycrystalline thin films and surface regions by X-ray diffraction. *Journal of Applied Crystallography,* 38**,** 1-29.

[Weng et al., 2009] WENG, C., LEE, W. & TO, S. 2009. Birefringence techniques for the characterization of residual stresses in injection-moulded micro-lens arrays. *Polymer Testing,* 28**,** 709-714.

[Wild, 1977] WILD, R. K. 1977. High temperature oxidation of austenitic stainless steel in low oxygen pressure. *Corrosion Science,* 17**,** 87-104.

[Wilson et al., 2007] WILSON, J. W., TIAN, G. Y. & BARRANS, S. 2007. Residual magnetic field sensing for stress measurement. *Sensors and Actuators A: Physical,* 135**,** 381-387.

[Winiarski et al., 2012] WINIARSKI, B., GHOLINIA, A., TIAN, J., YOKOYAMA, Y., LIAW, P. K. & WITHERS, P. J. 2012. Submicron-scale depth profiling of residual stress in amorphous materials by incremental focused ion beam slotting. *Acta Materialia,* 60**,** 2337-2349.

[Withers et al., 2001] WITHERS, P. J. & BHADESHIA, H. 2001. Residual stress. Part 1–measurement techniques. *Materials science and Technology,* 17**,** 355-365.

[Wong et al., 1988] WONG, A., DUNN, S. & SPARROW, J. 1988. Residual stress measurement by means of the thermoelastic effect. *Nature,* 332**,** 613.

[Wonneberger et al., 2019] WONNEBERGER, R., SEYRING, M., FREIBERG, K., CARLSSON, A., RENSBERG, J., ABENDROTH, B., STÖCKER, H., RETTENMAYR, M. & UNDISZ, A. 2019. Oxidation of stainless steel 316L – Oxide grains with pronounced inhomogeneous composition. *Corrosion Science,* 149**,** 178-184.

[Wood, 1961] WOOD, G. C. 1961. The oxidation of iron-chromium alloys and stainless steels at high temperatures. *Corrosion Science,* 2.

[Wu et al., 2015] WU, H. C., YANG, B., WANG, S. L. & ZHANG, M. X. 2015. Effect of oxidation behavior on the corrosion fatigue crack initiation and propagation of 316LN austenitic stainless steel in high temperature water. *Materials Science and Engineering: A,* 633**,** 176-183.

[Xiao et al., 2013] XIAO, J., PRUD'HOMME, N., LI, N. & JI, V. 2013. Influence of humidity on high temperature oxidation of Inconel 600 alloy: Oxide layers and residual stress study. *Applied Surface Science,* 284**,** 446-452.

[Xu et al., 2000] XU, C. & GAO, W. 2000. Pilling-Bedworth ratio for oxidation of alloys. *Material Research Innovations,* 3**,** 231-235.

[Xu et al., 2019] XU, Y., FU, H., FAN, L., LU, B., ZHAO, H. & DONG, H. 2019. Oxidation kinetics and mechanisms of aluminum modified ultra-pure low chromium ferritic stainless steels. *Corrosion Science***,** 108192.

[Yamauchi et al., 2006] YAMAUCHI, A., YAMAUCHI, Y., HIROHATA, Y., HINO, T. & KUROKAWA, K. 2006. TDS Measurement of Hydrogen Released from Stainless Steel Oxidized in H₂O-Containing Atmospheres. *Materials Science Forum,* 522-523**,** 163-170.

[Yang et al., 2013] YANG, C.-W., KIM, J.-H., TRIAMBULO, R. E., KANG, Y.-H., LEE, J.-S. & PARK, J.-W. 2013. The mechanical property of the oxide scale on Fe–Cr alloy steels. *Journal of Alloys and Compounds,* 549**,** 6-10.

[Yang et al., 2008] YANG, Y.-L., YANG, C.-H., LIN, S.-N., CHEN, C.-H. & TSAI, W.-T. 2008. Effects of Si and its content on the scale formation on hot-rolled steel strips. *Materials Chemistry and Physics,* 112**,** 566-571.

[Yang et al., 2004] YANG, Z., WALKER, M. S., SINGH, P., STEVENSON, J. W. & NORBY, T. 2004. Oxidation Behavior of Ferritic Stainless Steels under SOFC Interconnect Exposure Conditions. *Journal of The Electrochemical Society,* 151.

[Young, 2012] YOUNG, D. J. 2012. Diffusion in Internal Oxidation Reactions. *Defect and Diffusion Forum,* 323-325**,** 283-288.

[Young, 2016] YOUNG, D. J. 2016. *High temperature oxidation and corrosion of metals,* Elsevier.

[Young et al., 1987] YOUNG, E., GERRETSEN, J. & DE WIT, J. 1987. The oxygen partial pressure dependence of the defect structure of chromium (III) oxide. *Journal of the Electrochemical Society,* 134**,** 2257-2260.

[Young et al., 1985] YOUNG, E., STIPHOUT, P. & DE WIT, J. 1985. n-Type behavior of chromium (III) oxide. *Journal of The Electrochemical Society,* 132**,** 884-886.

[Yuan et al., 2016] YUAN, J., WANG, W., ZHANG, H., ZHU, L., ZHU, S. & WANG, F. 2016. Investigation into the failure mechanism of chromia scale thermally grown on an austenitic stainless steel in pure steam. *Corrosion Science,* 109**,** 36-42.

[Zhang, 2010] ZHANG, J. S. 2010. Environmental damage at high temperature. *High temperature deformation and fracture of materials.* UK: Woodhead Publishing LImited.

[Zhao et al., 1986] ZHAO, J., HUNTZ, A., COUFFIN, P. & BARON, J. 1986. An investigation of oxidation internal stresses in nicr alloy by X-ray diffraction. *Acta Metallurgica,* 34**,** 1351-1357.

[Zhao et al., 2002] ZHAO, Z., HERSHBERGER, J., YALISOVE, S. & BILELLO, J. 2002. Determination of residual stress in thin films: a comparative study of X-ray topography versus laser curvature method. *Thin Solid Films,* 415**,** 21-31.

[Zheng et al., 2010] ZHENG, S. J., WANG, Y. J., ZHANG, B., ZHU, Y. L., LIU, C., HU, P. & MA, X. L. 2010. Identification of MnCr2O4 nano-octahedron in catalysing pitting corrosion of austenitic stainless steels. *Acta Materialia,* 58**,** 5070-5085.

CHAPTER

3

Materials and Methods

Contents

CHAPTER 3 MATERIALS AND METHODS **73**

3.1 SAMPLE PREPARATION 73

3.1.1 Basic observation in advance *73*

3.1.2 Sample preparation for thermogravimetric analysis *75*

3.1.3 Cross section preparation for microscopic characterization after oxidation *75*

3.1.4 Sample preparation for growth stress determination by in-situ deflection *75*

3.2 THERMOGRAVIMETRIC ANALYSIS (TGA) 76

3.3 FIELD EMISSION SCANNING ELECTRON MICROSCOPY (FESEM) 78

3.4 X-RAY PHOTOELECTRON SPECTROSCOPY (XPS) 79

3.5 GRAZING INCIDENCE X-RAY DIFFRACTION (GIXRD) 82

3.5.1 Phase identification and quantification *84*

3.5.2 Residual stress measurement *86*

3.6 DEFLECTION EXPERIMENT 91

3.7 REFERENCE 93

Chapter 3 Materials and methods

In this chapter, the sample preparation for various experiments will be separately presented. We first start with the presentation of several essential techniques for oxidation research and their basic theories related, including thermogravimetric analysis (TGA), field emission scanning electron microscopy (FESEM), X-ray photoelectron spectroscopy (XPS), grazing incidence X-ray diffraction (GIXRD) and in-situ deflection method. Moreover, the control of experimental conditions such as oxidation temperature, duration and atmosphere applied for the high temperature oxidation tests and in-situ growth stress determination by in-situ deflection will be specifically declared.

3.1 Sample preparation

The raw material used in this thesis is a large piece of commercial 316L thin slab which measures 1000 × 500 × 1 mm^3. Then it was cut into small pieces using the cutting machine (ESCIL-ESC 250 GTL), among which the 10 × 10 × 1 mm^3 ones were prepared for oxidation tests and other basic observations, while the 10 × 40 × 1 mm^3 ones were done specifically for growth stress determinations by in-situ deflection. All the characterizations were based on the specimens grinded and polished, which will be introduced respectively in the following.

3.1.1 Basic observation in advance

The elementary metallographic observation and imprecise chemical composition analysis of the sample were carried out thanks to the optical microscopic inspection and EDX technique (ZEISS Sigma HD). The specimen for metallographic observation was grinded by first the SiC abrasive papers from P240 to P4000, and next the diamond suspension from 3 μm to 0.3 μm. Then it was polished by the colloidal silica suspension of 0.03 μm and adequately cleaned in flowing water. Finally, it was eroded for 30 seconds by wiping the “aqua regia” (3HCl+1HNO3) [*Vander Voort, 1999*]. Comparatively, the specimen for EDX characterization was prepared more simply, i.e., the grinding procedure with SiC abrasive papers was first repeated and the 15-minute cleaning was followed in the mixture of 1:1 ethanol and acetone using the ultrasonic machine. The results are shown in Figure 3.1 and Table 3.1 respectively, indicating that the average grain size is 23.5 ± 11 μm and the austenitic stainless steel investigated in this thesis can be regarded as the 17Cr-10Ni-Fe alloy.

Table 3.1 Chemical composition of AISI 316L stainless steel

Element	Fe	Cr	Ni	Mo	Mn	Cu	C	Si
wt.%	68.88	16.61	9.85	2.68	1.03	0.58	<0.03	0.37

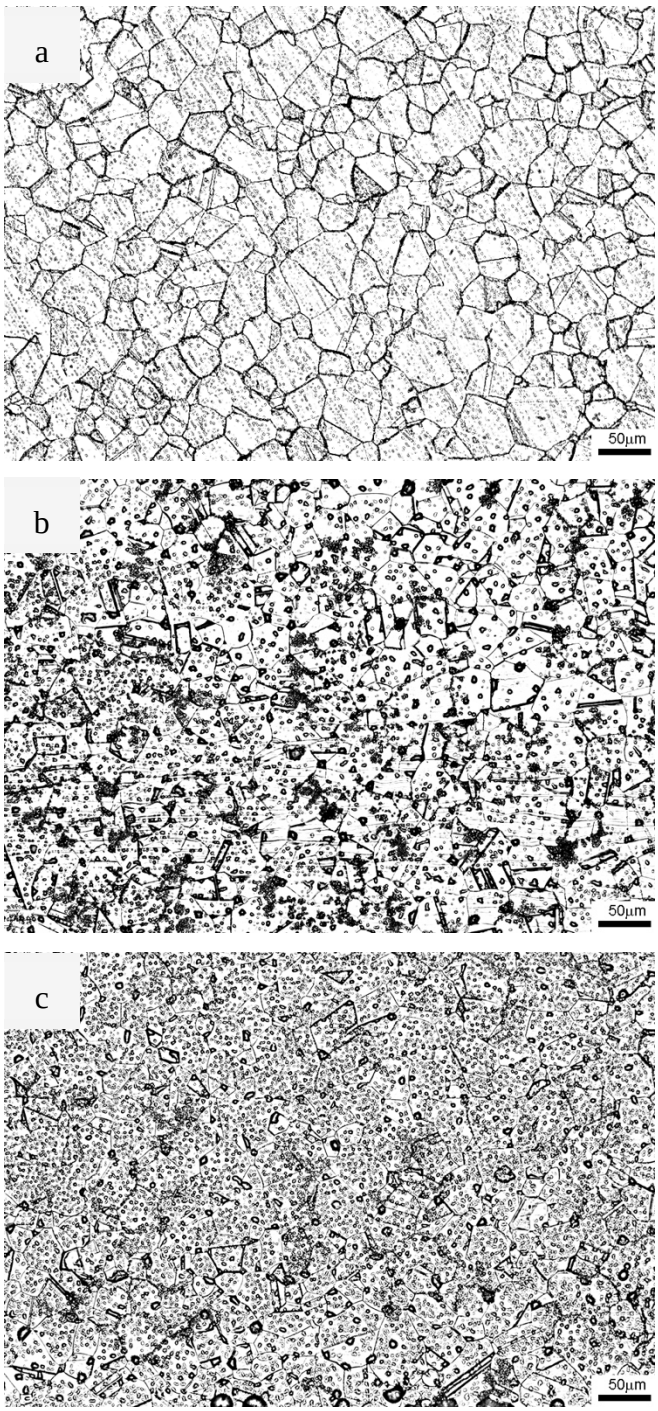

Figure 3.1 Metallographic microstructures of AISI 316L stainless steel from different views: (a) RD-TD; (b) RD-ND; (c) TD-ND.

3.1.2 Sample preparation for thermogravimetric analysis

A hole of 1mm in diameter in order to hang the sample to the balance was drilled in the edge center of $10 \times 10 \times 1$ mm^3 sample. All the surfaces were grinded by the SiC abrasive papers in the order of P240, P600, P1200, P2400 and P4000 for obtaining a uniform-roughness and clean surfaces. The samples were finally cleaned in 1:1 ethanol and acetone mixture for 20 minutes by ultrasonic machine and the liquid left on the surface was rapidly blown away by 2 bar pressed nitrogen.

3.1.3 Cross section preparation for microscopic characterization after oxidation

The key point of cross section preparation after oxidation is how to keep oxide scales intact during the cutting, grinding and polishing. Several routines of mounting such as the hot mounting and cold mounting using different mosaic composites were tried, until a method of cold mounting with a resin glue was finally chosen. A Si slice measuring $10 \times 10 \times 0.2$ mm^3 was stuck onto the oxidized surface with the glue and kept for 48 hours at room temperature for curing. A fresh cross section was then obtained by a cutting machine (ESCIL-ESC 250 GTL), which subsequently experienced manual grinding by the SiC abrasive papers of P600, P1200, P2400 orderly, then polishing in the colloidal silica suspension and cleaning thoroughly in flowing water. Finally, argon ion polishing was carried out thanks to the ion milling machine.

3.1.4 Sample preparation for growth stress determination by in-situ deflection

Considering Stoney's formula [*Stoney, 1909*], sample thickness should be controlled thin enough, normally around 0.2 mm in this thesis. The procedure of sample preparation consists of five steps (seen in Figure 3.2): initially all samples were roughly grinded by SiC abrasive papers for thickness reducing; fine grindings then started for further thickness decrease as well as surface polishing when the thickness decreased to around 0.25 mm; next the samples were pre-oxidized to form protective oxide scales in the resistance furnace at the oxidation temperatures set 10 degrees higher than those corresponding to the growth stress determination; afterwards the protective oxide scale on one surface was removed and polished again repeating the former polishing process; terminally the post-heating treatment of sample was performed so as to release the surface processing stress.

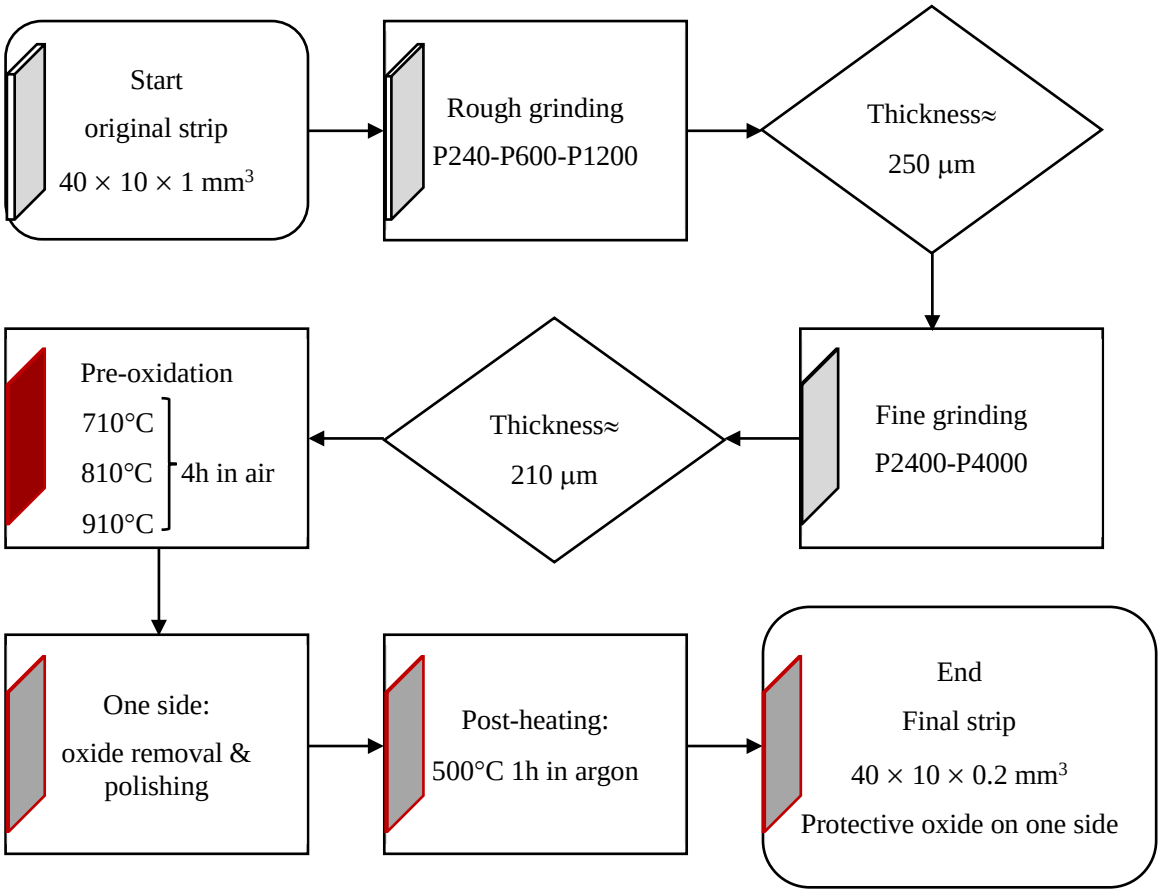

Figure 3.2 The flow diagram of the sample preparation for in-situ growth stress determination

3.2 Thermogravimetric analysis (TGA)

The oxidation rate is determined commonly by observing oxide mass accumulation with time. Thermogravimetric analysis (TGA) can be carried out continuously through a thermo-balance with quite high precision (< 5 mg) and sensitivity. In fact, the mass gain information recorded automatically offers not only the specific quantity of oxide formation but also more details about the oxidation process. For instance, the separation, fissuring or exfoliation of oxide layer can be recognized by comparing the recorded curve with the artificial one extrapolated from the initial results, as indicated by some abrupt changes as shown in Figure 3.3.

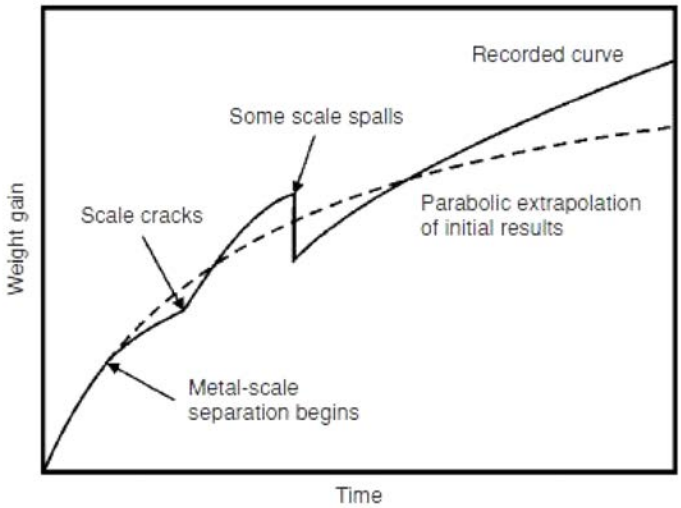

*Figure 3.3 Hypothetical mass-gain versus time curve for an oxidation reaction [*Birks et al., 2006*]*

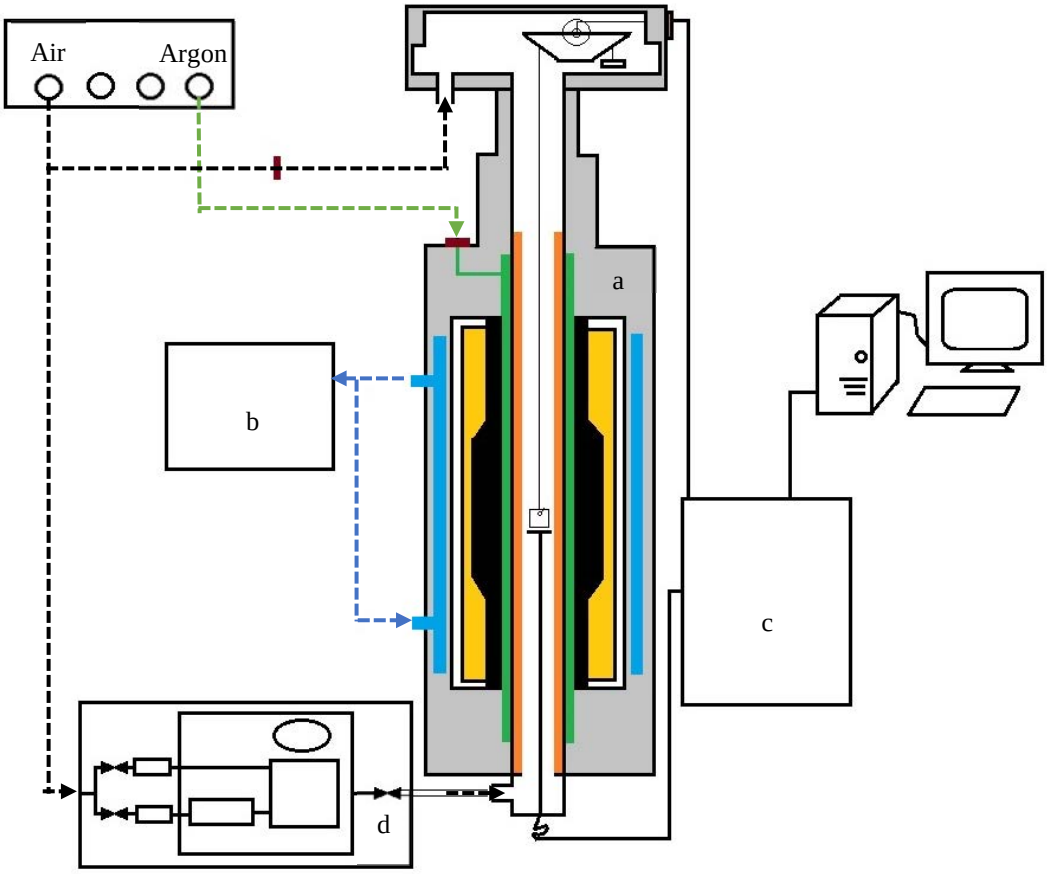

Figure 3.4 An overview of SETARAM TGA 92-16.18 apparatus schematic: (a) the furnace body; (b) the circulating cooling unit (LAUDA UKT 600); (c) the controller (CS 32); (d) the vapor generator

In this thesis, SETARAM TGA 92-16.18 apparatus (see Figure 3.4) was employed to accomplish the oxidation tests. The temperatures investigated in this thesis were 700°C, 800°C and 900°C, the corrosive atmosphere was the synthetic air (O_2 = 20%, N_2 = 80%, H_2O < 3 ppm, CO_2 < 1 ppm, CO < 1 ppm, total C_mH_m < 100 ppm) with different amounts of water vapor (0vol%, 1vol%, 2vol%, 4vol% and 8vol%), and the oxidation duration increased progressively (from 6 hours, 24 hours, 48 hours, 72 hours to 96 hours). The humidity level of reactive gas was controlled by a vapor generator (SERARAM D/WETSYS-2F) with the accuracy of ± 0.8% in relative humidity. By changing the relative humidity at a given gas temperature, the absolute humidity has been set as 0, 5, 10, 20 and 40 g/m^3 in order to obtain the corresponding water contents of 0, 1, 2, 4 and 8 vol.% respectively. The reproducibility of oxidation test is obligatory for guaranteeing the reliability of results, consequently each condition needed to be repeated until recurrence. Ultimately 190 specimens for oxidation tests were conducted in this thesis (It should be noted here that the number of different oxidation conditions to be studied is 75 considering the factor numbers of oxidation temperatures, oxidation duration and humidity. This means that this experiment needs at least 75 specimens, while the final specimen number, 190, is due to repeated experiments in some conditions to achieve reproducibility).

3.3 Field emission scanning electron microscopy (FESEM)

A focused electron beam emitted from the gun of scanning electron microscope scans over a surface to create an image. These electrons interact with the specimen, generating a variety of signals which can be collected and dealt to acquire information about the surface morphology and composition. With the help of EDX, the characterization of selected point locations or a two-dimension image on the sample can be performed, and this accessional function is particularly valuable in qualitatively or semi-quantitatively determining chemical compositions. For the FESEM, electrons from a field-emission cathode in the electron gun forms narrower probing beams at low and high electron energy, making spatial resolution improved as well as sample charging and damage minimized [*Goldstein et al., 2017*].

The primary SEM components comprise the source of electrons (gun), the column down which electrons travel (lenses), a sample stage, detectors, output devices and other infrastructure requirements. Figure 3.5 shows a schematic of SEM. Electrons generated in the electron gun experience the acceleration under high voltage and focusing through a combination of condensed lenses, reaching the apertures. Afterwards, a focused beam of electrons hits the surface of the sample mounted on the stage. Normally, the column of electron travel and sample chamber during the operation should be kept at a vacuum state which can be created by a series of pumps. The electrons interacting with the sample can produce secondary electrons,

backscattered electrons, and characteristic X-rays. These signals are amplified and then collected by diverse detectors to form images displayed on the computer screen. The electron beam can penetrate a few microns in depth on the sample, but the specific depth depends on the accelerating voltage and the density of the sample.

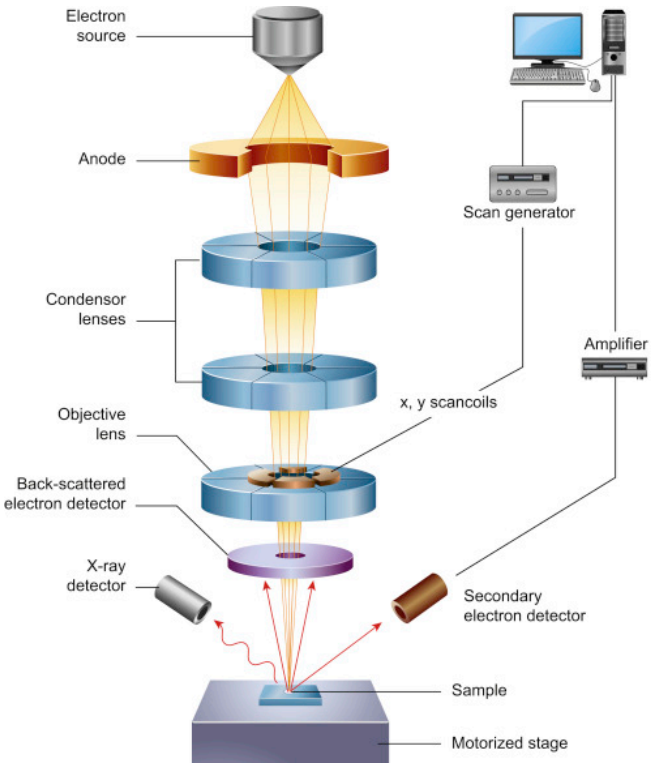

*Figure 3.5 A schematic of SEM [*Inkson, 2016*]*

In this thesis, FEG-SEM (ZEISS Sigma HD) with EDX was used for examining the surface and cross-section morphology, simultaneously determining the chemical compositions. The detective depth of this device is around 1 μm and the sensitivity of EDX for most elements is of the order of 1000 ppm.

3.4 X-ray photoelectron spectroscopy (XPS)

X-ray photoelectron spectroscopy is a preferred choice for elemental identification and chemical bond detection of oxide scales because such a highly surface sensitive technique owns outstanding features to distinguish between different compounds by resolving their chemical states. With assist of Argon ion sputtering, XPS can easily provide high-resolution compositional depth profiles in oxide scales [*Ma et al., 2018, Luo et al., 2018*].

Principles

Photoelectron emission process can be interpreted simply in three steps: initially, photoelectrons are produced when X-rays interact with the electrons in the atomic shell;

subsequently, part of these electrons travel to the surface and experience varieties of scattering processes; finally, electrons reaching the surface are emitted in the vacuum. Figure 3.6 illustrates the schematic description of related energy flow in XPS of solid surfaces. A core electron of solid with binding energy E_b acquires energy which is transferred from an incident X-ray with characteristic energy $h\upsilon$, resulting in being activated and moving to the surface of the solid. The kinetic energy E_{kin} measured by the analyzer is given:

$$E_{kin} = h\upsilon - E_b - \Phi_S - (\Phi_A - \Phi_S), \tag{3.1}$$

and it can be transposed:

$$E_b = h\nu - E_{kin} - \Phi_A, \tag{3.2}$$

where Φ_S and Φ_A are the work functions of the sample and analyzer respectively. Based on Equation (3.2), quantification by XPS can be carried out, because without the term of sample work function as well as the photoelectron energy and analyzer work function known as constants, the kinetic energy directly reflects the binding energy. Φ_A turns to be zero through energy calibration, then Equation (3.2) is simplified:

$$E_{kin} = h\upsilon - E_b, \tag{3.3}$$

From which binding energy of core electron can be identified by measuring kinetics energy conveniently.

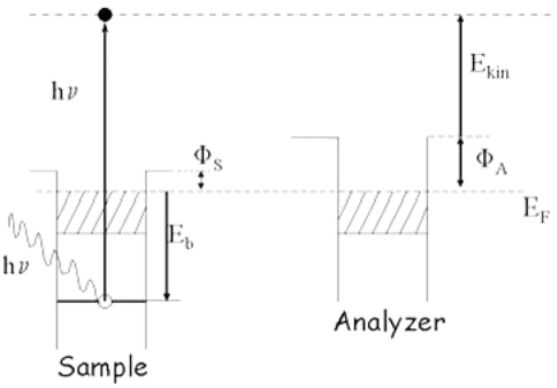

*Figure 3.6 Schematic description of related energy flow in XPS of solid surfaces [*Hofmann, 2012*]*

An XPS instrument is generally composed by an excitation X-ray source, the sample on the stage with three-direction movement, the most important electron energy analyzer equipped with detector and an auxiliary ion gun for sample cleaning and sputter depth profiling, which is shown in Figure 3.7. The working environment in electron spectroscopy is under vacuum in order to prevent electron scattering on gas molecules during the route from the sample to

analyzer as well as to minimize attenuation and distortion of the spectra by surface contamination. The zone of sample absorbs the energy from X-rays, leading to electron ejection with a range of energies and directions. A monochromator selects a narrow line from the natural emission, improving the energy resolution and removing the Bremsstrahlung background as well as the satellite peaks. After defined by the apertures, those emitted electrons are gathered continuously by the electron lens which are a set of electrostatic and/or magnetic units, and finally focused onto the analyzer entrance slit. In addition, the energy of those emitted electrons is reduced when they pass through the electron lens, and the last energy before they enter the analyzer is called the pass energy (PE). As the first and almost exclusively accepted analyzer by XPS, electrostatic hemispherical sector analyzer (HSA) shows the great potential in superior energy resolution and area transmission. It only permits the electrons with PE to arrive at the detector slits and onto the detectors themselves.

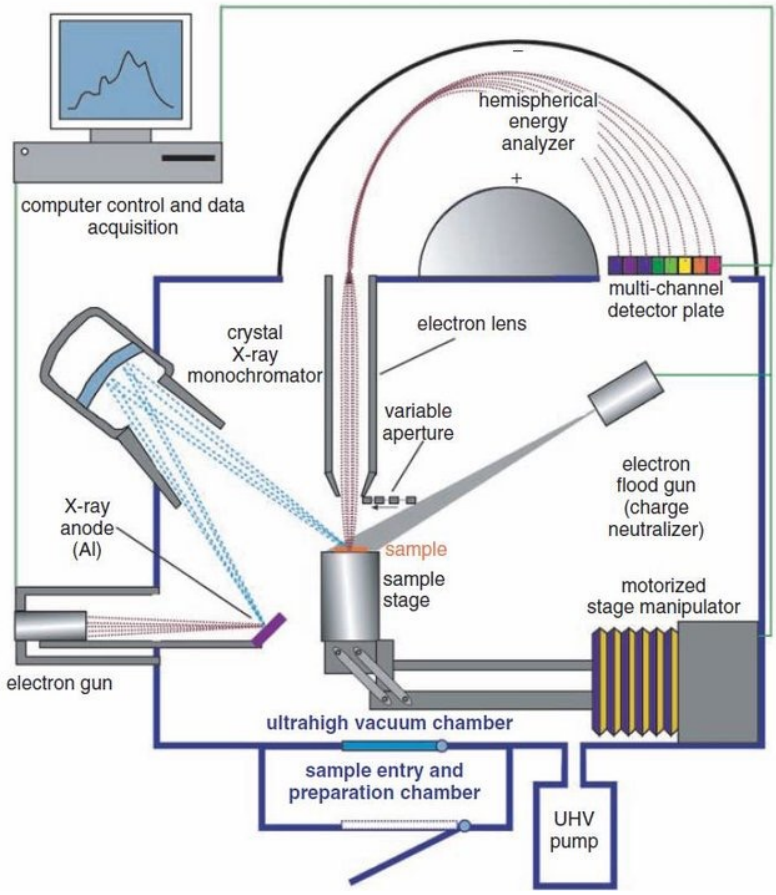

*Figure 3.7 A schematic of XPS using a monochromatized X-ray source. [*Vickerman et al., 2011*]*

In this thesis, XPS analysis was executed for the reactive element and OH^- distribution as a function of oxide scale depth. All spectra were conducted thanks to the K-Alpha XPS system from Thermo Fisher Scientific. The radiation source was a micro-focused monochromatic Al

Kα X-ray (1486.6 eV) with the operated power of 72W and the chosen spot of 200 μm. Charge compensation was performed by a dual flood gun supplying low-energy electrons. FAT (fixed analyzer transmission) mode of the hemispherical sector analyzer was brought into play with the pass energy of 50 eV, ensuring the balance between the energy resolution and the intensity. The 128-channel detector was employed whose energy channel was set in the step width of 0.1 eV. Depth profiling was assisted by an Ar^+ ion beam with the energy of 4 eV, creating the oval crater of around 5 × 8 mm^2 in area. Such a relatively large energy set was to conquer the sputtering rate deceleration caused by the coarse grains of oxides on the surface. Spectra were analyzed using CasaXPS software (version 2.3.19PR1.0). All samples measured in this thesis were thought to contain small amounts of adventitious C, consequently spectra were normalized by giving the C 1s peak a binding energy of 284.8 eV.

3.5 Grazing incidence X-ray diffraction (GIXRD)

No matter in industrials or in scientific laboratories, XRD is a formidable and dependable technique in the field of materials characterization to acquire information on an atomic scale from both crystalline and amorphous materials. Various sorts of materials such as powders, solids, thin films and nanomaterials can be examined employing X-ray diffractometers designed for diverse purposes. All kinds of structural-related results such as phase identification, crystalline structure, crystallite size, elastic distortion and residual stress, preferred orientation and layer thickness can be obtained thanks to the multiple configurations of X-ray diffractometer.

Max von Laue, in 1912, grasped that, it should be likely to diffract X-rays by a crystal so as to obtain information about its atomic arrangement if X-rays had a wavelength similar to the spacing of atomic planes in a crystal [*Laue, 1912*]. Later researchers developed the above view in the system of multiple atoms, proposing that phase could be identified by receiving those scattered and interfered waves in specific directions. Consequently, W. L. Bragg, in 1913, concluded a noted formula, Bragg's law, giving a general relationship between the wavelength of the incident X-ray and the spacing of atomic planes [*Bragg et al., 1913*]:

$$n\lambda = 2d\sin\theta, \tag{3.4}$$

where n is the order of reflection; λ is the wavelength of the X-ray; d is the interplanar spacing of the crystal and θ is the incident angle. Figure 3.8 illustrates the diffraction with respect to the Bragg's law.

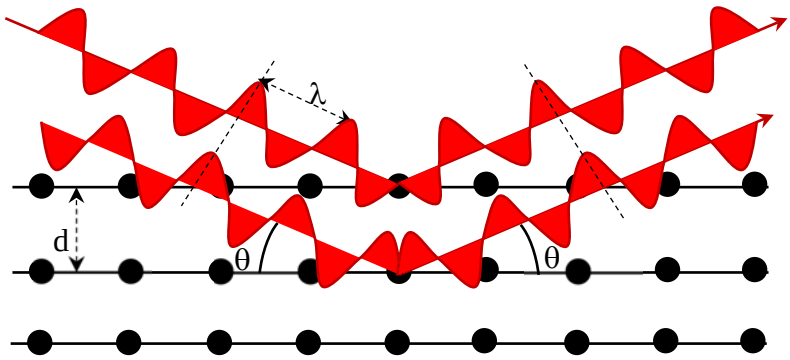

Figure 3.8 Diffraction with respect to the Bragg's law

An X-ray source, a sample stage flexible and an X-ray detector constitute the main of a diffractometer. X-rays are generated in a tube containing an anode, a cathode, a focusing cylinder and exit windows. Electrons are thermally emitted from the current passed tungsten filament, and then accelerated towards to the anode in a high voltage differential between the anode and the cathode. Electrons with sufficient energy bombard the target material, causing the inner shell electrons of target dislodged and characteristic X-ray spectra produced. For copper target, the characteristic wavelengthK_α equals 1.54187 Å (K_{α_1} = 1.540593 Å, K_{α_2} = 1.54442 Å and $K_{\alpha_2}/K_{\alpha_1}$ ratio = 0.5). These X-rays exit the tube through thin beryllium windows with focuses of line or point, and direct onto the sample after collimation. The detector receives the reflected X-rays and records the intensity. A peak in intensity is recorded when the geometry of the incident X-rays impinging the sample satisfies the Bragg equation leading to constructive interference, and converted to a count rate which is then output to the computer [*Suryanarayana et al., 2013*].

In this thesis, all X-ray diffraction measurements including phase identification, in-situ phase characterization at high temperature and residual stress examination were accomplished thanks to the PANalytical X'Pert PRO MRD system (see Figure 3.9). The high-resolution goniometer of 320 mm in radius was used with the minimum step size in ω and 2θ of 0.0001°. The parabolic X-ray mirror converting the divergent X-ray beam from a line focus tube to an intense monochromatic quasi parallel beam in one dimension was applied for phase measurements at a fixed angle of incidence on the oxide scales (For Cu radiation, the divergence angle can be reduced by the mirror from 0.8˚ to less than 0.05˚). Such mirror made it possible that a high peak intensity combined with a low background intensity and a good resolution. The X-ray lens collimating the divergent beam into a quasi-parallel beam in two dimensions was used for residual stress analysis with ψ tilts. Such lens prevented the measurements from being

influenced by defocusing effects, benefiting a precise determination of the peak position. Both phase identification and stress determination were performed relying on the X'Celerator, an ultra-fast X-ray detector efficiently processing high count rates without any compromise on resolution. Other configurations were installed individually corresponding to different measurement purposes, which will be presented in details below respectively. All XRD experiments were executed using Cu-Kα (λ = 0.154 nm) radiation under specific operated current and voltage (45 kV / 40 mA for phase identification and 40 kV / 40 mA for stress determination).

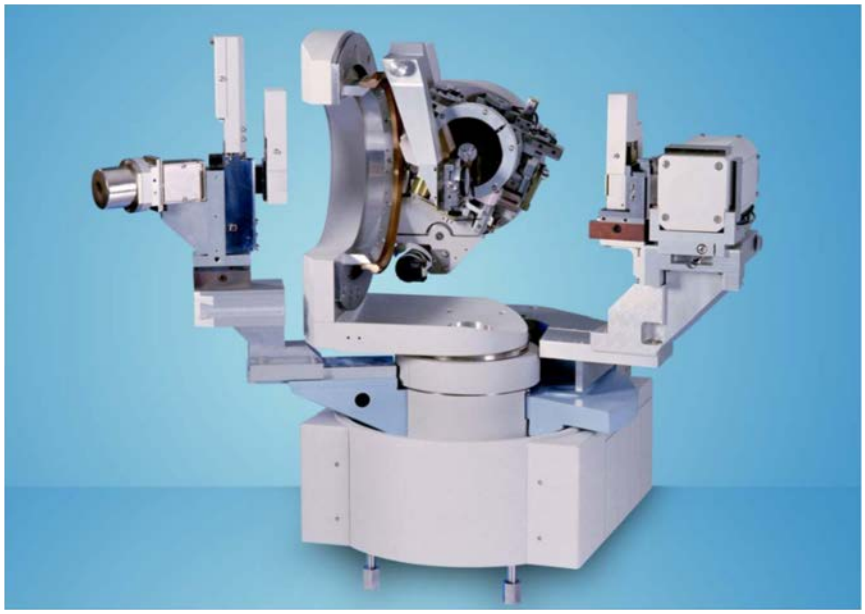

Figure 3.9 PANalytical X'Pert PRO MRD system

3.5.1 Phase identification and quantification

The optical path for phase identification was set as line focus, the divergence slit of 1/8°, the parabolic X-ray mirror, the automatic beam attenuator (an absorber which can be placed in the X-ray beam to reduce its intensity by a specific factor), the incident beam mask of 5 mm (it can be fitted in the incident beam path to control the axial width of the incident beam and thus to define the irradiated width of the sample), the all-purpose MRD cradle (sample stage), the anti-scatter slit of 5.5 mm, the soller slits assembly of 0.04 rad and the X'Celerator. Figure 3.10.a shows the X-ray optical path schematic for phase identification. In the case of in-situ phase characterization at high temperature, all optical modules kept the same except that the sample stage was substituted by the non-ambient sample stage.

A grazing incidence setup is the proper method for phase identification of oxide scales. Therefore, the chosen incident angles of 0.5°, 2° and 5° for GIXRD were performed, corresponding to the penetration depths calculated in App.2.2.1. 2θ scanned from 15° to 90°at

a step size of 0.05° and the incident angle dependent scan step size were set as 1200 s for 0,5°, 600 s for 2° and 300 s for 5°. Lingering the scan step size of small incident angles was to enhance the peak intensity received and improve the pattern smooth. The irradiated area on the sample was estimated about W × L mm^2, where W represents the irradiated width being 2 mm and L influenced by the incident angles represents the irradiated length, equaling 34.5 mm for 0.5°, 8,7 mm for 2° and 3.5 mm for 5° separately. Diffraction pattern analysis was performed using the software HighScore Plus (version 3.0e). New ICDD databases, PAN-ICSD database, COD/AMCSD database and PANalytical legacy databases were covered during the search-match-identify job.

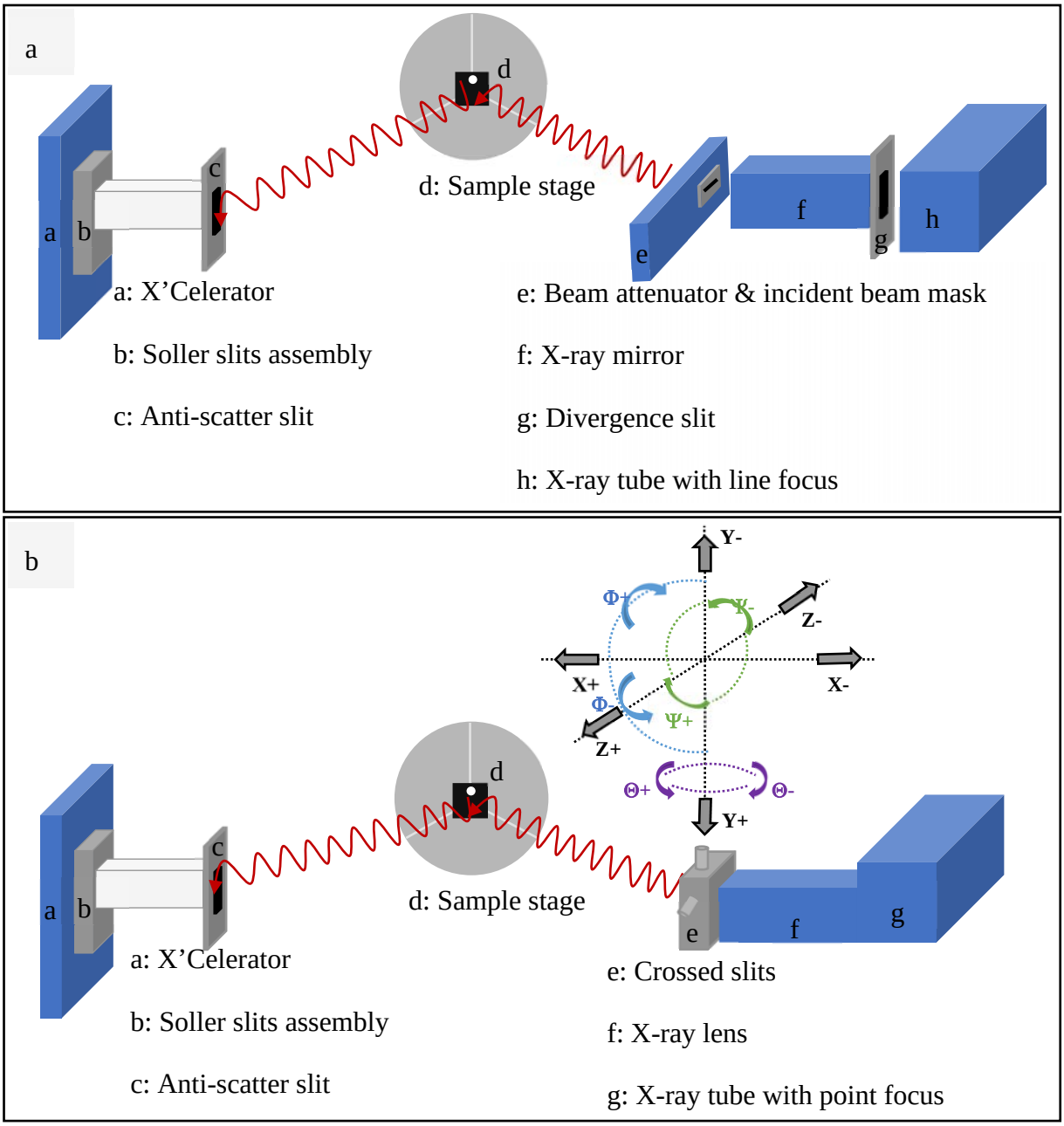

Figure 3.10 Optical path schematics for (a) phase identification (b) residual stress measurement with the five motorized movements of the sample stage shown

In addition, as XRD is appropriate for quality control, owning superior performance in detection limits (0.1 to 1wt.% per phase), phase quantification of oxidation products based on the Rietveld refinement was also conducted using the HighScore Plus software package (version 3.0e).

3.5.2 Residual stress measurement

XRD is a non-destructive and the most precise approach of residual stress determination for a wide variety of polycrystalline materials. XRD is able to uncover the stress caused crystal lattice spacing change, by which the elastic strain can be characterized using specific measured approaches.

The optical path for residual stress analysis in this work was set as point focus, the X-ray lens mounted with the crossed slits, the all-purpose MRD cradle (sample stage), anti-scatter slit of 5.5 mm, the soller slits assembly of 0.04 rad and the X'Celerator (see Figure 3.10.b)

Principles for residual stress determination by XRD

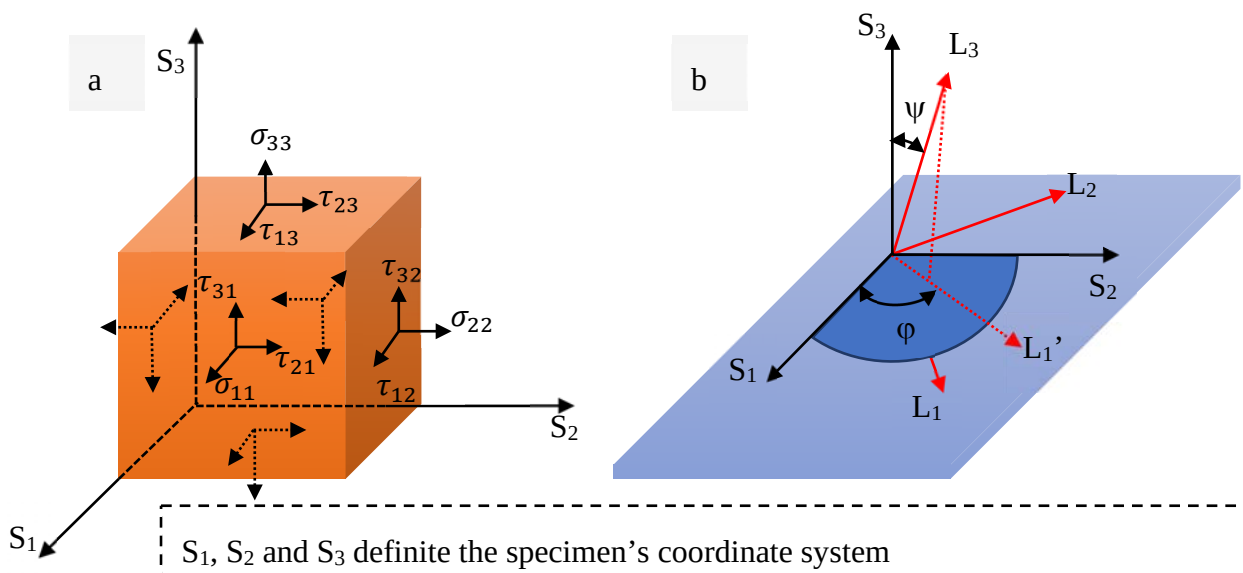

S_1, S_2 and S_3 definite the specimen's coordinate system

L_1, L_2 and L_3 definite the laboratory's coordinate system, where L_3 is the normal direction of the diffraction lattice planes {hkl}

φ is the angle between S_1 (a direction in the sample plane defined artificially) and L_1' (the projection direction of L_3 and the direction of the stress σ_φ measured)

ψ is the angle between the sample normal and the normal of diffraction lattice planes

Figure 3.11 The stress components (a) and the geometry correlated to residual stress determination (b)

Based on elasticity theory, the stress state of an arbitrary volume unit for an isotropic elastic solid can be expressed:

$$\varepsilon_{ij} = [(1+v)/E]\sigma_{ij} - \delta_{ij}(v/E)\sigma_{kk}, \tag{3.5}$$

where ε_{ij} and σ_{ij} represent the strain and stress; E and v represent the elastic modulus and Poisson's ratio; and δ_{ij} is the Kroenecker's delta.

The relationship between the stress component and strain component can be created relying on Hooke's law, which is written explicitly as the following formula set:

$$\left.\begin{aligned} \varepsilon_{11} &= (1/E)[\sigma_{11} - v(\sigma_{22}+\sigma_{33})], \\ \varepsilon_{22} &= (1/E)[\sigma_{22} - v(\sigma_{11}+\sigma_{33})], \\ \varepsilon_{33} &= (1/E)[\sigma_{33} - v(\sigma_{11}+\sigma_{22})], \\ \varepsilon_{12} &= (1/2G)\tau_{12}, \\ \varepsilon_{23} &= (1/2G)\,\tau_{23}, \\ \varepsilon_{31} &= (1/2G)\,\tau_{31}. \end{aligned}\right\}, \tag{3.6}$$

where, the shear modulus $G = E/[2(1+v)]$.

For creating the connection between the lattice spacing change and the geometry of the specimen, a transformation of the strain tensor (from the specimen's coordinate system to the laboratory's) is needed. The transformations can be conducted using the following relation:

$$\boldsymbol{\varepsilon}'_{mn} = \boldsymbol{\alpha}_{mi}\boldsymbol{\alpha}_{nj}\boldsymbol{\varepsilon}_{ij}, \tag{3.7}$$

where $\boldsymbol{\alpha}_{mi}$ is the transformation matrix for the coordinate system between the specimen's and laboratory's, generally defining the cosine of the angle between $\boldsymbol{x}_i$ in the old coordinate system and $\boldsymbol{x}_m$ in the new coordinate. The detailed derivation of the transformation relation is introduced in Annex E.

$(\varepsilon'_{33})^{\{hkl\}}_{\varphi\psi}$, measured at angles φ and ψ, is expressed in terms of lattice spacings with respect to the formulas [*15305, 2008*]:

$$\left.\begin{aligned} (\varepsilon'_{33})^{\{hkl\}}_{\varphi\psi} &= \ln\left(d_{\varphi\psi}/d_0\right) = \ln\left(\sin\theta_0/\sin\theta_{\varphi\psi}\right), && (1) \\ (\varepsilon'_{33})^{\{hkl\}}_{\varphi\psi} &\cong \left[\left(d_{\varphi\psi}-d_0\right)/d_0\right], && (2) \\ (\varepsilon'_{33})^{\{hkl\}}_{\varphi\psi} &\cong -\cot(\theta_0)\Delta\theta_{\varphi\psi}. && (3) \end{aligned}\right\}, \tag{3.8}$$

where $d_{\varphi\psi}$ denotes the d-spacing measured for the plane family {hkl} whose normal is in the direction defined by φ and ψ; d_0 denotes the d-spacing of the same plane family under the

unstressed state; θ_0 denotes the Bragg angle related to d_0; and $\theta_{\varphi\psi}$ denotes the Bragg angle related to $d_{\varphi\psi}$.

Simultaneously, $(\varepsilon'_{33})_{\varphi\psi}^{\{hkl\}}$ can be determined employing Equation (3.7):

$$(\varepsilon'_{33})_{\varphi\psi}^{\{hkl\}} = \cos^2\varphi\sin^2\psi\,\varepsilon_{11} + \sin 2\varphi\sin^2\psi\varepsilon_{12} + \cos\varphi\sin 2\psi\,\varepsilon_{13} + \sin^2\varphi\sin^2\psi\varepsilon_{22} + \sin\varphi\sin 2\psi\,\varepsilon_{23} + \cos^2\psi\varepsilon_{33}. \quad (3.9)$$

Equation (3.9) is then expressed in terms of stress:

$$(\varepsilon'_{33})_{\varphi\psi}^{\{hkl\}} = (1/E)[\sigma_{11} - v(\sigma_{22} + \sigma_{33})]\cos^2\varphi\sin^2\psi + [(1+v)/E]\tau_{12}\sin 2\varphi\sin^2\psi + [(1+v)/E]\tau_{13}\cos\varphi\sin 2\psi + (1/E)[\sigma_{22} - v(\sigma_{11} + \sigma_{33})]\sin^2\varphi\sin^2\psi + [(1+v)/E]\tau_{23}\sin\varphi\sin 2\psi + (1/E)[\sigma_{33} - v(\sigma_{22} + \sigma_{33})]\cos^2\psi, \quad (3.10)$$

with the $\sin^2\psi$ grouped into one term:

$$(\varepsilon'_{33})_{\varphi\psi}^{\{hkl\}} = [(1+v)/E][\sigma_{11}\cos^2\varphi + \tau_{12}\sin 2\varphi + \sigma_{22}\sin^2\varphi - \sigma_{33}]\sin^2\psi + [(1+v)/E]\sigma_{33} - (v/E)(\sigma_{11}+\sigma_{22} + \sigma_{33}) + [(1+v)/E](\tau_{13}\cos\varphi + \tau_{23}\sin\varphi)\sin 2\psi \quad (3.11)$$

The stress components σ_φ, as the normal stress at the angle of φ, is defined:

$$\sigma_\varphi = [\sigma_{11}\cos^2\varphi + \tau_{12}\sin 2\varphi + \sigma_{22}\sin^2\varphi]. \quad (3.12)$$

Generally, for residual stress analysis, two stress states are of interest, i.e., uniaxial and biaxial states.

For uniaxial stress state,

$$\sigma_{ij} = \begin{bmatrix} \sigma_{11} & 0 & 0 \\ 0 & 0 & 0 \\ 0 & 0 & 0 \end{bmatrix}, \quad (3.13)$$

thus, $(\varepsilon'_{33})_{\varphi\psi}^{\{hkl\}}$can be deduced:

$$(\varepsilon'_{33})_{\varphi\psi}^{\{hkl\}} = (d_{\varphi\psi} - d_0)/d_0 = [(1+v)/E]\sigma_{11}\cos^2\varphi\sin^2\psi - (v/E)\sigma_{11} = [(1+v)/E]\sigma_\varphi\sin^2\psi - (v/E)\sigma_{11} = [(1+v)/E]\sigma_\varphi\sin^2\psi + \varepsilon_{33}. \quad (3.14)$$

For biaxial stress state,

$$\sigma_{ij} = \begin{bmatrix} \sigma_{11} & \tau_{12} & 0 \\ \tau_{21} & \sigma_{22} & 0 \\ 0 & 0 & 0 \end{bmatrix}, \quad (3.15)$$

$$(\varepsilon'_{33})^{\{hkl\}}_{\varphi\psi} = [(1+v)/E][\sigma_{11}\cos^2\varphi + \tau_{12}\sin 2\varphi + \sigma_{22}\sin^2\varphi]\sin^2\psi - (v/E)(\sigma_{11} + \sigma_{22}) = [(1+v)/E]\sigma_\varphi \sin^2\psi - (v/E)(\sigma_{11}+\sigma_{22}) = [(1+v)/E]\sigma_\varphi \sin^2\psi + \varepsilon_{33}. \quad (3.16)$$

It can be found:

$$(\varepsilon'_{33})^{\{hkl\}}_{\varphi\psi} - \varepsilon_{33} = \left(d_{\varphi\psi} - d_0\right)/d_0 - (d_{33} - d_0)/d_0 = \left(d_{\varphi\psi} - d_{33}\right)/d_0 \approx \left(d_{\varphi\psi} - d_{33}\right)/d_{33} = \left(d_{\varphi\psi} - d_{\psi=0}\right)/d_{\psi=0}. \quad (3.17)$$

The relationship between the d-spacing change measured and the associated stress is then obtained, which is also the theory basis of $\sin^2\psi$ method:

$$\sigma_\varphi = \{E/[(1+v)\sin^2\psi]\}\left(d_{\varphi\psi} - d_{\psi=0}\right)/d_{\psi=0}. \quad (3.18)$$

In practice, 2θ scans within a small range corresponding to the specific plane family are performed at a series of psi angles. The in-plane stress is then achieved by extracting the slope of plot of d-spacing vs $\sin^2\psi$. Two kinds of configurations for 2θ scan are commonly used, i.e., the ω-method for which the planes of psi and 2θ scan overlap and the χ-method for which the two planes said above are perpendicular. Normally, the χ-method is better at error control for the specimen centering, whose superior advantages are shown in the following aspects: first, the effect of absorption factor can be ignored cause the distances of X-ray passing at diverse psi angles are almost the same; second, the mutual non-influenced psi and 2 theta angles increase their applied ranges; third, the resolution is improved because the reduced defocusing benefits the diffracted spectra symmetry. Consequently the χ-method is preferred, which is also employed in this thesis. Furthermore, that the line fitted in the d-spacing vs $\sin^2\psi$ plot is not a straight line is always found during the data treatment, which can be interpreted by the sin2ψ term in Equation (3.11). The sin2ψ term describes curved deviations of the data points with positive or (pseudo-) negative tilts with respect to the general straight-line behavior. Normally such deviations can be explained as the result of instrument if the stress state is purely biaxial, otherwise it is caused by a stress-gradient, shear stress or texture. Therefore, in the latter case an average normal stress is present in principle perpendicular to the sample surface, which is assumed artificially as zero.

In this thesis, all residual stress measurements and data treatments are performed with respect to the European standard NF EN 15305 (version of April 2009) [*15305, 2008*]. Considering the high-resolution configurations of XRD instrument, the relatively severe peak shifting caused by low Bragg angle chosen can be ignored. The factor needed to be considered for choosing an appropriate Bragg angle is that the peak intensity should be sufficient enough so as to guarantee the accuracy of peak position definition to some extent. Therefore, the d-spacing change of the

{104} plane family of Cr_2O_3 (and/or (Cr, Fe)$_2O_3$) was selected for analyzing the residual stresses in the corundum-type oxide (main Cr_2O_3 and (Cr, Fe)$_2O_3$) scales; the d-spacing change of the {113} plane family of $MnCr_2O_4$ (and/or $Mn_{1.5}Fe_{1.5}O_4$, Fe_3O_4, $NiFe_2O_4$) was selected for analyzing the residual stresses in the spinel-type oxide (main $MnCr_2O_4$) scales. Residual stresses in this thesis were analyzed on the premise of elastic isotropy, elastic constants needed were consequently the bulk material properties Young's modulus (E) and Poisson's ration (ν) of each main oxide investigated, which are listed in Table 3.2. The GIXRD with the incident angles of 0.5° and 2° was also applied for residual stress analysis of oxide scales, with the irradiated area of 6mm in width and 219 mm, 55 mm and 22 mm in length in case of psi angle equaling 0°. 2θ scans were performed in the range around 33.5° ± 2°and 35.5° ± 2°separately with respect to those two plane families mentioned above, during which the step size was set 0.025° with the time per step size of 630 s, 315 s and 230 s corresponding to the different incident angles of 0.5°, 2° and 5° respectively. Thirteen peaks measured at different Psi angles (from -35° to +35°) were recorded for each plane family. Furthermore, the average residual stress profiles in the corundum-type oxide (main Cr_2O_3 and (Cr, Fe)$_2O_3$) scales were studied for part of samples. The X-ray penetration depths changed by setting a series of various incident angles and they could be estimated using the method in App. 2.2.2. The d-spacing change of the {104} plane family of Cr_2O_3 (and/or (Cr, Fe)$_2O_3$) was selected. Other measuring parameters keep the same. Data treatment was accomplished thanks to the software X'Pert Stress (version 1.0a). According to the European standard NF EN 15305 (version of April 2009) [*15305, 2008*], criteria on the uncertainty of the normal stress, u(σ), is given:

if $|\sigma| < E/400(1+\upsilon)$, then u(σ) $\leq E/5000(1+\upsilon)$ or $\leq 1/4\,|\sigma|$ whichever is the largest;

if $|\sigma| \geq E/400(1+\upsilon)$, then u(σ) $\leq E/1600(1+\upsilon)$.

Considering these two cases, it can be roughly obtained that the uncertainty of normal stress should be controlled within a quarter of normal stress itself.

Table 3.2 Elastic constants (at room temperature) of bulk oxides used in this study

Oxide	**E [GPa]**	**ν**	**Ref.**
Cr_2O_3	280	0.29	[*Robertson et al., 1990*]
Fe_2O_3	220	0.19	[*Robertson et al., 1990*]
$MnCr_2O_4$	177	0.32	[*De Jong et al., 2015*]

3.6 Deflection experiment

It must be admitted that the oxide scales are subjected to internal stresses whenever is during oxidation or cooling from high temperatures, and the stresses may ultimately relax through cracking or spalling, resulting in the loss of protective capability. Obviously, compared with the thermal stress caused by the thermal expansion coefficient difference between the oxide and metal, the growth stress influenced by many factors and formed during the oxidation is rather interesting, because it is closely linked to the morphology and growth chemistry of oxide scales.

The first time that deflection method was used for the oxidation growth stress characterization was in 1950, by Dankov and Churaev [*Dankov et al., 1950*]. For many years, this method based on the Stoney's equation has been gradually developed and improved. The specimen requires a thin rectangular strip with the length far greater than its thickness and width. The specimen is protected on one surface from pre-oxidation and the other large surface generates a bend in the specimen due to oxidation induced stress generation. The growth stress σ_{ox} can then be evaluated through the deflection D corresponding to the bending, using the elastic model which will be introduced in detail in Section 5.1.

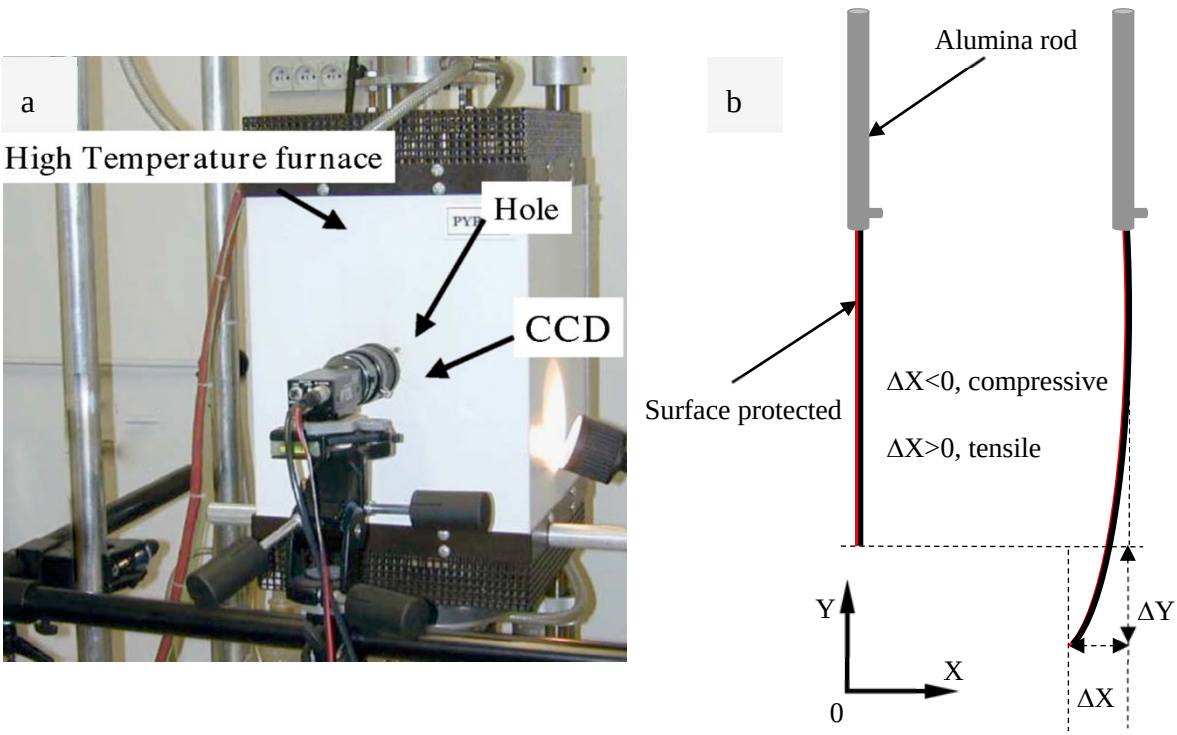

*Figure 3.12 Photography of the setup for in-situ growth stress determination [*Huntz et al., 2007*] (a) and schematic of the oxidation growth stress induced bending (b)*

In this thesis, a homemade assembly was employed for the growth stress of oxidation measurement, which is illustrated in Figure 3.12. The primary constituents of the apparatus are the resistance furnace, the circuit of gas and cooling and the CCD camera connected to the computer. The specimen prepared following what is introduced in Section 3.1.4 was fixed one end to an alumina rod by a screw and set into the furnace. The lamp was then turned on to compensate brightness through the hole on the right, facilitating to monitor the position change of the specimen when the light inside the furnace is not sufficient. All records from the CCD camera during the oxidation were saved automatically according to the acquired procedures set by the software attached with the camera. A variety of experimental conditions were performed with respect to the former ones of oxidation tests, i.e., these strips were oxidized respectively at 700°C, 800°C and 900°C for 3 hours in air with different amounts of water vapor (0%, 1%, 2%, 4% and 8%). Besides, the blank tests in argon were employed to eliminate the pseudo-bending caused by the strip elongation at high temperatures. For data treatment, the tip position change of the specimen was of interest, which is measured and saved as a set of (X, Y) coordinates thanks to the image processing software Image J (version 1.52K). ΔX presents the instantaneous deflection value, which was finally converted to the in-plane strains or stresses.

3.7 Reference

[15305, 2008] 15305, E. 2008. Nondestructive Testing—Test Method for Residual Stress Analysis by X-Ray Diffraction.

[Birks et al., 2006] BIRKS, N., MEIER, G. H. & PETTIT, F. S. 2006. *Introduction to the high temperature oxidation of metals*, Cambridge University Press.

[Bragg et al., 1913] BRAGG, W. H. & BRAGG, W. L. 1913. The reflection of X-rays by crystals. *Proceedings of the Royal Society of London. Series A, Containing Papers of a Mathematical and Physical Character,* 88**,** 428-438.

[Dankov et al., 1950] DANKOV, P. & CHURAEV, P. The effect of deformation of a metal surface layer under oxidation. Dokl. Akad. Nauk SSSR, 1950. 1221-1125.

[De Jong et al., 2015] DE JONG, M., CHEN, W., ANGSTEN, T., JAIN, A., NOTESTINE, R., GAMST, A., SLUITER, M., ANDE, C. K., VAN DER ZWAAG, S. & PLATA, J. J. 2015. Charting the complete elastic properties of inorganic crystalline compounds. *Scientific data,* 2**,** 150009.

[Goldstein et al., 2017] GOLDSTEIN, J. I., NEWBURY, D. E., MICHAEL, J. R., RITCHIE, N. W., SCOTT, J. H. J. & JOY, D. C. 2017. *Scanning electron microscopy and X-ray microanalysis*, Springer.

[Hofmann, 2012] HOFMANN, S. 2012. *Auger-and X-ray photoelectron spectroscopy in materials science: a user-oriented guide*, Springer Science & Business Media.

[Huntz et al., 2007] HUNTZ, A.-M., ANDRIEUX, M., VAHLAS, C., SOVAR, M.-M., SAMELOR, D. & GLEIZES, A. N. 2007. Phase transformations of metallorganic chemical vapor deposition processed alumina coatings investigated by in situ deflection. *Journal of The Electrochemical Society,* 154**,** P63-P68.

[Inkson, 2016] INKSON, B. 2016. Scanning electron microscopy (SEM) and transmission electron microscopy (TEM) for materials characterization. *Materials characterization using nondestructive evaluation (NDE) methods.* Elsevier.

[Laue, 1912] LAUE, M. V. 1912. *Eine quantitative prüfung der theorie für die interferenz-erscheinungen bei röntgenstrahlen*, Verlag der Kgl. Bayer. Akad. der Wiss.

[Luo et al., 2018] LUO, H., YU, Q., DONG, C., SHA, G., LIU, Z., LIANG, J., WANG, L., HAN, G. & LI, X. 2018. Influence of the aging time on the microstructure and electrochemical behaviour of a 15-5PH ultra-high strength stainless steel. *Corrosion Science,* 139**,** 185-196.

[Ma et al., 2018] MA, L., WIAME, F., MAURICE, V. & MARCUS, P. 2018. New insight on early oxidation stages of austenitic stainless steel from in situ XPS analysis on single-crystalline Fe–18Cr–13Ni. *Corrosion Science,* 140**,** 205-216.

[Robertson et al., 1990] ROBERTSON, J. & MANNING, M. 1990. Limits to adherence of oxide scales. *Materials Science and Technology,* 6**,** 81-92.

[Stoney, 1909] STONEY, G. G. 1909. The tension of metallic films deposited by electrolysis. *Proceedings of the Royal Society of London. Series A, Containing Papers of a Mathematical and Physical Character,* 82**,** 172-175.

[Suryanarayana et al., 2013] SURYANARAYANA, C. & NORTON, M. G. 2013. *X-ray diffraction: a practical approach*, Springer Science & Business Media.

[Vander Voort, 1999] VANDER VOORT, G. F. 1999. *Metallography, principles and practice*, ASM International.

[Vickerman et al., 2011] VICKERMAN, J. C. & GILMORE, I. S. 2011. *Surface analysis: the principal techniques*, John Wiley & Sons.

CHAPTER

4

Oxidation of AISI 316L Stainless Steel – Thermochemical Aspect

Contents

CHAPTER 4 OXIDATION OF AISI 316L SS – THERMOCHEMICAL ASPECT ····· **97**

4.1 OXIDATION IN DRY AIR ····· 97

4.1.1 Kinetics ····· *97*

4.1.2 Morphology and microstructure ····· *100*

4.1.2.1 Surface ····· 100

4.1.2.2 Cross-section ····· 103

4.1.3 Phases ····· *105*

4.1.4 Discussion ····· *108*

4.1.4.1 Inward growth vs outward growth ····· 108

4.1.4.2 Oxide composition ····· 109

4.1.4.3 Phase transformation at higher temperatures ····· 110

4.1.4.4 Proposed growth mechanisms in dry air ····· 111

4.2 OXIDATION IN HUMID AIR ····· 113

4.2.1 Kinetics ····· *113*

4.2.2 Morphology and microstructure ····· *116*

4.2.2.1 Surface ····· 116

4.2.2.2 Cross-section ····· 120

4.2.3 Phases ····· *124*

4.2.4 XPS Depth profile ····· *128*

4.2.5 Discussion ····· *133*

4.2.5.1 Oxidation kinetics ····· 133

4.2.5.2 Grain size ····· 137

4.2.5.3 Internal oxidation ····· 138

4.2.5.4 Martensitic phase transformation ····· 139

4.2.5.5 Oxide composition and proposed growth mechanisms in humid air ····· 140

4.3 SUMMARY ····· 141

4.4 REFERENCE ····· 143

Chapter 4 Oxidation of AISI 316L SS – thermochemical aspect

As mentioned before, the oxidation issue generally concerns the oxidation kinetics and oxidation mechanism. The oxidation kinetics is usually referred to as the oxidation rate, activation energy, atomic diffusion, etc. The oxidation mechanism usually involves the oxide constituent distribution, oxide surface morphology, oxide scale microstructure and some mechanical aspects such as internal stresses evolution, etc., of which the former three, together with the oxidation kinetics can be classified into the regime of thermochemical studies. The core issue of the thermochemical studies is to investigate the oxide scale microstructure, including the oxidation products and their distributions, which is of great importance since it provides the most information about oxidation and determines the protectivity of the oxide layer. So, in this chapter, we present firstly the thermochemical results concerning the oxidation of AISI 316L SS at 700˚C, 800˚C and 900˚C in air with different water vapor contents. The profound influence of water vapor is analyzed from the aspects of kinetics, microstructure, phase constituent and elemental distribution of the oxide's formation. The internal stress evolution which is regarded as a part of thermomechanical studies, will be presented in details in the next chapter.

4.1 Oxidation in dry air

The investigation for the oxidation of AISI 316L SS in dry air has been firstly carried out, as contrast with the latter study related to water vapor effects.

4.1.1 Kinetics

The oxide mass accumulation versus oxidation time has been recorded using the thermogravimetric analyzer. Figure 4.1 illustrates the mass gain curves recording the 96-hour isothermal oxidation of AISI 316L SS in dry air between 700 and 900˚C. It is clear that the accumulation of oxide scales rises with increasing oxidation temperature, i.e., 0.02732 mg/cm^2 at 700˚C, 0.07975 mg/cm^2 at 800˚C and 0.2567 mg/cm^2 at 900˚C respectively.

When the specimen has been oxidized for several hours at a given temperature, a compact and perfectly adhesive oxide scale gradually forms on its whole surface. At this time, the oxidation rate-controlling process turns to the anion and cation countercurrent diffusion within the oxide scale, where the parabolic rate law, described as Equation (2.31), is obeyed. If the oxide thickness x in Equation (2.31) is replaced by the mass gain per unit area $(\Delta M/S)$, it can thus be noticed that the plot of $(\Delta M/S)^2$ as a function of t shows a linear relationship when the parabolic rate law is satisfied:

$$(\Delta M/S)^2 = k_p t, \tag{4.1}$$

with k_p another type of parabolic rate constant calculated through the mass gain.

The squaring of mass gain per unit area for the 96-hour oxidation at the above temperatures has been calculated and plotted as a function of oxidation time as seen in Figure 4.2, indicating that the oxidation of AISI 316L SS in dry air at 700 ˚C, 800 ˚C and 900˚C follows the parabolic rate law. It means that the oxide scales formed on AISI 316L SS were likely to play a role of protective barrier at the selected temperatures within a quite long time to impede the metallic cations and oxygen anions inter-diffusion and reaction. The difficulty of ions diffusion is enhanced with thickening the oxide scales, whereby the scaling rate decreases versus the oxidation time. The corresponding oxidation rate constants k_p are tabulated in Table 4.1.

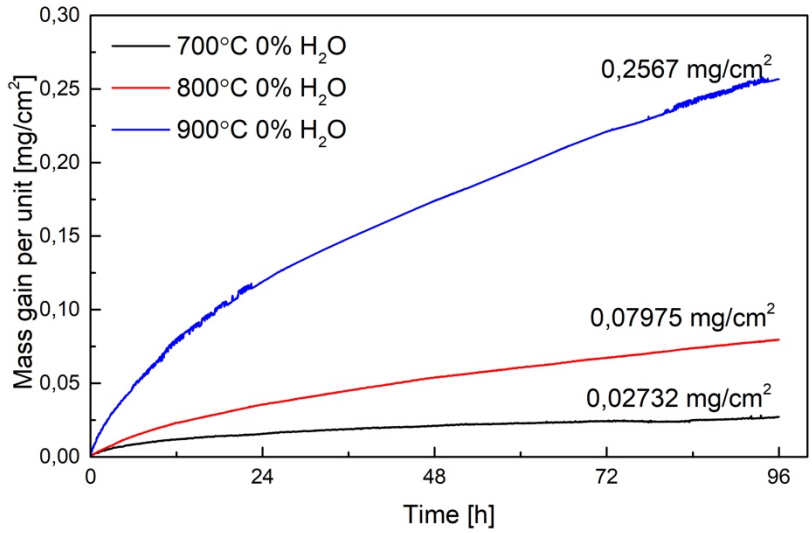

Figure 4.1 Mass gain curves of AISI 316L SS oxidized at 700˚C, 800˚C and 900˚C for 96 hours in dry air

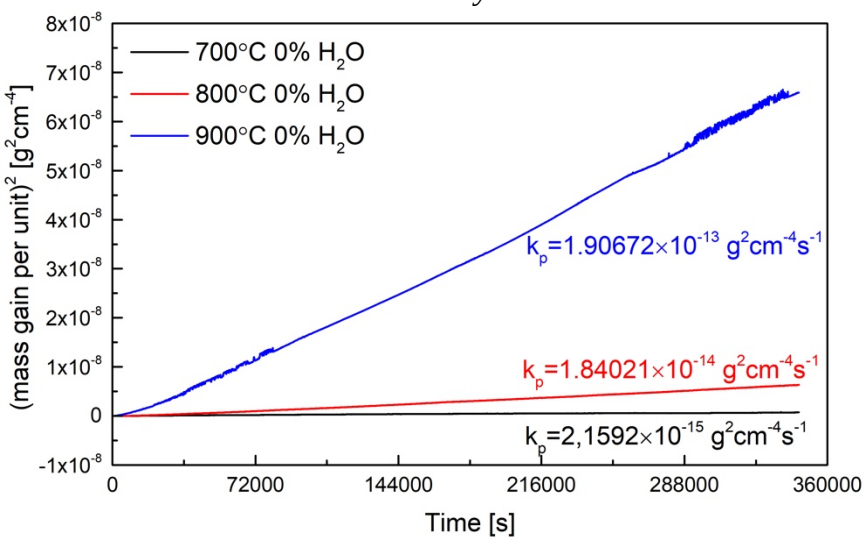

Figure 4.2 Linear relationship between $(\Delta M/S)^2$ and time showing the parabolic rate law obeyed for the oxidation of AISI 316L SS at 700˚C, 800˚C and 900˚C for 96 hours in dry air

Table 4.1 k_p calculated for the oxidation of AISI 316L SS in dry air at the given temperatures

Temperature	**700˚C**	**800˚C**	**900˚C**
$\boldsymbol{k_p}$ **($g^2cm^{-4}s^{-1}$)**	2.15920×10^{-15}	1.84021×10^{-14}	1.90672×10^{-13}

The Arrhenius equation:

$$k_p = k_0 \exp[-Q/(RT)], \tag{4.2}$$

where k_0 is a constant; Q the activation energy for oxidation; R the gas constant and T the temperature in kelvin. Equation (4.2) can be rewritten as a natural logarithm form:

$$\ln k_p = \ln k_p - [Q/(RT)], \tag{4.3}$$

where the item with the activation energy, $-Q/R$, is the slope for the plot of $\ln k_p$ and $1/T$. Therefore, the activation energy Q for the oxidation of AISI 316L SS in dry air between 700˚C and 900˚C can be estimated, i.e., 194 kJ/mol, illustrated as the black dash line fitted linearly from the star scatters in Figure 4.3.

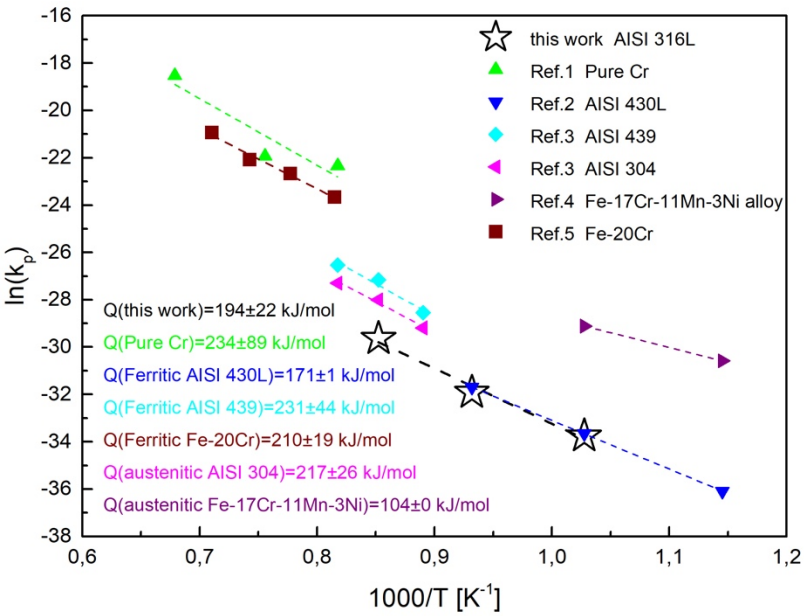

*Figure 4.3 Plots of ln(k_p) as a function of (1000/T) from this work and other studies for calculating the oxidation activation energies of Cr_2O_3 formation on various substrates (Ref.1: [*Dorcheh et al., 2018*], Ref.2: [*Karczewski et al., 2019*],Ref.3: [*Huntz et al., 2007*], Ref.4: [*Perez et al., 2000*], Ref.5: [*Wei et al., 2018*])*

Some oxidation activation energy values in other studies related to chromia formation at high temperatures in dry air on different substrates are also summarized in Figure 4.3. The activation energy in this work is comparable with those in other similar studies.

4.1.2 Morphology and microstructure

The specimens after oxidation have been observed using SEM/EDX to investigate the oxide surface morphology, surface elemental constituents and cross-section microstructure of oxide scale.

4.1.2.1 Surface

SEM surface images of some oxide scales formed in dry air are displayed in Figure 4.4, showing the morphology changement versus the oxidation time and temperature.

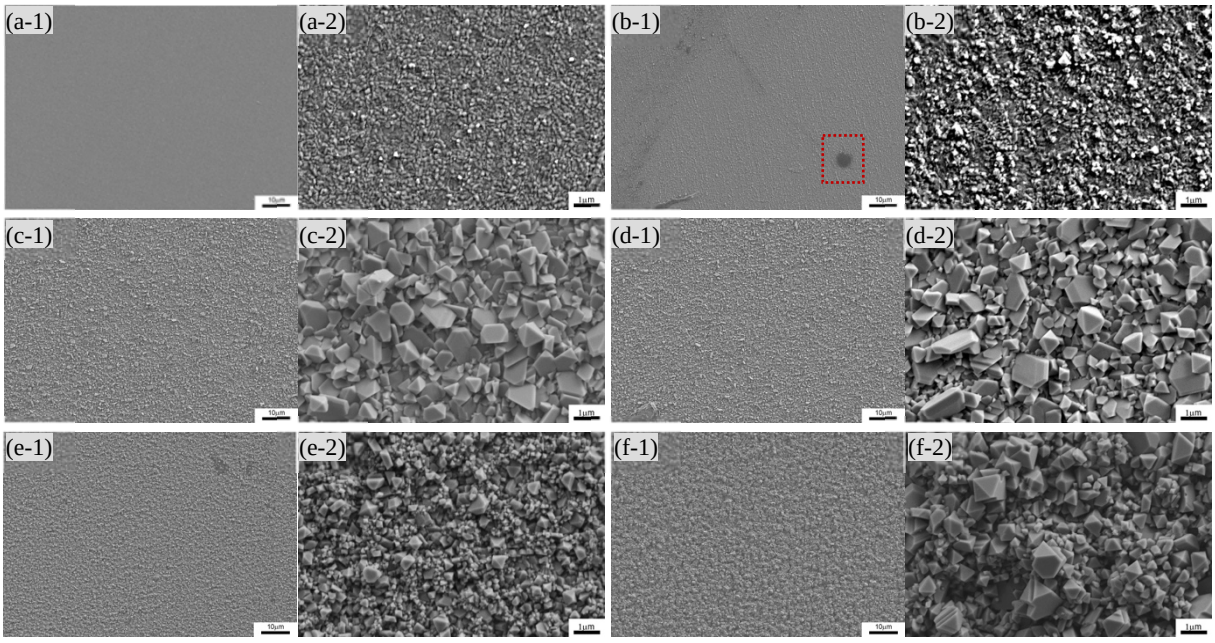

Figure 4.4 SEM images illustrating the oxide surface morphology development versus the oxidation time and temperature: 6 hours (a) and 72 hours (b) at 700˚C; 6 hours (c) and 72 hours (d) at 800˚C; 6 hours (e) and 72 hours (f) at 900˚C, where "X-2" is the local enlargement of "X-1"

It can be found that the oxide surface at 700˚C is the smoothest, smoother than those formed at 900˚C and 800˚C. The enlarged images provide more details, i.e., the oxide scales can be regarded as consisting of the continuous base oxide layer and oxide grains above. The main difference lies in the size of oxide grains and its distribution. From the simple observation by naked eye, oxide grains formed at 700˚C are the smallest while those formed at 800˚C are the largest, and the oxide grains size formed at 700˚C and 900˚C are distributed more homogeneously. At 900˚C, the oxide grains grew gradually upon oxidation, leading to a regular octahedral shape. While at 800˚C, the octahedral oxide grains coexisted with other irregular shaped grains. For the oxide scales formed at 700˚C, the grinding trace before oxidation can be

observed. The black zone marked with red dash frame is due to the inhomogeneous oxide thickness.

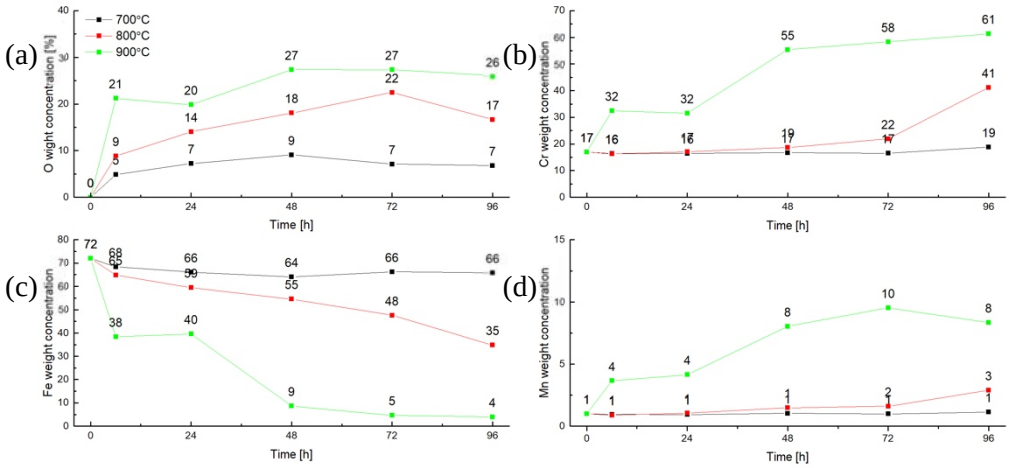

Figure 4.5 EDX quantitative elemental analysis of the oxide as a function of oxidation time at 700 ˚C, 800 ˚C and 900˚C in dry air: O (a); Cr (b); Fe (c); Mn (d)

The semi-quantification elemental analysis of the oxide scale has been carried out with the help of EDX. For SEM, the depth resolution of electron beam is around 1 μm. Hence, it can be simply thought that the surface elemental quantification analysis can be regarded as the element distribution for a volume confined with 1 μm in depth just beneath the oxide surface. Figure 4.5 displays the weight concentration development of interested elements (e.g., O, Cr, Fe and Mn) with increasing the oxidation time in the oxide scales formed between 700˚C and 900˚C in dry air. At 700˚C, compared with the original weight concentration of each element before oxidation, the oxygen content rises and Fe content accordingly declines, while the changement of other elements versus the oxidation time is not obvious. At 800˚C, with longer oxidation time, the increase of Cr and Mn contents inside the surface area gradually stands out. At 900˚C, the weight concentrations of Cr, Mn and O increase even profoundly versus the oxidation time.

Oxide grain sizes are of great interest to the investigation of oxide surface morphology. In this work, the average grain size is evaluated using the software ImageJ as the following (see Figure 4.6): firstly measure the length of an arbitrary line, e.g., Line i in Figure 4.6.a; then plot the profile of Line i and obtain a set of peaks which reflect the gray value difference between the grain center and grain boundary, shown in Figure 4.6.b; next count the number of these peaks and calculate the average grain size based on the corresponding length; finally repeat the above steps at least eight times in various directions.

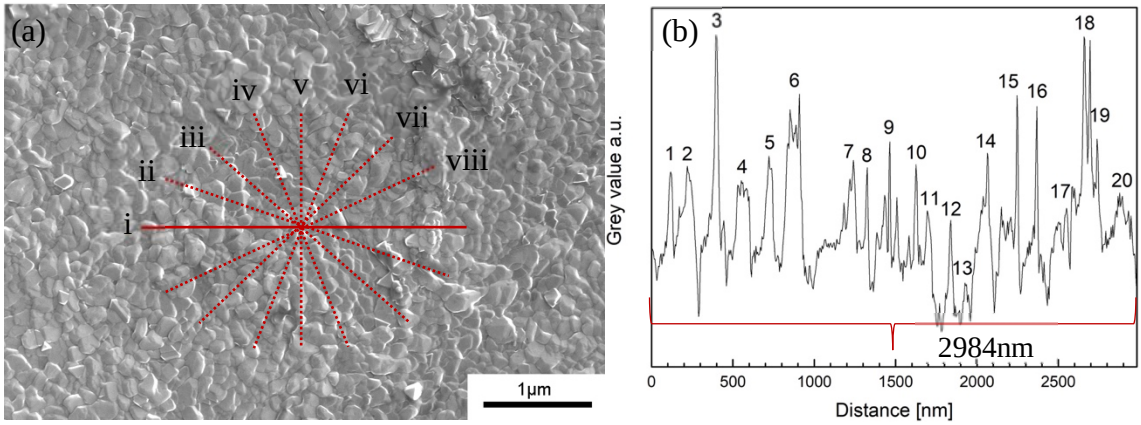

Figure 4.6 SEM image with eight lines measured (a) and plot profile of line i (b) showing the grain size determination process

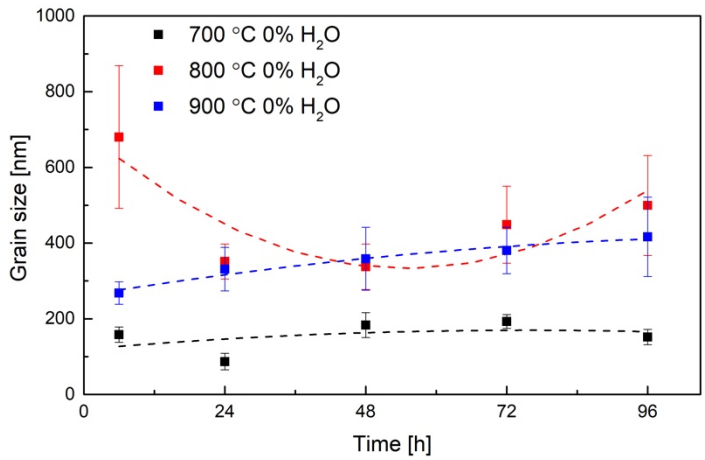

Figure 4.7 Size development of oxide grains on the oxide surface for AISI 316L SS oxidized at 700˚C, 800˚C and 900˚C in dry air based on the ex-situ SEM observations

Figure 4.7 illustrates the oxide grain size evolution versus the oxidation time and temperature for AISI 316L SS oxidized at 700˚C, 800˚C and 900˚C for from 6 hours to 96 hours in dry air. Visibly, the average sizes of oxide grains formed at 700˚C are the smallest (between 150 nm to 200 nm), and the sizes of the ones formed at 800˚C and 900˚C are similar (between 250 nm to 500 nm) with an exception of oxide grains formed after 6-hour oxidation at 800˚C. Such particular situation is probably related to the grain growth mechanism at 800˚C in this work, which will be discussed in Section 4.1.4.4. The oxide grains, on the whole, grew with increasing the oxidation time at different temperatures. In addition, the error bars reflect the size distribution, implying that the sizes of oxide grains formed at 700˚C are the most homogeneous, followed by the ones of oxide grains formed at 900˚C and 800˚C.

4.1.2.2 Cross-section

The cross-section microstructures of oxide scales and EDX mappings of elements interested are illustrated in Figure 4.8 - Figure 4.10 for AISI 316L SS after oxidation in dry air at 700˚C, 800˚C and 900˚C for 96 hours respectively. These figures confirm the temperature dependence of oxide scale microstructures for AISI 316L SS oxidized in dry air. With consideration of the corresponding oxide surface morphologies, the following results can be deduced:

- At 700˚C (see Figure 4.8)

The base oxide is studded with some small oxide grains sporadically. From the cross-section images, the MO/M interface seems flat. The elemental mappings suggest that the oxide scale contains oxygen, chromium, iron, manganese and nickel. The distribution of oxygen is inhomogeneous, showing higher affinity with chromium and manganese. The region with less oxygen in the oxide scale mainly comprises iron and nickel. No evident stratification phenomenon can be found besides a very thin layer with enriched chromium oxide appears discontinuously at the interface.

- At 800˚C (see Figure 4.9)

Compared with 700˚C, oxide grains grow larger obviously and show the octahedral shape. The cross-sectional image displays an oxide scale with two layers (marked with yellow arrows), i.e., the continuous thin layer inside and a coarse layer consisting of oxide grains outside. According to the elemental mappings, the inner layer is composed by chromium oxides, while the outer layer is composed by chromium and manganese containing oxide grains as well as nickel and iron compound grains. Moreover, a zone with chromium and manganese depleted appears just beneath the MO/M interface. Some “Kirkendall” voids are also present at the interface, as a result of diffusing capability difference between different elements.

- At 900˚C (see Figure 4.10)

It can be found from the surface image that large oxide grains are embedded in between the clusters of small octahedral oxide grains. The MO/M interface becomes rough but the joint is good between the oxide scale and substrate. The raised part of the substrate contributes to the adhesion of the oxide scale, acting as a pinning role. The elemental mappings indicate that the oxide scale consists of oxygen, chromium and manganese. Consequently, the more extensive zone of chromium and manganese depletion can be found.

The oxide scale formed at 900˚C is complicated so that a line scan profile of oxide scale has been carried out to better understand the element distribution versus depth profile, illustrated in Figure 4.11. A black dash line located at 3.5 μm in Figure 4.11.b is an indication of the interface

of two oxide layers, which is in accordance with Figure 4.11.a. Considering the concentration evolution of each element along the depth, it confirms that the inner layer is rich in chromium oxide, below which is the internal oxidation zone consisting of iron and chromium containing oxides, while the outer layer comprises a near-surface layer of manganese and chromium rich oxides as well as an outermost grain-like layer of nickel and iron rich oxides.

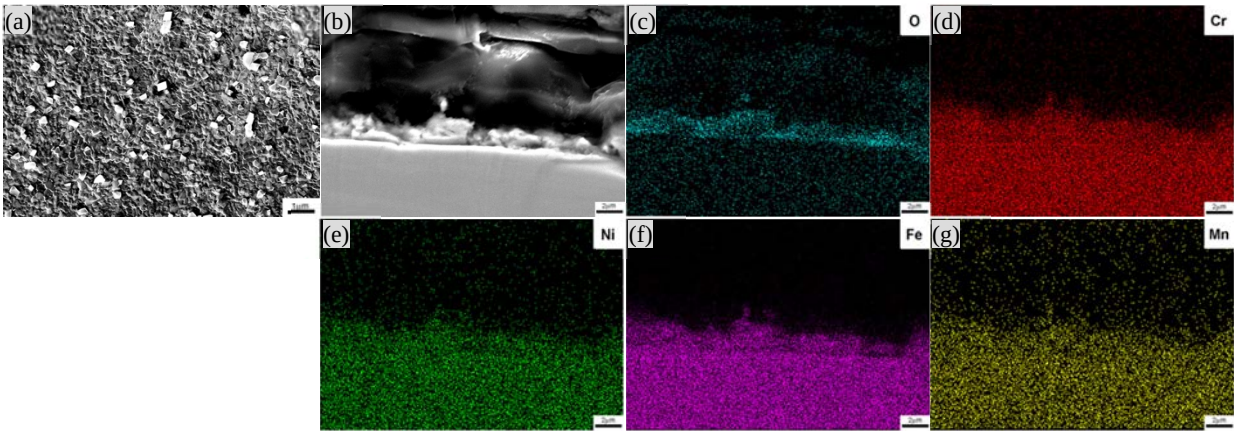

Figure 4.8 SEM images and EDS mapping of oxide scale oxidized at 700˚C for 96 hours in dry air: surface (a); cross-section (b); O mapping (c); Cr mapping (d); Ni mapping (e); Fe mapping (f); Mn mapping (g)

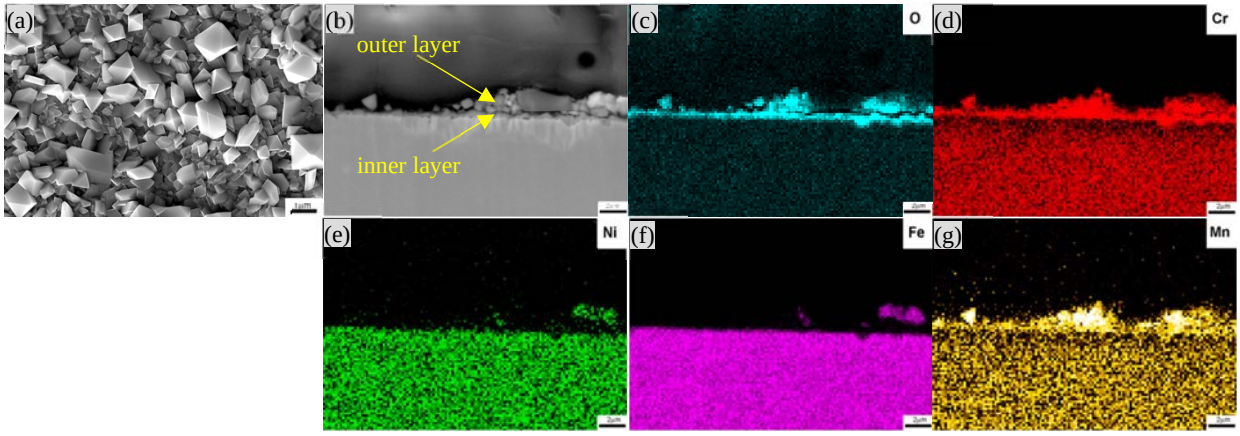

Figure 4.9 SEM images and EDS mapping of oxide scale oxidized at 800˚C for 96 hours in dry air: surface (a); cross-section (b); O mapping (c); Cr mapping (d); Ni mapping (e); Fe mapping (f); Mn mapping (g)

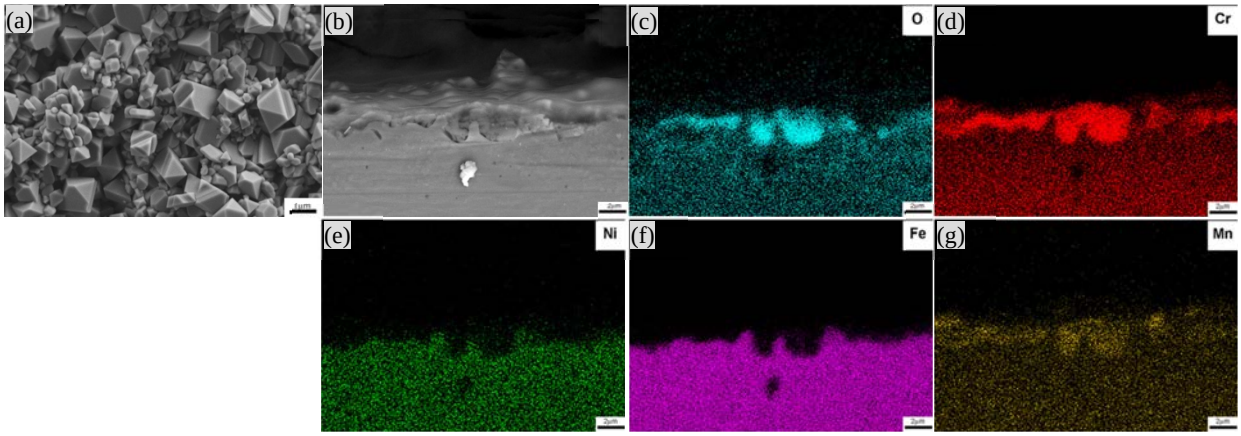

Figure 4.10 SEM images and EDS mapping of oxide scale oxidized at 900˚C for 96 hours in dry air: surface (a); cross-section (b); O mapping (c); Cr mapping (d); Ni mapping (e); Fe mapping (f); Mn mapping (g)

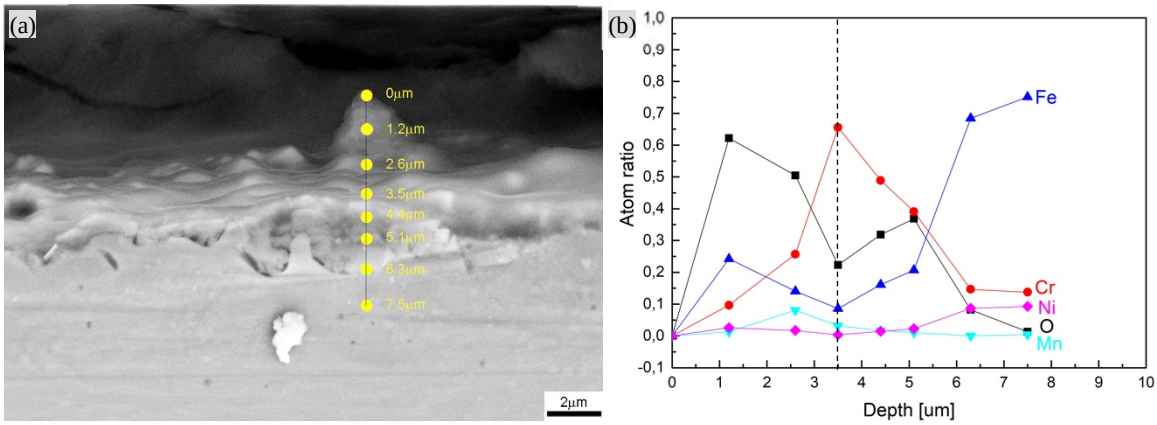

Figure 4.11 EDX line scan analysis of oxide cross-section after oxidation at 900˚C for 96 hours in dry air: SEM image (a) and corresponding line scan analysis (b)

The determination of oxide thicknesses can be seen in Appendix 1.

4.1.3 Phases

Figure 4.13.a-c display the diffracted patterns of the oxide scales after oxidation at 700˚C, 800˚C and 900˚C for 6 hours to 96 hours in dry air and also illustrates the oxide phase distribution along the X-ray penetration depth. To quantitatively analyze the phases, the Rietveld method has been employed to refine the selected diffraction patterns within the 2θ of 20˚ - 80˚, shown in Figure 4.12. In this example, the goodness indicators R_{wp}, R_{exp} and GOF are 1.66129, 1.95481 and 1.38459 respectively, showing a good refinement result. The goodness indicators for all the refinements in this thesis are tabulated in Appendix 4.

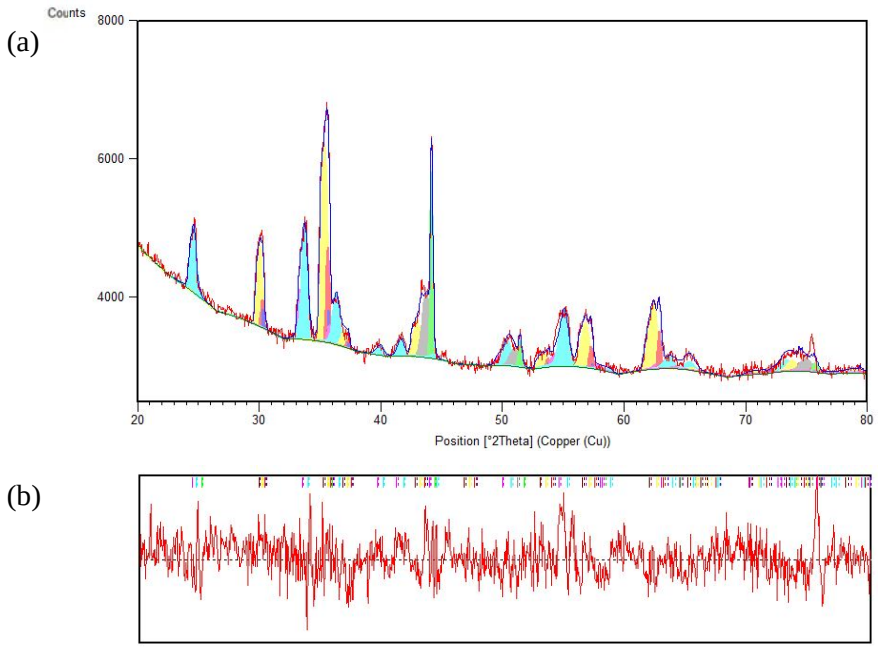

Figure 4.12 Rietveld refinement of diffracted pattern for AISI 316L SS oxidized at 900˚C for 6 hours in dry air: analyzing graphic (a) and difference plot (b)

Figure 4.13.d-f display the concentration evolution of each phase versus the oxidation time and temperature under different X-ray penetration depths.

The oxide scales formed at 700˚C mainly comprise the corundum-type oxides such as chromia (Cr_2O_3), hematite (Fe_2O_3), their solid solution $(Fe, Cr)_2O_3$ and the solid solution of Fe_2O_3 and Mn_2O_3 (represented by $FeMnO_3$ in this work). $FeMnO_3$ prefers concentrating near the MO/M interface, while chromia is rich at the outer part of oxide scales. The metallic compound of nickel and iron ($FeNi_3$) is also detected in the oxide scales, concentrating in the intermediate part. After long time oxidation, a small number of spinel-type oxides generate at the surface, identified as $MnCr_2O_4$ in this thesis. In addition, the inner part of oxide scale after 96-hour oxidation contains large amount of wüstite (FeO).

To observe the oxide scales formed at 800˚C, only two incident angles 0.5˚ and 2˚ have been applied during the XRD experiment of phase identification, representing the X-ray penetration depths of around 380 nm and 1230 nm respectively. With the apparent stratification behavior considered, the phase distribution of the oxide scales formed at 800˚C can be easily described, i.e., the inner oxide layer mainly consists of the corundum-type oxides such as Cr_2O_3 and/or $(Fe, Cr)_2O_3$, while the outer grain-like oxide layer is composed by the spinel-type oxides such as $MnCr_2O_4$, $Fe_{1.5}Mn_{1.5}O_4$ and/or Fe_3O_4. Moreover, $FeNi_3$ also exists within the oxide scale especially during the initial 48-hour oxidation. After 72-hour oxidation, few $FeNi_3$ is observed at the oxide surface (Figure 4.13.d), so the component containing Fe and Ni shown in Figure

4.9.e-f may comprise only a small amount of $FeNi_3$. Martensite phase appears near the MO/M interface in the substrate.

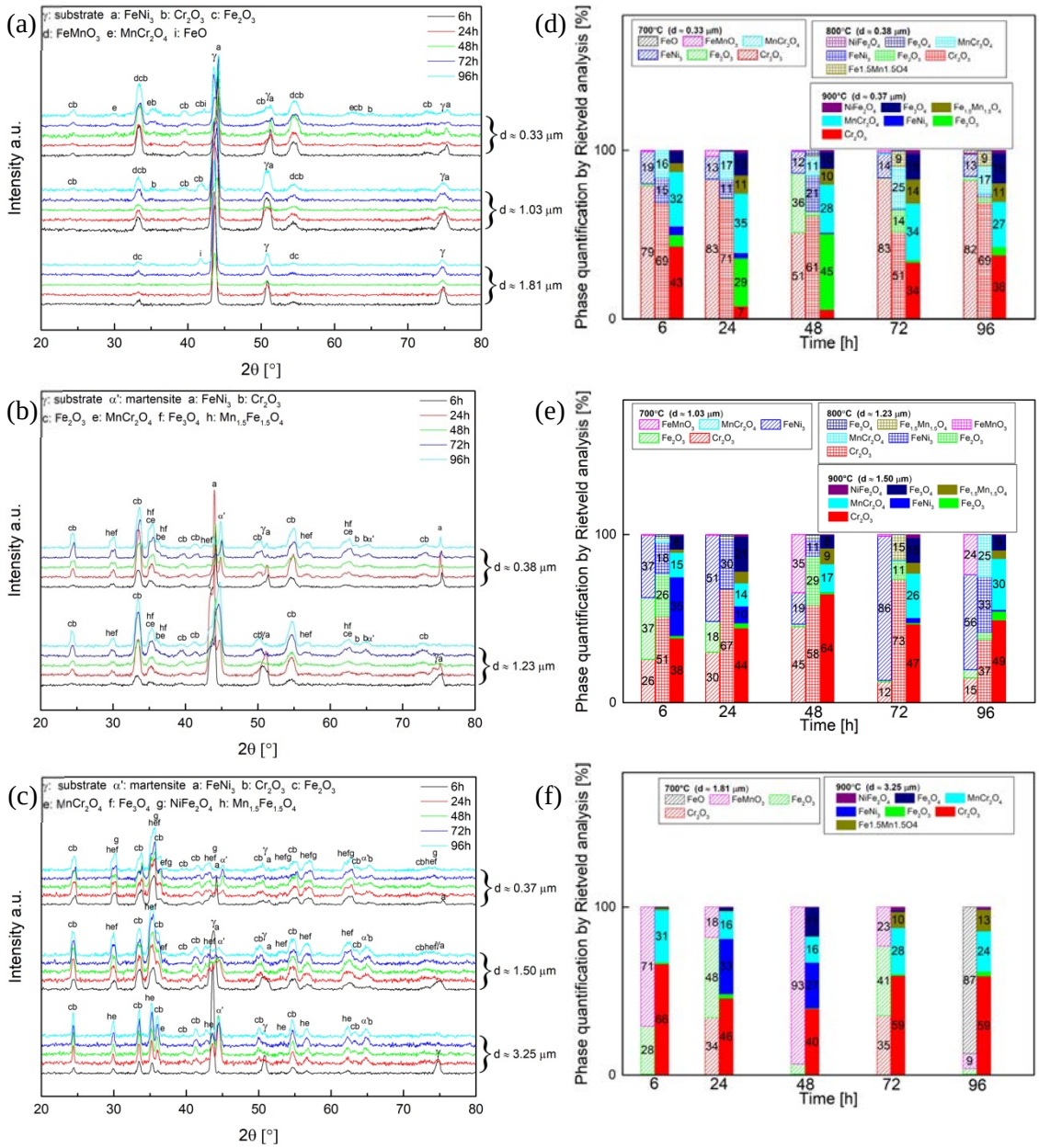

Figure 4.13 GIXRD patterns of the oxide scales after oxidation for different durations in dry air at 700 ˚C (a), 800 ˚C (b) and 900 ˚C (c) and corresponding quantitative phase composition analyses with respect to different X-ray penetration depths: 330 - 380 nm (d); 1.03 – 1.50 μm (e); 1.81 – 3.25 μm (f)

The phase constituent of the oxide scales formed at 900˚C is similar to the one formed at 800˚C. The inner layer is dominated by the corundum-type oxides, i.e., Cr_2O_3 and/or $(Fe, Cr)_2O_3$, but Cr_2O_3 is rather rich. The outer layer by contrast contains more spinel-type oxides, forming a continuous layer, which is composed by $MnCr_2O_4$, $Fe_{1.5}Mn_{1.5}O_4$, Fe_3O_4 and $NiFe_2O_4$. It should

be noted here that the concentration of $NiFe_2O_4$ content is quite low. According to the EDX line scan (see Figure 4.11), the contents of Fe and Ni increase at the outermost surface, from which $NiFe_2O_4$ can be expected.

4.1.4 Discussion

4.1.4.1 Inward growth vs outward growth

The scaling process is supported by the countercurrent diffusion of metallic cations and oxygen anions within the oxide scale. The general features of the development of the main oxides interested have been recognized [*Saunders et al., 2008*]. Normally, the outward diffusion of chromium predominates during the formation of chromia, which is similar to the growth of the metal deficit iron oxides (e.g., FeO, Fe_3O_4). The position where theses oxides prefer forming is in the intermediate or the outer part of oxide scale. Both cation interstitials and cation vacancies may be present. While the growth of Fe_2O_3 relies more on the inward diffusion of oxygen. In this case, the main defects are oxygen vacancies.

In this thesis, the oxide scale formed at 700˚C shows the significance of oxygen inward diffusion. It can be found from the element content evolution versus the oxidation time (Figure 4.5) and the element distribution along the oxide depth profile (Figure 4.8): chromium and manganese do not increase obviously after quite long-time oxidation, implying the slow cation outward diffusion process whereas oxygen inward diffusion is relatively important; moreover, the occurrence of a discontinuous layer of chromia at the MO/M interface possibly ascribes to the inward diffusion of oxygen. Similarly, Sabioni has suggested that oxygen ion inward diffusion is predominant for chromia growth kinetics on austenitic stainless steels in air at 700˚C [*Sabioni et al., 2012a, Sabioni et al., 2012b*]. However, the oxide scales formed at higher temperatures suggest that cation outward diffusion becomes more significant, which can be noticed from Figure 4.5, Figure 4.9 and Figure 4.10. For the oxide scale formed at 900˚C, chromium and manganese rise dramatically versus the oxidation time while iron shows a large decrease accordingly. The trend at 800˚C is similar but develops much slower (see Figure 4.5). The formation of Kirkendall voids at the MO/M interface is also attributed to the large amounts of cations diffused outwards, leaving a chromium and manganese depleted zone behind in the subscale of the substrate (see Figure 4.9 and Figure 4.10).This mechanism has also been proposed in [*Cox et al., 1973, Gong et al., 2010*].

It should be pointed out that this thesis just provides a qualitative analysis in regard with the growth form. It is believed that for such complicated oxidation process of AISI 316L SS, both inward growth and outward growth exist. To determine that which one predominates during the

growth, more detailed investigations of the defect structures and oxygen pressure within the oxide scale are needed.

4.1.4.2 Oxide composition

The establishment of thermodynamic modellings for ternary system related such as Mn-Cr-O and Fe-Cr-O systems at high temperatures provides a potent theory foundation to determine the oxide composition distribution formed under various conditions. Any type of phase diagram can be calculated thanks to computational thermodynamics, for instance, the Mn-Cr-O phase diagrams either isothermal or isobaric [*Jung, 2006*], shown in Figure 4.14; the Fe-Cr-O isothermal phase diagrams at 700˚C and 800˚C [*Oum et al., 2016*], shown in Figure 2.3.

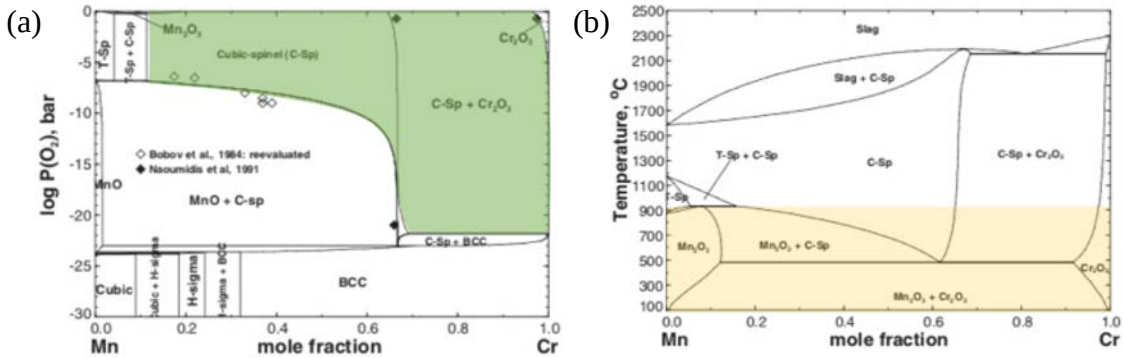

Figure 4.14 Calculated Mn-Cr-O phase diagrams: isothermal, 800℃ (a); isobaric, air (b) [Jung, 2006]

According to Figure 2.3.a, combining the previous EDX quantitative analysis, the stability of Cr_2O_3 can be confirmed in the oxide scale formed at 700˚C (Cr: 16 – 19%; Fe: 64 – 68%; O: 5 – 9%). Further considering the concentration gradient of oxygen and metallic element within the oxide scale, local stable zones can also consist of $(Cr, Fe)_2O_3$ or FeO. $(Cr, Fe)_2O_3$ is stabilized at higher oxygen pressure and covers a large range of the Fe/Cr weight fraction, indicating that the outer oxide scale prefers comprising the solid solution oxide $(Fe, Cr)_2O_3$. By contrast FeO or Cr_2O_3 will become stable with decreasing the oxygen partial pressure corresponding to the higher iron or chromium content respectively. Therefore, the oxide scale of AISI 316L SS formed at 700˚C may contain the $(Fe, Cr)_2O_3$ in the most region, while Cr_2O_3 or FeO gradually enriches near the MO/O interface with increasing the oxidation time, depending on the contents of chromium and iron. Moreover, manganese is an active component with fast diffusion velocity (Mn diffusion in chromia film formed on Ni-Cr alloy at 700˚C, $p_{O_2} = 0.0001$ atm: $D_b = 6.23 \times 10^{-18}$ cm^{2}s^{-1}, $D_{gb} = 1.53 \times 10^{-13}$ cm^{2}s^{-1}) [*Sabioni et al., 2005, Sabioni et al., 2007*], which is possible to exist in the form of solid solution oxide (see

the yellow highlight region in Figure 4.14.b as an example). Hence, in the manganese containing region with few chromium, the solid solution oxide $FeMnO_3$ is likely to form.

With increasing the oxidation temperature, manganese can draw more attention. The green highlight region in Figure 4.14.a is of interest to the oxidation of AISI 316L, confirming the stability of cubic spinel (e.g., $MnCr_2O_4$) and chromia, which is in good agreement to experimental observations in this thesis. In addition, the Fe-Cr-O isothermal phase diagram at 800˚C is similar to the one at 700˚C, indicating the stability of solid solution oxide $(Fe, Cr)_2O_3$. Therefore, the main phase constituent of the oxide scales formed at 800˚C and 900˚C is the inner corundum-type oxides (Cr_2O_3 and/or $(Fe, Cr)_2O_3$) and outer spinel-type oxides ($MnCr_2O_4$). Considering the complexity of element diffusion at higher temperature, the outer spinel oxides may also consist of Fe-rich, Fe-Mn and/or Ni-Fe spinel oxides.

4.1.4.3 Phase transformation at higher temperatures

Martensitic phase transformation occurred in the substrate near the M/MO interface after oxidation for 24 hours at 800˚C and 900˚C, illustrated in Figure 4.13.b-c. As introduced in Section 2.3.3.3, such phenomenon has also been noticed in [*Duh et al., 1988, Duh et al., 1990, Jervis et al., 1990*]. In this work, an in-situ XRD experiment has been carried out for the specimen with phase transformed. The changement of the peaks between 42˚ and 47˚ of 2θ angle has been monitored during the temperature increase and subsequent decrease, illustrated in Figure 4.15.

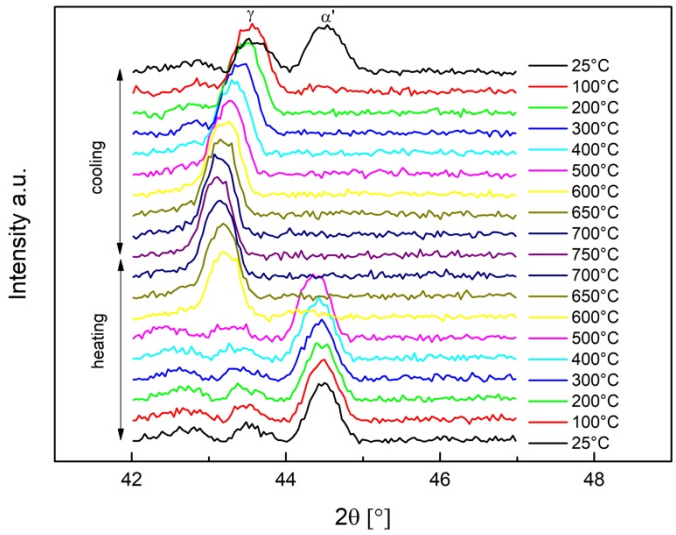

Figure 4.15 In-situ XRD monitoring the martensitic phase transformation for AISI 316L oxidized at 900˚C for 24 hours in dry air

The result suggests that α'-martensite first disappears with increasing the temperature and recovers with decreasing the temperature, implying that oxidation induced phase

transformation happened during the cooling after the isothermal oxidation. Martensitic transformation prefers occurring in the substrate near the interface where chromium and manganese are depleted, which is in accordance with [*Butler et al., 1986, Susan et al., 2012*]. According to [*Calmunger et al., 2015*], α'-martensite plays a role of grain refinement in order to promote the formation of protective chromia layer. The observation in this work verifies this point of view directly that intact inner Cr-rich oxide layers only formed at 800˚C and 900˚C with depletion zones beneath.

4.1.4.4 Proposed growth mechanisms in dry air

Based on the previous results and analyses, the oxidation process of AISI 316L SS in dry air has been summarized and displayed in Figure 4.16.

At 700˚C, a thin layer consisting of corundum-type oxides forms and gradually thickens due to the countercurrent diffusion of reactants. As oxygen diffuses faster than chromium in the oxide scale formed on AISI 304 austenitic SS in air at 700˚C [*Sabioni et al., 2012b*], this corundum-type oxide layer is first rich in iron and subsequently contains more chromium as a result of selective oxidation. The iron oxides formed before are replaced by chromium oxides or dissolved partially with chromium oxides to form their solid solution oxides. The iron exists in other forms such as the precipitation of iron and nickel metallic compound. Manganese ions migrate faster than other ions across the corundum-type oxide scale and show a good affinity with oxygen [*Sabioni et al., 2007*] so that minor manganese can be present in the form of solid solution oxide. After oxidation for a while, the most of oxide scale is composed by $(Fe, Cr)_2O_3$, with $FeMnO_3$ and $FeNi_3$ embedded. At the interface, Cr_2O_3 is stable near the grain boundary due to the fast diffusion of chromium through the grain boundary, while the region far from the grain boundary consists of FeO.

At 800˚C, a protective chromium rich oxide layer generates quickly since high temperature promotes the cation diffusion. Manganese and chromium migrate faster through the grain boundaries towards the surface than across the lattice (e.g. Cr diffusion in the oxide scale formed on AISI 304 SS in air at 800˚C: $D_{\mathrm{b}} = 1.0 \times 10^{-19}$ cm^2s^{-1} , $D_{\mathrm{gb}} = 1.4 \times 10^{-14}$ cm^2s^{-1} [*Sabioni et al., 2012b*]), whereby some spinel-type oxide grains nucleate dispersedly near the grain boundary on the surface. Due to the limit of bulk diffusion in the initial stage of oxidation, these grains gradually coalesce and grow, forming large oxide grains. After oxidation for long, a spinel-type oxide layer mainly composed by $MnCr_2O_4$ and $Mn_{1.5}Fe_{1.5}O_4$ spreads over the surface with the corundum-type oxide layer beneath.

At 900˚C, an oxide scale with two-layer structure forms quickly. The inner layer comprises the corundum-type oxides and the outer layer the spinel-type oxides. Considering the gradient of chromium and oxygen concentrations, these oxides distribute along the direction from the interface towards the surface as: Cr_2O_3, $(Fe, Cr)_2O_3$, $MnCr_2O_4$, $Mn_{1.5}Fe_{1.5}O_4$, Fe_3O_4 and $NiFe_2O_4$.

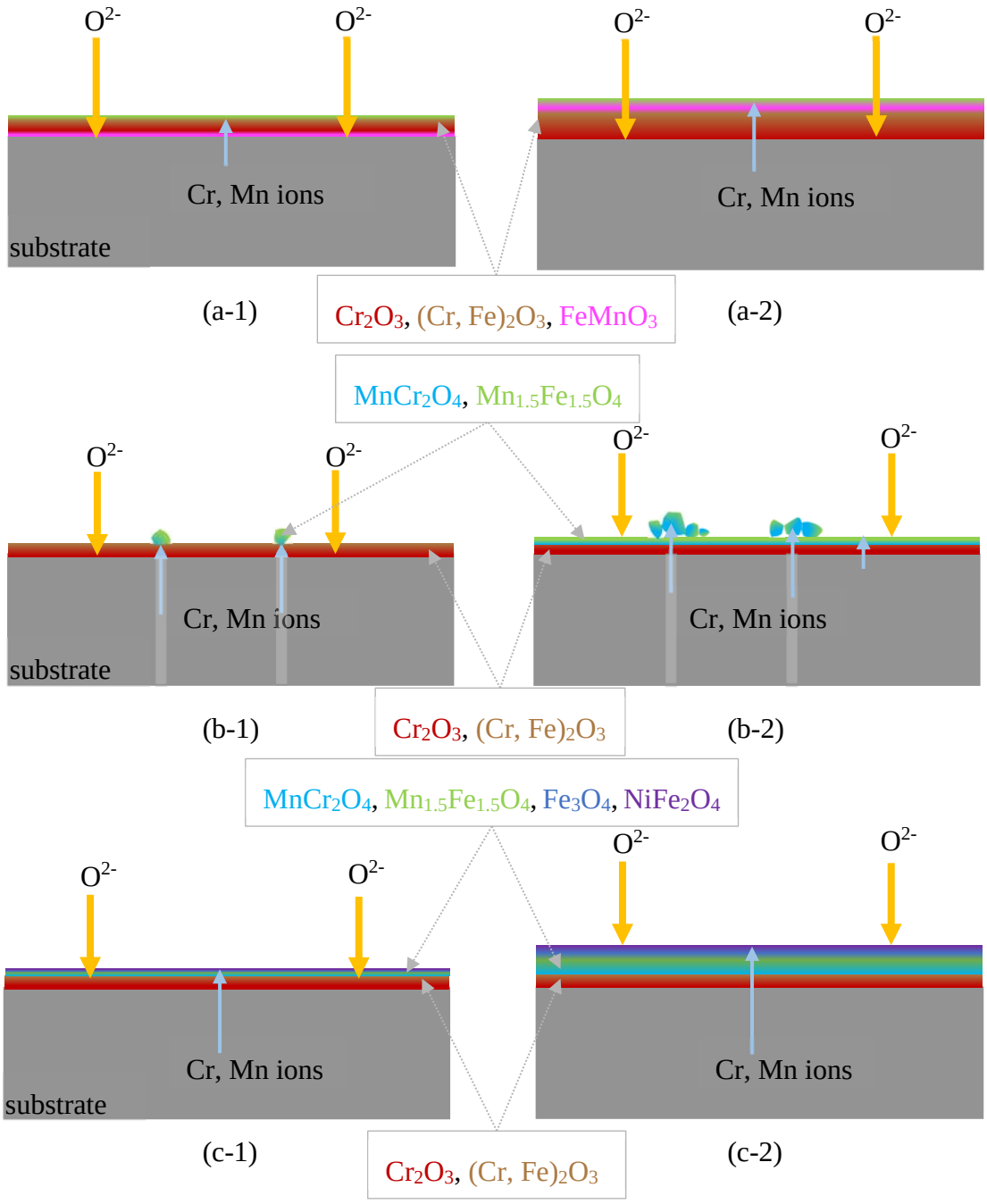

Figure 4.16 Schematic presentation of AISI 316L SS oxidized at 700˚C (a), 800˚C (b) and 900˚C (c) in dry air

4.2 Oxidation in humid air

The investigation for the oxidation of AISI 316L SS in humid air has been performed subsequently. This section studies the effects of water vapor on the oxidation mechanism with the presence of water vapor and its various contents considered.

4.2.1 Kinetics

Figure 4.17 illustrates the mass gain curves of the 96-hour and initial 6-hour isothermal oxidations of AISI 316L SS at 700˚C, 800˚C and 900˚C respectively in wet air. In this thesis, five different humidity has been considered, i.e., 0 vol.% (as a contrast), 1 vol.%, 2 vol.%, 4 vol.% and 8 vol.% water vapor containing air, to investigate the effects of water vapor on the oxidation of AISI 316L SS. It is known that oxides accumulate in dry air with increasing the oxidation time. With water vapor introduced, mass gains show the temperature and water content dependence.

At 700˚C (see Figure 4.17.a-b), compared with the situation in dry air, the oxides accumulate faster in the 1% and 2% water containing air and this trend is preserved within the oxidation duration investigated in this work. As a contrary, during the oxidation in the 4% and 8% water containing air, mass loss can be found. According to Figure 3.3, it can be deduced that cracks continuously generate during the oxidation in the 1% and 2% water containing air.

At 800˚C (see Figure 4.17.c-d), mass loss can be observed in the presence of water vapor and becomes serious with increasing the water vapor content. It should be noted that mass loss brings into play after oxidation for around 10 hours. Additionally, breakaway oxidation occurs in the 8% water containing air after 72-hour oxidation at 800˚C.

At 900˚C (see Figure 4.17.e-f), the oxides grow faster in the 1% water containing air in the initial 6-hour oxidation. During the long-time oxidation, oxides lose more with increasing the water content, meanwhile, the oxides grow dramatically after 6-hour oxidation in the 8% water containing air and after 24-hour oxidation in the 1% water containing air respectively, indicating the occurrence of breakaway oxidation.

By only considering the process before breakaway oxidation, the mass gains at different temperatures in the presence of water vapor, show similar trends to the ones at the corresponding temperatures in dry air. The plots of $(\Delta M/S)^2$ as a function of oxidation time for 24-hour oxidation under different temperatures and humidity have been drawn in Figure 4.18. The linear relationship between the above variables under selected conditions confirms that the oxidation of AISI 316L SS in wet air between 700˚C and 900˚C also follows the

parabolic rate law for the stage before breakaway oxidation. The oxidation rate constants are accordingly calculated and tabulated in Table 4.2.

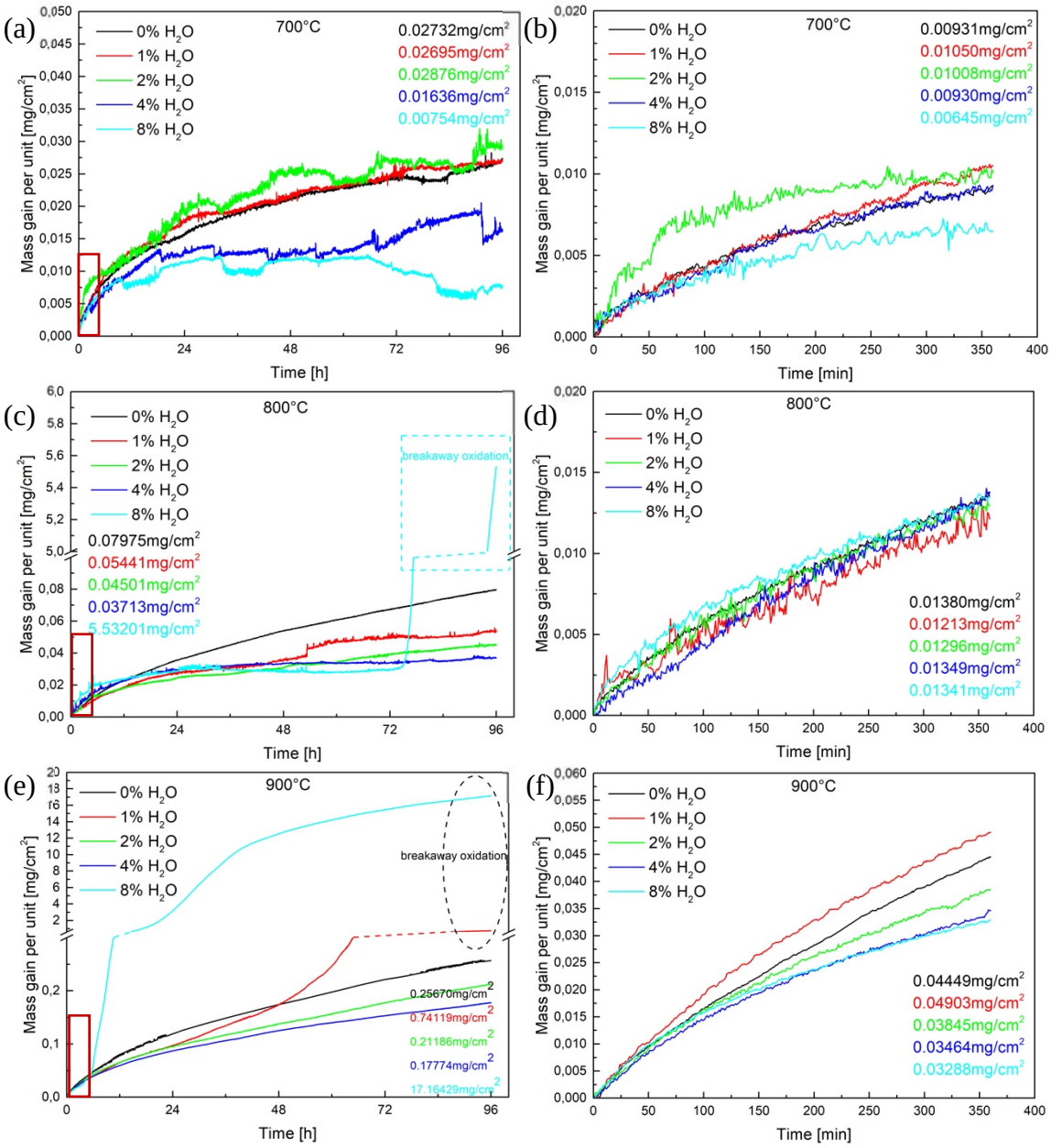

Figure 4.17 Mass gain curves of AISI 316L SS oxidized at 700˚C, 800˚C and 900˚C for 96 and 6 hours in humid air: 96 hours (a) and 6 hours (b) at 700˚C; 96 hours (c) and 6 hours (d) at 800˚C; 96 hours (e) and 6 hours (f) at 900˚C

Similarly, the oxidation activation energies for AISI 316L SS oxidized in the air with different water vapor contents have been calculated, as shown in Figure 4.19.

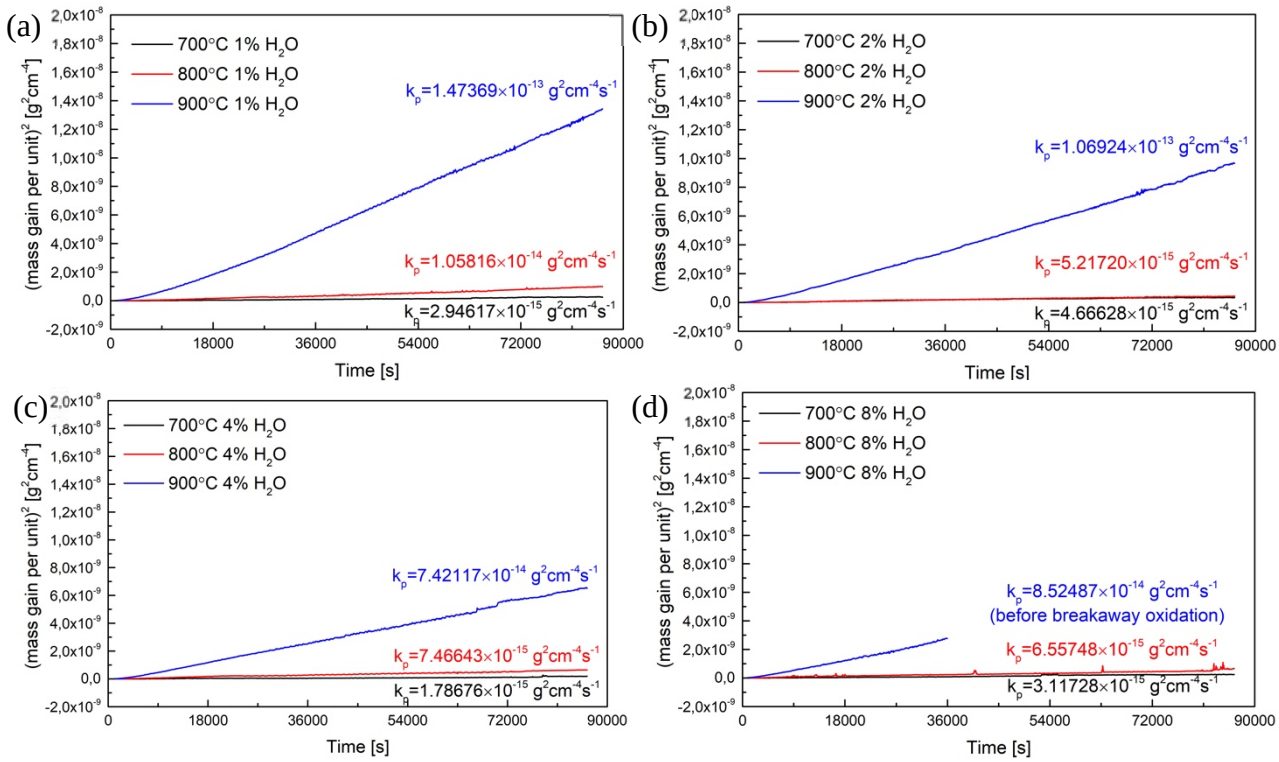

Figure 4.18 Linear relationship between $(\Delta M/S)^2$ and time showing the parabolic rate law obeyed for the oxidation of AISI 316L SS at 700˚C, 800˚C and 900˚C for 24 hours in humid air (exception: the initial 10 hours before breakaway oxidation considered for the oxidation at 900˚C in 8% water vapor containing air): air containing 1% water vapor (a); air containing 2% water vapor (b); air containing 4% water vapor (c); air containing 8% water vapor

Table 4.2 k_p ($g^2cm^{-4}s^{-1}$) calculated for the oxidation of AISI 316L SS in wet air at the given temperatures matching the results shown in Figure 4.2 and Figure 4.18

Water content (vol.%)	700˚C	800˚C	900˚C
0	2.15920×10^{-15}	1.84021×10^{-14}	1.90672×10^{-13}
1	2.94617×10^{-15}	1.05816×10^{-14}	1.47369×10^{-13}
2	4.66628×10^{-15}	5.21720×10^{-15}	1.06924×10^{-13}
4	1.78676×10^{-15}	7.46643×10^{-15}	7.42117×10^{-14}
8	3.11728×10^{-15}	6.55748×10^{-15}	8.52487×10^{-14}

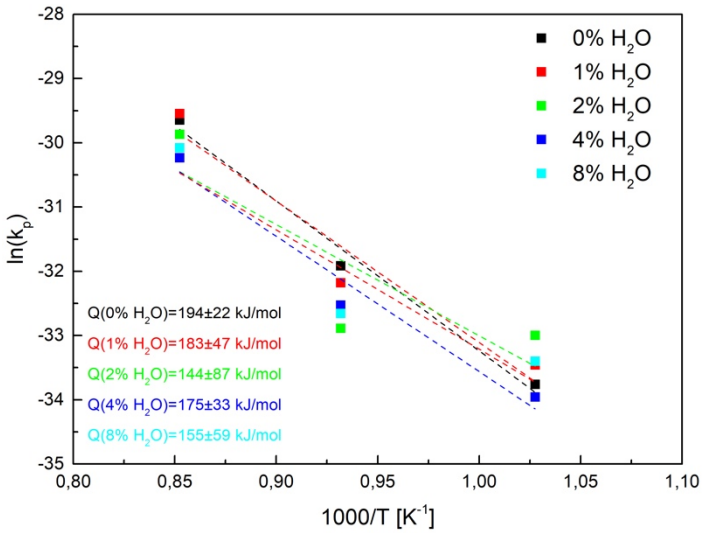

Figure 4.19 Plots of ln (k_p) as a function of (1000/T) for the oxidation activation energies of AISI 316L SS oxidized between 700˚C and 900˚C in the air with different water vapor contents

4.2.2 Morphology and microstructure

The specimens after oxidation in wet air have also been observed using SEM/EDX to investigate the oxide surface morphology, surface elemental constituent and cross-section microstructure of the oxide scale.

4.2.2.1 Surface

Figure 4.20 displays the morphology observation of the oxide scales grown on AISI 316L SS at 700˚C, 800˚C and 900˚C for 72 hours in the air with different amounts of water vapor. Compared with the morphologies of the oxide scales formed at the same temperatures for the same durations in dry air (see Figure 4.4.b, Figure 4.4.d and Figure 4.4.f), no obvious changes have been found except the ones after breakaway oxidation.

At 700˚C, the oxide scales consist of the base oxide and small oxide grains. The mass gain curves suggest the formation of cracks in the oxide scales formed in wet air but none is observed from the SEM image, indicating the following possibilities: first, these are probably the micro-cracks which can self-repair during continuous oxidation; second, these cracks are present within the inner part of the oxide scales. EDX point scan has been carried out to analyze the elemental compositions of the base oxide (Point A in Figure 4.20.a-2) and oxide grains (Point B in Figure 4.20.a-2) in the oxide scale grown at 700˚C for 72 hours in the 1% water containing air. The result is tabulated in Table 4.3, from which it can be found that the elemental constituents of these two points are similar except the manganese content. The negative values mean the relatively low concentration of element at Point B compared with that at Pont A. It

means that the formation of oxide grains possibly ascribes to the enrichment of manganese. Moreover, some holes and locally raised oxides are observed on the surfaces of the oxide scales grown respectively in the 4% and 8% water containing air respectively, marked with the red dash boxes in Figure 4.20.c-1 and Figure 4.20.d-1. From their enlarged images, the former is supposed to be caused by the incomplete integration of oxides while the latter by the inhomogeneous distribution of the oxide grain nuclei.

Table 4.3 Elemental compositions of the points in Figure 4.20.a-2 (wt.%)

Element	O	Cr	Fe	Mn	Ni
Point A (base oxide)	8.53	16.68	65.56	0.76	8.47
Point B (oxide grain)	8.27	16.29	65.58	0.96	8.90
Relative change (B/A-1)	-0.03	-0.02	0.003	0.26	0.05

At 800˚C, the surface of the oxide scale is composed by the dense oxide grains, which seems to be finer and more homogeneous than those formed in dry air. It is of interest that breakaway oxidation occurs in the 8% water containing air. The surface morphology of which is displayed in Figure 4.20.h. The zones marked with “I” and “II” illustrate the morphology features without and with the breakaway oxidation happened respectively. The former is similar with others while the latter shows thicker and multi-layer oxide scale due to local spalling.

At 900˚C, the clusters consisting of smaller oxide grains gradually form with increasing the water vapor content in the air, as shown in Figure 4.20.j and Figure 4.20.k. These grains may coalesce into the flower-like large oxide grains in the 2% water containing air, marked with the red dash boxes in Figure 4.20.j. According to the mass gain curves, breakaway oxidation has happened after 72-hour oxidation in the 1% and 8% water containing air (to be more exact, according to the mass gain results shown in Figure 4.17.e, breakaway oxidation happened after 24-hour oxidation in the 1% water containing air and after 6-hour oxidation in the 8% water containing air). The morphologies of which are illustrated in Figure 4.20.i and Figure 4.20.l respectively. In the first case with 1% water vapor, the oxide scale morphology shows no apparent distinction compared with that in dry air without breakaway oxidation (see Figure 4.4.f); in the second case with 8% water vapor, the oxide scale morphology shows pronounced difference compared with others, the features of which will be discussed in Section 6.4.

The EDX semi-quantification elemental analysis of oxide scale surface has also been carried out for the oxide scales formed in wet air (see Figure 4.21). The effects of water vapor cannot be recognized from the obtained results. But in general, the oxide scales formed at 800˚C in

wet air show a trend of containing less chromium and more iron after 96-hour oxidation with increasing the water vapor content (marked with boxes in Figure 4.21.b). The oxide scales grown at 900˚C in the 1% and 8% water containing air contain more chromium before breakaway oxidation. A sharp rise of iron and rapid decrease of chromium and manganese accompany the breakaway oxidation.

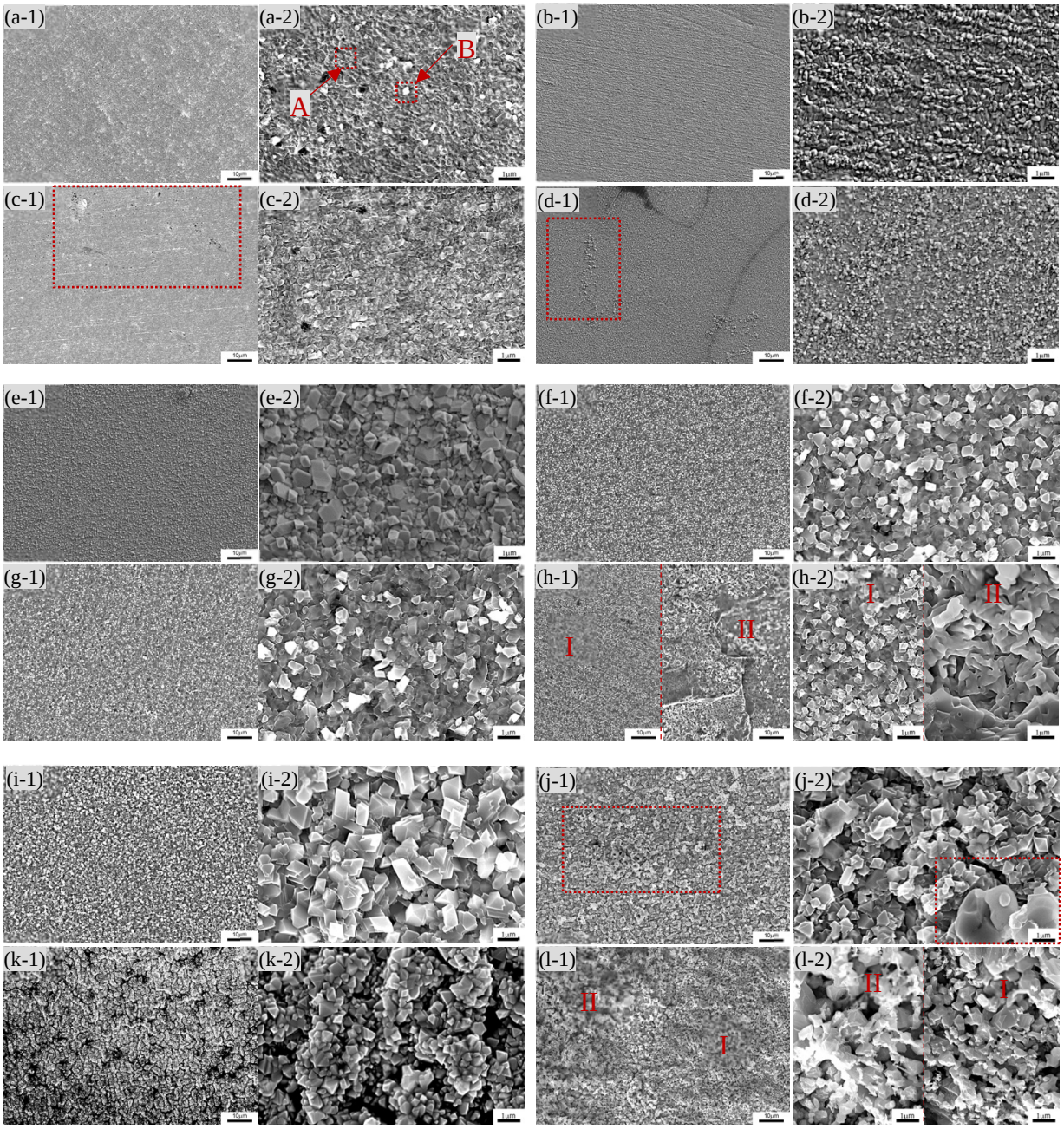

Figure 4.20 SEM images illustrating the oxide surface morphology development after 72 hour oxidation versus the temperature and humidity: at 700˚C in the air with 1% (a), 2% (b), 4% (c) and 8% (d) water vapor; at 800˚C in the air with 1% (e), 2% (f), 4% (g) and 8% (h) water vapor; at 900˚C in the air with 1% (i), 2% (j), 4% (k) and 8% (l) water vapor, where "2"

marked is the local enlargement of "1" marked and Roman numerals represent different oxidation zones on the same specimen

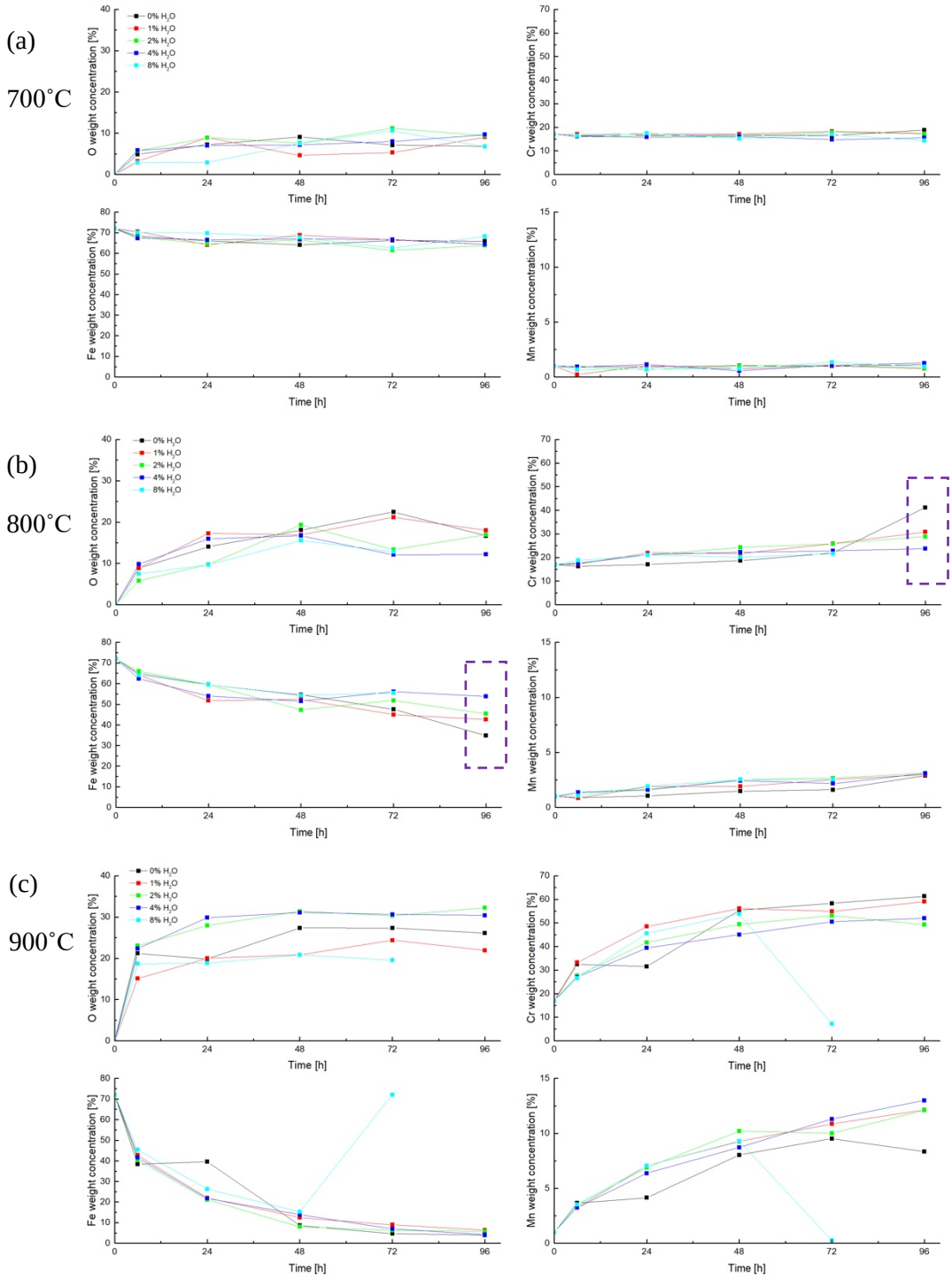

Figure 4.21 EDX quantitative elemental analyses of oxide surface as a function of oxidation time in the air with different water vapor contents (0, 1, 2, 4 and 8%) at different temperatures: 700˚C (a); 800˚C (b) and 900˚C (c)

4.2.2.2 Cross-section

The cross-section microstructures of oxide scales and EDX mappings of elements interested are illustrated in Figure 4.22 - Figure 4.30, in regard to AISI 316L SS oxidized at 700˚C, 800˚C and 900˚C for 96 hours in the 1%, 2% and 4% water containing air respectively. Similar with the situation in dry air, the features of cross-section microstructure show the clear temperature dependence as well as the sensibility to water vapor content.

- At 700˚C (see Figure 4.22 - Figure 4.24)

It can be found that the reaction region gradually enlarges with increasing the water vapor content. The oxide scales contain incompletely oxidized zones, in other words, metals or metallic compounds are present in the oxide scales. Moreover, these zones expand with improving the humidity. From element mapping, a thin layer consisting of chromium rich oxide prefers forming near the flat MO/M interface. No cracks can be seen on the surface of the oxide scale formed in the 1% water containing air, illustrated in Figure 4.22.a, but the through-scale crack and debonding of scale can be found from the cross-section image in this case, shown in Figure 4.22.b. Two possibilities can explain this phenomenon: first, the sample preparation may be responsible for the scale damage; second, cracks along the interface are more likely to exist in the original oxide scale. From Figure 4.23.a, the box region is likely to be a healed crack on the surface of the oxide scale formed in the 2% water containing air. In this case, through-scale cracks and local decohesion are present, which can be recognized through Figure 4.23.b - Figure 4.23.g. In addition, the internal oxidation zone has been detected in this case, comprising chromium rich oxides. The oxide scale displayed in Figure 4.24 shows a great number of cracks or voids. It can be deduced from the fluctuated surface in this case that the surface oxide scale deforms, which is probably driven by the layer enriched in metals beneath.

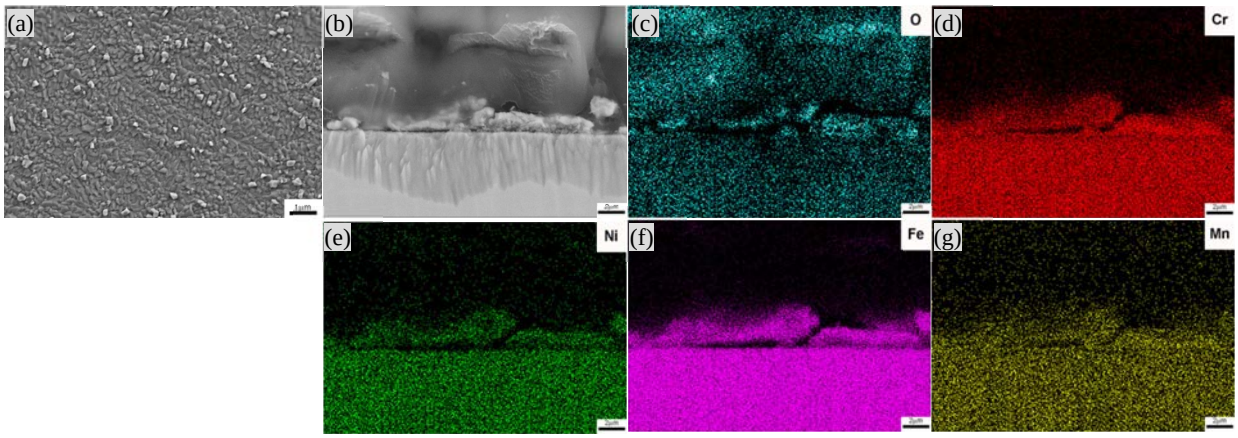

Figure 4.22 SEM images and EDS mapping of oxide scale grown at 700˚C for 96 hours in 1% water vapor containing air: surface (a); cross-section (b); O mapping (c); Cr mapping (d); Ni mapping (e); Fe mapping (f); Mn mapping (g)

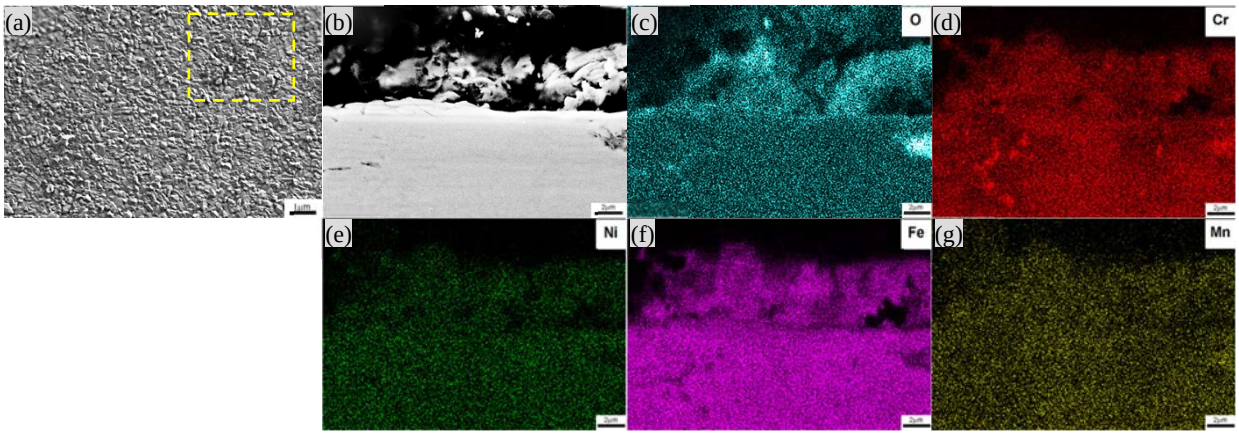

Figure 4.23 SEM images and EDS mapping of oxide scale grown at 700˚C for 96 hours in 2% water vapor containing air: surface (a); cross-section (b); O mapping (c); Cr mapping (d); Ni mapping (e); Fe mapping (f); Mn mapping (g)

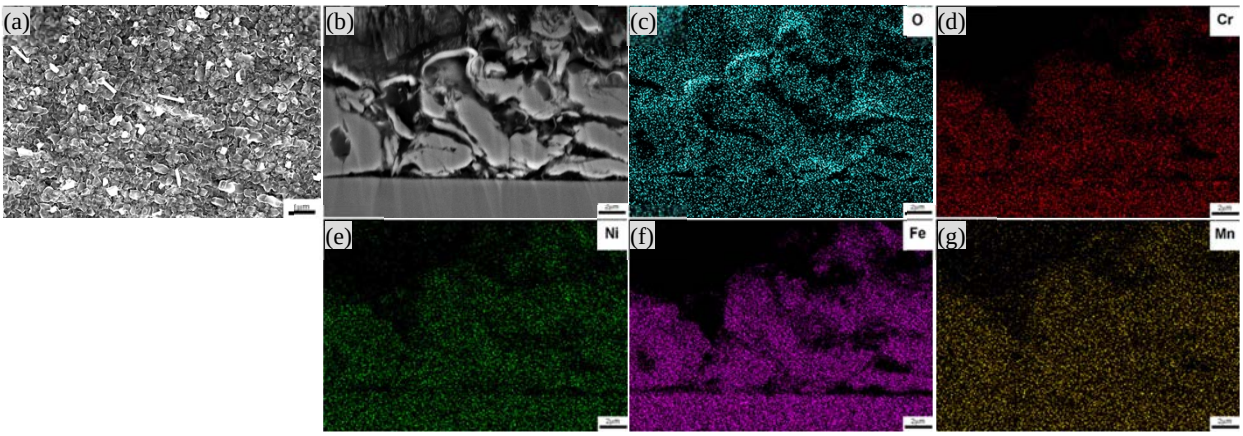

Figure 4.24 SEM images and EDS mapping of oxide scale grown at 700˚C for 96 hours in 4% water vapor containing air: surface (a); cross-section (b); O mapping (c); Cr mapping (d); Ni mapping (e); Fe mapping (f); Mn mapping (g)

- At 800˚C (see Figure 4.25 - Figure 4.27)

Compared with the oxide scale formed in dry air, the thicknesses of the oxide scales formed at 800˚C decrease in the presence of water vapor. The grain-like layer turns to grow on the whole surface with water vapor introduced, leading to a more homogenous distribution of grains. The element constituents of the oxide scales formed in wet air are similar to that in dry air, but the distribution has changed, especially for the oxide scale formed in 2% water containing air. A

serious corrosion can be found in this case, causing the internal oxidation as well as the apparent deformed interface.

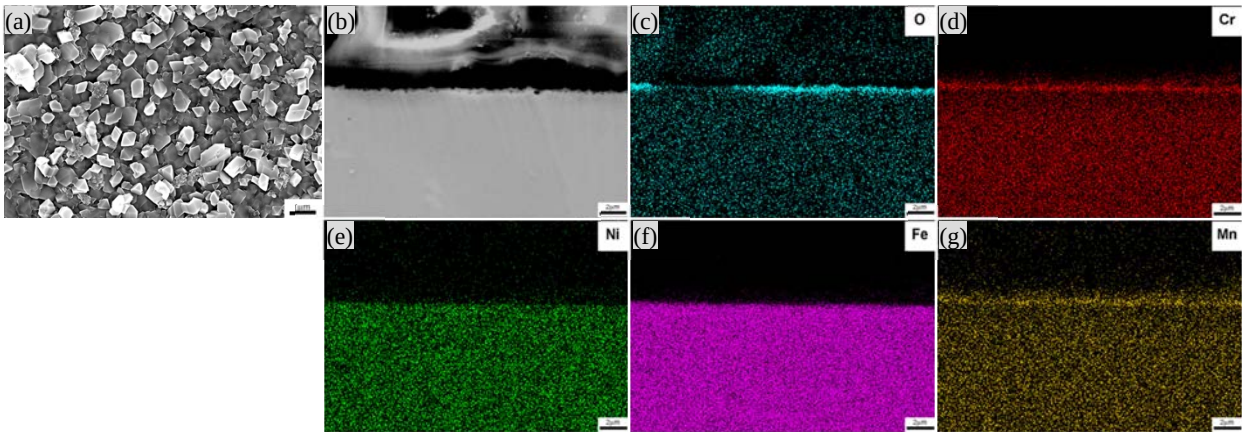

Figure 4.25 SEM images and EDS mapping of oxide scale grown at 800˚C for 96 hours in 1% water vapor containing air: surface (a); cross-section (b); O mapping (c); Cr mapping (d); Ni mapping (e); Fe mapping (f); Mn mapping (g)

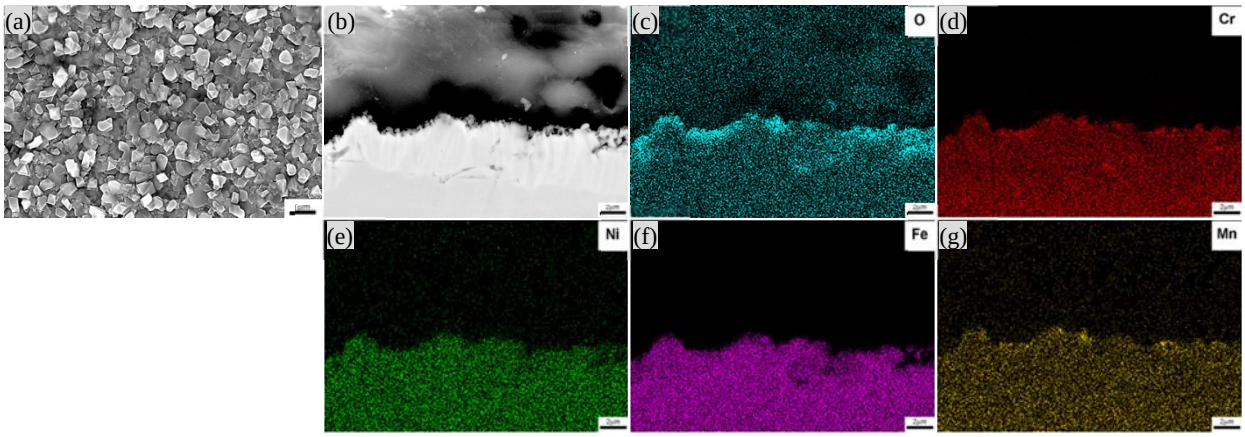

Figure 4.26 SEM images and EDS mapping of oxide scale grown at 800˚C for 96 hours in 2% water vapor containing air: surface (a); cross-section (b); O mapping (c); Cr mapping (d); Ni mapping (e); Fe mapping (f); Mn mapping (g)

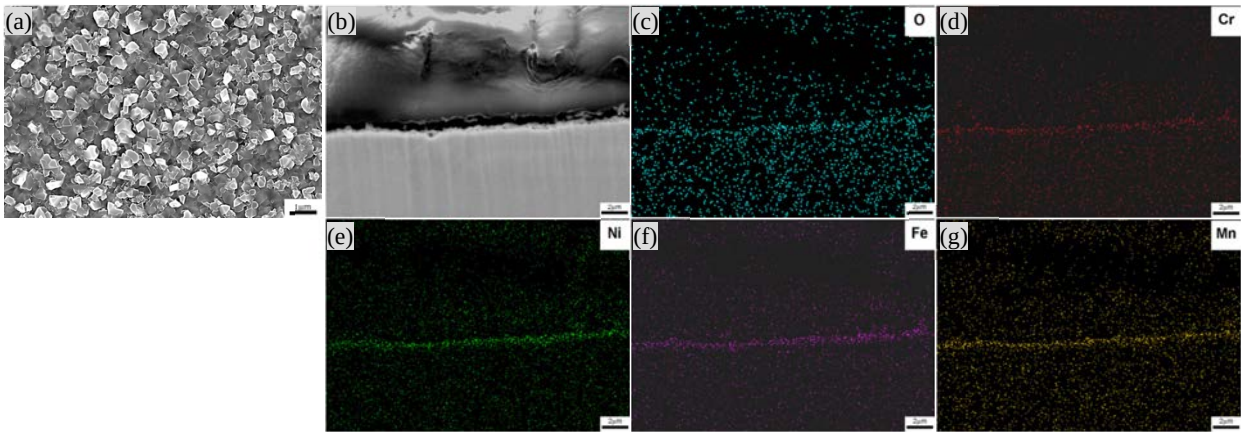

Figure 4.27 SEM images and EDS mapping of oxide scale grown at 800˚C for 96 hours in 4% water vapor containing air: surface (a); cross-section (b); O mapping (c); Cr mapping (d); Ni mapping (e); Fe mapping (f); Mn mapping (g)

- At 900 ˚C (see Figure 4.28 - Figure 4.30)

The oxide scales grown at 900˚C in wet air are mainly composed of oxygen, chromium and manganese, which are comparable to those formed in dry air. However, water vapor impacts the microstructures of oxide scales. A severe internal oxidation appears in the oxide scale formed in the 1% water containing air, shown in Figure 4.28. The element mappings indicate that the internal oxidation zone consists of silicon oxides. The silicon oxides also distribute along the interface where the "Kirkendall" voids are present. As observed from the surface morphology image (seen in Figure 4.20.j-2), the flower-like large grain clusters are present on the oxide scale formed in the 2% water containing air, which can also be found in Figure 4.29. Here, the result of EDX mappings implies that these oxide grains contain chromium, iron, nickel, manganese and oxygen.

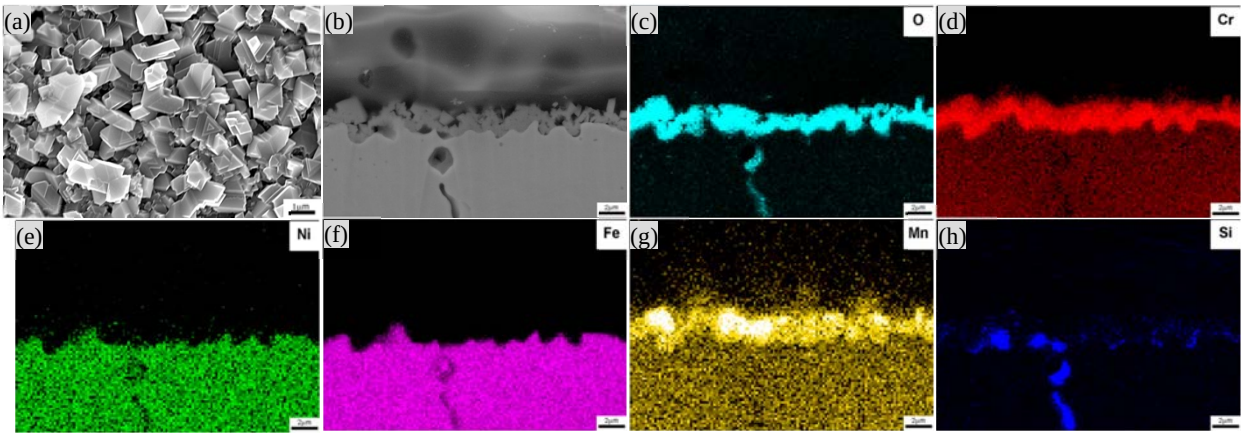

Figure 4.28 SEM images and EDS mapping of oxide scale grown at 900˚C for 96 hours in 1% water vapor containing air: surface (a); cross-section (b); O mapping (c); Cr mapping (d); Ni mapping (e); Fe mapping (f); Mn mapping (g); Si mapping (h)

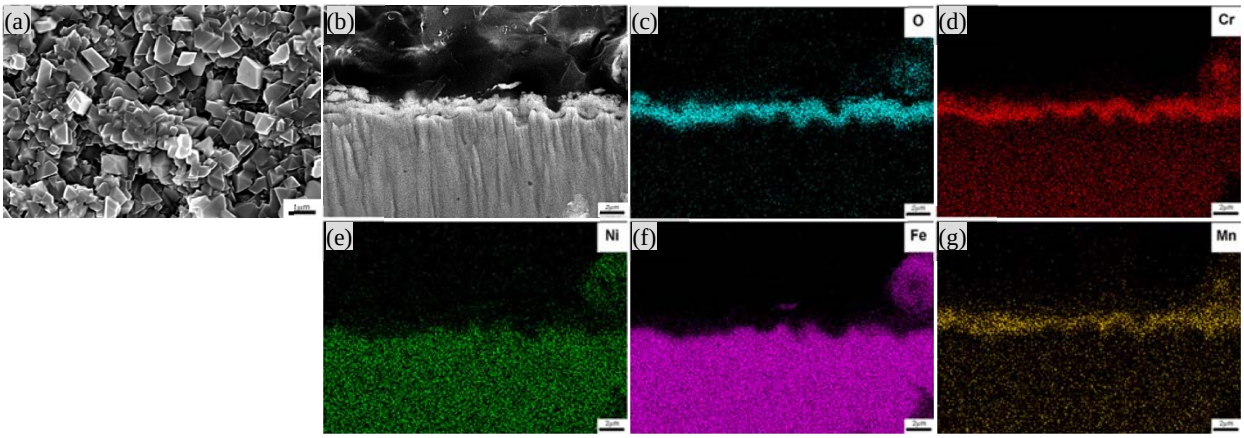

Figure 4.29 SEM images and EDS mapping of oxide scale grown at 900˚C for 96 hours in 2% water vapor containing air: surface (a); cross-section (b); O mapping (c); Cr mapping (d); Ni mapping (e); Fe mapping (f); Mn mapping (g)

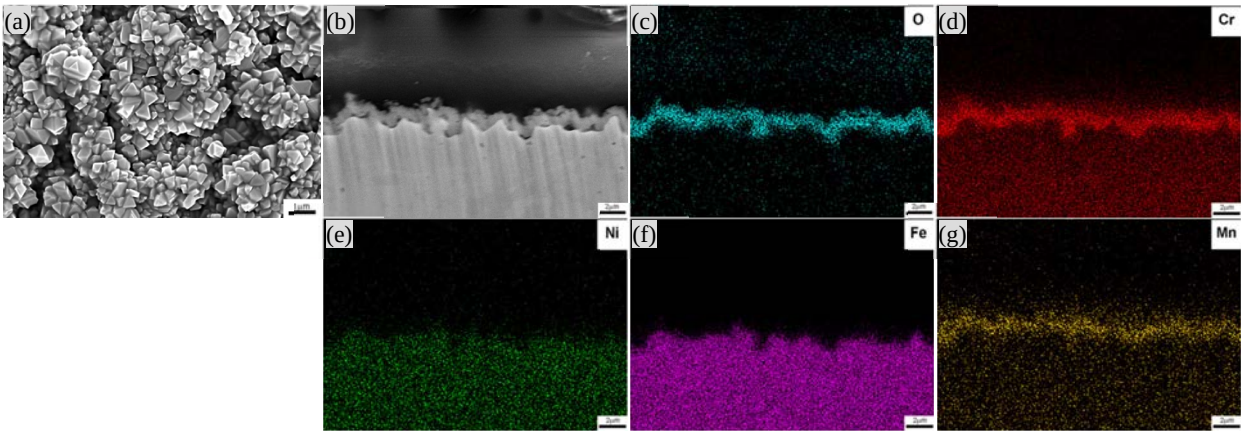

Figure 4.30 SEM images and EDS mapping of oxide scale grown at 900˚C for 96 hours in 4% water vapor containing air: surface (a); cross-section (b); O mapping (c); Cr mapping (d); Ni mapping (e); Fe mapping (f); Mn mapping (g)

4.2.3 Phases

Figure 4.31 illustrates the diffracted patterns of the oxide scales after oxidation at 700˚C, 800˚C and 900˚C for 6 hours and 96 hours in humid air (Notes: the oxide scales formed at 800˚C and 900˚C for 96 hours in the 8% water containing air are broken so the ones after 72-hour oxidation with the same other conditions have been chosen). Three grazing incidence angles, i.e., 0.5˚, 2˚ and 5˚, have been employed during the phase identification to investigate the oxide phase

distribution along the depth. The corresponding X-ray penetration depth of which are also calculated and listed just beside the diffracted pattern. Similarly, the quantification analysis of oxide phase has been carried out for the oxide scales obtained under all conditions investigated except the broken ones, as displayed in Figure 4.32.

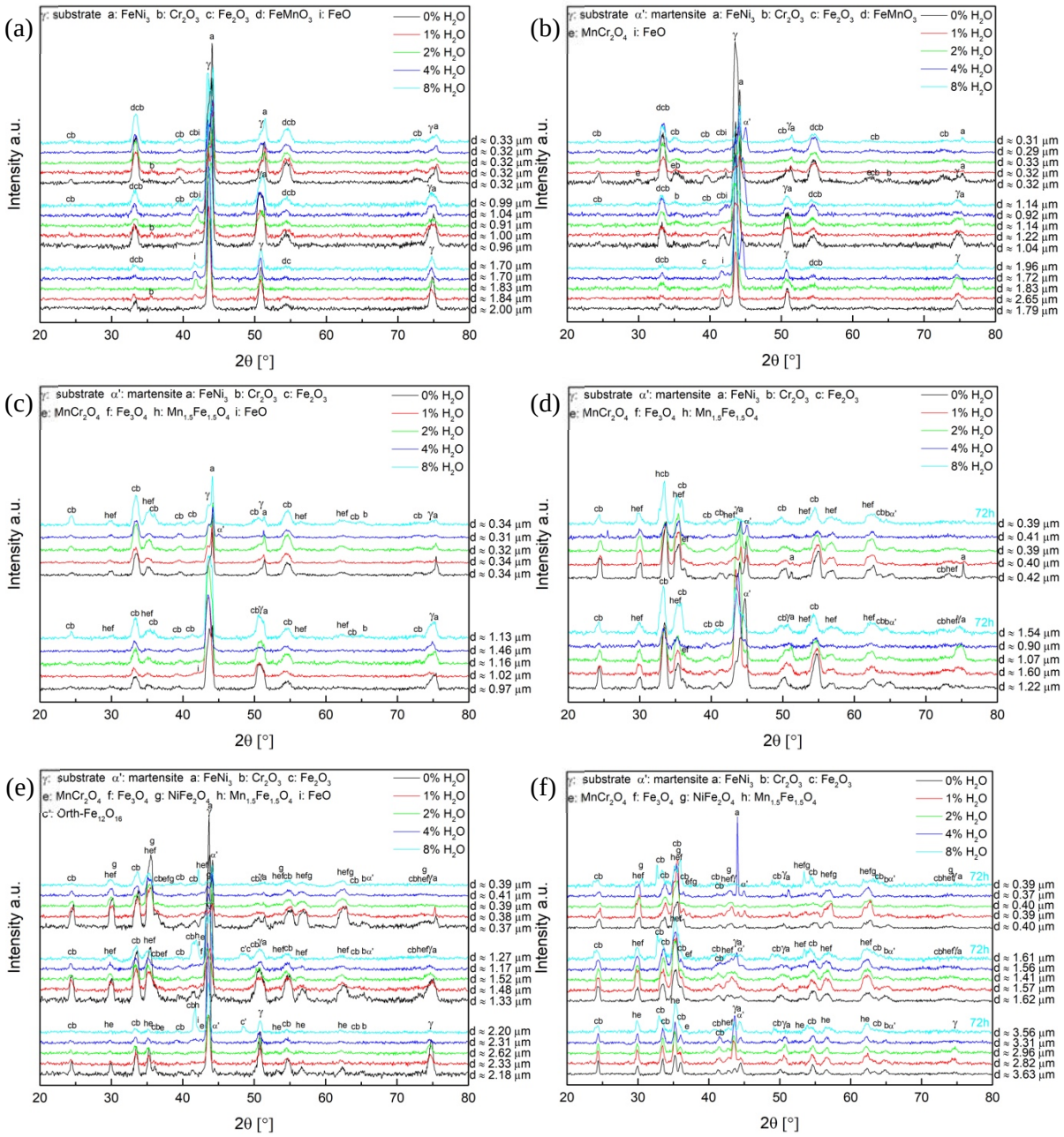

Figure 4.31 GIXRD patterns of the oxide scales after short and long time oxidation at different temperatures in the air with different water vapor contents at: 700˚C for 6 hours (a) and 96 hours (b); 800˚C for 6 hours (c) and 96 hours (d); 900˚C for 6 hours (e) and 96 hours (f)

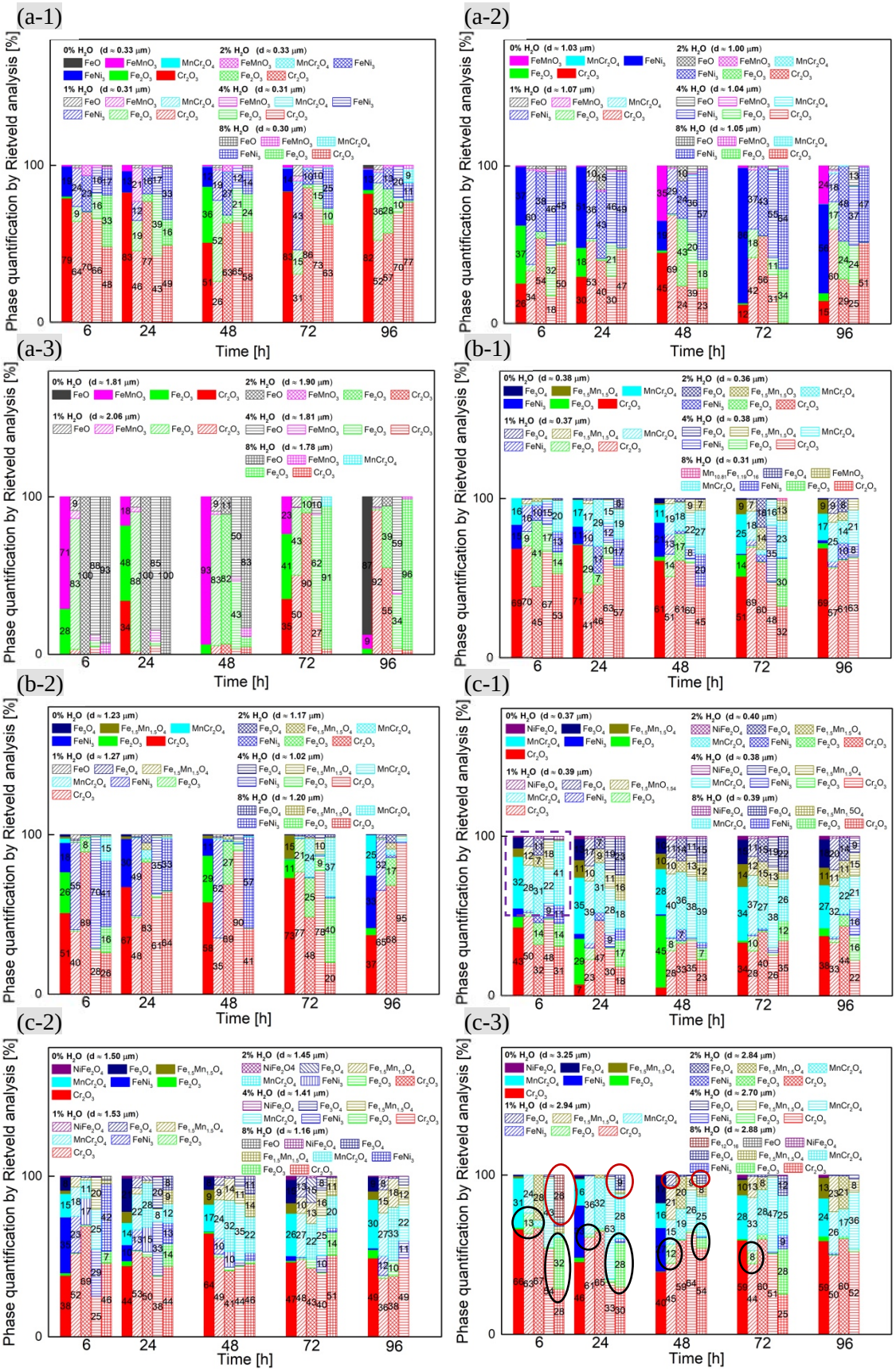

Figure 4.32 Quantitative phase composition analyses of oxide scales as a function of oxidation time and water vapor contents, obtained under different X-ray penetration depths: 300 - 330 nm (a-1), 1.00 – 1.07 µm (a-2) and 1.78 – 2.06 µm (a-3) at 700˚C; 310 - 380 nm (b-

1) and 1.02 – 1.27 μm (a-2) at 800˚C; 370 - 400 nm (c-1), 1.16 – 1.53 μm (c-2) and 2.70 – 3.25 μm (c-3) at 900˚C

- At 700˚C (see Figure 4.31.a - Figure 4.31.b and Figure 4.32.a)

Since the thicknesses of the oxide scales are lower than the X-ray penetration depths, the oxide scales formed in the 0% and 1% water containing air can be totally analyzed. The thicknesses of the oxide scales grown in the 2%, 4% and 8% water containing air vary from 962, 5257 and 5637 nm to 3380, 8823 and 5693 nm along the oxidation time respectively, indicating that these diffracted results only reflect the outer part of the oxide scales. The information of inner oxide scales can be obtained using other methods such as EDX element mapping and XPS depth profiling etc.

Based on the existing results, it is agreed that the corundum-type oxides, i.e., Cr_2O_3 and $(Fe, Cr)_2O_3$, always predominate in the oxide scales grown at 700˚C in humid air. The following features can also be found for the oxidation at 700˚C in humid air:

1. After the initial 6-hour oxidation, the formation of wüstite (FeO) has been found in the inner part of oxide scales. Moreover, the oxides near the surface usually contain more iron oxides with increasing the humidity except the one formed in 2% water containing air. It contains more iron and manganese solid solution oxides. Chromia prefers concentrating near the MO/M interface or in the intermediate part.
2. With increasing the oxidation time, at the MO/M interface chromia gradually accumulates for the oxide scales formed in the 1% water containing air. While for the oxide scales grown in the 2%, 4% and 8% water containing air, the wüstite in the intermediate part is likely to be replaced by hematite and subsequently by chromia.
3. After long-time oxidation, the content of chromia on the surface rise with increasing the water content. Moreover, martensitic phase transformation is present in the oxide scale grown in the 4% water containing air.

- At 800˚C (see Figure 4.31.c - Figure 4.31.d and Figure 4.32.b)

The phase constituents of the oxide scales grown at 800˚C in humid air are similar to those formed in dry air. The oxide scale is composed by the corundum-type oxides, i.e., Cr_2O_3, Fe_2O_3 and their solid solution oxide, and spinel-type oxides, i.e., $MnCr_2O_4$, $Mn_{1.5}Fe_{1.5}O_4$, and Fe_3O_4. And the spinel-type oxide phases, aggregate in the presence of water vapor. Similar to the situation at 700˚C, the outer layer of oxide scales contains more iron oxides in presence of water vapor after the initial 6-hour oxidation. For the oxide scales with a final breakaway oxidation,

the content of chromia within the oxide scale experiences a first growth then a fast decline. A sudden increase of iron oxides and disappearance of metallic compounds are the remarkable onset of breakaway oxidation.

- At 900˚C (see Figure 4.31.e - Figure 4.31.f and Figure 4.32.c)

The oxide phases in humid air basically keep the same as those after oxidation in dry air, i.e., the inner layer of corundum-type oxides and the outer layer of spinel-type oxides. For the oxide scales grown in humid air, the part near the surface keeps same amount of chromia and forms more spinel-type oxides. The conditions of humidity where the breakaway oxidation finally appears have been confirmed, i.e., 1% and 8% water vapor. Comparing the thicknesses of oxide scales formed at 900˚C in the air with 1% and 8% water vapor (see Table App. 4.1) with the X-ray penetration depths displayed in Figure 4.32.c, the marked zones in Figure 4.32.c-3 can be supposed to represent the weigh fractions of iron oxides (black: Fe_2O_3, red: Fe_3O_4) in the inner part of oxide scales formed at 900˚C in the air with 1% and 8% water vapor for different durations. Thus, according to the quantitative phase composition analysis, it can be concluded that iron oxides are enriched in the inner part of oxide scales grown in these two cases when breakaway oxidation appears. Similarly, Figure 4.32.c-1 suggests that the oxide surface formed in the 8% water containing air always contains quite large amounts of iron oxides (magnetite and hematite) under the conditions investigated in this work.

4.2.4 XPS Depth profile

The surface analysis and depth profiling have been done for AISI 316L SS oxidized at 700˚C and 800˚C for 24 hours in the 0%, 2% and 8% water containing air using the XPS technique. Figure 4.33 presents an XPS survey spectra of the oxide scale after 24-hour oxidation at 800˚C in dry air, illustrating the features of peaks interested in this thesis as well as the changes versus the sputtering depth. At the surface, carbon (C 1s) as a contamination, Oxygen (O 1s), chromium (Cr 2p), manganese (Mn 2p), iron (Fe 2p) can be observed apparently. With increasing the etch time, more information of the substrate stands out, for instance, nickel (Ni 2p) and molybdenum (Mo 3d and Mo 3p) can also be detected.

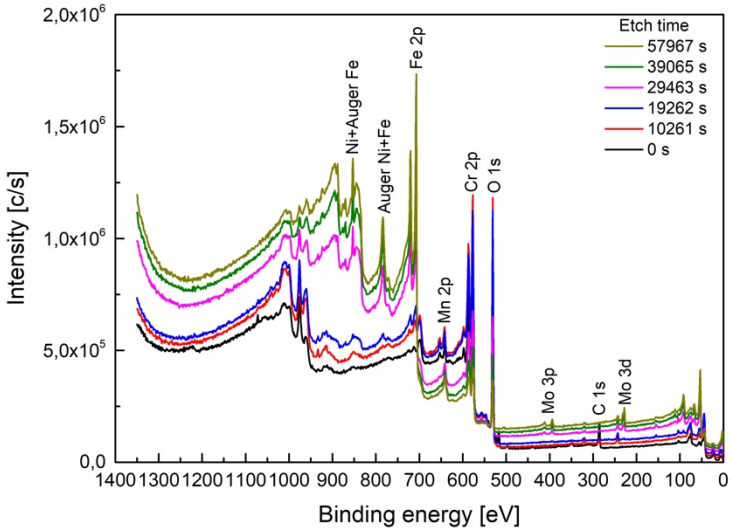

Figure 4.33 XPS survey spectra obtained at different etch time of AISI 316L SS oxidized at 800˚C for 24 hours in dry air

Based on the separated files of the XPS spectra for each element, the region fitting has been carried out to the elements interested. Consequently, depth profiling of oxide scales can be achieved, shown in Figure 4.34. Here, the sputtering time has been transferred to the sputtering depth, the theoretical basis of which is introduced in Appendix 4. Moreover, Appendix 4 also gives the definition of the MO/M interface during the XPS data treatment. These profiles benefit to perfect the information of oxide compositions in regard to the corresponding growth conditions.

It is obvious from Figure 4.34 that the element distribution along the sputtering depth shows a similar trend in the oxide scales formed under different conditions investigated.

1. Chromium rich oxides predominate in the oxide scales, confirming the selective oxidation behavior of chromium-containing steels. Considering the existence of iron, chromium and iron solid solution oxides are possible to form, which has been verified by XRD analysis.

2. Manganese can be detected near the surface in a quantity, implying this active component plays a nonnegligible role in the oxidation of AISI 316L SS. Combining the previous results in this thesis, it is clear that manganese usually concentrates in the surface oxide grains formed at 700˚C, which may be either in the form of the solid solution oxide in most cases or spinel-type oxides. The latter type prefers existing in the air with large humidity. For the oxide scales formed at 800˚C, manganese is present in the outer layer mainly consisting of the Cr-Mn spinel oxides. This finding is also appropriate for the case at 900˚C.

3. Silicon is observed at the M/MO interface, which is also detected in the EDX mappings due to the internal oxidation (Figure 4.28). This thesis will not pay much attention to the effects of silicon.

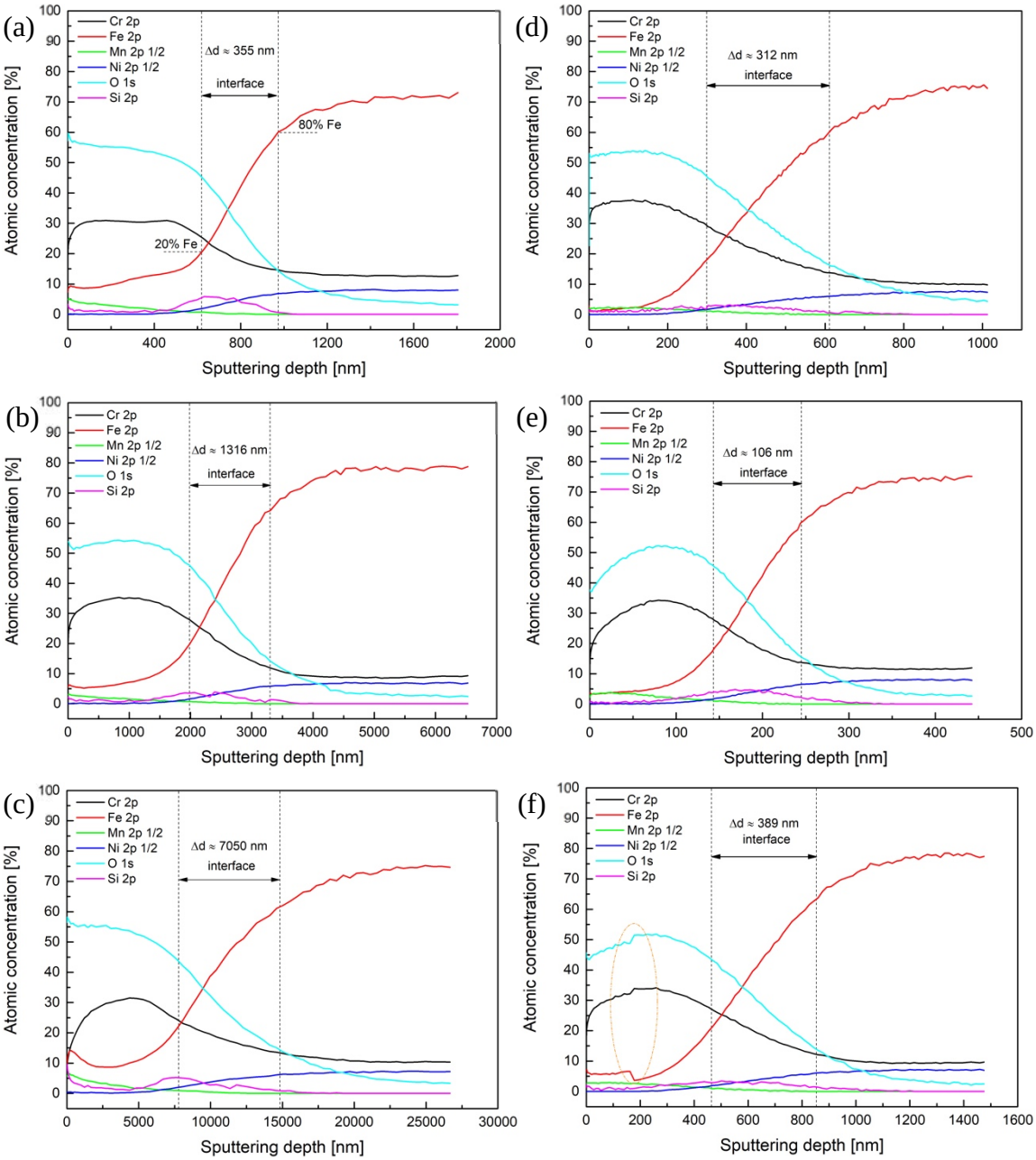

Figure 4.34 XPS depth profiles of the oxide scales formed at 700˚C in the air with 0% (a), 2% (b) and 8% (c) water vapor and 800˚C in the air with 0% (d), 2% (e) and 8% (f) water vapor

Meanwhile, some minor differences can also be found.

1. According to Figure 4.34.a-c, the region of MO/M interface expands (from 355 nm to 7050 nm) with increasing the humidity (from 0% to 8% water vapor) for the oxidation of AISI 316L SS at 700˚C. Moreover, the oxidation reaction zones are qualitatively thought to

increase with increasing water vapor content (see Figure 4.8, Figure 4.22 - Figure 4.24). These two observations are probably due to the water enhanced inward diffusion.

2. In the oxide scale grown at 700˚C in the 8% water containing air, iron near the surface first rises and subsequently decreases along the sputtering depth. It indicates this oxide scale has an iron rich region in the outer part, which is different from the oxide scales formed in other humidity. This phenomenon has also been observed by XRD quantification analysis (Figure 4.32.a-1). It is probably due to the evaporation of chromium rich oxides at the surface, leaving a relative high content of iron behind. According to the element mappings of oxide scale after 96-hour oxidation at 700˚C in the 4% water containing air (Figure 4.24), iron is likely to form metallic compounds, e.g. $FeNi_3$.

3. Inflection points occur in Figure 4.34.f, showing a sudden change of chromium, iron and oxygen contents. This probably ascribes to the instrumental error correlated to the microstructure of oxide scale. The change of beam focus on this specimen has been found after XPS profiling experiment. It means that the specimen displaced due to the accidental interaction of the ion beam and oxide grains during the sputtering.

The position where hydroxides generate within the oxide scale is of interest, especially in the presence of water vapor. Therefore, oxygen profiling has been carried out to determine the distribution of oxide and hydroxide versus the sputtering depth. Figure 4.35.a illustrates the integrated XPS spectra of O 1s peak obtained from the oxide scale after 24-hour oxidation at 800˚C in dry air, indicating an apparent decline of oxygen content towards the M/MO interface. Each of the O 1s spectra in Figure 4.35.a has been refined, one example of which showing the refinement process is displayed in Figure 4.35.b. Obviously, the feature of O 1 s peak is determined by two parts, i.e., the O^{2-} peak denoting oxide species and the OH^- peak denoting hydroxide species. The reference binding energies for O^{2-} and OH^- during the refinement are set as 530.1 eV and 531.7 eV respectively [*Jung et al., 2012*].

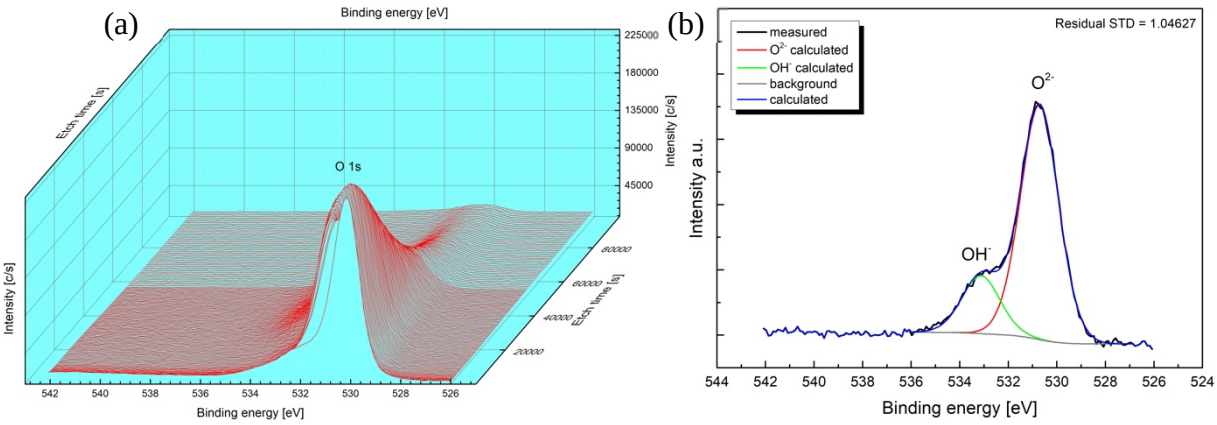

Figure 4.35 XPS spectra of O 1s peak versus the etch time where the front one is from the surface before etching (a) and schematic presentation of O 1s peak fitting for the pattern obtained after 29463-second etching (b) for AISI 316L SS oxidized at 800˚C for 24 hours in dry air

Figure 4.36 presents the XPS depth profiles of O^{2-} and OH^{-} for AISI 316L SS oxidized at 700˚C and 800˚C for 24 hours in the 0%, 2% and 8% water containing air. It is clear that hydroxides prefer forming at the MO/M interface as well as at the surface no matter in dry or humid air, which is in accordance with the studies in [*Xiao, 2014, Li, 2016*]. Other studies also suggest that hydrogen is often detected at the M/MO interface and even in the sublattice of underlying substrate [*Brady et al., 2011, Dumerval et al., 2014*], supporting the observation in this thesis. In general, oxides are dominant rather than hydroxides for the oxidation of AISI 316L SS no matter there is water vapor in air or not. For the oxide scales formed at 700˚C, the influence of humidity on the distribution of OH^{-} along the oxide thickness is not observed in this thesis. The relatively high content of hydroxides at 700˚C in dry air may ascribe to two possibilities, i.e., the impurities of the reactive gas during the oxidation or long-term storage before XPS profiling. While for the oxide scales formed at 800˚C, the fraction of hydroxides at both the surface and interface increases with increasing the water vapor content in air.

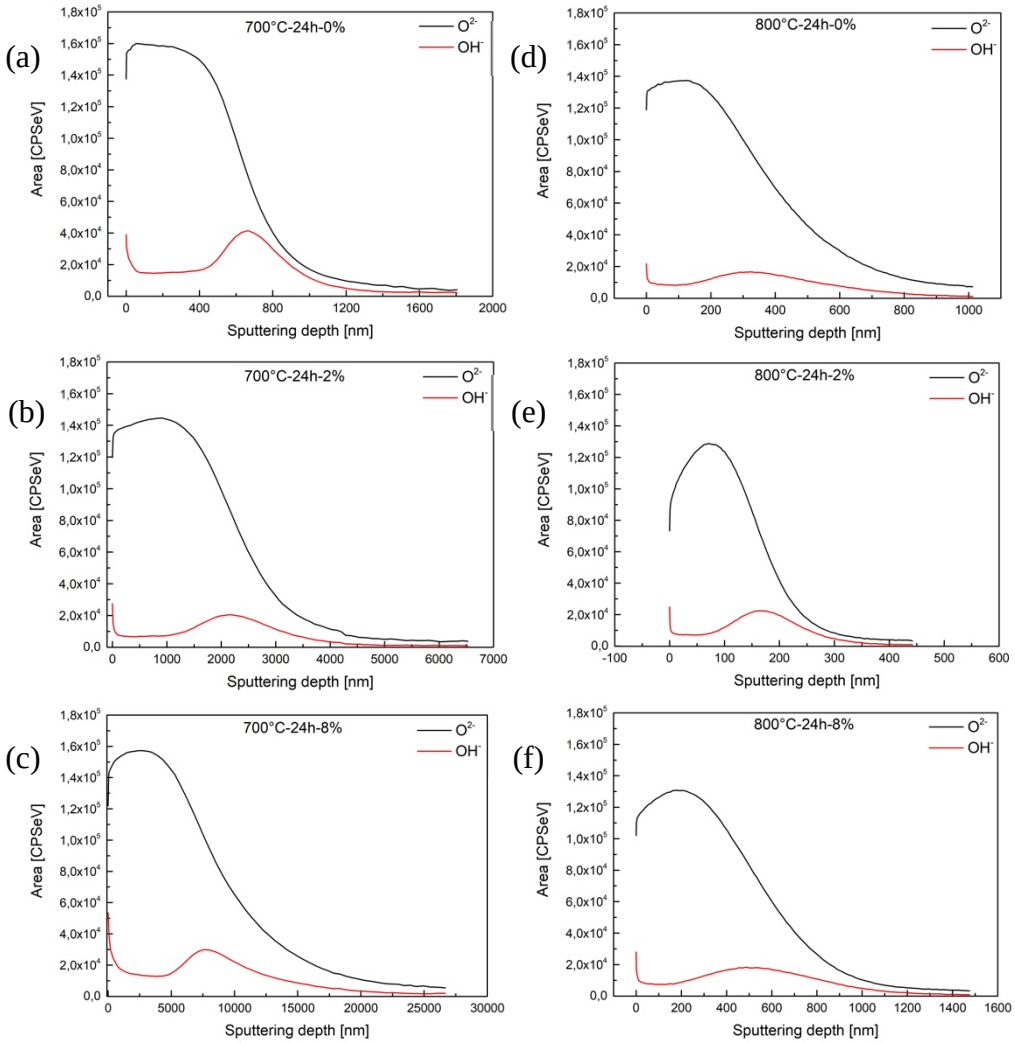

Figure 4.36 XPS depth profiles of O^{2-} and OH^{-} for AISI 316L SS oxidized at 700˚C in the air with 0% (a), 2% (b) and 8% (c) water vapor and 800˚C in the air with 0% (d), 2% (e) and 8% (f) water vapor

4.2.5 Discussion

4.2.5.1 Oxidation kinetics

As observed from Figure 4.17, the effects of water vapor on the oxidation kinetics of AISI 316L SS can be described from two aspects. On one hand, water vapor may promote the formation of oxide to some extent, which is demonstrated by more mass accumulation in some cases with water vapor introduced. This finding is also in agreement to other related studies. For instance, Huntz found water vapor accelerated the oxidation rate of stainless steel at 900˚C [*Huntz et al., 2007*], so did Buscail [*Buscail et al., 2015*]. On the other hand, water vapor causes the formation of volatiles, which is obvious from the mass loss. And this effect becomes significant with increasing the oxidation time. The stabilities of Cr-containing volatiles have been evaluated under various conditions [*Ebbinghaus, 1993, Beverskog et al., 1997, Opila et al., 2007*], and

finally $CrO_2(OH)_2$ is supposed to be the main product of volatilization at moderate temperature (500 – 900˚C) especially in the presence of water vapor. Generally, the generation of $CrO_2(OH)_2$ follows the chemical reaction below:

$$1/2\,\mathrm{Cr_2O_3} + 3/4\mathrm{O_2(g)} + \mathrm{H_2O(g)} = \mathrm{CrO_2(OH)_2(g)}. \tag{4.4}$$

Combining Equation (4.4) and gas transport theory in the viscous flow regime, the mass loss rate can thus be evaluated [*Young et al., 2006*], which is also employed in this thesis.

The Gas/MO and MO/M interfaces are expressed schematically in Figure 2.4. The evaporation issue can be solved using the corresponding gas transport theory based on the assumption that the reactive gas flows past the flat surface. The molar flux J_{Cr} can thus be calculated by:

$$J_{\mathrm{Cr}} = (k_{\mathrm{m}}/RT)p_{\mathrm{CrO_2(OH)_2}}, \tag{4.5}$$

where $p_{\mathrm{CrO_2(OH)_2}}$ is the partial pressure difference of volatile gas between the oxide surface and the bulk-gas; k_{m} is the mass-transfer coefficient, given by:

$$k_{\mathrm{m}} = 0.664(D^4/\upsilon)^{1/6}(\mathrm{v}/L)^{1/2}, \tag{4.6}$$

where D is the binary gas diffusion coefficient; υ the kinematic viscosity; v and L the bulk-gas linear velocity and the sample length, taken as 0.92 mm/s and 10 mm respectively in the work. D is evaluated based on the simplified model of a binary gas mixture, i.e., N_2-$CrO_2(OH)_2$. The mass-transfer parameters related to the evaporation for the oxidation of AISI 316L SS in humid air are tabulated in Table 4.4.

Table 4.4 Mass-transfer parameters correlated

Temperature (˚C)	**Water content (%)**	***D* (cm²/s)**	***υ* (cm²/s)**	**k_{m} (cm/s)**
700	1	0.91 ± 0.06	0.312	0.22997 ± 0.03700
	2		0.312	0.22994 ± 0.03610
	4		0.313	0.22982 ± 0.03698
	8		0.312	0.22999 ± 0.03710
800	1	1.06 ± 0.07	0.333	0.24339 ± 0.04036
	2		0.334	0.24329 ± 0.04035
	4		0.336	0.24310 ± 0.04031
	8		0.335	0.24319 ± 0.04033
	1		0.312	0.26900 ± 0.04522

900	2	1.24 ± 0.08	0.312	0.26896 ± 0.04521
	4		0.313	0.26883 ± 0.04519
	8		0.312	0.26903 ± 0.04522

According to Equation (4.4), the equilibrium partial pressure of $CrO_2(OH)_2$ can be given by:

$$p_{CrO_2(OH)_2} = K_{(4.4)} p_{O_2}^{3/4} p_{H_2O}. \tag{4.7}$$

Consequently, the mole flux of $CrO_2(OH)_2$ can be calculated, listed in Table 4.5.

Table 4.5 Mass loss rates of $CrO_2(OH)_2$ under different humidity

Temperature (˚C)	**Water content (%)**	$p_{CrO_2(OH)_2}$ **(atm)**	J_{Cr} **(g/cm²s)**
700	1	1.7188×10^{-8}	$(5.84 \pm 0.94) \times 10^{-12}$
	2	3.3782×10^{-8}	$(1.15 \pm 0.18) \times 10^{-11}$
	4	6.5390×10^{-8}	$(2.22 \pm 0.36) \times 10^{-11}$
	8	1.2229×10^{-7}	$(4.16 \pm 0.67) \times 10^{-11}$
800	1	3.3183×10^{-8}	$(1.15 \pm 0.19) \times 10^{-11}$
	2	6.2571×10^{-8}	$(2.25 \pm 0.37) \times 10^{-11}$
	4	1.2111×10^{-7}	$(4.35 \pm 0.72) \times 10^{-11}$
	8	2.2649×10^{-7}	$(8{,}14 \pm 1.35) \times 10^{-11}$
900	1	5.3081×10^{-8}	$(2.11 \pm 0.35) \times 10^{-11}$
	2	1.0433×10^{-7}	$(4.15 \pm 0.70) \times 10^{-11}$
	4	2.0194×10^{-7}	$(8.02 \pm 1.35) \times 10^{-11}$
	8	3.7765×10^{-7}	$(1.50 \pm 0.25) \times 10^{-10}$

It can be deduced from Table 4.5 that the evaporation rate is sensitive to both the water content and oxidation temperature, i.e., it may increase with increasing the humidity and temperature for AISI 316L SS oxidized in this work. For the condition where breakaway oxidation happened, the evaporation rate also respects this trend, indicating that breakaway oxidation is attributed to not only the volatile formation but also other possibilities such as the chemical composition (iron-rich oxide formation), internal stresses (tensile growth stress) etc., which will be further studied in Section 6.4.

Moreover, combining the evaporation rates with the corresponding measured TG results yields the true mass gain curves, illustrated in Figure 4.37.

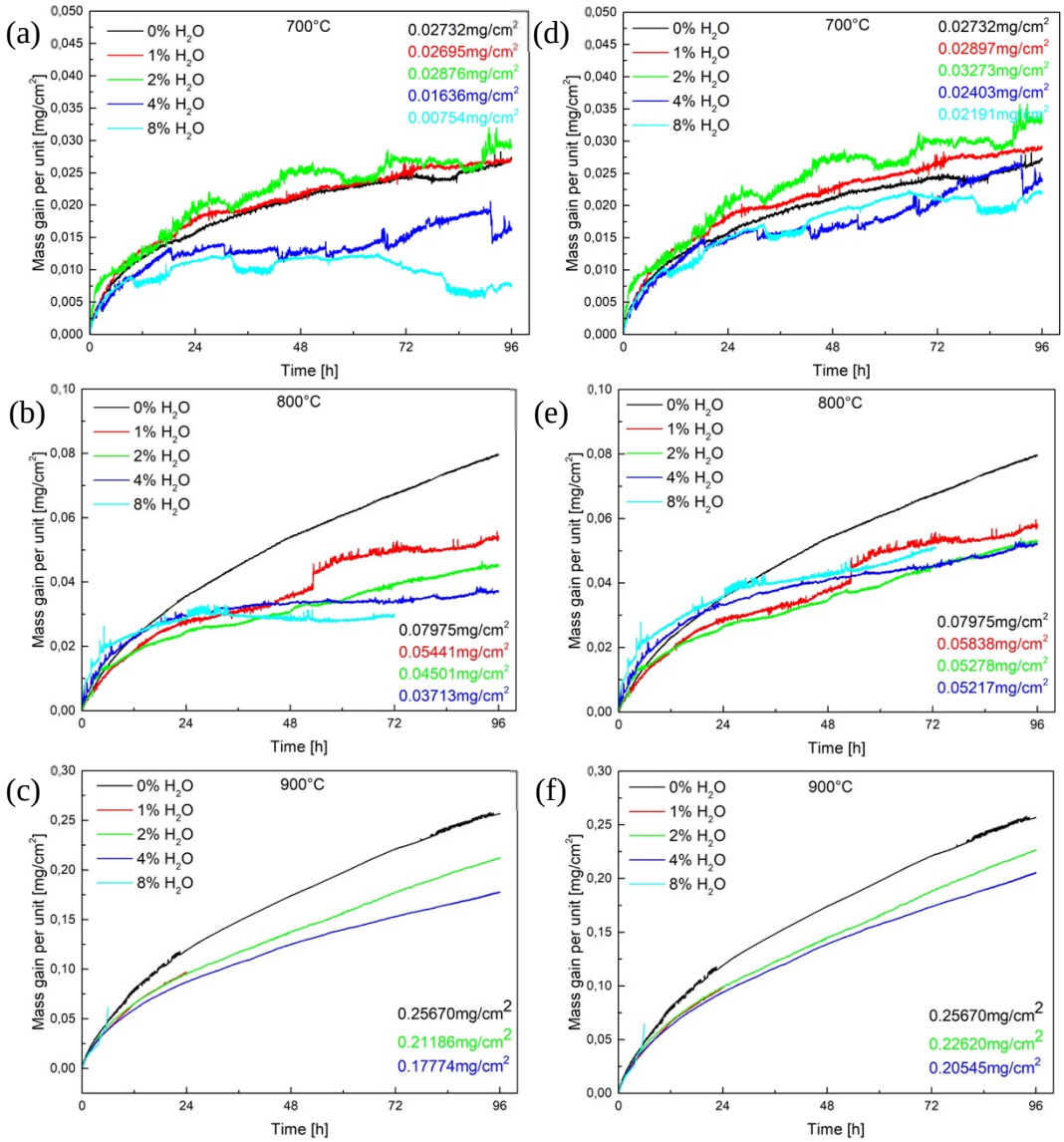

Figure 4.37 The measured mass gains (a-c) and true mass gains with volatile mass compensated (d-f) for AISI 316L SS oxidized between 700˚C and 900˚C in humid air for 96 hours (before breakaway oxidation)

Figure 4.37 verifies that water vapor is beneficial to the oxide growth in some cases, for instance, the oxidation at 700˚C in the 1% and 2% water containing air for 96 hours and the initial 24-hour oxidation at 800˚C in the 4% and 8% water containing air. Water vapor creates another diffusion path based on the dissociation mechanism [*Fujii et al., 1964*], facilitating oxygen to migrate inwards, which is specially significant for the oxidation at 700˚C. Simultaneously, water vapor promotes to form vacancies or voids within the oxide scale so as to improve cation diffusion [*Luo et al., 2018*], which is reflected more apparently at higher temperatures. According to quantitative phase constituent analysis (see Figure 4.32.c-1), the box zones represent the weight fraction of spinel oxides including $MnCr_2O_4$, $Mn_{1.5}Fe_{1.5}O_4$, Fe_3O_4 and $NiFe_2O_4$ The reason of choosing this zone is that the X-ray penetration depth (around 0.4 μm)

indicates the outer surface region and 6-hour oxidation may limit the effect of evaporation. It can thus be observed that the weight fractions of spinel oxides are 36%, 50%, 52%, 43% and 44% for AISI 316L SS oxidized at 900˚C for 6 hours in the air with 0%, 1%, 2%, 4% and 8% water vapor respectively, which suggests that the oxide scale usually contains more spinel oxides near the surface than that formed in dry air. That water vapor may promote cation outward diffusion is possibly supported by this observation accordingly.

4.2.5.2 Grain size

The development of oxide grain size on the surface versus the humidity has been investigated and displayed in Figure 4.38. In general, the average grain sizes of oxides formed on AISI 316L SS at 700˚C and 800˚C in the presence of water vapor is smaller than those formed in dry air. Qualitatively, it can be thought that water vapor plays a role of grain refinement during the oxidation of AISI 316L SS at 700˚C and 800˚C. Similar effects of water vapor have also been found in [*Jacob et al., 2002, Zurek et al., 2008, Young, 2008*]. It is possible to be associated with water transport during oxidation. Young has given a relatively reasonable interpretation in [*Young, 2008*] that water vapor makes cation outward diffusion suppressed and oxygen inward diffusion promoted, refining the grain size consequently. For the oxidation at 900˚C in this work, the obtained result cannot verify the grain refinement effect of water vapor, which is probably because the mechanism suggested by Young is no longer appropriate in this case.

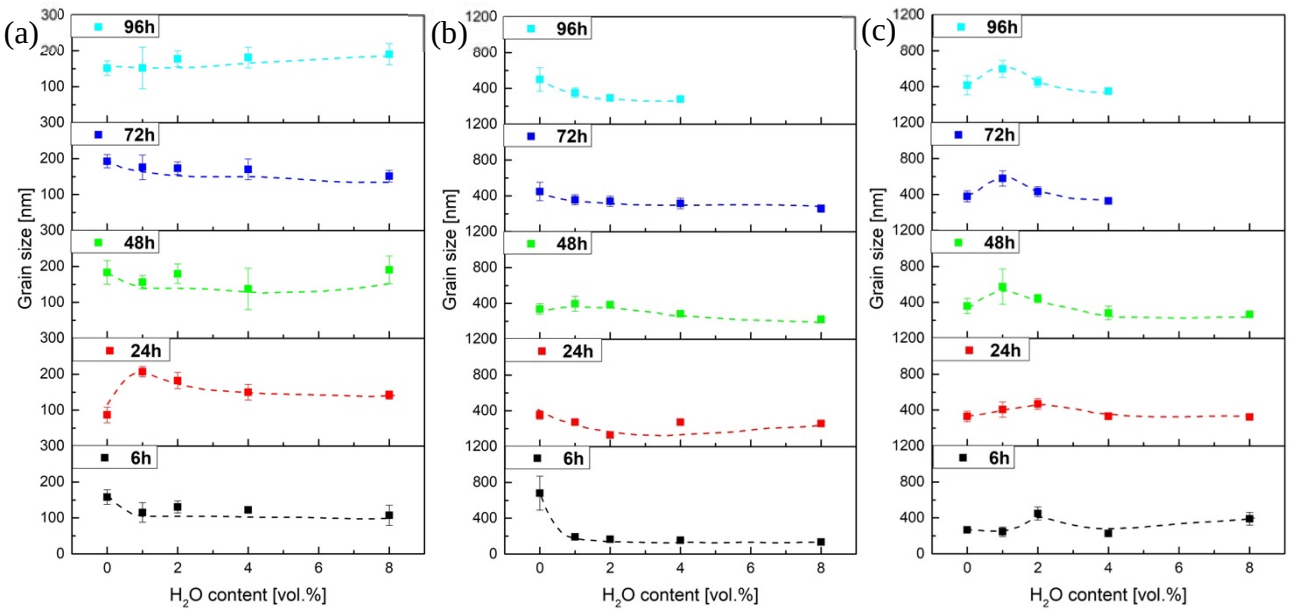

Figure 4.38 Sizes of grains on the oxide surface as a function of water content for the oxidation at 700˚C (a), 800˚C (b) and 900˚C (c) for different durations

4.2.5.3 Internal oxidation

Generally, internal oxidation may happen in two ways [*Young, 2016*]: a reactive metallic component which is selectively oxidized cannot arrive at the surface in time; long-time-consumption induced barren zone of one reacting component satisfies the condition of internal oxidation. In this work, internal oxidation is observed for AISI 316L SS oxidized for 96 hours at 700˚C and 800˚C in the air with 2% water vapor (see Figure 4.23 and Figure 4.26) as well as at 900˚C in the air with 1% water vapor (see Figure 4.28). These figures indicate that corrosive species have already penetrated into the substrate, possibly through either the grain boundaries or the microcracks, and thus form oxides in the substrate near the interface. At 700˚C and 800˚C chromium rich oxides generate in the inner oxidation zone. The internal oxidation thus probably ascribes to the strengthened oxygen inward diffusion due to the presence of water vapor or other factors such as the effect of tensile internal stresses (discussed in Section 6.1). However, silicon oxides are dominant at 900˚C. This indicates that a large amount of chromium ions diffuse towards to the surface at 900˚C, leading to an inward increased vacancies and chromium depleted zone in the substrate. The flux of vacancies may penetrate into the substrate thus condense out into voids [*Hou, 2016*]. Therefore, protective silicon oxides are likely to form sometimes with voids generated when internal oxidation happens for the oxidation of AISI 316L SS at 900˚C in the air with 1% water vapor.

Wagner proposed an expression of internal oxidation kinetics as [*Wagner, 1959*]:

$$x^2 = 2k_p t = 2\left[\left(N_{\mathrm{O}}^{(s)} D_{\mathrm{O}}\right)/(\eta N_{\mathrm{B}})\right] t, \tag{4.8}$$

where $N_{\mathrm{O}}^{(s)}$ is the solubility of oxygen in the alloy; D_{O} is the diffusivity of oxygen in the alloy; η is the ratio of oxygen atom to solute atom in the precipitated oxide; N_{B} is the mole fraction of B of the alloy. For Fe-Cr alloys oxidized at 1073K, the critical Cr content for external protective chromia formation is given by [*Ani et al., 2009*]:

$$N_{\mathrm{Cr}}^{*} \geq \left[\left(\pi g^{*} N_{\mathrm{O}}^{(s)} D_{\mathrm{O}} \mathrm{V}_{alloy}\right)/2\eta D_{\mathrm{Cr}} V_{\mathrm{CrO}_{1.5}}\right]^{1/2}, \tag{4.9}$$

where D_{Cr} is the diffusivity of chromium in the alloy; $V_{\mathrm{CrO}_{1.5}}$ and V_{alloy} are molar volumes of alloy and $CrO_{1.5}$ respectively; g^{*} is the volume fraction of internal oxide precipitates.

In the study of Ani, the ratio of critical Cr concentration for a protective scale formation in wet atmosphere and the one in dry atmosphere is around 1.2 according to Equation (4.9) [*Ani et al., 2009*], implying that more chromium is needed to form protective chromia in the presence of water vapor. The internal oxidation of Fe-13Cr-5Ni alloy at 700˚C in synthetic gases (Ar-21%O_2 and Ar-21%O_2-15%H_2O) has been properly studied in [*Liu et al., 2012*] with similar

conclusions obtained. Based on the findings by Ani and Liu that more chromium is needed to form protective chromia in the presence of water vapor, it is reasonable to say that for the alloys with the same Cr concentration oxidized in dry and wet atmospheres respectively, internal oxidation would happen more easily in wet atmosphere. This is validated by the observation in this work that internal oxidation is present for the oxidation of AISI 316L SS in the 2% water containing air at 700˚C and 800˚C as well as in the 1% water containing air at 900˚C. However, the presence of water vapor seems not the only one mechanism to explain this phenomenon because internal oxidation did not appear for all the cases with water vapor in this work.

4.2.5.4 Martensitic phase transformation

As introduced in Section 4.1.4.3, martensitic phase transformation is present for the oxidation at 800˚C and 900˚C in dry air, which mainly ascribes to the formation of chromium and manganese barren zone in the substrate after an adequate outward diffusion of cations. Interestingly, martensitic phase is also detected (see Figure 4.31.b) for AISI 316L SS oxidized at 700˚C for long time in the 4% containing air after. The similar in-situ X-ray phase monitoring has also been conducted to the corresponding specimen, as illustrated in Figure 4.39. It also suggests that martensitic phase prefers forming during the cooling process and vanishes gradually with reheating the specimen.

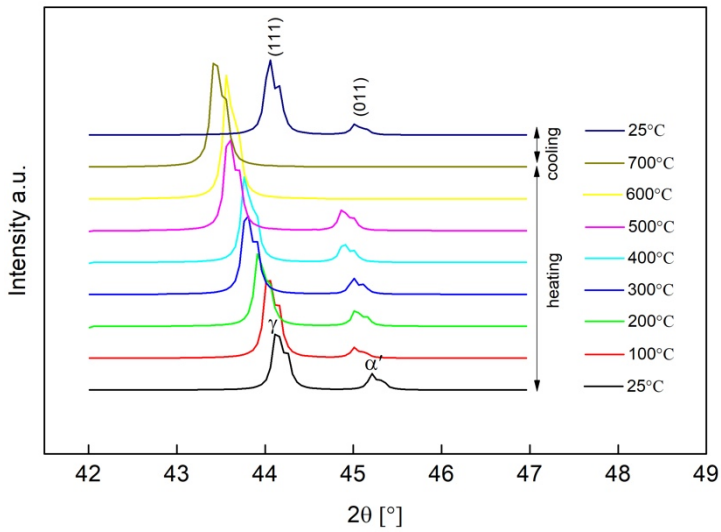

Figure 4.39 In-situ XRD monitoring the martensitic phase transformation for AISI 316L after oxidation at 700˚C for 96 hours in the 4% water containing air

Combining the information of EDX mapping (see Figure 4.24) and X-ray penetration depth evaluation, it can be observed that martensitic phase occurs in the intermediate part of oxide scale where metallic iron and nickel are rich. Therefore, this phenomenon cannot be simply interpreted by the elemental depletion in the substrate and the growth mechanism should be

considered. Water vapor penetrate into the substrate in a quite depth, being hindered at the interface consisting of chromium rich oxide layer. This protective layer impedes the interdiffusion between the anions and cations. Moreover, oxidation continues in the outer part. Due to the enhanced cation outward migration [*Luo et al., 2018*], more voids are present and form cracks easily after being stressed. These cracks further offer many fast diffusion paths. At the surface, an oxide layer always exists and experiences evaporation, where the formation of protective oxides is supported by the outward cation diffusion. Therefore, chromium and manganese are relatively poor in the intermediate part of oxide scale where martensitic phase prefers forming during the cooling.

4.2.5.5 Oxide composition and proposed growth mechanisms in humid air

Based on the previous results, it can be thought that the oxide compositions in humid air have not an apparent distinction compared with those in dry air. The oxide scale is composed by corundum-type oxides at 700˚C, while at higher temperature (800˚C and 900˚C), an outer layer of spinel-type oxides ($MnCr_2O_4$ predominates) and an inner layer of corundum-type oxides (Cr_2O_3 predominates) constitute the oxide scale.

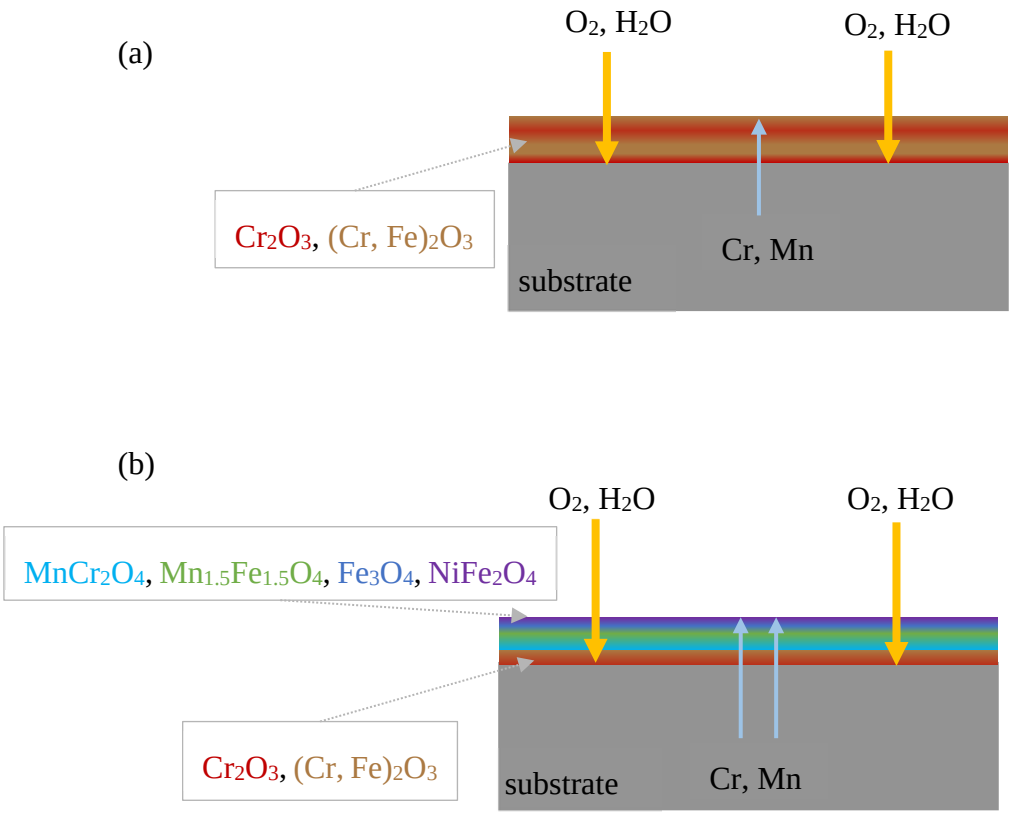

Figure 4.40 Schematic presentation of AISI 316L SS oxidized at 700˚C (a), 800˚C and 900˚C (c) in humid air

However, the growth process is influenced by water vapor, as displayed in Figure 4.40. In the presence of water vapor, inward diffusion of oxide species is motivated owing to the dissociation mechanism, and simultaneously outward diffusion of metallic ions is also enhanced due to easier formation of voids. Consequently, the differences of component distribution and microstructure appear.

For the oxidation at 700˚C, the corundum-type oxide layer shows three zones with characteristic phase constituents. Water vapor and oxygen diffuse inward, forming a chromia rich layer at the interface. At the surface, chromium and manganese oxides grow outward but gradually evaporate, forming an iron rich oxide layer finally. Due both to the cation outward diffusion and insufficient supply of chromium and manages, the intermediate layer turns enriched in iron oxides (FeO) and metallic compounds of iron and nickel.

At 800˚C, the enhanced inward diffusion causes the formation of metallic compounds as in the case at 700˚C or the appearance of internal oxidation. And the improved cation diffusion contributes to a fast formation of spinel oxides at the surface. Similarly, at 900˚C the obvious enrichment of spinel oxides near the surface and the fast chromia formation leaving an internal oxidation zone behind are also attributed to the increased cation outward diffusion.

4.3 Summary

In this chapter, the thermochemical study of AISI 316L SS oxidized at 700˚C, 800˚C and 900˚C in the air with 0%, 1%, 2%, 4% and 8% water vapor has been carried out. The is part mainly concerns the oxidation kinetics, oxide surface morphology and cross-section microstructure, oxide phase constituent and its quantitative distribution as well as the elemental profile versus the oxide thickness. Discussions center around the oxide growth mechanisms in the presence or absence of water vapor.

- Kinetics

The oxidation rate of AISI 316L SS in dry and humid air obeys the parabolic rate law before breakaway oxidation. Breakaway oxidation is present after oxidation at 800˚C in the 8% water containing air as well as at 900˚C in the 1% and 8% water containing air.

- Composition

At 700˚C, a single layer oxide scale has formed on the substrate, where corundum-type oxide (Cr_2O_3, chromium and iron solid solution oxide) is dominant together with some metallic

compounds of iron and nickel ($FeNi_3$). At 800˚C and 900˚C, the oxide scale consists of a two-layer structure with an outer spinel-type oxides ($MnCr_2O_4$) and inner corundum-type oxides (Cr_2O_3).

- Morphology

At 700˚C, the oxide scale is composed by the base oxide imbedded with some manganese rich oxide grains. At 800˚C and 900˚C, the oxide scale shows a grain-like surface consisting of manganese, chromium and iron containing spinel oxides. Moreover, iron oxide grains maybe present at the surface at 800˚C. The spinel oxide clusters prefer forming at 900˚C in humid air. A surface of irregular shaped oxides with a complex structure occur after breakaway oxidation. Water vapor plays a role of grain refinement.

- Diffusion

In dry air, oxygen inward diffusion is significant for the oxidation at 700˚C, while cation outward diffusion predominates for the oxidation at 800˚C and 900˚C. In the presence of water vapor, both inward and outward diffusions are enhanced. The latter case is more obvious during the oxidation at 900˚C, which can be recognized through the enrichment of spinel oxide layer near the surface as well as the increased chromia content near the interface accompanied with an internal oxidation zone beneath. For the oxidation at 800˚C, both sceneries can take place.

- Breakaway

For AISI 316L SS oxidized at 800˚C in the 8% water containing air, breakaway oxidation happens with a rapid growth of iron oxides and the annihilation of iron and nickel metallic compounds within the oxide scale. At 900˚C, a large amount of chromia forms quickly in the 1% water containing air with an inner zone relatively rich in iron oxides, while more iron oxides are present across the oxide scale formed in the 8% water containing air. All indicates that water vapor promotes the fast-outward growth of chromium oxides as well as consumes protective oxides through evaporation, whereby the supply of chromium is insufficient and the growth of iron rich oxides is motivated.

4.4 Reference

[Ani et al., 2009] ANI, M. H. B., KODAMA, T., UEDA, M., KAWAMURA, K. & MARUYAMA, T. 2009. The Effect of Water Vapor on High Temperature Oxidation of Fe-Cr Alloys at 1073 K. *Materials Transactions,* 50**,** 2656-2663.

[Beverskog et al., 1997] BEVERSKOG, B. & PUIGDOMENECH, I. 1997. Revised pourbaix diagrams for chromium at 25–300 C. *Corrosion Science,* 39**,** 43-57.

[Brady et al., 2011] BRADY, M. P., FAYEK, M., KEISER, J. R., MEYER, H. M., MORE, K. L., ANOVITZ, L. M., WESOLOWSKI, D. J. & COLE, D. R. 2011. Wet oxidation of stainless steels: New insights into hydrogen ingress. *Corrosion Science,* 53**,** 1633-1638.

[Buscail et al., 2015] BUSCAIL, H., ROLLAND, R. & PERRIER, S. 2015. Influence of water vapour on 316L oxidation at high temperature-in situ X-Ray diffraction.

[Butler et al., 1986] BUTLER, E. & BURKE, M. 1986. Chromium depletion and martensite formation at grain boundaries in sensitised austenitic stainless steel. *Acta Metallurgica,* 34**,** 557-570.

[Calmunger et al., 2015] CALMUNGER, M., ERIKSSON, R., CHAI, G., JOHANSSON, S. & MOVERARE, J. J. 2015. Surface phase transformation in austenitic stainless steel induced by cyclic oxidation in humidified air. *Corrosion Science,* 100**,** 524-534.

[Cox et al., 1973] COX, M., MCENANEY, B. & SCOTT, V. 1973. Vacancy condensation and void formation in duplex oxide scales on alloys. *Philosophical Magazine,* 28**,** 309-319.

[Dorcheh et al., 2018] DORCHEH, A. S., SCHÜTZE, M. & GALETZ, M. C. 2018. Factors affecting isothermal oxidation of pure chromium in air. *Corrosion Science,* 130**,** 261-269.

[Duh et al., 1990] DUH, J. & WANG, C. 1990. Formation and growth morphology of oxidation-induced ferrite layer in Fe-Mn-Al-Cr-C alloys. *Journal of Materials Science,* 25**,** 2063-2070.

[Duh et al., 1988] DUH, J.-G., LEE, J. & WANG, C.-J. 1988. Microstructural development in the oxidation-induced phase transformation of Fe-Al-Cr-Mn-C alloys. *Journal of materials science,* 23**,** 2649-2660.

[Dumerval et al., 2014] DUMERVAL, M., PERRIN, S., MARCHETTI, L., TABARANT, M., JOMARD, F. & WOUTERS, Y. 2014. Hydrogen absorption associated with the corrosion mechanism of 316L stainless steels in primary medium of Pressurized Water Reactor (PWR). *Corrosion Science,* 85**,** 251-257.

[Ebbinghaus, 1993] EBBINGHAUS, B. B. 1993. Thermodynamics of gas phase chromium species: the chromium oxides, the chromium oxyhydroxides, and volatility calculations in waste incineration processes. *Combustion and Flame,* 93**,** 119-137.

[Fujii et al., 1964] FUJII, C. & MEUSSNER, R. 1964. The Mechanism of the High-Temperature Oxidation of Iron-Chromium Alloys in Water Vapor. *Journal of the Electrochemical Society,* 111**,** 1215-1221.

[Gong et al., 2010] GONG, Y. F. & DE COOMAN, B. C. 2010. Kirkendall void formation during selective oxidation. *Metallurgical and Materials Transactions A,* 41**,** 2180-2183.

[Hou, 2016] HOU, P. Y. 2016. Oxidation of Metals and Alloys. *Reference Module in Materials Science and Materials Engineering.* Elsevier.

[Huntz et al., 2007] HUNTZ, A. M., RECKMANN, A., HAUT, C., SÉVÉRAC, C., HERBST, M., RESENDE, F. C. T. & SABIONI, A. C. S. 2007. Oxidation of AISI 304 and AISI 439 stainless steels. *Materials Science and Engineering: A,* 447**,** 266-276.

[Jacob et al., 2002] JACOB, Y., HAANAPPEL, V., STROOSNIJDER, M., BUSCAIL, H., FIELITZ, P. & BORCHARDT, G. 2002. The effect of gas composition on the isothermal oxidation behaviour of PM chromium. *Corrosion Science,* 44**,** 2027-2039.

[Jervis et al., 1990] JERVIS, T., WILLIAMSON, D., HIRVONEN, J.-P. & ZOCCO, T. 1990. Characterization of the surface oxide formed by excimer laser surface processing of AISI 304 stainless steel. *Materials Letters,* 9**,** 379-383.

[Jung, 2006] JUNG, I. 2006. Critical evaluation and thermodynamic modeling of the Mn–Cr–O system for the oxidation of SOFC interconnect. *Solid State Ionics,* 177**,** 765-777.

[Jung et al., 2012] JUNG, R.-H., TSUCHIYA, H. & FUJIMOTO, S. 2012. XPS characterization of passive films formed on Type 304 stainless steel in humid atmosphere. *Corrosion Science,* 58**,** 62-68.

[Karczewski et al., 2019] KARCZEWSKI, J., BRYLEWSKI, T., MIRUSZEWSKI, T., ANDERSEN, K. B., JASINSKI, P. Z. & MOLIN, S. 2019. High-temperature kinetics study of 430L steel powder oxidized in air at 600–850 °C. *Corrosion Science,* 149**,** 100-107.

[Li, 2016] LI, N. 2016. *Étude du comportement à l'oxydation et des contraintes résiduelles lors de l'oxydation sous air humide de l'alliage AISI 430.* Paris Saclay.

[Liu et al., 2012] LIU, L., YANG, Z. G., ZHANG, C., UEDA, M., KAWAMURA, K. & MARUYAMA, T. 2012. Effect of water vapour on the oxidation of Fe–13Cr–5Ni martensitic alloy at 973K. *Corrosion Science,* 60**,** 90-97.

[Luo et al., 2018] LUO, L., SU, M., YAN, P., ZOU, L., SCHREIBER, D. K., BAER, D. R., ZHU, Z., ZHOU, G., WANG, Y., BRUEMMER, S. M., XU, Z. & WANG, C. 2018. Atomic origins of water-vapour-promoted alloy oxidation. *Nat Mater,* 17**,** 514-518.

[Opila et al., 2007] OPILA, E. J., MYERS, D. L., JACOBSON, N. S., NIELSEN, I. M., JOHNSON, D. F., OLMINSKY, J. K. & ALLENDORF, M. D. 2007. Theoretical and experimental investigation of the thermochemistry of CrO2 (OH) 2 (g). *The Journal of Physical Chemistry A,* 111**,** 1971-1980.

[Oum et al., 2016] OUM, M., HONG, J.-E. & STEINBERGER-WILCKENS, R. Thermochemical and Kinetic Modelling of Chromium-Rich Alloys. Proc. 12th European SOFC and SOE Forum, Lucerne, 2016. 5-8.

[Perez et al., 2000] PEREZ, F., CRISTOBAL, M., HIERRO, M., PEDRAZA, F., ARNAU, G. & MERINO, T. 2000. Effect of yttrium and erbium ion implantation on the oxidation behaviour of the AISI 304 austenitic steel. *Surface and Coatings Technology,* 126**,** 116-122.

[Sabioni et al., 2007] SABIONI, A., HUNTZ, A., BORGES, L. & JOMARD, F. 2007. First study of manganese diffusion in Cr2O3 polycrystals and thin films by SIMS. *Philosophical Magazine,* 87**,** 1921-1937.

[Sabioni et al., 2005] SABIONI, A. C. S., HUNTZ, A. M., SILVA, F. & JOMARD, F. 2005. Diffusion of iron in Cr2O3: polycrystals and thin films. *Materials Science and Engineering: A,* 392**,** 254-261.

[Sabioni et al., 2012a] SABIONI, A. C. S., RAMOS, R. P. B., JI, V. & JOMARD, F. 2012a. Oxygen Diffusion Study in Oxidation Films of the AISI 304 Austenitic Stainless Steel. *Defect and Diffusion Forum,* 323-325**,** 345-351.

[Sabioni et al., 2012b] SABIONI, A. C. S., RAMOS, R. P. B., JI, V., JOMARD, F., MACEDO, W. A. D. A., GASTELOIS, P. L. & TRINDADE, V. B. 2012b. About the Role of Chromium and Oxygen Ion Diffusion on the Growth Mechanism of Oxidation Films of the AISI 304 Austenitic Stainless Steel. *Oxidation of Metals,* 78**,** 211-220.

[Saunders et al., 2008] SAUNDERS, S. R. J., MONTEIRO, M. & RIZZO, F. 2008. The oxidation behaviour of metals and alloys at high temperatures in atmospheres containing water vapour: A review. *Progress in Materials Science,* 53**,** 775-837.

[Susan et al., 2012] SUSAN, D. F., KNOROVSKY, G., ROBINO, C., MICHAEL, J. R., RODRIGUEZ, M. A. & PERRICONE, M. J. 2012. Surface alloy depletion and martensite formation during glass to metal joining of austenitic stainless steels. *Science and Technology of Welding and Joining,* 17**,** 321-332.

[Wagner, 1959] WAGNER, C. 1959. Reaction types in the oxidation of alloys. *Z. Elektrochem.,* 63**,** 772-782.

[Wei et al., 2018] WEI, L., ZHENG, J., CHEN, L. & MISRA, R. D. K. 2018. High temperature oxidation behavior of ferritic stainless steel containing W and Ce. *Corrosion Science,* 142**,** 79-92.

[Xiao, 2014] XIAO, J. 2014. *Etude de la cinétique d'oxydation et contraintes résiduelles de l'Inconel 600 sous air humide.* Paris 11.

[Young, 2008] YOUNG, D. J. 2008. Effects of Water Vapour on the Oxidation of Chromia Formers. *Materials Science Forum,* 595-598**,** 1189-1197.

[Young, 2016] YOUNG, D. J. 2016. *High temperature oxidation and corrosion of metals,* Elsevier.

[Young et al., 2006] YOUNG, D. J. & PINT, B. A. 2006. Chromium Volatilization Rates from Cr2O3 Scales into Flowing Gases Containing Water Vapor. *Oxidation of Metals,* 66**,** 137-153.

[Zurek et al., 2008] ZUREK, J., YOUNG, D., ESSUMAN, E., HÄNSEL, M., PENKALLA, H., NIEWOLAK, L. & QUADAKKERS, W. 2008. Growth and adherence of chromia based surface scales on Ni-base alloys in high-and low-pO2 gases. *Materials Science and Engineering: A,* 477**,** 259-270.

CHAPTER

5

Oxidation of AISI 316L SS - thermomechanical

Contents

CHAPTER 5 OXIDATION OF AISI 316L SS - THERMOMECHANICAL ASPECT **149**

5.1 GROWTH STRESS 149

5.1.1 Deflection results *151*

5.1.2 Elastic analysis *153*

5.1.3 About creep analysis *155*

5.2 THERMAL STRESS 158

5.3 RESIDUAL STRESS 162

5.3.1 In dry air *162*

5.3.2 In humid air *166*

5.4 DISCUSSION 175

5.4.1 Deformation *175*

5.4.2 Damages *176*

5.4.2.1 Under tension 177

5.4.2.2 Under compression 178

5.4.3 Temperature and humidity dependences of residual stress *182*

5.5 SUMMARY 183

5.6 REFERENCE 186

Chapter 5 Oxidation of AISI 316L SS - thermomechanical aspect

The metallic component exposed at high temperatures in the oxidative atmosphere experiences not only the thermochemical attacks but also the thermomechanical ones. The ability of oxidation resistance for the stainless steel used in high temperature techniques is guaranteed by the dense, intact and adherent protective oxide scale on its surface. During oxidation, stresses appear inevitably when oxide scales generate on the substrate. The role of these stresses is important because they can impact directly the growth of oxide scales as well as determine the lifetime of the component. Breakdown of protective oxide scale means the failure of metallic materials. Therefore, it is of great significance to investigate the mechanical behaviors of protective oxide scale during oxidation.

The thermochemical aspect of AISI 316L oxidized at 700˚C, 800˚C and 900˚C in the air with 0%, 1%, 2%, 4% and 8% water vapor has been studied in the previous chapter. The protective oxide scale for AISI 316L under the conditions investigated in this work is the corundum-type chromium rich oxides (Cr_2O_3 and/or $(Cr, Fe)_2O_3$). This chapter will focus on the internal stresses in these oxide scales formed under corresponding conditions. Internal stresses are divided into three parts in this thesis, i.e., growth stresses, thermal stresses and residual stresses with consideration of isothermal oxidation process, cooling process and the stage at room temperature after oxidation.

In Chapter 4, the features of oxide scales formed in this work have been observed regarding to different temperatures and humidity, and different oxidation growth mechanisms have been further suggested. There is reason to believe that the internal stress evolution in the oxide scale may show distinctions under different conditions. This chapter will first study the average growth stress in the oxide scale, subsequently the thermal stresses within the oxide scales under corresponding conditions through theoretical calculation, and finally the residual stresses in the oxide scales. Discussions regarding to possible deformation behaviors (plastic deformation), observed damages (cracks, decohesion, local spalling and/or breakdown) and correlated affecting factors will be conducted.

5.1 Growth stress

This thesis uses in-situ deflection test to estimate the growth stresses developed within the oxide scales formed on AISI 316L SS at 700˚C, 800˚C and 900˚C for short-term duration (the initial 3-hour oxidation) in the air with 0%, 1%, 2%, 4% and 8% water vapor respectively. The related theory and method have been introduced in Section 3.6. Considering the sample preparation process which is presented in Section 3.1.4, the final strip to be deflected may have a minor

bending caused by asymmetry on the two sides with and without protective oxide scales. Such natural bending may lead to the interference on the value of deflection as a result of substrate elongating at high temperature. It is known that the determination of growth stress relies on the value of deflection. Therefore, contrast experiments at various temperatures have been carried out in pure argon atmosphere to minimized the additional deflection errors caused by the substrate elongation.

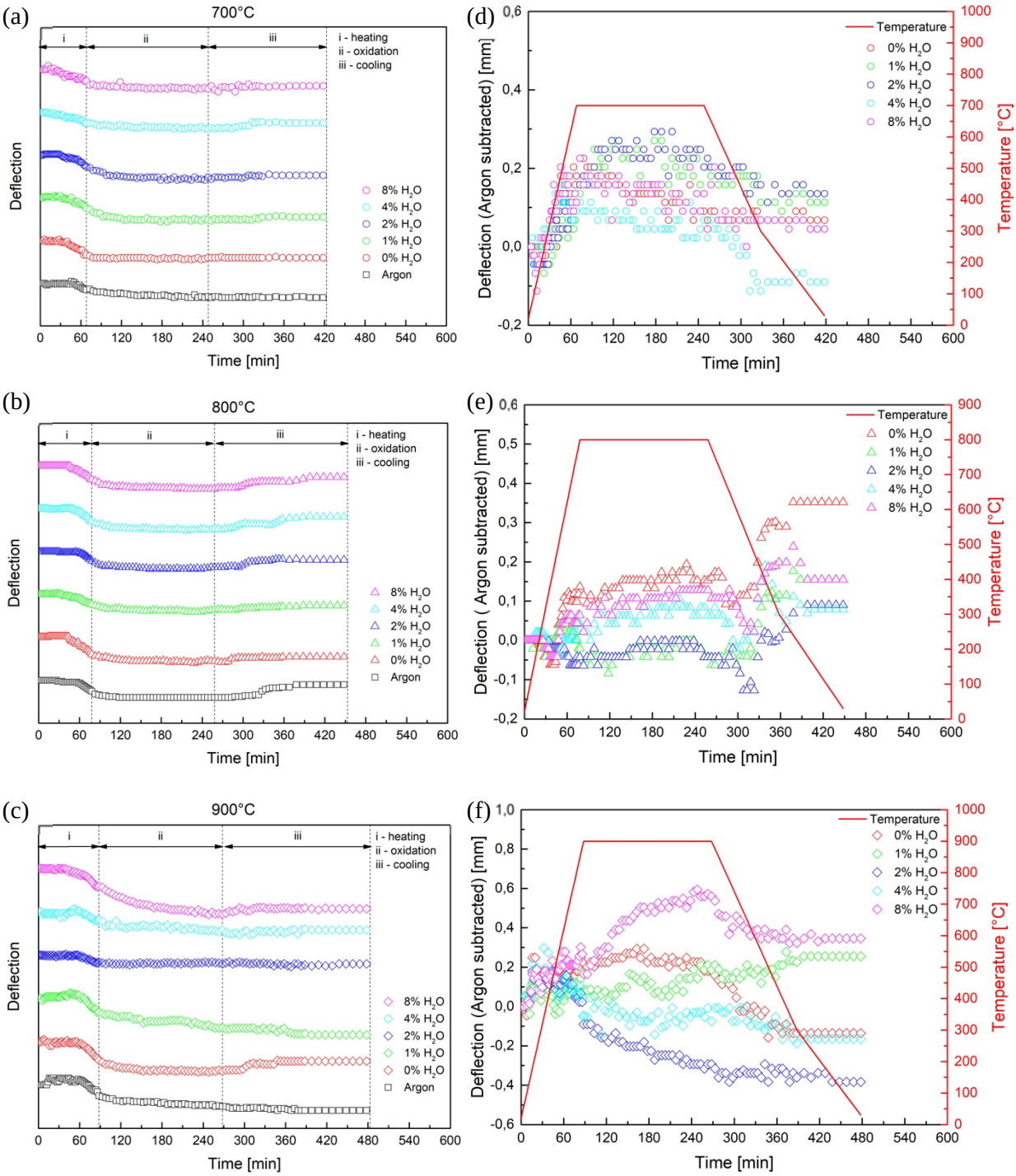

Figure 5.1 Raw data of deflection experiment in different atmospheres at 700˚C (a), 800˚C (b) and 900˚C (c) with corresponding results after deflections in argon subtracted (d-f)

5.1.1 Deflection results

Figure 5.1.a-c display the relative deflected levels at 700˚C, 800˚C and 900˚C in the air with different humidity investigated in this work. Deflection is also determined in argon (marked as black) at those three temperatures, indicating that elongation does contribute to the final values of deflection. The net deflected curves have been obtained by subtracting the corresponding deflection values measured in argon, shown in Figure 5.1.d-f.

The isothermal oxidation process is of interest for the growth stress characterization because the heating process and cooling process are more complicated where chemical equilibria cannot be easily established. In addition, during the heating process the growth stress determination may be influenced since oxide scale has not formed on the whole surface. Hence, this thesis only considers the deflection values measured during the isothermal oxidation process, illustrated in Figure 5.2. And particular attention will be paid to the initial period (the initial 3-hour oxidation) during the stress determination to better understand the stress development.

Figure 5.2 is the summary of deflection values of the isothermal oxidation process for AISI 316L SS oxidized at 700˚C, 800˚C and 900˚C for 3 hours in the 0%, 1%, 2%, 4% and 8% water containing air respectively. The values at the onset of isothermal oxidation have been normalized to zero. As introduced in Section 3.6, the positive deflected values mean the oxide scale is subject to tensile stresses, while the negative ones represent the compressive stresses. Generally, compressive stress is rather welcomed for the thin film, because it is beneficial to the adherence of the substrate and oxide scale.

Assuming the system of chromia/AISI 316L SS in this work, PBR can thus be calculated through Equation (2.48), i.e., around 2.1 [*Hancock et al., 1974*]. This value is larger than 1, indicating compressive stresses within oxide scales. However, practical examples have not shown identical results since totally inward diffusion model is no longer suitable for complicated diffusion processes in this work. Analysis combining the growth stress evolution with the specific diffusion process is in need with respect to the detailed conditions.

It can be observed from the deflection results in this work that:

At 700˚C (see Figure 5.2.a), tensile stresses act apparently within the oxide scales grown in the air with 1% and 2% water vapor, while the oxide scales formed in the air with 0%, 4% and 8% water vapor are generally subject to compressive stresses. According to the deflection curves obtained in different humidity at 700˚C, the magnitudes of deflection can be estimated, i.e., less than 0.08, 0.20, 0.16, 0.08 and 0.08 mm respectively in the air with 0% to 8% water vapor.

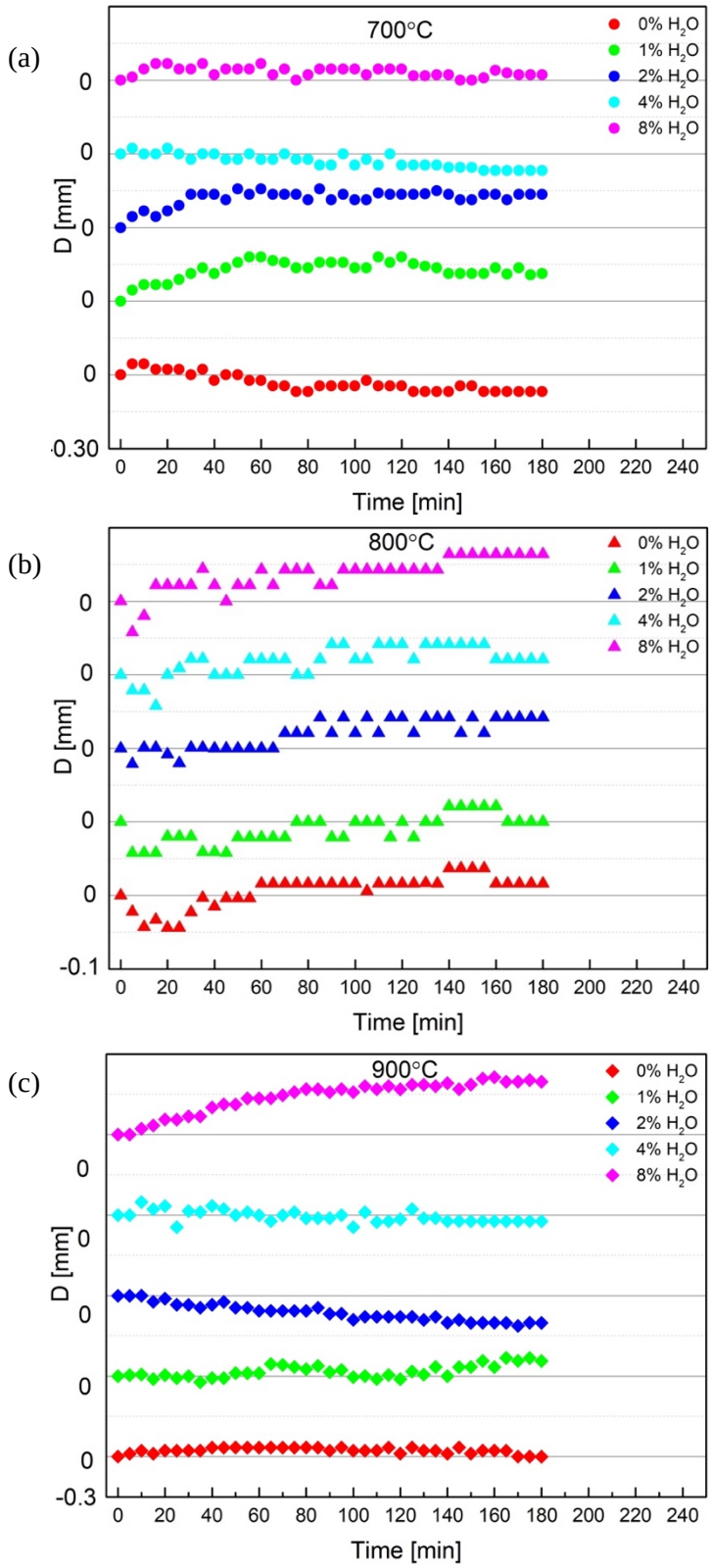

Figure 5.2 Deflection results during isothermal oxidation at 700˚C (a), 800˚C (b) and 900˚C (c) in the air with different water vapor contents

At 800˚C (see Figure 5.2.b), after 3-hour oxidation, the oxide scales grown in all humidity investigated in this work are subject to tensile stresses in different levels; the rise of compressive stresses with a subsequent decline during the initial period of isothermal oxidation may ascribe

respectively to the generation and coalescence of oxide grains at the surface [*Chason et al., 2002, Chason et al., 2015*], which is in accord to the observation at 800˚C that oxide grains first grow and subsequent coalesce into the grain-like layer (Section 4.1.4.4 and Section 4.2.5.5). Moreover, the magnitudes of deflection are estimated, i.e., less than 0.05, 0.05, 0.05, 0.05 and 0.08 mm respectively in the air with 0% to 8% water vapor.

At 900˚C (see Figure 5.2.c), the oxide scale grown in the 8% water containing air suffers large tensile stresses; the one formed in the air with 1% water vapor also shows a similar trend. The magnitudes of deflection are also estimated, i.e., less than 0.08, 0.14, 0.24, 0.08 and 0.45 mm respectively in the air with 0% to 8% water vapor.

Huntz, Evans and Zhao etc. have made attempts on the analysis of growth stress during the isothermal oxidation by deflection method. The data of deflection experiment was initially treated using an elastic analysis [*J. G. Zhao, 1984*], and subsequently a viscoplastic analysis [*Evans, 1995*].

5.1.2 Elastic analysis

In 1980, Delaunay accumulated mass of deflection data related to the oxidation of various alloys which formed either chromia or alumina [*D. Delaunay, 1980*]. He calculated the oxide growth stress using the formula proposed by Norin [*Norin, 1975*]:

$$\sigma_{\mathrm{ox}} = (E_{\mathrm{m}} t_{\mathrm{m}}^2 D)/[3(1 - v_{\mathrm{m}}^2) L^2 t_{\mathrm{ox}}], \tag{5.1}$$

where t_{m} and t_{ox} are the thicknesses of the substrate and oxide respectively; D the deflection determined in the experiment; L the original length of the specimen.

Similarly, Equation (5.1) has also been employed in this thesis to calculate the in-plane growth stresses in the oxide scales as a function of oxidation time for AISI 316L oxidized in 700˚C, 800˚C and 900˚C in the air with 0%, 1%, 2%, 4% and 8% water vapor, illustrated in Figure 5.3. The parameters used for elastic calculation are tabulated in Table 2.1. It should be noted here that the elastic moduli of AISI 316L SS are obtained at room temperature, while their values, especially Young's modulus, are usually smaller at higher temperature (e.g., the Elastic moduli of Cr_2O_3 formed on AISI 316 SS at 700˚C and 800˚C are 256 GPa and 212 GPa respectively [*Nicholls et al., 1994*]).

For AISI 316L oxidized in dry air at the temperatures investigated, qualitatively, the in-plane growth stresses within the oxide scales decrease with increasing the temperature, i.e. from -2.57 GPa at 700˚C to 0 GPa at 900˚C. It can thus be thought that for AISI 316L SS oxidized in dry air, the growth stresses within the oxide scales developed during the isothermal oxidation make

a smaller contribution to the final residual stresses within the oxide scales at higher temperatures. However, when water vapor is introduced, the in-plane growth stresses within the oxide scales show strong sensitivity to humidity, particular for the oxidation of AISI 316L SS at 700˚C and 900˚C. The final stable growth stresses developed under different conditions studied in this work are listed in Table 5.1.

Table 5.1 Stabilized In-plane growth stresses (GPa) of oxide scales for AISI 316L oxidized between 700˚C and 900˚C in the air with different humidity (elastic analysis)

Water content (vol.%)	**0**	**1**	**2**	**4**	**8**
700˚C	-2.57	4.35	7,98	-2.53	1.12
800˚C	0.53	0	1.39	0.77	1.96
900˚C	0	1.03	-2.39	-0.53	4.47

In addition, the deviation and fluctuation can be observed in the curves of growth stress. The former ascribes to the constant repetition process of the fast stress accumulation and subsequent relaxation during the isothermal oxidation, while the latter to the repetition of stress relaxation after a short-term stress accumulation, the process of which is relatively slow compared with the former case. As introduced in Section 2.4.2, stress release can be conducted in several forms, e.g., the deformation of the substrate and oxide scale, the formation of micro-cracks, decohesion and local spalling etc. Stresses can in turn re-accumulate through several ways, for instance, new oxides generate at the previous forming cracks (self-healing) [*Schütze, 1997*] or at grain boundaries within the oxide scales [*Rhines et al., 1970*]. The interaction of these two processes (stress release and stress accumulation) leads to a final equilibrium state, i.e., the final stable growth stress.

It should also be noticed that quite large values of in-plane growth stress have been obtained using the elastic model. Some have reached dozens of gigapascals (e.g., 4.35 and 7.98 GPa at 700˚C in the air with 1% and 2% water vapor; 4.47 GPa at 900˚C in the air with 8% water vapor). Normally, cracks or local spallation of oxide scales may happen as a result of large elastic loading where the stored elastic energy is far more than the fracture resistance [*Birks et al., 2006*]. In the case of oxidation at 700˚C in the air with 1% and 2% water vapor, cracks can form according to the fluctuation of their mass gain curves (see Figure 4.17.b). However, no obvious local spalling or cracking is found on the sample oxidized at 900˚C for the initial 6-hour oxidation in the air with 8% water vapor. Plastic deformation of both the substrate and oxide scale without damages can thus be expected as the main form of stress release for AISI

316L SS at 900˚C in the air with 8% water vapor. This indicates that elastic analysis cannot satisfy the analysis of growth stresses in the case where plastic deformation cannot be ignored.

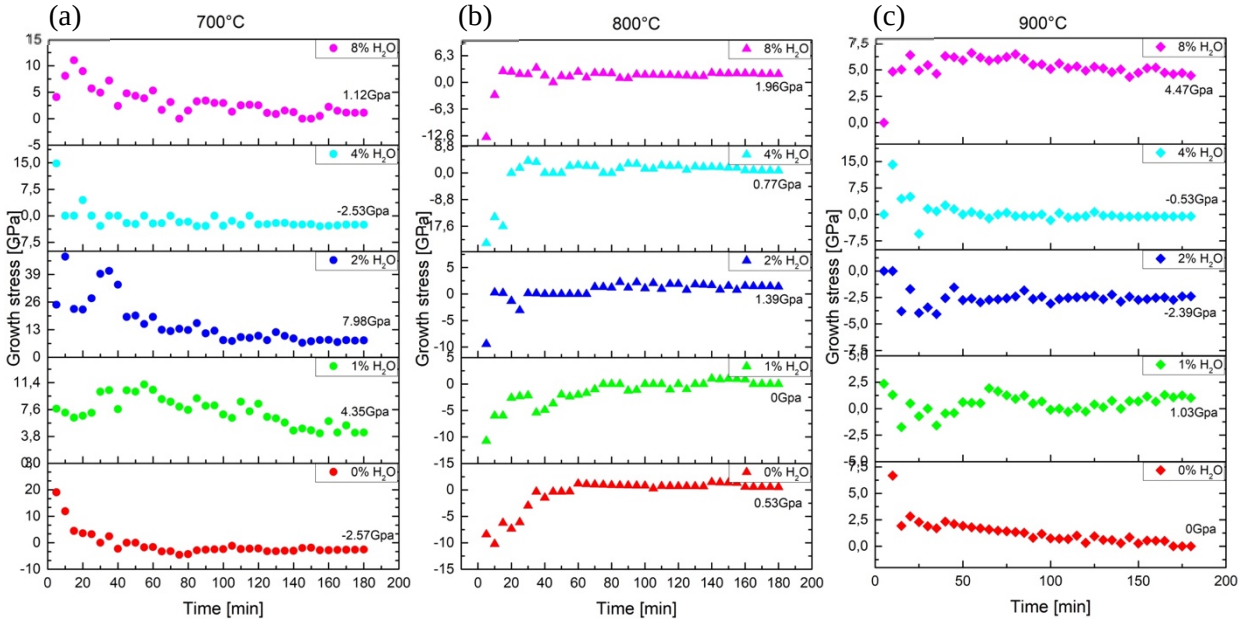

Figure 5.3 Elastic analysis of growth stress evolution for short-term oxidation of AISI 316L SS between 700˚C and 900˚C in the air with different humidity

5.1.3 About creep analysis

As introduced in Section 2.4.2.1, high temperature is possible to motivate plastic deformation for both the metallic substrate and oxide scales. In this work, creep of AISI 316L SS can be first responsible for the large deflection at the temperatures investigated. Moreover, plastic deformation of oxides is also present at higher temperatures (especially at 900˚C). Figure 2.19 suggests that chromia will plastically deform in the form of dislocation climb under high loading (shear stress: several hundreds of megapascals) and Coble creep at low loading (shear stress: lower than 100 MPa) between 700˚C and 900˚C.

Based on the experimental results of Delaunay, Zhao and Huntz have established a theoretical model to perfect the elastic analysis [*J. G. Zhao, 1984*], proposing the locations of the neutral axes as:

$$y_{\mathrm{m}}^{*} \approx t_{\mathrm{m}}/3, \tag{5.2}$$

$$y_{\mathrm{ox}}^{*} \approx (E_{\mathrm{m}} t_{\mathrm{m}}^{2})/(6E_{\mathrm{ox}} t_{\mathrm{ox}}), \tag{5.3}$$

and the corresponding stress distribution, given by:

$$\sigma_{\mathrm{m}}(y) = \{E_{\mathrm{m}}[y - (1/3)t_{\mathrm{m}}](2D)\}/(3L^{2}), \tag{5.4}$$

$$\sigma_{\mathrm{ox}}(y) \approx \sigma_{\mathrm{ox}} = (-E_{\mathrm{m}} t_{\mathrm{m}}^{2} D)/(3L^{2} t_{\mathrm{ox}}), \tag{5.5}$$

where, as shown in Figure 5.4.a, y_{m}^{*} and y_{ox}^{*} are the neutral axes of substrate and oxide respectively. This model suggests the neutral axis of oxide scale lies outside, which is suitable for the thin oxide scale under compressive stresses [*Evans, 1995*].

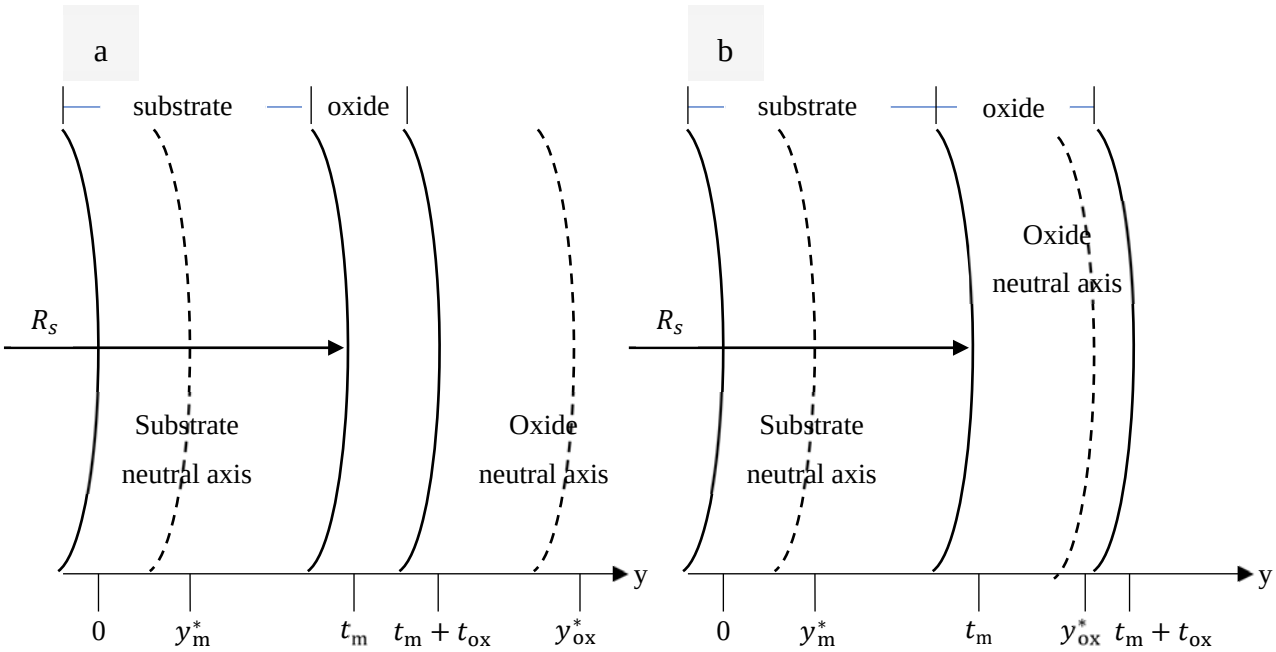

*Figure 5.4 Imaginary system for determining the stresses in the oxide and substrate: the oxide neutral axis outside the oxide (a); the oxide neutral axis inside the oxide (b) [*J. G. Zhao, 1984, Evans, 1995*]*

In 1995, by considering that viscoplastic strains appear in both the substrate and oxide scale, Evans first proposed a creep analysis for the deflection test, importing the Norton equation $\dot{\varepsilon} = C(\sigma)^{n}$ [*Norton, 1929*] to establish the relationship between the instantaneous creep rate $\dot{\varepsilon}$ and the change rate of curvature radius $\dot{R}_{\mathrm{s}}$ [*Evans, 1995*]:

$$\dot{\varepsilon}_{\mathrm{m}} = \mathrm{C}_{\mathrm{m}}(\sigma_{\mathrm{m}})^{n_{\mathrm{m}}} = \dot{R}_{\mathrm{s}}(\mathrm{d}\varepsilon_{\mathrm{m}}/\mathrm{d}R_{\mathrm{s}}) = \left[-\dot{R}_{\mathrm{s}}(y - y_{\mathrm{m}}^{*})\right]/[(R_{\mathrm{s}} - t_{\mathrm{m}} + y_{\mathrm{m}}^{*})^{2}], \qquad (5.6)$$

$$\dot{\varepsilon}_{\mathrm{ox}} = \mathrm{C}_{\mathrm{ox}}(\sigma_{\mathrm{ox}})^{n_{\mathrm{ox}}} = \dot{R}_{\mathrm{s}}(\mathrm{d}\varepsilon_{\mathrm{ox}}/\mathrm{d}R_{\mathrm{s}}) = \left[-\dot{R}_{\mathrm{s}}(y - y_{\mathrm{ox}}^{*})\right]/[(R_{\mathrm{s}} - t_{\mathrm{m}} + y_{\mathrm{ox}}^{*})^{2}], \qquad (5.7)$$

where C is a constant for a given temperature; n the creep index; the subscripts m and ox represent the substrate and oxide respectively. The variation of stress across the substrate is then given with respect to the balances of forces and moments around the M/MO interface, by:

$$\sigma_{\mathrm{m}}(y) = \left\{\left|\left[-\dot{R}_{\mathrm{s}}(y - y_{\mathrm{m}}^{*})\right]/[\mathrm{C}_{\mathrm{m}}(R_{\mathrm{s}} - t_{\mathrm{m}} + y_{\mathrm{m}}^{*})^{2}]\right|\right\}^{1/n_{\mathrm{m}}}. \qquad (5.8)$$

Similarly, the variation of stress across the oxide is given in two cases.

if $y_{\mathrm{ox}}^{*} > (t_{\mathrm{m}} + t_{\mathrm{ox}})$, i.e., the oxide neutral axis lies outside the oxide scale, as shown in Figure 5.4.a, meaning each region in the oxide scale is compressive:

$$\sigma_{\mathrm{ox}}(y) = -\{[-\dot{R}_{\mathrm{s}}(y_{\mathrm{ox}}^{*} - y)]/[\mathrm{C}_{\mathrm{ox}}(R_{\mathrm{s}} - t_{\mathrm{m}} + y_{\mathrm{ox}}^{*})^{2}]\}^{1/n_{\mathrm{ox}}}; \tag{5.9}$$

if $(t_{\mathrm{m}} + t_{\mathrm{ox}}) > y_{\mathrm{ox}}^{*} > t_{\mathrm{m}}$, i.e., the oxide neutral axis lies inside the oxide scale, as shown in Figure 5.4.b, meaning the region $(y > y_{\mathrm{ox}}^{*})$ is tensile while the region $(y_{\mathrm{ox}}^{*} > y > t_{\mathrm{m}})$ is compressive:

$$\sigma_{\mathrm{ox}}(y) = \{|-\dot{R}_{\mathrm{s}}(y - y_{\mathrm{ox}}^{*})/\mathrm{C}_{\mathrm{ox}}(R_{\mathrm{s}} - t_{\mathrm{m}} + y_{\mathrm{ox}}^{*})^{2}|\}^{1/n_{\mathrm{ox}}}. \tag{5.10}$$

In addition, R_{s} is the radius of curvature, the relationship of which with the deflection D is given by:

$$D = L^{2}/(2R_{\mathrm{s}}). \tag{5.11}$$

This method has been well employed in the investigations correlated to the oxide growth stress determination such as in alumina-forming ferritic steel [*Saunders et al., 1997*], in alumina-forming alloys [*Li et al., 1999*] or coupled with the numerical simulation [*Huntz et al., 2002*].

In this thesis, creep analysis of deflection data has also been tried, but no satisfactory results have been obtained. Possibly the reason is that the creep model suggested by Evans etc. is no more appropriate to the growth stress analysis in this work. The problems being present in this work are:

1. An original bending of the strip exists after sample preparation (see Figure 3.2) due to the protective oxide scale on the convex side. This leads to a negative value of the curvature radius if using this creep model to analyze the growth stress during the isothermal oxidation.
2. During the previous data treatment in this work, the position of oxide neutral axis is normally assumed initially (e.g., outside the oxide scale), but the final result of oxide neutral axis calculated using this creep model could not match the previous assumption (e.g., the result shows the oxide neutral axis lies inside the oxide scale). This may be also related to the physical model of the strip, as expressed in item 1.
3. It can be observed from Figure 5.2 that the direction of deflection sometimes can change, indicating the modification of stress state (e.g., from compression to tension). It brings the difficulty to use this creep model to study the stress state transformation with respect to oxidation time.

Based on these occurring problems, several solutions may be effective as the following:

1. It may be possible to re-build a creep model based on the study of Evans etc. but using the physical model in this work. To be more detailed, during the original stage of isothermal oxidation, a “negative” curvature radius is necessary to be imported.

2. Considering the stress state transformation, treating the data in segmentation may work. And in each segmentation, only one stress state is required.

5.2 Thermal stress

The stresses developed during the cooling process have been calculated based on Equations (2.52) - (2.55). Based on the oxide constituent and distribution which have been ensured in Chapter 4, an appropriate simplification of the oxide structural models has been done for thermal stress calculation.

The oxide scales formed at 700˚C can be seen as a single oxide layer consisting of corundum-type oxides (mixtures of Cr_2O_3 and Fe_2O_3). The ones formed at 800˚C and 900˚C can be seen as a two-layer structure with an outer spinel-type oxide layer (mixtures of $MnCr_2O_4$, $Mn_{1.5}Fe_{1.5}O_4$ and Fe_3O_4) and an inner corundum-type oxide layer (mixtures of Cr_2O_3 and Fe_2O_3).

According to Equations (2.55), the average of thermal expansion coefficient for the joint oxide scale is first worked out using the parameters listed in Table 5.2. The thickness of each oxide layer can be evaluated by combining the weight fraction of each layer and corresponding mass gain, which can be obtained from XRD phase quantification analysis (see Figure 4.13.d-f and Figure 4.32). The mixed oxides in a single layer is approximatively treated in the way of multi-layer oxide scale. The results are tabulated in Table 5.3.

Table 5.2 Thermal expansion coefficients of selected oxides

Oxide	$\alpha \times 10^6$ (K^{-1})	Temperature range (˚C)	Ref.
Cr_2O_3	7.3	100~1000	[*Tylecote, 1960*]
Fe_2O_3	12.2	100~1000	[*Rigby, 1946*]
$FeMnO_3$	9.01	100~700	[*Li et al., 2016*]
FeO	15.2	400~800	[*Robertson et al., 1990*]
	12.2	100~1000	[*Tylecote, 1960*]
$MnCr_2O_4$	9.5	25~700	[*Parmelee et al., 1932*]
	9.2	25~800	
	8.9	25~900	
Fe_3O_4	15.6	25~700	
	15.5	25~800	
	15.1	25~900	
	8.4	25~700	

$Mn_{1.5}Fe_{1.5}O_4$	8.3	25~800
$FeCr_2O_4$	8.4	25~700
	8.5	25~800

In Table 5.3, average thermal expansion coefficients of corundum-type oxide scale (mixtures of Cr_2O_3 and Fe_2O_3) $\bar{\alpha}_{co}$, spinel-type oxide scale $\bar{\alpha}_{sp}$ (mixtures of $MnCr_2O_4$, $Mn_{1.5}Fe_{1.5}O_4$ and Fe_3O_4) and the two-layer structure oxide scale $\bar{\alpha}_{ox}$ can be seen. At the same time, thermal stresses of the spinel-type oxide scale σ_{sp} (orange highlight in Table 5.3) as well as the total thermal stresses of the corundum-type stresses σ_{co} (green highlight in Table 5.3), i.e., the sum of the stresses acted by the upper spinel-type oxide scale σ_{co-sp} and lower substrate σ_{co-su}.

These results in Table 5.3 show that the outer spinel layer formed at 800˚C and 900˚C in this work is generally subject to compressive thermal stresses. In general, the magnitudes of thermal stresses in the outer spinel layer are observed less than 1 GPa at 800˚C and 0.5 GPa at 900˚C respectively. This may indicate that for AISI 316L SS oxidized at 800˚C and 900˚C for 6 hours to 96 hours in the air with 0%, 1%, 2% 4% and 8% water vapor, stress relaxation during the cooling process at 900˚C is greater than that at 800˚C. One possibility may account for this observation that plastic deformation after oxidation at 900˚C is of importance to stress relaxation. Furthermore, the outer spinel layer also acts small tensile stresses on the corundum layer. Under the constraint of substrate, the corundum layer formed at 700˚C is subject to compressive stresses; the corundum layer formed at 800˚C and 900˚C are also subject to compressive stresses due to the combined contribution of the substrate and the upper spinel layer.

Table 5.3 Thermal expansion coefficients and thermal stresses evaluated

T	Humidity	Time	$\bar{\alpha}_{co}$	$\bar{\alpha}_{sp}$	$\bar{\alpha}_{ox}$	σ_{sp}	σ_{co-sp}	σ_{co-su}	σ_{co}
(˚C)	(vol.%)	(h)	(10^6 ˚C^{-1})			(GPa)			
700	0	6	9.7	-	-	-	-	-2.287	-2.287
		24	8.8	-	-	-	-	-2.707	-2.707
		48	7.4	-	-	-	-	-3.434	-3.434
		72	7.5	-	-	-	-	-3.354	-3.354
		96	8.2	-	-	-	-	-2.984	-2.984
	1	6	7.7	-	-	-	-	-3.275	-3.275
		24	7.4	-	-	-	-	-3.446	-3.446
		48	7.3	-	-	-	-	-3.483	-3.483

		72	8.4	-	-	-	-	-2.869	-2.869
		96	8.1	-	-	-	-	-3.029	-3.029
	2	6	7.5	-	-	-	-	-3.350	-3.350
		24	7.4	-	-	-	-	-3.434	-3.434
		48	10.0	-	-	-	-	-2.185	-2.185
		72	7.3	-	-	-	-	-3.499	-3.499
		96	9.1	-	-	-	-	-2.555	-2.555
	4	6	10.0	-	-	-	-	-2.180	-2.180
		24	8.9	-	-	-	-	-2.639	-2.639
		48	8.6	-	-	-	-	-2.789	-2.789
		72	8.2	-	-	-	-	-2.962	-2.962
		96	9.2	-	-	-	-	-2.486	-2.486
	8	6	7.4	-	-	-	-	-3.414	-3.414
		24	7.3	-	-	-	-	-3.474	-3.474
		48	9.0	-	-	-	-	-2.578	-2.578
		72	12.0	-	-	-	-	-1.526	-1.526
		96	7.3	-	-	-	-	-3.493	-3.493
800	0	6	8.6	10.3	8.6	-0.363	0.021	-3.201	-3.180
		24	7.3	10.7	7.4	-0.797	0.026	-4.006	-3.980
		48	8.6	9.3	8.6	-0.171	0.004	-3.195	-3.191
		72	7.8	8.3	7.8	-0.117	0.019	-3.674	-3.655
		96	7.7	9.2	8.1	-0.233	0.130	-3.745	-3.615
	1	6	7.4	10.8	7.5	-0.764	0.036	-3.947	-3.911
		24	7.4	12.8	7.4	-1.219	0.015	-3.944	-3.928
		48	7.3	11.7	7.4	-0.954	0.045	-4.001	-3.957
		72	8.1	10.9	8.1	-0.618	0.012	-3.480	-3.468
		96	7.3	12.8	7.5	-1.265	0.053	-4.007	-3.953
	2	6	7.6	9.6	7.6	-0.461	0.009	-3.793	-3.784
		24	7.4	11.1	7.8	-0.750	0.117	-3.939	-3.822
		48	8.3	9.9	8.4	-0.346	0.011	-3.329	-3.318
		72	8.6	9.5	8.8	-0.163	0.055	-3.196	-3.141

		96	8.0	11.4	8.4	-0.703	0.093	-3.509	-3.415
	4	6	7.4	9.0	7.4	-0.366	0.015	-3.943	-3.928
		24	7.4	9.9	7.5	-0.568	0.014	-3.912	-3.898
		48	7.5	12.2	7.6	-1.075	0.052	-3.893	-3.840
		72	7.7	9.5	7.8	-0.383	0.049	-3.749	-3.701
		96	7.3	9.4	7.4	-0.448	0.019	-4.007	-3.988
	8	6	8.8	9.2	8.9	-0.078	0.028	-3.083	-3.056
		24	7.3	9.1	7.4	-0.379	0.013	-3.979	-3.966
		48	7.3	11.9	7.4	-1.021	0.031	-3.995	-3.964
		72	10.2	9.4	9.9	0.105	-0.063	-2.431	-2.495
		96	-	-	-	-	-	-	-
900	0	6	7.3	9.0	7.7	-0.259	0.143	-4.469	-4.326
		24	7.5	9.5	7.9	-0.345	0.150	-4.353	-4.203
		48	7.3	12.3	9.1	-0.701	0.652	-4.491	-3.839
		72	7.3	8.9	7.8	-0.232	0.166	-4.467	-4.302
		96	7.5	8.7	7.8	-0.194	0.132	-4.381	-4.250
	1	6	7.9	8.9	8.1	-0.170	0.060	-4.036	-3.977
		24	7.4	9.0	7.9	-0.237	0.155	-4.408	-4.253
		48	8.1	9.5	8.6	-0.210	0.181	-3.926	-3.745
		72	7.9	8.8	8.2	-0.125	0.127	-4.069	-3.942
		96	7.3	8.6	7.9	-0.173	0.190	-4.481	-4.291
	2	6	7.3	8.4	7.6	-0.176	0.094	-4.469	-4.375
		24	7.4	8.9	7.8	-0.235	0.133	-4.442	-4.309
		48	7.3	8.7	7.8	-0.209	0.159	-4.490	-4.331
		72	7.5	8.9	7.9	-0.226	0.150	-4.368	-4.218
		96	7.4	8.6	7.8	-0.195	0.138	-4.451	-4.313
	4	6	7.3	9.0	7.9	-0.230	0.215	-4.477	-4.262
		24	7.5	9.0	8.3	-0.136	0.288	-4.342	-4.054
		48	7.4	8.8	7.8	-0.231	0.139	-4.451	-4.312
		72	7.3	8.9	7.9	-0.206	0.218	-4.482	-4.264
		96	7.4	9.1	8.1	-0.233	0.228	-4.421	-4.193

	6	9.5	10.3	9.6	-0.169	0.030	-3.081	-3.051
	24	9.2	10.4	9.6	-0.160	0.125	-3.206	-3.081
8	48	7.7	9.6	8.3	-0.295	0.211	-4.208	-3.997
	72	9.4	11.1	10.0	-0.225	0.176	-3.089	-2.913
	96	-	-	-	-	-	-	-

5.3 Residual stress

After isothermal oxidation and cooling process, self-equilibrated stresses are always present between the oxide scales and the substrate, i.e. residual stresses of oxide scales, which is of great interest in this thesis. Therefore, the determination of residual stresses in the oxide scales have been carried out using the classical $\sin^2\psi$ method, which has been introduced profoundly in Section 3.5.2. The residual stresses in the corundum-type oxides formed between 700˚C and 900˚C as well as the ones in the spinel-type oxides formed at 800˚C and 900˚C have been determined respectively. As mentioned in Section 3.5.2, the residual stress level in the corundum-type oxides (Cr_2O_3, Fe_2O_3 and their solid solution oxides) has been studied by selecting the {104} plane family; while the residual stress level in the spinel-type oxides ($MnCr_2O_4$ predominates) has been studied by choosing the {113} plane family. The elastic moduli of each pure component are tabulated in Table 3.2 and the process to calculate the elastic moduli of solid solution oxides are introduced in Appendix 5. This thesis determines the uniaxial stress state of oxides. For polycrystalline oxides, inner uniformity and elastic isotropy are assumed in this thesis. The effects of texture are ignored.

5.3.1 In dry air

Figure 5.5 illustrates the residual stress evolution in the corundum-type and spinel-type oxide scales formed in dry air between 700˚C and 900˚C respectively (Spinel-type oxide layer is absent at 700˚C so that no related data is shown in Figure 5.5.b). As the legends shown in Figure 5.5, the value of “d” denotes the X-ray penetration depth, the residual stress level is thus the average one within the detected zone. It can be observed from Figure 5.5.a that the in-plane residual stresses in the corundum oxides for AISI 316L SS oxidized in dry air for 6 hours to 96 hours between 700˚C and 900˚C are compressive. Figure 5.5.a also shows that the compressive residual stress level in the corundum oxides formed at 900˚C is smaller than that at 700˚C; after 48-hour oxidation, compressive residual stresses in the corundum oxides formed at 800˚C are smaller than those at 700˚C. One possibility accounts for smaller residual stress level at higher temperature for AISI 316L SS oxidized in dry air between 700˚C and 900˚C for 6 hours to 96

hours is that at 900˚C and 800˚C, creep of both AISI 316L and oxide scale is more likely to happen compared with that at 700˚C.

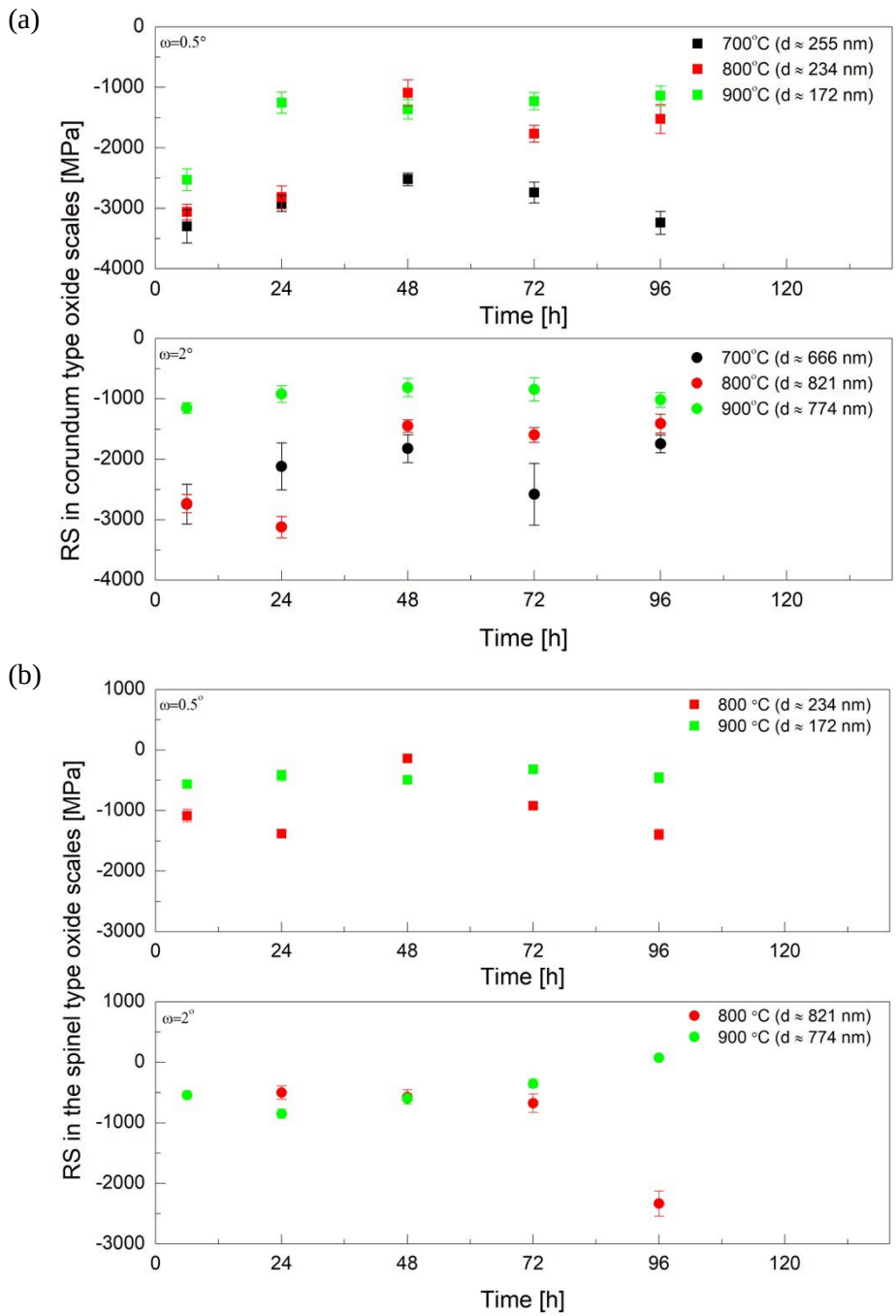

Figure 5.5 Residual stresses in the oxide scales formed in dry air as a function of oxidation time: in corundum-type oxides (a); in spinel-type oxides (b)

For AISI 316L SS oxidized at 700˚C in dry air, compressive residual stresses in the corundum-type oxide scales release first (-3500 MPa to -2500 MPa in the outer part; -3000 MPa to -2000 MPa in the inner part) then accumulate again (-2500 MPa to -3500 MPa in the outer part from 48-hour to 96-hour oxidation; -2000 MPa to – 2500 MPa in the inner part from 48-hour to 72-

hour oxidation) after 48-hour oxidation in regardless of stress relaxation in the inner part after 96-hour oxidation. Considering the difficulty of plastic deformation at 700˚C, one possible mechanism is proposed that stresses may release through microcrack formation and re-accumulate through subsequent new oxide formation [*Schütze, 1997*]. After 96-hour oxidation at 700˚C, the thickness of oxide scale has reached around 1.8 μm (see Table App. 1.1), so the average residual stress in the corundum-type oxide scale should consider the one determined with the X-ray penetration depth of 666 nm. It can thus be observed that compressive stresses in the inner part of corundum-type oxide scale reduce after 96-hour oxidation at 700˚C in dry air. This is due to the formation of wüstite within the inner oxide scale (see Figure 4.13.f). The effect of wüstite on the stress development will be discussed in detail in Section 6.3.2. The formation of wüstite in the inner part of oxide scale and the corresponding stress evolution are formulated as the following: cracking is likely to appear in order to release stresses in the corundum-type oxides at 700˚C in dry air during the initial 48-hour oxidation; if the oxygen inward diffusion is dominant for the new oxide formation within the oxide scale (discussed in Section 4.1.4.1), the crack would thus be repaired, where compressive stresses are possible to accumulate [*Rhines et al., 1970*]; during the self-repair process, chromium content in the inner part, may not be enough to form entire chromia layer (see Figure 4.8), whereby wüstite (wüstite is easy to form in the inner layer where oxygen partial pressure is low) probably forms instead (see Figure 4.13.f); FeO usually shows a better potential to deform so that stresses in the inner part may release, which is in accord to the observation of residual stress relaxation in the inner part after 96-hour oxidation (see Figure 5.5.a).

From Figure 5.5.b, the outermost spinel-type oxides formed at 900˚C keep the same stress level (around 500 MPa) and the stresses in the inner part gradually relax (-1000 MPa to 0 MPa). This indicates that the outermost layer has reached a steady state due to the constrain-free surface. But the inner can be affected by the corundum-type oxide scale. During thin film formation, the nucleation and growth of grains usually lead to compressive stresses while the coalesce of grains into a layer will lead to tensile stresses [*Chason, 2012*]. It can be observed that the surface of oxide scale formed at 800˚C after 96-hour oxidation in dry air consists of relatively large grains or grain clusters (see Figure 4.9). Based on Chason, it is thus deduced that compressive residual stress accumulation in the spinel-type oxide scale after 96˚C at 800˚C ascribes to large grain or grain cluster growth.

Residual stress can be simply regarded as the combined contribution of growth stress and thermal stress. Table 5.4 shows the comparison of residual stress in the corundum-type oxide

scale determined by XRD and calculated by the sum of the corresponding growth stress and thermal stress.

Table 5.4 Comparison of the residual stress calculated by the thermal and growth stress and determined by XRD method (in the corundum-type oxide scales)

T (˚C)	Time (h)	Growth stress (GPa)	Thermal stress (GPa)	Residual stress calculated (GPa)	Residual stress determined by XRD (GPa)	Difference (GPa)
700	6	-2.57	-2.287	-4.857	-2.742	-2.115
	24		-2.707	-5.277	-2.115	-3.162
	48		-3.434	-6.004	-1.821	-4.183
	72		-3.354	-5.924	-2.579	-3.345
	96		-2.984	-5.554	-1.743	-3.811
800	6	0.53	-3.180	-2.650	-2.730	0.080
	24		-3.980	-3.450	-3.121	-0.329
	48		-3.191	-2.661	-1.448	-1.213
	72		-3.655	-3.125	-1.595	-1.530
	96		-3.615	-3.085	-1.408	-1.677
900	6	0	-4.326	-4.326	-1.149	-3.177
	24		-4.203	-4.203	-0.919	-3.284
	48		-3.839	-3.839	-0.812	-3.027
	72		-4.302	-4.302	-0.844	-3.458
	96		-4.250	-4.250	-1.014	-3.236

It can thus be observed from Table 5.4 that for the corundum-type oxide scales formed under the conditions investigated in this work, the compressive residual stresses determined by XRD method are generally smaller than those calculated. The magnitudes of difference between XRD determination and calculation can be obtained for the oxidation of AISI 316L SS oxidized at 700˚C, 800˚C and 900˚C for 6 hours to 96 hours (-2.115 GPa to -4.183 GPa at 700˚C; 0.080 GPa to 1.677 GPa at 800˚C; -3.027 GPa to -3.458 GPa at 900˚C). In the case at 700˚C, it indicates an obvious stress relaxation process, possibly by the formation of micro-cracks (proposed in the previous part of Section 5.3.1) or plastic deformation of substrate during the oxidation and cooling. In the case at 800˚C, stress relaxation by the plastic deformation of substrate is likely to account for this observation. In the case at 900˚C, this may ascribe to the stress relief mainly through the plastic deformation of both the substrate and oxide scale during

the oxidation and cooling, being verified also by the presence of wavy MO/M interface (see Figure 4.10.b and Figure 4.11.a).

In addition, for the oxidation of AISI 316L SS under the conditions investigated in this work, it can be deduced from Table 5.4 that: at 700˚C, both growth stresses and thermal stresses are of importance to the final residual stresses; at 800˚C and 900˚C, considering the growth stresses in the oxide scales are quite small (0.53 GPa and 0 GPa, in Table 5.1), it can thus be considered that for AISI 316L SS oxidized at 800˚C and 900˚C in dry air, thermal stresses developed during the cooling process make more contribution to the final residual stresses than growth stresses developed during the isothermal oxidation.

5.3.2 In humid air

Figure 5.6 - Figure 5.10 display the residual stress evolution in the corundum-type (Cr_2O_3 and/or $(Cr, Fe)_2O_3$) oxide scales formed at 700˚C, 800˚C and 900˚C as well as in the spinel-type (mainly considering $MnCr_2O_4$) oxide scales formed at 800˚C and 900˚C in the air with 0%, 1%, 2%, 4% and 8% water vapor. The effects of water vapor on residual stress within the oxide scales are complex and profound.

At 700˚C (see Figure 5.6)

For the oxidation of AISI 316L SS at 700˚C in the air with 0%, 1%, 2%, 4% and 8% water vapor, stresses developed during the isothermal oxidation and cooling process are both of importance to residual stresses (see Table 5.1 and Table 5.3). After 6-hour oxidation, the residual stresses in the corundum-type oxide scales formed under different humidity show a great distinction, which may be interpreted by the combined effect of growth stress and thermal stress: the relatively low compressive stress levels developed in the 1% and 2% water containing air (-763MPa and -1873 MPa in the outer part; 445 MPa and -1985 MPa in the inner part) may probably ascribe to the tensile growth stresses generated during the oxidation (see Figure 5.3.a); another low compressive stress level developed in the 4% water containing air (-1950 MPa in the outer part and -2142 MPa in the inner part) may be caused by the corresponding low thermal stress (see Table 5.3).

More attention should be paid to the residual stress levels determined under deeper X-ray penetration depths (d: 657 - 792 nm, see the legends in the right side of Figure 5.6), which may provide more information of the average residual stresses within the whole oxide scales as the scale thickening with oxidation time. For AISI 316L SS oxidized at 700˚C in air with different humidity studied in this work, it can be observed that after 48-hour oxidation, the average residual stresses in the corundum-type oxide scale formed in humid air are generally larger than

those formed in dry air (see the right side in Figure 5.6). One hypothetical process accounting for this observation is that: cracks are likely to form within the oxide scales and cracks prefer forming in the presence of water vapor, which can be verified by the fluctuation of mass gain curves (see Figure 4.17.a); in the presence of water vapor, voids are more likely to generate within the oxide scale [*Luo et al., 2018*], which are easy to form cracks when stressed; stresses may release through cracking, probably leading to the decrease of compressive residual stresses in the oxide scales (see the relaxation of compressive residual stress during the initial 24-hour oxidation at 700˚C in the 2%, 4% and 8% water containing air, shown in the right side of Figure 5.6); owing to the self-healing ability of AISI 316L SS during the oxidation, new oxides may form at the sides of crack as well as at the tip and base of the crack; if oxygen inward diffusion is dominant during the self-healing process, lateral growth strains are possible to generate at the position where new oxides form [*Clarke, 2003*], leading to compressive stresses within the oxide scale. Another possibility may also account for this observation (the average residual stresses in the corundum-type oxide scale formed in humid air are generally larger than those formed in dry air): water vapor may enhance the oxygen inward diffusion based on the dissociation mechanism proposed in [*Fujii et al., 1964*]; assuming the inward diffusing oxygen motivates oxide formation at grain boundaries within the oxide scale, stresses may thus develop [*Rhines et al., 1970*].

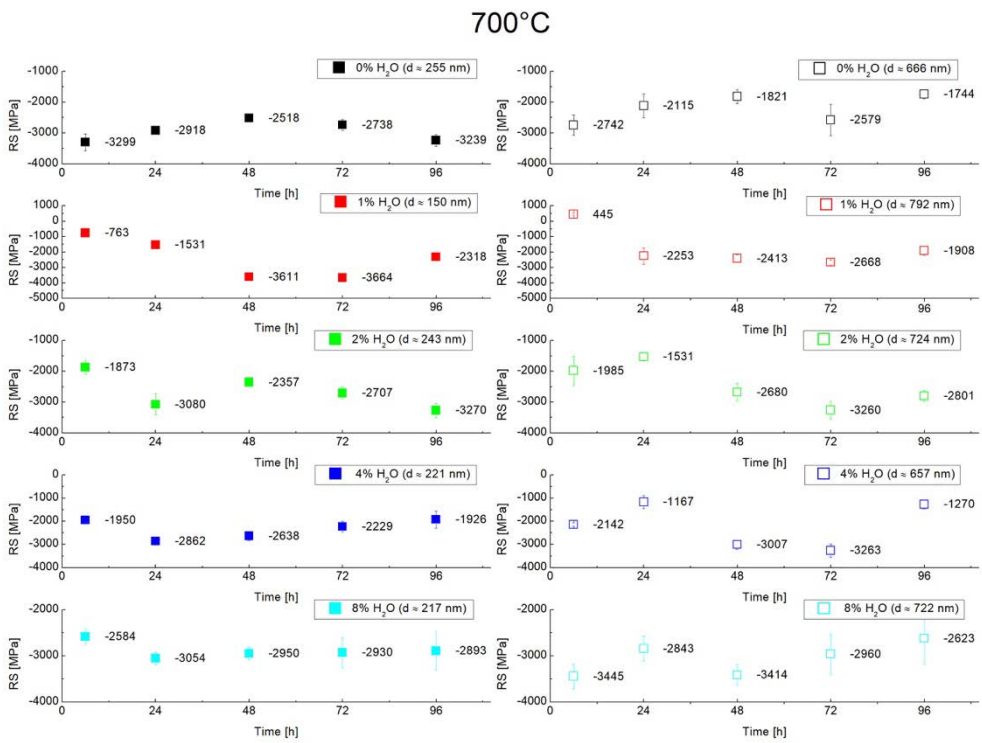

Figure 5.6 Residual stress evolution in the corundum oxide scales formed at 700˚C in the air with different water vapor contents

In addition, for AISI 316L SS oxidized at 700˚C for 6 hours to 96 hours in the air with 0%, 1%, 2%, 4% and 8% water vapor, the trend of residual stress is similar in both the inner and outer parts of corundum-type oxide scale for the oxidation in the air with 0% and 1% water vapor, while apparently different in the air with 2%, 4% and 8% water vapor.

1. The similar trend of stress between two parts may imply the relatively homogeneous distribution of oxide components in the inner part and outer part of oxide scales formed at 700˚C in the 0% and 1% water containing air. (see Figure 4.8 and Figure 4.22).

2. For the oxidation at 700˚C in the 4% and 8% water containing air, the oxide scale tends to form a single layer consisting of three zones with different phases (see Figure 4.24; no SEM image of oxide scale formed at 700˚C in the air with 8% water vapor is illustrated in this thesis, but its oxide component distribution can be comparable with that formed in the air with 4% water vapor, shown in Figure 4.32.a). Combining the X-ray penetration depths displayed in the legends of Figure 5.6 with the thicknesses of oxide scales listed in Table App. 1.1, it can be deduced that for the oxide scales formed at 700˚C in the 4% and 8% water containing air, the outermost zone with the X-ray penetration depth of around 200 nm contains the corundum-type oxides (Cr_2O_3 and $(Fe, Cr)_2O_3$, see Figure 4.32.a); the zone with the depth of around 700 nm represents the transition one between the outermost and intermediate zones, where iron rich oxides and metallic compounds ($(Fe, Cr)_2O_3$ and $FeNi_3$, see Figure 4.32.b) are present; according to the quantitative phase analysis with the X-ray penetration depth of around 2 μm (see Figure 4.32.c), more wüstite and hematite can be observed in the intermediate zone of oxide scale. Hence, the reason of distinct trend between the outer and inner parts may be that the inner part (the zone that "inner part" represents may probably vary from the intermediate zone to the transition zone between the outer and intermediate zones as the oxide scale thickening) may be influenced by the development of oxide component distribution: wüstite may first predominate and facilitate stresses to release by plastic deformation (detailed discussion will be done in Section 6.3.2), which probably accounts for the stress relief in the inner part after 24-hour oxidation at 700˚C in the air with 4% and 8% water vapor (see the right side of Figure 5.6); stress re-accumulation in the inner part after 48-hour oxidation at 700˚C in the air with 4% and 8% water vapor may possibly be the result of iron rich oxide (hematite or Fe-rich $(Cr, Fe)_2O_3$) formation within the oxide scale (see Figure 4.32.a-2), since hematite usually relies on inward growth [*Saunders et al., 2008*] which may cause stress by forming new oxides at grain boundaries in the transition zone [*Rhines et al., 1970*]; the apparent stress relaxation after 96-hour

oxidation at 700˚C in the 4% and 8% water containing air can be deduced as the result of crack formation in the oxide scales, which can be confirmed by Figure 4.17.a.

3. For the oxidation at 700˚C in the 2% water containing air, it can be observed that cracks generate more frequently than those in the 0% and 1% water containing air (see Figure 4.17.a), which leads to the constant self-repair process during the oxidation; so, the different trend of residual stress between the inner part and outer part of oxide scales formed at 700˚C in the air with 2% water vapor may be attributed to the complicated process of randomly occurring cracking and concomitant healing. Moreover, considering that for the initial 72-hour oxidation of AISI 316L SS in the 2% water containing air, the similar trends of residual stress (see the right side of Figure 5.6) and phase constituents (see Figure 4.32.a) can be observed with those in the 4% and 8% water containing air. It can thus be deduced that the mechanism proposed for the residual stress evolution in the 4% and 8% water containing air may be also appropriate to explain the residual stress evolution in the 2% water containing air for the initial 72-hour oxidation.

At 800˚C (see Figure 5.7 and Figure 5.8)

It has been observed that the growth stress is less significant to the determination of residual stress after oxidation of AISI 316L SS at 800˚C in dry air, because its value is nearly zero (see Table 5.1). However, for AISI 316L oxidized at 800˚C in the 2% and 8% water containing air, growth stresses developed during the isothermal oxidation may bring into play for residual stresses, which can be easily observed from the ones determined after short-term oxidation (e.g. 6 hours in this work), i.e., that the residual stress levels are relatively low (-1746 MPa and -2546 MPa) in the corundum-type oxide scales grown at 800˚C for 6 hours in the air with 2% and 8% water vapor are probably attributed to the tensile growth stresses developed during the isothermal oxidation.

It should be noted here that the residual stresses determined with the X-ray penetration of around 200 nm (the left sides of Figure 5.7 and Figure 5.8) may reflect more information of stress level within the oxide grains on the surface because the sizes of the surface oxide grains formed at 800˚C in this work are comparable with these detected depths (see Figure 4.38).

For the oxide scale formed at 800˚C in the 1% water containing air, the growth stress of which is around 0 GPa according to Table 5.1, the residual stress evolution in the corundum-type oxide scale has the identical trend with the thermal stress evolution (see Table 5.3); the residual stress determined after 6-hour oxidation does not follow this trend, which is supposed to be caused by the inaccuracy of the residual stress determination in the too thin oxide scale (≈ 75 nm, Table

App. 1.1) after short-term oxidation. The similar phenomenon has also been observed in the spinel-type oxide. It can thus be summarized that thermal stresses play an important role in the determination of residual stresses in the oxide scales formed at 800˚C in the air with 1% water vapor (especially for 24 hours to 72 hours).

For the oxide scale grown at 800˚C in the 2% water vapor, it can be observed from Figure 5.7 and Figure 5.8 (the right sides) that residual stresses develop in a similar trend for both the corundum-type and spinel-type oxide scales before 96-hour oxidation. After 96-hour oxidation, the suddenly increased compressive stress appears in the corundum-type oxides with stresses relax in the spinel-type oxides. The reasons for this distinct trend of residual stress in these two layers are as follows: more $(Fe, Cr)_2O_3$ is observed in the corundum-type oxide scale (see Figure 4.32.b-2) after 96-hour oxidation, which causes lateral growth strains within the oxide scale [*Srolovitz et al., 1984, Clarke, 2003*] and thus cause compressive stresses; more magnetite is observed in the spinel-type oxide scale after 96-hour oxidation, which may improve the creep ability of the spinel oxide scale (discussed in detail in Section 6.3.1). Moreover, stress relaxation can be seen from Figure 5.7 in the outer part of corundum-type oxide scale after 48-hour oxidation; the iron and nickel metallic compound ($FeNi_3$) is observed to be oxidized into hematite (see Figure 4.32.b-1); considering the growth of hematite usually relies on the oxygen inward diffusion [*Saunders et al., 2008*], it can thus be assumed that microcracks may generate in the outer part of the corundum-type oxide scale so as to create the diffusion path for oxygen and stresses may in turn release through microcracks.

For the oxidation at 800˚C in the air with 4% and 8% water vapor, large compressive stress is present in the outer part of spinel-type oxide scale after 6-hour oxidation, which can be deduced to ascribe to the formation of the spinel-type oxide grains clusters on the surface, since grain formation on the surface usually causes compressive stresses and grain coalescence into a layer usually causes tensile stresses [*Chason et al., 2002*]; so the subsequent stress relaxation in the outer part of spinel-type oxide scale after 24h is due to that the oxide grains coalesce into an oxide layer.

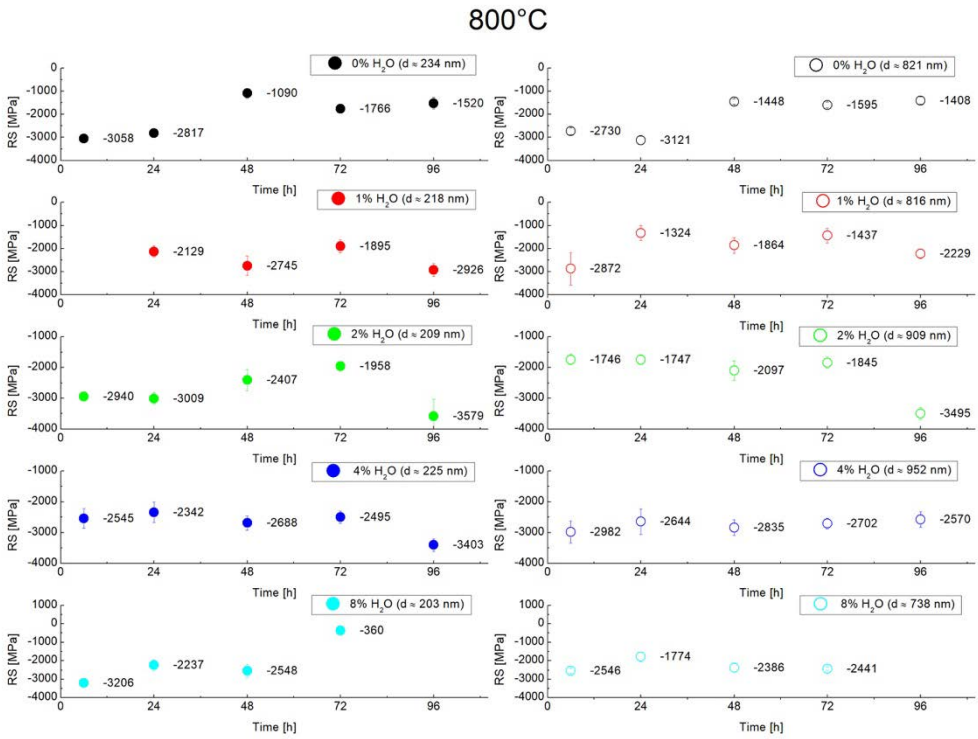

Figure 5.7 Residual stress evolution in the corundum oxide scales formed at 800˚C in the air with different water vapor contents

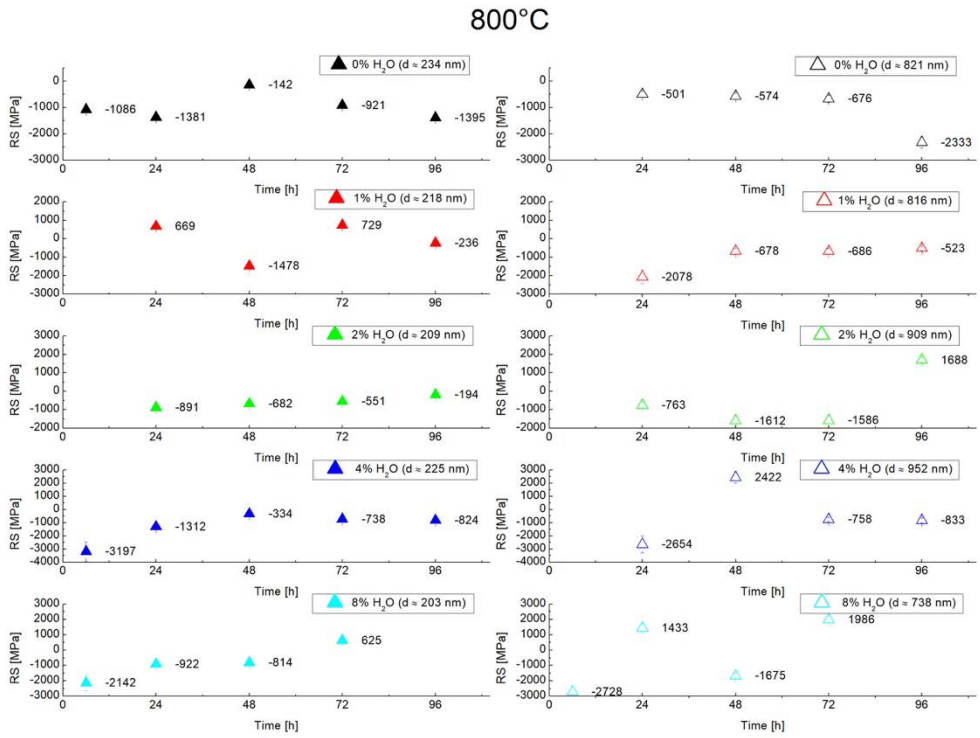

Figure 5.8 Residual stress evolution in the spinel oxide scales formed at 800˚C in the air with different water vapor contents

Now considering the residual stress evolution in the inner part of spinel-type oxide scale formed at 800˚C in the air with 4% and 8% water vapor (navy-blue and sky-blue points at the right side of Figure 5.8), the trend of "S" in shape can thus be observed. Two possible mechanisms can be assumed to interpret these two residual stress evolutions respectively. For the oxidation of AISI 316L SS at 800˚C in the 4% water containing air, $FeNi_3$ is observed to be oxidized into hematite after 48-hour oxidation (see Figure 4.32.b-2) which indicates the formation of microcracks (the same mechanism has been proposed in the previous part "at 800˚C" in 5.3.2) and compressive stress can thus release; the subsequent stress re-accumulation after 72-hour oxidation may probably ascribe to the formation of new spinel-type oxides (see Figure 4.32.b-2. For the oxidation of AISI 316L SS at 800˚C in the 8% water containing air, $FeNi_3$ is observed to be oxidized into hematite after 24-hour oxidation (see Figure 4.32.b-1); since the growth of hematite usually relies on the oxygen inward diffusion [*Saunders et al., 2008*], it can thus be assumed that the diffusion path for oxygen may be created by microcracks within the oxide scale; the tensile growth stress may also promote the crack formation (see Figure 5.2.b); hence, the compressive stress relaxation after 24-hour oxidation is supposed to be as the result of microcrack formation; after 48-hour oxidation, new spinel-type oxide formation (see Figure 4.23.b-1) probably accounts for the stress re-accumulation; breakaway oxidation occurs after 72-hour oxidation at 800˚C in the 8% water containing air, local spallation is observed at the edge of the specimen oxidized at 800˚C for 72 hours in the air with 8% water vapor (see Figure 6.3)., which may lead to the compressive stress relaxation.

At 900˚C (see Figure 5.9 and Figure 5.10)

The cases without breakaway oxidation are considered first, i.e., oxidation of AISI 316L SS at 900˚C in the air with 2% and 4% water vapor (Section 5.3.1 has discussed the case without breakaway oxidation in dry air).

1. It can be observed in common that the trends of stress evolution are identical in the outer spinel-type oxide layer and inner corundum-type oxide layer for the oxidation of AISI 316L SS in the air with 2% water vapor (green points in Figure 5.9 and Figure 5.10), which implies a good connection between these two layers; and the compressive residual stresses in these two layer show a trend of relief before 96-hour oxidation, which can be viewed as the result of the gradual creep of both the substrate and oxide scale. After 96-hour oxidation, residual stress re-accumulation can be observed in both the corundum-type oxide scale and the spinel-type oxide scale; in the corundum-type oxide scale, more hematite is present after 96-hour oxidation (see Figure 4.32.c-1 and Figure 4.32.c-2), the growth of which probably counts on the oxygen inward diffusion [*Saunders et al., 2008*], and generation of lateral

stress strain and concomitant stress accumulation [*Srolovitz et al., 1984, Clarke, 2003*] are thus assumed to exist during the formation of new hematite within the oxide scale; in the spinel-type oxide scale, considering the fact that the presence of magnetite may benefit the creep of the oxide scale at 900˚C (discussed in Section 6.3.1), the re-accumulation of compressive residual stress after 96-hour is thus likely due to the decrease of magnetite (see Figure 4.32.c-1 and Figure 4.32.c-2).

2. For the oxidation of AISI 316L SS at 900˚C in the air with 4% water vapor, it can be observed that compressive residual stresses gradually release as oxidation continues in the outer part of corundum-type oxide scale with an exception that stress re-accumulates after 48-hour oxidation; one possibility accounts for this stress evolution is that chromia near the surface may lose due to the evaporation effect in the presence of water vapor, which may cause stress relaxation in the outer part of the corundum-type oxide scale (chromia dominates at 900˚C, see Figure 4.32.c-1); more chromia is observed after 48-hour oxidation so that stresses may accumulate. In the spinel-type oxide scales formed at 900˚C in the air with 4% water vapor, it can be observed that residual stresses tend to release upon oxidation, where the driving force is supposed to be the creep of both the substrate and the oxide scale (wavy MO/M interface can be observed, see Figure 4.30)

Now considering the case with breakaway oxidation, i.e., oxidation of AISI 316L SS at 900˚C in the air with 1% and 8% water vapor.

For AISI 316L SS oxidized at 900˚C in the 1% and 8% water containing air, breakaway oxidation happens after 24-hour and 6-hour oxidation respectively (Figure 4.17.e). It can be observed that residual stresses do not release rapidly as breakaway oxidation appears, especially for the oxidation of AISI 316L at 900˚C in the air with 1% water vapor (see red points in Figure 5.9 and Figure 5.10), which implies that chemical attacks are dominant during the incubation period of breakaway oxidation under this condition. It can be realized that compressive stresses may release first through plastic deformation of both the substrate and oxide scale and subsequently through cracking or spalling (e.g., debonding of the two layers in the oxide scale formed at 900˚C for 24 hours in the air with 8% water vapor can be observed, as shown in Figure 6.5; local spallation can also be observed on the oxide scale formed at 900˚C for 96 hour in the air with 1% water vapor).

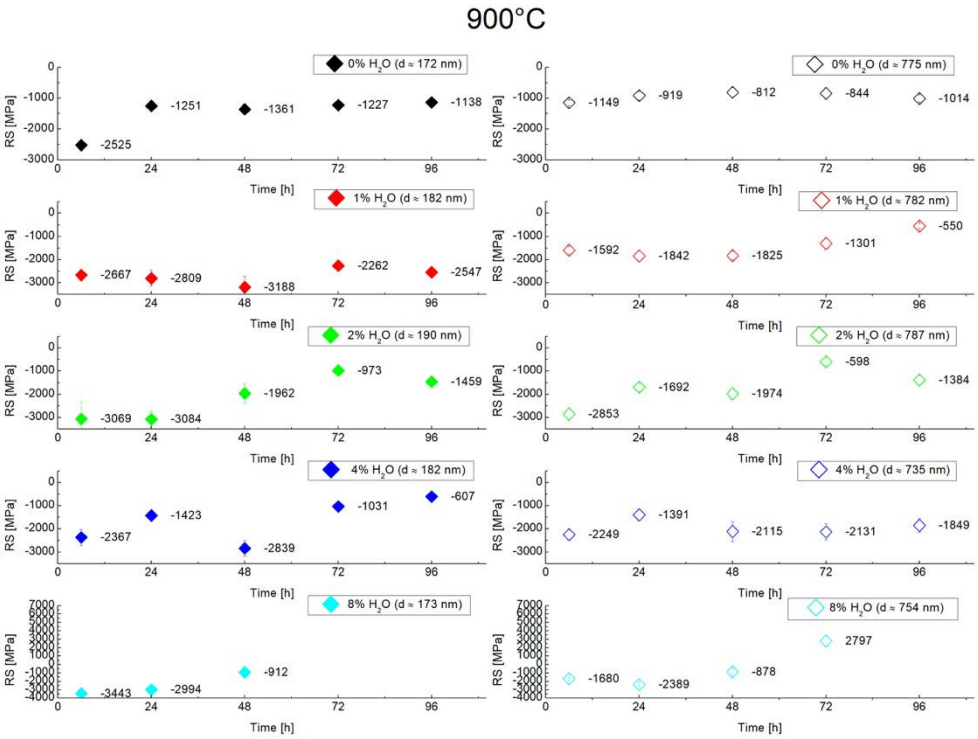

Figure 5.9 Residual stress evolution in the corundum oxide scales formed at 900˚C in the air with different water vapor contents

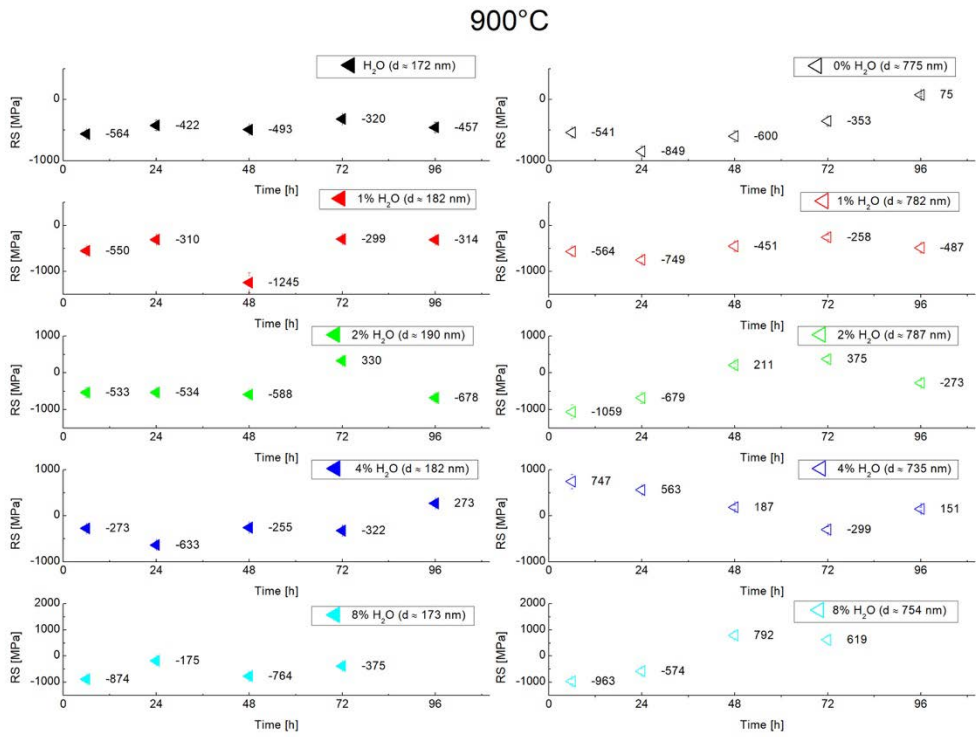

Figure 5.10 Residual stress evolution in the spinel oxide scales formed at 900˚C in the air with different water vapor contents

5.4 Discussion

In the previous sections of this chapter, some discussions have already been conducted in regard with the effects of thermo-chemo-mechanical conditions. The following will mainly discuss the phenomena related to the thermomechanical behaviors. The synthetic analysis will be done in Chapter 6.

5.4.1 Deformation

Elastic deformation of either the substrate or the oxide scale is the first response to stress accumulation. However, when the stored elastic energy within the oxide scale reaches a critical one, stress relief will be conducted in other ways, such as plastic deformation, cracking, spalling etc. Normally during the oxidation of steels at high temperatures, plastic deformation of the substrate plays a key role in the reduction of stress generated without any macroscopic material separations. Moreover, creep of oxides may also be present (see Section 2.4.2.1).

One of the interesting phenomena in this work is the formation of the wavy MO/M interface at 900˚C, which can be observed in Figure 4.10, Figure 4.28 - Figure 4.30. This is supposed to appear during the cooling process after the oxidation at 900˚C, where the thermal stress is the driving force. At the M/MO interface, tractive compressive and tensile stresses act on the oxide and substrate, leading to a wavy interface, which is schematically displayed in Figure 5.11 based on the work of Evans [*A. G. Evans, 1983*].

In this simplified model, an approximate expression to describe the stress normal to the interface as [*A. G. Evans, 1983*]:

$$\sigma_n = \{\Delta\varepsilon[1/\kappa + E_{\mathrm{ox}}(1+v_{\mathrm{m}})(r/R_{\mathrm{s}})][\sin(2\pi y/\lambda)]\}/(1+r/x), \qquad (5.12)$$

Where $\kappa = [(1+v_{\mathrm{ox}})/(2E_{\mathrm{ox}}) + (1-2v_{\mathrm{m}})/E_{\mathrm{m}}]$; $\Delta\varepsilon$ is the strain difference between the oxide and substrate; λ and r the wavelength and amplitude of the interface respectively; R_{s} the radius of curvature of the surface; y the location along the interface; x the thickness of the oxide scale.

According to Equation (5.12), the interface stresses increase with decreasing the amplitude of the interface. That is the reason why the good adherence may be present for the MO/M interface with a marked roughness. In the premise that no serious debonding happens, the oxide scale and substrate with a good ability of plastic deformation is beneficial for the wavy interface formation. In this work, water promotes the generation of vacancies or vacancy clusters [*Luo et al., 2018*], probably improving the creep ability of oxides [*Schütze, 1997*]. Simultaneously, the increased outward cations leave vacancies behind in the substrate, which may enhance the

plastic deformation of the substrate. Therefore, for AISI 316L SS oxidized at 900˚C in this work, the wavy interface prefers forming in humid air and the thermal stress during the cooling is a kind of external loading to motivate the tractions of both substrate and oxides. It should be noted here that wavy interface may be present for AISI 316L SS at 900˚C in dry air (see Figure 4.10) but the morphology of the oxide scale cross-section can also be influenced by internal oxidation.

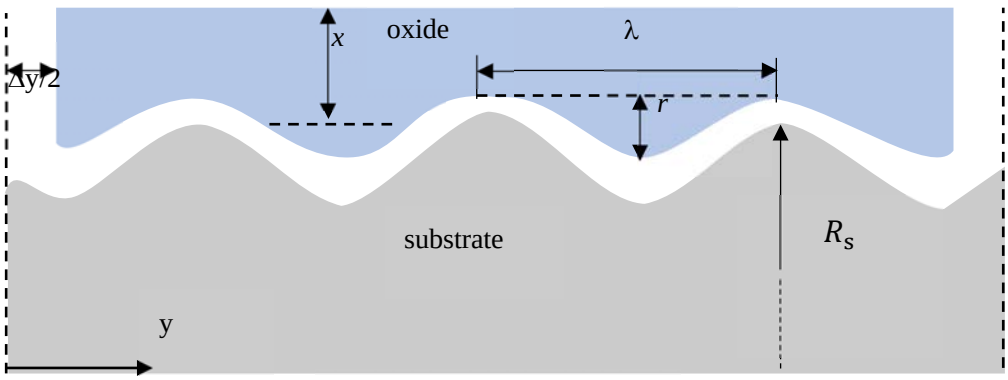

(a) Unconstrained

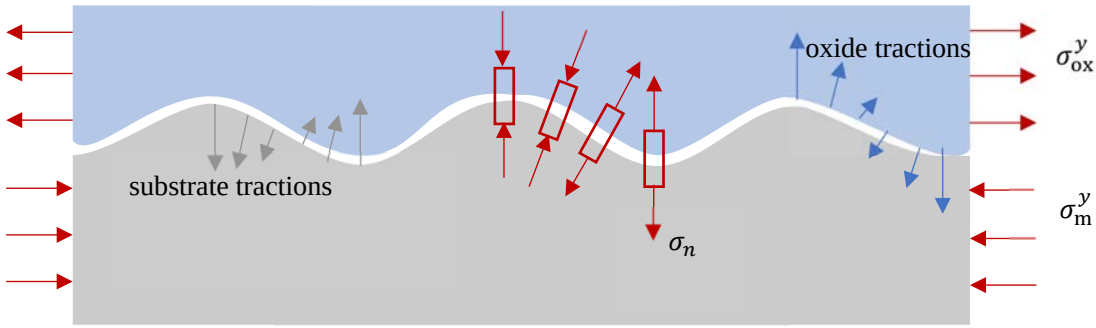

(b) Displacement continuity

*Figure 5.11 Schematic of the stress distribution at a wavy M/MO interface [*A. G. Evans, 1983*]*

5.4.2 Damages

Evans has analyzed the possible damages of oxide scales qualitatively [*Evans, 1988*], and he has divided them into two situations concerning different stress states within the oxide scales, as shown in Figure 2.20. The stresses developed during the oxidation have been investigated in Section 5.1, indicating that the oxide scales may be subject to either compressive or tensile stresses during the oxidation for AISI 316L SS oxidized between 700˚C and 900˚C in the air with different water contents. The possible damages expressed in this thesis generally refer to cracks, debonding (local separation of two parts within the oxide scale or at the M/MO interface but without oxide peeling, similar to “detachment”, e.g., Figure 5.12), local spalling or spalling

(breakdown of oxide scale, e.g., Figure 6.3) and delamination (separation of laminar oxide scale, e.g., Figure 6.4).

5.4.2.1 Under tension

Cracks is derived from the physical defects in the oxide scales under stress [*Hancock et al., 1988*]. For instance, tensile stresses develop during the oxidation of AISI 316L SS at 700˚C in the air with 1% and 2% water vapor. Cracking can be observed through their mass gain curves, as shown in Figure 4.17.a.

In the regime of linear elasticity, the crack forming stress at defects can be expressed as [*Schütze, 1997*]:

$$K = \sigma_{\mathrm{ox}}\sqrt{\pi c}f, \tag{5.13}$$

where K is the stress intensity factor; f a factor related to the geometry ($f \approx 1$); c the half length of the defect within the scale or the whole length of the defect at the surface.

In practice, various defects co-exist in the oxide scale. Hancock and Nicholls have established a composite defect model; To determine c for the composite defect, they have successfully worked it out using the standard technique (PD 6493) [*Hancock et al., 1988*], where the stress intensity factor is normally attributed to three aspects, given by:

$$K = \sqrt{(K_{\mathrm{I}}^2 + K_{\mathrm{II}}^2) + (1 + v_{\mathrm{ox}})K_{\mathrm{III}}^2}, \tag{5.14}$$

where K_{I} is the stress intensity factor from tensile stress; K_{II} the one from shear stress normal to the tip of the crack; K_{III} the one parallel to the tip of the crack.

The critical stress intensity factor for cracking formation is called the fracture toughness K_{c}, which can be described in regard with the critical surface energy γ_{c} (the intrinsic surface energy γ_{i}) and the effective elastic modulus of oxide E_{ox}^*, as:

$$K_{\mathrm{c}} = \sqrt{(\gamma_{\mathrm{c}}E_{\mathrm{ox}}^*)}/\sqrt{1 - v_{\mathrm{ox}}^2} = \sqrt{2\gamma_{\mathrm{i}}E_{\mathrm{ox}}}. \tag{5.15}$$

When the value of tensile stress reaches a critical one, the crack growth occurs. For a pure elastic tension loading, the condition below is then satisfied:

$$K_{\mathrm{I}} \geq K_{\mathrm{Ic}}, \tag{5.16}$$

where K_{Ic} is the critical stress intensity factor, i.e., the fracture toughness of model I. And the critical strain ε_{c} for through-scale cracking is now given by:

$$\varepsilon_{\mathrm{c}} = K_{\mathrm{Ic}}/\left(E_{\mathrm{ox}}\sqrt{\pi c}f\right). \tag{5.17}$$

When the creep behavior of oxide exists, Equation (5.17) is also appropriate if the deformation map combined (see Figure 2.19) to evaluate the critical creep strain rate $\dot{\varepsilon}_c^{cr}$ at the critical stress σ_c.

Therefore, within the elastic regime, it can be simply thought that the critical strain for through-scale cracking is determined by the size of defects in a given oxide scale under tensile loading. Comparing the mass gain curves obtained from the oxidation at 700˚C in the 1% and 2% water vapor in Figure 4.17.a, for the oxide scales under tension, cracks generate more frequently in the case with more water vapor (here, 2% water vapor). It has been known that water vapor facilitates the formation of vacancies as well as the vacancy clusters [*Luo et al., 2018*], hence the size of vacancy defects may become larger if more water is introduced. Qualitatively, it can be deduced that for AISI 316L oxidized at 700˚C, water vapor may promote the formation of cracks within the oxide scales under tensile stresses.

5.4.2.2 Under compression

According to the description of Evans [*Evans, 1988*], for the oxide scale which is subject to the tensile stress, it is not easy to effect spallation. While under compressive stress, debonding-like phenomena such as the crack along the M/MO interface, scale buckling etc. may lead to the final spalling [*Evans, 1989*]. Evans has proposed the oxide scale under compressive stresses may suffer spalling in two routes, i.e., wedging process and buckling process [*Evans, 1988*].

Wedging process

This form of spallation usually happens to the oxide scale with good adherence to the substrate or quite thick oxide scales [*Evans, 2005*]. For instance, wedging is likely to happen during the cooling process for AISI 316L SS after oxidation at 700˚C in the 1% water containing air, as illustrated in Figure 4.22. The development in detail can be expected as the following: a shear stress induced crack first forms through the oxide scale; subsequently the sliding of the oxide motivated by the sustained compressive stress acts along the shear surface, with an out-of-plane tensile stress accordingly developed; as a result, a crack parallel to the M/MO interface generates, which promotes the spalling when meeting another through-scale crack or propagating into the oxide layer.

For AISI 316L SS oxidized at 700˚C in the air with 1% water vapor, the morphology of the oxide scale cross-section implies the presence of wedging process (see Figure 4.22); since oxide scale formed under this condition is subject to tensile growth stresses (see Table 5.1), wedging process is likely to occur during the cooling process. In addition, according to Figure 4.22, oxides can be observed to form at the base of the lateral crack at the MO/M interface, which

would hinder the separation of the oxide scale; this probably indicates the self-repair process of oxide scales under this condition.

Buckling process

For the strong oxides with weak adherence, spalling often occurs as buckling forms, such as chromia, which has been reported several times [*Dorcheh et al., 2018, Sun et al., 2008, Zhong et al., 2012*].

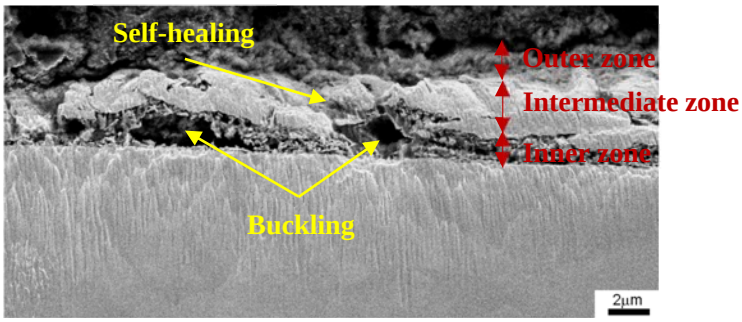

Figure 5.12 Buckling presentation for AISI 316L SS oxidized at 700˚C for 48 hours in the air with 4% water vapor

In this thesis, buckling can be observed for AISI 316L SS after 48-hour oxidation at 700˚C in the 4% water containing air, illustrated in Figure 5.12. As introduced in Section 4.2, the oxide scale formed in this case is regarded consisting of a single layer with three zones rich in different components, the growth mechanism of which has been proposed in Section 4.2.5.5. It should be noted here that the intermediate zone contains more metal deficit iron oxides with Fe-Ni metallic compounds, which shows that the oxide scale is relatively strong.

The buckling process can be explained by Figure 5.13. It derives from a crack-like defect at the M/MO interface, seen in Figure 5.13.a. A crack along the interface forms under the shear stress with Equation (5.16) satisfied, the criterion of which can be given by [*EVANS et al., 1993*]:

$$-\varepsilon_{\mathrm{c}}^{\mathrm{i}} = \left[K_{\mathrm{Ic}}/\left(\sqrt{\pi c}f\right)\right]\{[(1 + r/t_{\mathrm{ox}})(1 + v_{\mathrm{ox}})]/2E_{\mathrm{ox}}\}, \tag{5.18}$$

where $\varepsilon_{\mathrm{c}}^{\mathrm{i}}$ is the critical strain for the beginning of debonding; r the amplitude of interfacial roughness. The critical compressive strain $\varepsilon_{\mathrm{c}}^{\mathrm{b}}$ to activate the buckling can be expressed as [*Timoshenko, 1936*]:

$$-\varepsilon_{\mathrm{c}}^{\mathrm{b}} = [1.22(t_{\mathrm{ox}}/R)^2]/(1 - v_{\mathrm{ox}}^2), \tag{5.19}$$

where R is the radius of the detachment area.

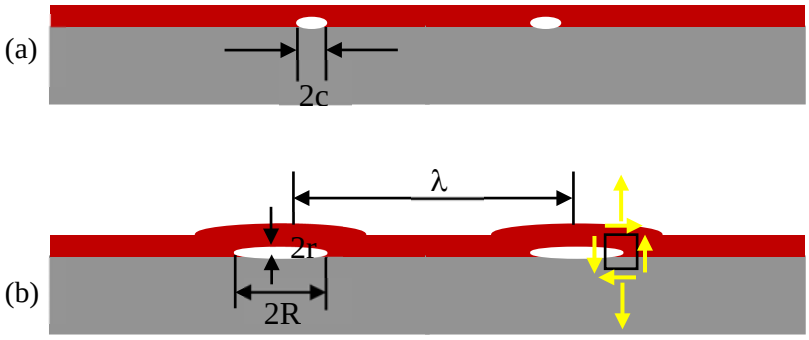

Figure 5.13 Schematic presentation of buckling process

It can also be noted in Figure 5.13.b that a kink stress concentration occurs at the boundary line of the debonding zone, where the tensile stress perpendicular to the interface can be viewed as the dominant driving force for the detachment propagation [*Schütze, 1997*]. Hence the kink stress σ_{k} can be given by [*Evans et al., 1989a, Evans et al., 1989b*]:

$$\sigma_{\mathrm{k}} = [1.22E_{\mathrm{ox}}(t_{\mathrm{ox}}/R)^2]/(1-v_{\mathrm{ox}})^2. \tag{5.20}$$

The crack parallel to the interface may deflect towards to the surface if its length approaches a critical one $R_{\mathrm{c}}^{\mathrm{s}}$, and spalling will accordingly happen at the tip of this crack, which can be calculated by [*A. G. Evans, 1983*]:

$$R_{\mathrm{c}}^{\mathrm{s}} = 1.9t_{\mathrm{ox}}(E_{\mathrm{ox}}/\sigma_{\mathrm{ox}})^{1/2}. \tag{5.21}$$

At this time, the critical stain within the oxide for spallation can be obtained by [*Evans et al., 1989b*]:

$$-\varepsilon_{\mathrm{c}}^{\mathrm{s}} = \sqrt{2\gamma_{\mathrm{f}}^{\mathrm{i}}/[t_{\mathrm{ox}}E_{\mathrm{ox}}(1-v_{\mathrm{ox}})]}, \tag{5.22}$$

where $2\gamma_{\mathrm{f}}^{\mathrm{i}}$ is the fracture energy of the M/MO interface directly influenced by the aggregation of interfacial defects [*S. Baleix, 2002*] and given by [*Robertson et al., 1990*]:

$$\gamma_{\mathrm{f}}^{\mathrm{i}} = \gamma_{\mathrm{i}}[1+(0.1E_{\mathrm{ox}}r)/(2\gamma_{\mathrm{i}}\lambda)]\left[1-\left(A_{\mathrm{sep}}/A_0\right)\right], \tag{5.23}$$

where γ_{i} is the intrinsic surface energy; A_0 the initial surface without any separations; A_{sep} the surface with the delamination or separation situated. Robertson calculated some correlated mechanical parameters from atomistic data, as listed in Table 5.5.

*Table 5.5 Surface fracture energy and fracture toughness for selected oxides at room temperature [*Robertson et al., 1990*]*

Oxide	**Cr_2O_3**	**Fe_2O_3**	**FeO**	**Fe_3O_4**	**$FeCr_2O_4$**	**$MnFe_2O_4$**	**SiO_2**
γ_i (J/m^2)	5.8	6.0	3.0	4.5	5.0	3.0	4.4
K_{Ic} (MPa•m$^{1/2}$)	1.8	1.6	0.9	1.4	1.5	0.8	0.9

For AISI 316L SS oxidized at 700˚C for 48 hours in the air with 4% water vapor, shown in Figure 5.12, the thickness of the oxide scale is around 8 μm. Assuming the oxide scale comprises chromia which suffers the total compressive stress of -5.1 GPa (-2.5 GPa from the oxidation and -2.6 GPa from cooling), the critical radius of debonding area for spalling can thus be evaluated through Equation (5.21), i.e., about 110 μm. This value is far larger than the one observed, indicating that no spallation happens in this case, which is in accord to the reality. Now considering the case with breakaway oxidation occurred, e.g., the oxide scale formed at 900˚C for 24 hours in the 8% water containing air, the thickness is observed through SEM, i.e., around 6 μm (see Figure 6.5). The inner oxide scale consists of chromia which is subject to the compressive stress of -3 GPa during the cooling process (This is an extreme situation, i.e., the highest temperature (900˚C) and the largest humidity (8%) investigated in this work, where the creep of both the oxide and substrate may be relatively serious compared with other situations. So, the plastic deformation has to be considered during the growth stress analysis. The value of growth stress (4.47GPa) by elastic analysis is probably invalid. Therefore, the contribution of thermal stress is only considered here.). Similarly, the critical radius for this condition is thus worked out as 110 μm. This calculated value is so quite large that for AISI 316L SS oxidized at 900˚C for 24 hours in the air with 1% water vapor, no spalling is really observed as well. This suggests that breakdown of oxide scale relies on the accumulated process of interface defects where breakaway oxidation may probably promote the growth of these defects through fast oxide generation.

Moreover, with the assumption that chromia layer is subject to the compressive stress of -2 GPa, the critical (t_{ox}/R) for the onset of buckling can be estimated according to Equation (5.19), i.e., 0.073. It can be deduced that when the size of defect at the M/MO interface reaches 200 nm for example, buckling probably happens when the thickness of chromia layer reaches 15 nm. This indicates that it is easy for AISI 316L SS to form buckling. In the presence of water vapor, voids are probably promoted in the oxide scale [*Luo et al., 2018*] and cation outward diffusion may thus be enhanced. The flux of vacancies caused by cation outward diffusion migrates towards the substrate and vacancies possibly condense out into voids near the MO/M interface

[*Hou, 2016*], which may facilitate compressive stresses to relax, possibly in the form of buckling. It should be noted here that deformation is another important form of stress relaxation especially at higher temperatures (e.g., oxidation of AISI 316L SS at 900˚C in this work), which may be the reason that buckling is not present in the oxide scale formed at 900˚C according to the observation by SEM.

Similarly, if assuming that the compressive stress is mainly attributed to the cooling process, the critical temperature difference T_c^B to activate the spallation through buckling can thus be given by [*Wells et al., 1975*]:

$$T_c^B = (1/\Delta\alpha)\sqrt{[(1.052t_{ox}^4)/R^4] + [(1.041\gamma_f)/(E_{ox}t_{ox})]} \tag{5.24}$$

Based on Equation (5.24), the relationship $T_c^B \propto {t_{ox}}^{-1/2}$can be obtained. T_c^B decreases with increasing the thickness of oxide scale, from which it can be deduced that to satisfy Equation (5.24) (spalling may happen during cooling process), the thickness of oxide scale is of importance at a given temperature. In this thesis, local spalling or delamination of oxide scales is observed in the following cases for AISI 316L SS: after 72-hour oxidation at 800˚C in the air with 8% water vapor; after 72-hour oxidation at 900˚C in the air with 1% and 8% water vapor respectively. It can be observed from the mass gain curves shown in Figure 4.17 that no spallation is present during the isothermal oxidation in these cases. Therefore, spalling can be deduced to occur during cooling. According to Table APP. 1.1, the thicknesses of oxide scales grown in these cases (41 μm, 1.8 μm and 66 μm for AISI 316L after 72h-oxidation at 800˚C in the 8% water containing air, at 900˚C in the 1% water containing air and at 900˚C in the 8% water containing air respectively) are larger than those grown at the same temperature with the same humidity. Qualitatively, it can be assumed that large-size defects may form at the interface as the thick oxide scale forms rapidly in the presence of breakaway oxidation and thus motivate the final breakdown of oxide scale.

5.4.3 Temperature and humidity dependences of residual stress

For AISI 316L SS oxidized in dry air, the levels of residual stress in the corundum-type oxide scales show the temperature dependence. On the whole, residual stresses are smaller in the oxide scales grown at higher temperature. Similar phenomena have also been found in other studies, such as [*Bernard et al., 2002, Liu et al., 2011*].

At 900˚C, cation outward diffusion is proposed to be dominant during the oxidation of AISI 316L SS in this work, the formation of oxide will not lead to large lateral growth strains accordingly unless oxides formed at defects or grain boundaries [*Rhines et al., 1970*]; furthermore, the increased number of thermal vacancies (either Schottky defects or Frenkel pair)

exponentially grows with temperature [*A. V. Roshchin, 2003*], improving the lattice diffusion and thus the creep behavior, so it can be assumed that more stresses can relax at 900˚C through the plastic deformation of both the substrate and oxide scale; therefore, compared with the residual stresses in the oxide scales formed at 700˚C in dry air, smaller compressive residual stresses are present in the oxide scale formed at 900˚C in dry air in this work (see Figure 5.5).

For the oxidation of AISI 316L SS oxidized at 700˚C in dry air in this work, oxygen inward diffusion is supposed to be of great importance (Section 4.1.4.4 and Section 4.2.5.5); during the inward diffusion of oxygen, new oxide formation within the oxide scale may cause lateral growth strains, which probably leads to larger compressive stresses [*Srolovitz et al., 1984, Clarke, 2003*].

However, the situation turns complicated with water vapor introduced. Water vapor has a double-edged effect. The dissociation mechanism may enhance the inward diffusion of oxygen species which may cause lateral growth strains; on the other hand, water vapor may promote the generation of voids, which may benefit stress relaxation by either annihilating voids under stressed or improving creep of the oxide scale [*Schütze, 1997*]. In addition, for AISI 316L SS oxidized in the presence of water, the oxide surface is possible to be influenced by the evaporation of chromium (see the part "at 900˚C" in Section 5.3.2); e.g. the iron-rich oxides become more as chromium-containing volatile forming; if more magnetite (or wüstite) grows on the surface, the plastic property of the oxide scale near the surface is expected to be improved.

5.5 Summary

This chapter centers around the thermomechanical aspect for AISI 316L SS oxidized at 700˚C, 800˚C and 900˚C for 6 hours to 96 hours in the air with 0%, 1%, 2%, 4% and 8% water vapor. The in-plane growth stresses, thermal stresses and in-plane residual stresses in the oxide scales have been studied using the in-situ deflection method, theoretical calculations and XRD method respectively.

- Stress generation

For the oxidation of AISI 316L SS in dry air, the growth stress developed at 700˚C is of significance for the final stress state. Since thermal stresses are more significant at higher temperatures. The growth stress is quite sensitive to humidity. Either compressive or tensile growth stresses can act on the oxide scales formed at 700˚C and 900˚C in the presence of water vapor. The oxide scales formed at 800˚C are subject to tensile stresses during the isothermal oxidation.

Thermal stresses of the outer spinel-type oxide scale grown at 800˚C and 900˚C are compressive. The outer spinel layer acts on the corundum-type oxide scale with a relatively small tensile stress. The corundum-type oxide scale suffers compressive stress during the cooling in total. The thermal stress of corundum-type oxide scales shows sensitivity to the oxidation temperature, i.e., it increases with increasing the temperature.

- Stress release

Stresses relax in several ways for the oxidation of AISI 316L SS at 700˚C, 800˚C and 900˚C in this work. The substrate can deform plastically in the form of dislocation climb or creep. At high temperature, oxides are also likely to deform plastically by Coble creep. Moreover, microcracks generate during the isothermal oxidation and concomitant self-healing of oxides is a stress generation process. Wedging and buckling are observed in the oxide scales grown at 700˚C in the air with 1% and 4% water vapor respectively. But neither of the two conditions saw spalling, due respectively to the oxide self-healing in the first case and the critical condition is not satisfied in the latter case. At higher temperatures, no apparent through-scale cracks, wedging or buckling have been observed before breakaway oxidation. Two possibilities are responsible for that: stress relief mainly counts on the plastic deformation of both the substrate and the oxide scale; cracks have been healed rapidly during oxidation. Spallation of oxide scale relies on the accumulation of interface defects where breakaway oxidation plays a role of promotion.

- Residual stress

In dry air, residual stresses in the corundum-type oxide scales show temperature dependence. In general, water vapor impacts the residual stress evolution within the oxide scales intricately and profoundly. But it can be simply elucidated as following:

About stress relaxation

1. Water may promote void formation, and microcracks can thus easily generate under stress, benefiting the stress release;
2. Vacancies or voids motivated by water facilitate the plastic deformation of oxides.

About stress accumulation

1. At the cracks promoted by water, new oxide formation can cause lateral growth strains, increasing stress levels;
2. Water assisted inward diffusion of oxygen is possible to generate lateral growth strains during the growth of new oxides within the oxide scale, leading to compressive stresses;

3. Water affects oxygen partial pressure within the oxide scale, changing the oxide phase constituent and distribution, and thus affects the stress development (this may also explain the stress relaxation).

5.6 Reference

[A. G. Evans, 1983] A. G. EVANS, G. B. C. A. R. E. D. 1983. A.G.Evans On the mechanical behavior of brittle coatings and layers. *Oxidation of Metals,* 20**,** 193-216.

[A. V. Roshchin, 2003] A. V. ROSHCHIN, V. E. R. 2003. Diffusion of anions and cations in oxide crystal lattices during the reduction and oxidation of metals. *RUSSIAN METALLURGY METALLY C/C OF IZVESTIIA-AKADEMIIA NAUK SSSR METALLY 1,* 2003**,** 1-5.

[Bernard et al., 2002] BERNARD, O., AMIRI, G., HAUT, C., FELTZ, B., HUNTZ, A. & ANDRIEUX, M. 2002. Mechanical and microstructural characterisation of oxide films damage. *Materials Science and Engineering: A,* 335**,** 32-42.

[Birks et al., 2006] BIRKS, N., MEIER, G. H. & PETTIT, F. S. 2006. *Introduction to the high temperature oxidation of metals,* Cambridge University Press.

[Chason, 2012] CHASON, E. 2012. A kinetic analysis of residual stress evolution in polycrystalline thin films. *Thin Solid Films,* 526**,** 1-14.

[Chason et al., 2015] CHASON, E., ENGWALL, A. M., MILLER, C. M., CHEN, C. H., BHANDARI, A., SONI, S. K., HEARNE, S. J., FREUND, L. B. & SHELDON, B. W. 2015. Stress evolution during growth of 1-D island arrays: Kinetics and length scaling. *Scripta Materialia,* 97**,** 33-36.

[Chason et al., 2002] CHASON, E., SHELDON, B. W., FREUND, L. B., FLORO, J. A. & HEARNE, S. J. 2002. Origin of compressive residual stress in polycrystalline thin films. *Phys Rev Lett,* 88**,** 156103.

[Clarke, 2003] CLARKE, D. R. 2003. The lateral growth strain accompanying the formation of a thermally grown oxide. *Acta Materialia,* 51**,** 1393-1407.

[D. Delaunay, 1980] D. DELAUNAY, A. M. H., P. LACOMBE 1980. Mechanical stresses developed in high temperature resistant alloys during isothermal and cyclic oxidation treatments. *Corros. Sci,* 20**,** 1109-1117.

[Dorcheh et al., 2018] DORCHEH, A. S., SCHÜTZE, M. & GALETZ, M. C. 2018. Factors affecting isothermal oxidation of pure chromium in air. *Corrosion Science,* 130**,** 261-269.

[Evans et al., 1989a] EVANS, A. & CANNON, R. Stresses in oxide films and relationships with cracking and spalling. Materials Science Forum, 1989a. Trans Tech Publ, 243-268.

[Evans et al., 1989b] EVANS, A. G. & HUTCHINSON, J. W. 1989b. Effects of non-planarity on the mixed mode fracture resistance of bimaterial interfaces. *Acta Metallurgica,* 37**,** 909-916.

[EVANS et al., 1993] EVANS, H., MITCHELL, G., LOBB, R. & OWEN, D. 1993. PrOC. R. Soc.(London) A.

[Evans, 1988] EVANS, H. E. 1988. Spallation of oxide from stainless steel AGR nuclear fuel cladding: mechanisms and consequences. *Materials Science and Technology,* 4**,** 414-420.

[Evans, 1989] EVANS, H. E. 1989. Cracking and spalling of protective oxide layer. *Materials Science and Engineering: A,* 1989**,** 139-146.

[Evans, 1995] EVANS, H. E. 1995. A creep analysis of the deflection test for evaluation oxide growth stresses. *Materials Science and Engineering: A,* A203**,** 117-127.

[Evans, 2005] EVANS, H. E. 2005. Spallation models and their relevance to steam-grown oxides. *Materials at High Temperatures,* 22**,** 155-165.

[Fujii et al., 1964] FUJII, C. & MEUSSNER, R. 1964. The Mechanism of the High-Temperature Oxidation of Iron-Chromium Alloys in Water Vapor. *Journal of the Electrochemical Society,* 111**,** 1215-1221.

[Hancock et al., 1974] HANCOCK, P. & HURST, R. 1974. The mechanical properties and breakdown of surface oxide films at elevated temperatures. *Advances in corrosion science and technology.* Springer.

[Hancock et al., 1988] HANCOCK, P. & NICHOLLS, J. R. 1988. Application of fracture mechanics to failure of surface oxide scales. *Materials Science and Technology,* 4**,** 398-406.

[Hou, 2016] HOU, P. Y. 2016. Oxidation of Metals and Alloys. *Reference Module in Materials Science and Materials Engineering.* Elsevier.

[Huntz et al., 2002] HUNTZ, A., AMIRI, G. C., EVANS, H. & CAILLETAUD, G. 2002. Comparison of oxidation-growth stresses in NiO film measured by deflection and calculated using creep analysis or finite-element modeling. *Oxidation of Metals,* 57**,** 499-521.

[J. G. Zhao, 1984] J. G. ZHAO, A. M. H. 1984. Theoretical analysis of the deflection test used in single-surface oxidation of metallic samples. *Journal of materials science,* 19**,** 3166-3172.

[Li et al., 1999] LI, M., LI, T., GAO, W. & LIU, Z. 1999. Determination of oxide growth stress by a novel deflection method. *Oxidation of metals,* 51**,** 333-351.

[Li et al., 2016] LI, Z. J., WANG, S. F., LI, B. & XIANG, X. A New Method for Synthesis of FeMnO3 Ceramics and its Phase Transformation. Journal of Nano Research, 2016. Trans Tech Publ, 122-131.

[Liu et al., 2011] LIU, W. N., SUN, X., STEPHENS, E. & KHALEEL, M. 2011. Effect of substrate thickness on oxide scale spallation for solid oxide fuel cells. *Corrosion Science,* 53**,** 2406-2412.

[Luo et al., 2018] LUO, L., SU, M., YAN, P., ZOU, L., SCHREIBER, D. K., BAER, D. R., ZHU, Z., ZHOU, G., WANG, Y., BRUEMMER, S. M., XU, Z. & WANG, C. 2018. Atomic origins of water-vapour-promoted alloy oxidation. *Nat Mater,* 17**,** 514-518.

[Nicholls et al., 1994] NICHOLLS, J. R., HALL, D. J. & TORTORELLI, P. F. 1994. Hardness and modulus measurements on oxide scales. *Materials at High Temperatures,* 12**,** 141-150.

[Norin, 1975] NORIN, A. 1975. Mechanical stresses developed in austenitic Fe-Cr-Ni alloys by oxidation in a CO 2 atmosphere. *Oxidation of Metals,* 9**,** 259-274.

[Norton, 1929] NORTON, F. H. 1929. *The creep of steel at high temperatures,* McGraw-Hill Book Company, Incorporated.

[Parmelee et al., 1932] PARMELEE, C. W., BADGER, A. E. & BALLAM, G. A. 1932. A study of a group of typical spinels. University of Illinois at Urbana Champaign, College of Engineering ….

[Rhines et al., 1970] RHINES, F. & WOLF, J. 1970. The role of oxide microstructure and growth stresses in the high-temperature scaling of nickel. *Metallurgical Transactions,* 1**,** 1701-1710.

[Rigby, 1946] RIGBY, G. R., LOWELL, G. H. B. AND GREEN, A. T. 1946. *Br. Ceram. Soc. Trans.,* 45**,** 137.

[Robertson et al., 1990] ROBERTSON, J. & MANNING, M. 1990. Limits to adherence of oxide scales. *Materials Science and Technology,* 6**,** 81-92.

[S. Baleix, 2002] S. BALEIX, G. B., P. LOURS 2002. Oxidation and oxide spallation of heat resistant cast steels for superplastic forming dies. *Materials Science and Engineering: A,* 327**,** 155-166.

[Saunders et al., 1997] SAUNDERS, S., EVANS, H., LI, M., GOHIL, D. & OSGERBY, S. 1997. Oxidation growth stresses in an alumina-forming ferritic steel measured by creep deflection. *Oxidation of metals,* 48**,** 189-200.

[Saunders et al., 2008] SAUNDERS, S. R. J., MONTEIRO, M. & RIZZO, F. 2008. The oxidation behaviour of metals and alloys at high temperatures in atmospheres containing water vapour: A review. *Progress in Materials Science,* 53**,** 775-837.

[Schütze, 1997] SCHÜTZE, M. 1997. *Protective oxide scales and their breakdown,* Wiley.

[Srolovitz et al., 1984] SROLOVITZ, D. & RAMANARAYANAN, T. A. 1984. An elastic analysis of growth stresses during oxidation. *Oxidation of metals,* 22**,** 133-146.

[Sun et al., 2008] SUN, X., LIU, W. N., STEPHENS, E. & KHALEEL, M. A. 2008. Determination of interfacial adhesion strength between oxide scale and substrate for metallic SOFC interconnects. *Journal of Power Sources,* 176**,** 167-174.

[Timoshenko, 1936] TIMOSHENKO, S. 1936. Theory of elastic stability.

[Tylecote, 1960] TYLECOTE, R. 1960. Factors influencing the adherence of oxides on metals. *J. Iron Steel Inst,* 196**,** 135-141.

[Wells et al., 1975] WELLS, C., FOLLANSBEE, P. & DILS, R. Mechanisms of dynamic degradation of surface oxides. Proc. of Symp. on Stress Effects and the Oxidation of Metals, 1975, 200-244, 1975.

[Zhong et al., 2012] ZHONG, X., WU, X. & HAN, E.-H. 2012. The characteristic of oxide scales on T91 tube after long-term service in an ultra-supercritical coal power plant. *The Journal of Supercritical Fluids,* 72**,** 68-77.

CHAPTER

6

Comprehensive analyses of oxidation mechanism

Contents

CHAPTER 6 SYNTHESIS ANALYSES OF OXIDATION MECHANISM **191**

6.1 TENSILE STRESS ENHANCED OXYGEN INWARD DIFFUSION 191

6.2 SELF-HEALING OF OXIDE SCALES 193

6.3 CHEMICAL DEPENDENCE OF STRESSES 196

6.3.1 Fe_3O_4 ..... *196*

6.3.2 FeO *197*

6.4 BREAKAWAY OXIDATION 198

6.4.1 Morphology and microstructure *198*

6.4.2 Internal stresses *202*

6.4.3 Breakaway oxidation of AISI 316L in humid air *205*

6.5 SUMMARY 206

6.5.1 Combined actions of water vapor and stress *206*

6.5.2 Proposed oxidation mechanism *207*

6.6 REFERENCE 209

Chapter 6 Comprehensive analyses of oxidation mechanism

Chapter 4 and Chapter 5 have studied the oxidation behaviors of AISI 316L SS between 700˚C and 900˚C in the air with different amounts of water vapor mainly using thermochemical and thermomechanical analysis respectively. It has been mentioned several times in this thesis that high temperature oxidation of AISI 316L SS in humid air is a complicated issue which not only thermochemical attacks but also complex thermo-chemo-mechanical conditions should be considered. Some discussions concerning the synergistic effects have been conducted in Chapter 5 because single thermomechanical analysis is insufficient to explain the corresponding observations. This indicates that the internal stress evolution is closely related to the oxide growth process, including oxide phase constituents, phase distribution within the oxide scale, microstructure of oxide scale, and effects of temperature or humidity etc. Furthermore, internal stresses can in turn impact the oxide growth process; by affecting two factors which can influence the oxidation process, i.e., the chemical potential (to impact diffusion) and the free energy of the reaction (to impact internal oxidation) [*Krishnamurthy et al., 2003*]. Therefore, based on the investigations of thermochemical and thermomechanical aspects, this chapter will discuss some interesting phenomena during the oxidation of AISI 316L SS, with consideration of thermo-chemo-mechanical effects.

6.1 Tensile stress enhanced oxygen inward diffusion

In-plane growth stresses developed during the isothermal oxidation have been studied in Section 5.1. The oxide scales grown in the air with 1% and 2% water vapor at 700˚C and in the air with 1% and 8% at 900˚C are subject to tensile stresses. At 800˚C, oxide scales formed in the air with 2% and 8% water vapor are subject larger tensile stresses. It is of interest that the cross-section images of the oxide scales formed in the conditions mentioned above illustrate a similar feature that oxide scales may be no longer protective, which can be verified by the corresponding SEM observations of oxide cross-section or surface morphology, e.g.: for AISI 316L SS oxidized at 700˚C for 96 hours in the air with 1% water vapor, through-scale cracks can be observed (see Figure 4.22); for AISI 316L SS oxidized at 700˚C for 96 hours in the air with 2% water vapor, debonding of oxide scale and internal oxidation can be observed (see Figure 4.23); for AISI 316L SS oxidized at 800˚C for 96 hours in the air with 2% water vapor, the serious internal oxidation zone can be observed (see Figure 4.26); for AISI 316L SS oxidized at 800˚C for 72 hours in the air with 8% water vapor, breakaway oxidation is present after 72-hour oxidation (see Figure 4.17.c) and local spalling at the edge of the specimen can be observed (see Figure 6.3); for AISI 316L SS oxidized at 900˚C for 96 hours in the air with 1% water vapor, breakaway oxidation happens after 24-hour oxidation (see Figure 4.17.e) and

apparent internal oxidation can be observed too (see Figure 4.28); for AISI 316L SS oxidized at 900˚C for 96 hours in the air with 8% water vapor, breakaway oxidation happens after 6-hour oxidation (see Figure 4.17), delamination and local breakdown of oxide scale can be observed (see Figure 6.4).

When stresses act on the oxide scales, the interatomic distances in the crystal lattice of oxide can be modified. One of the properties which are of significance for diffusion of oxygen species is the oxygen ion conductivity during oxidation. It is inevitably influenced by the applying stress. The oxygen ion conductivity σ_{ion} can be expressed with the Arrhenius equation [*Petrowsky et al., 2009*], as:

$$\sigma_{\mathrm{ion}} = (\sigma_0/T)e^{-E_{\mathrm{A}}/k_{\mathrm{B}}T}, \tag{6.1}$$

where σ_0 is the pre-exponential factor.

It has been suggested that tensile stress facilitates to expand the migration volume whereby the activation energy for the oxygen ion hopping is decreased [*Kilner, 2008, Fluri et al., 2016*]. Consequently, for the oxidation of AISI 316L, it can be assumed that tensile stresses promote the inward diffusion of oxygen. Moreover, tensile loading may promote cracking within the oxide scale during oxidation, which can be verified by the formation of cracks in the oxide scales formed at 700˚C in the air with 1% and 2% water vapor (see Figure 4.17.a and Figure 5.2.a); these cracks may generate the fast-inward diffusion paths of oxygen.

Now considering the effect of water vapor, the dissociation mechanism in regard to oxygen species inward diffusion has been proposed [*Fujii et al., 1964*]; water may promote the formation of vacancies and vacancy clusters within the oxide scale [*Luo et al., 2018*]; ion mobility can be improved as the concentration of vacancies increases within the oxide scale [*A. V. Roshchin, 2003*]; hence, it can be deduced that the inward diffusion of oxygen may be enhanced in the presence of water vapor.

Considering the positive effects of tensile stresses and water vapor on the inward diffusion of oxygen, internal oxidation may be triggered when the oxide scale grows in humid air and suffers tensile growth stresses.

The effect of tensile stresses on the occurrence of breakaway oxidation in this work will be discussed in Section 6.4.

6.2 Self-healing of oxide scales

When the oxide scale is subject to either tensile or compressive stresses, cracking and spalling (through either wedging or buckling) may occur during the high temperature oxidation of steels. However, spalling may not happen rapidly after cracking within the oxide scale because steels are first likely to heal themselves by forming new oxides at the position of cracks [*Schütze, 2016*].

To considerate the self-healing process during the oxidation of AISI 316L SS in this work, the cases at 700˚C in the 2% and 4% water containing air will be taken as an example. In the first case (700˚C, 2% water), tensile stresses act on the oxide scale during the isothermal oxidation (see navy-blue points in Figure 5.2.a); while in the second case (700˚C, 4% water), compressive stresses act on the oxide scale during the isothermal oxidation (see sky-blue points in Figure 5.2.a). In these two cases, cracking is present during oxidation, which can be verified by the fluctuation of their mass gain curves (see green and blue lines in Figure 4.17.a). No spalling is observed meaning self-healing process is possibly present. The presence of crack healing may also be supported by the surface morphology of the oxide scale formed at 700˚C in the air with 2% water vapor, i.e. the surface of oxide scale shows a mark of healed-crack (marked with box in Figure 4.23.a).

- Self-healing for AISI 316L SS oxidized at 700˚C in the 2% water containing air

Since oxygen inward diffusion is of importance during the oxidation of AISI 316L SS at 700˚C (see Section 4.1.4.4), the healing process may probably rely on oxygen inward diffusion; moreover, according to the description of Schütze in regard to two extreme situations of scale healing-process (self-healing entirely relies on cation outward diffusion or entirely relies on anion inward diffusion, see Section 2.4.2.2), for the oxidation of AISI 316L SS at 700˚C in the air with 2% water vapor, the in-growing oxide into the substrate and cracks in the oxide scale can be observed (internal oxidation shown in Figure 4.23), which is an obvious feature proposed by Schütze that oxygen inward diffusion predominates during self-healing. Therefore, it can be qualitatively thought that self-healing during the oxidation of AISI 316L SS at 700˚C in the 2% water containing air mainly counts on the oxygen inward diffusion. In fact, such healing form is harmful, since the crack tip where stresses concentrate may lead to further growth of crack, which may probably propagate towards the substrate and finally grow in the metal [*Schütze, 1997*], leading to the internal oxidation as observed in this case (see Figure 4.23).

- Self-healing for AISI 316L SS oxidized at 700˚C in the 4% water containing air

An interesting phenomenon in this case is that buckling may be present for AISI 316L SS oxidized at 700˚C for 48 hours in the air with 4% water vapor, as illustrated in Figure 5.12. The buckling forming process is proposed schematically in Figure 6.1.

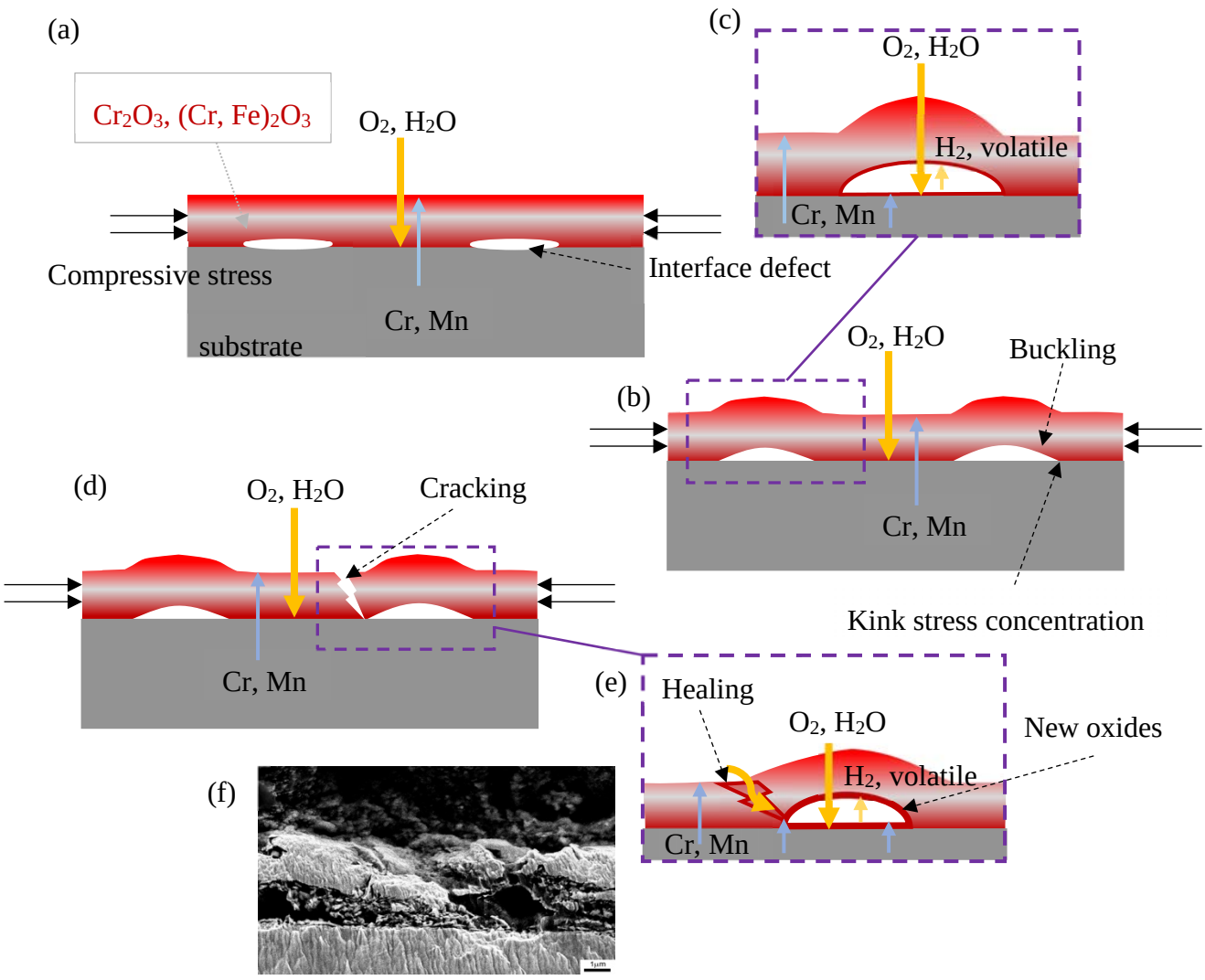

Figure 6.1 Schematic presentation of self-healing process for AISI 316L SS after buckling: initiation (a); buckling (b) and diffusion within the interfacial void (c); cracking (d) and healing (e); corresponding SEM observation for the specimen after 48-hour oxidation at 700˚C in the 4% water containing air (f)

In the presence of water, Kirkendall vacancies can be more likely to form along the MO/M interface (Figure 6.1.a) because water vapor may promote the formation of vacancies and vacancy clusters [*Luo et al., 2018*], which trend to migrate towards the substrate and probably condense out into Kirkendall voids at the M/MO interface [*Wang et al., 2014, Huang et al., 2018*]; these interfacial defects grow up gradually as vacancies cluster, reaching the critical size for buckling generation (Figure 6.1.b) [*Timoshenko, 1936*]; during this stage, a small transport

system has been established within the voids owing to the dissociation mechanism in the presence of water vapor [*Fujii et al., 1964*], and the outward diffusing hydrogen and volatile promote the expansion of voids and oxides generated at the exterior edge of the void (Figure 6.1.c) [*Othman et al., 2009, Dorcheh et al., 2018*]; with compressive stress accumulated, cracks prefer generating at the point of kink stress concentration (Figure 6.1.d) [*Schütze, 1997*]; afterwards, new oxides form to heal the cracks by both oxygen inward diffusion and cation outward diffusion (Figure 6.1.e). The final morphology can be seen in Figure 6.1.f.

However, under the same condition upon long-term oxidation (AISI 316L SS oxidized at 700˚C for 96 hours in the 4% water containing air), a more complicated microstructure has been observed, as shown in Figure 4.24. As discussed in Section 4.2.5.5, the oxide scale gradually forms a single corundum-type oxide layer with three zones rich in different oxide components, i.e., iron-rich $(Fe, Cr)_2O_3$ in the outer zone due to the evaporation of chromium oxides; chromium-rich oxides (Cr_2O_3) near the MO/M interface due to the water enhanced inward diffusion and the supply of chromium from the substrate; the intermediate zone with Fe-Ni metallic compounds ($FeNi_3$) and metal deficient iron oxides (FeO). In premise of such structure, the base of crack can be quickly healed and subsequently closed (see Figure 4.24 and Figure 5.12) by oxygen inward diffusion; it can thus be deduced that oxygen partial pressure may decrease in the intermediate zone as the base of crack closes up. Moreover, the repair of cracks near the MO/M interface may count on the cation diffusion, which can be deduced from the flat MO/M interface (shown in Figure 4.24, Figure 5.12 and Figure 6.1.f) with respect to the proposal by Schütze [*Schütze, 1997*]; it can thus be assumed that chromium rich oxides (Cr_2O_3) at the MO/M interface may act as a diffusion barrier between oxygen species and protective metallic ions. Considering the effects of relatively low oxygen partial pressure in the intermediate zone and the protective cation diffusion barrier (Cr_2O_3 layer) at the MO/M interface, a slow self-healing process in the intermediate zone can be proposed. Consequently, it can be further proposed that the previous cracks usually preserve and new cracks keep forming if continuously stressed, during which water promotes the formation of voids (dissociation mechanism) and further accelerates the formation of cracks within this zone since these voids may easily form cracks under stress. For AISI 316L SS oxidized at 700˚C for 96 hours in the 4% water containing air, this proposed mechanism may account for the microstructure of oxide scale formed under this condition, as illustrated in Figure 4.24.

6.3 Chemical dependence of stresses

For the oxidation of AISI 316L studied in this work, the stress development shows the sensibility to the oxide constituents. This part will discuss two oxides which may impact the internal stress development within the oxide scale formed in this work.

6.3.1 Fe_3O_4

In this work, magnetite (Fe_3O_4) is generally observed in the spinel-type oxide scale formed at 800˚C and 900˚C (see Figure 4.13.b-c and Figure 4.31.c-f); moreover, the content of magnetite is usually smaller than that of the principle spinel-type oxides ($MnCr_2O_4$ and/or $Mn_{1.5}Fe_{1.5}O_4$) (see Figure 4.13.e-f and Figure 4.32.b-c). The following example may indicate the effect of magnetite on the stress development: for the oxide scale formed at 800˚C for 96 hours in the air with 2% water vapor, its SEM cross-section image is illustrated in Figure 6.2, showing a good connection between the outer spinel-type oxide layer and inner corundum-type oxide layer; however, the trends of residual stress in these two layers are opposite after 96-hour oxidation (see green points in Figure 5.7 and Figure 5.8), i.e., compressive residual stresses accumulate in the inner corundum-type oxide scale while they relax in the outer spinel-type oxide scale after 96-hour oxidation.

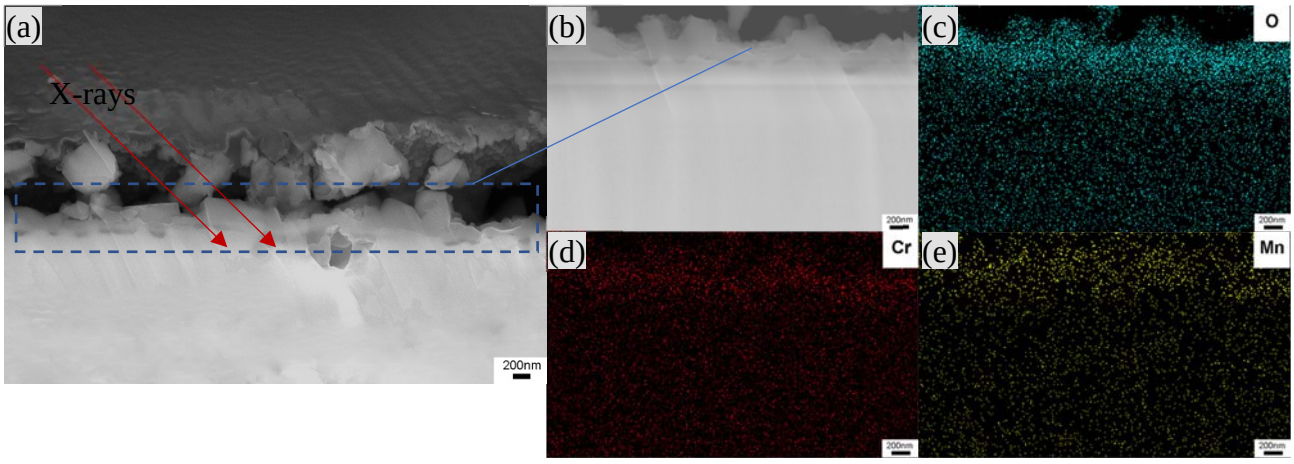

Figure 6.2 SEM/EDX observation of the oxide scale formed at 800˚C for 96 hours in the air with 2% water vapor: image showing the X-ray penetration depth for residual stress determination (a); the enlarged region interested in the discussion (b) and corresponding EDX element mappings (c-e)

According to the quantitative phase analysis under the comparable X-ray penetration depth (d=1.17 μm, see Figure 4.32.b-2) as the one for residual stress determination (d=909 nm, see

Figure 5.8), it can be found that more magnetite forms in the inner part of spinel-type oxide scale, which is supposed to account for the stress relaxation in the spinel-type oxide scale.

Magnetite is a metal deficit oxide in which cation interstitials prefers forming in the inner part of oxide scale where oxygen partial pressure is relatively low [*Dieckmann, 2005*]. This leads to the increased number of interstitials compared with the previous oxide scale, which is helpful for lowering the creep rate [*Schütze, 1997*], thus stresses can release more. In the presence of water vapor, the formation of magnetite can be assumed to be promoted especially near the oxide surface, since chromium-rich oxides are likely to form volatiles whereby more magnetite may generate near the surface; this can be generally verified in Figure 4.32.b-1 and Figure 4.32.c-1.

6.3.2 FeO

In this work, wüstite (FeO) is usually observed in the oxide scales formed at 700˚C. The following example indicates the effect of wüstite on the stress development: stress relaxation appears in the inner part of oxide scale after 96-hour oxidation at 700˚C in dry air (see Figure 5.5.a); large amount of wüstite is observed in the inner part of oxide scale formed under this condition (see Figure 4.13.f). Hence, it can be deduced that the formation of wüstite in the inner part of the oxide scale formed at 700˚C for 96 hours in dry air may account for the stress relaxation in the inner part of its oxide scale.

It has been known that FeO is a highly metal deficiency oxide [*Kofstad, 1988*]. Normally, the defect structure of FeO comprises the iron vacancy clusters [*Hazen et al., 1984*], indicating a better diffusion property than other oxides with low degrees of disorder such as chromia [*Schütze, 1997*].

For FeO, the dominant creep mechanism between 650˚C and 1300˚C has been confirmed (stress range: 15 ~ 60 MPa, $\dot{\varepsilon} > 10^{-4}\text{s}^{-1}$, grain size: 10 μm), i.e., dislocation creep [*Reppich, 1967*]; and for chromia, assuming under the same condition of stress range, strain rate range, grain size and temperature as for FeO, it can be observed in Figure 2.19 that the dominant creep mechanism may also be dislocation creep.

The relationship reflecting the diffusion coefficient D_{eff} and strain rate $\dot{\gamma}$ under dislocation creep can be expressed as:

$$\dot{\gamma} = \left[\left(A_1 D_{\text{eff}} G \bar{b}\right)/(kT)\right]\left(\tau/G^n\right), \tag{6.2}$$

where A_1 is a constant; G the shear modulus; $\bar{b}$ the Burgers vector; k the Boltzmann constant; n the stress exponent.

It should be noted here that for AISI 316L SS oxidized at 700˚C for 96 hours in dry air, FeO is observed in the inner part of oxide scale (see Figure 5.5.a) where low oxygen partial pressure is present (It probably equals to the equilibrium oxygen partial pressure of the system Cr/Cr_2O_3, around 10^{-30} atm according to Figure 2.2), so it can be qualitatively thought that the main defects of chromia (n-type) are chromium interstitials (see Figure 2.8).

Since wüstite has the higher degree of disorders than that of chromia [*Hazen et al., 1984, Schütze, 1997*], the diffusion coefficient of iron vacancy clusters in wüstite can be supposed larger than that of the chromium interstitials in chromia, implying the higher strain rate of wüstite according to Equation (6.2). Finally, it can be further deduced that the creep of oxide scale mainly comprising chromia may be improved with wüstite introduced.

In addition, it has been reported that the plasticity of FeO increases in the presence of water vapor [*Tuck et al., 1969*]. This can be due to the increase of dislocation density and/or mobility of iron vacancy clusters in FeO. This mechanism suggested by Tuck is obtained based on the oxidation of iron. Moreover, iron interstitials increase with increasing dissolved hydrogen, leading to fast cation diffusion [*Terachi et al., 2008*]. However, this cannot be supported in this work. Because the oxide constituents at 700˚C are so complex that the creep of FeO can be interfered seriously by other components and also because the complicated reactive atmosphere in this work compared with PWR primary water.

6.4 Breakaway oxidation

In this work, breakaway oxidation happens for AISI 316L SS oxidized at 800˚C in the air with 8% water vapor after 72 hours (see Figure 4.17.c), at 900˚C in the air with 1% water vapor after 24 hours and with 8% water vapor after 6 hours (see Figure 4.17.e).

6.4.1 Morphology and microstructure

Figure 6.3 displays the surface observation of oxide scale formed at 800˚C for 72 hours in the 8% water containing air, implying the feature of local spalling (fragments of oxide scale can be found at bottom of the tube after oxidation under this condition). It should be noted that spalling starts from the edge of the specimen, the possible mechanism of which can be assumed that stresses can relax through the creep of substrate and strains may thus constantly accumulate at the edge [*Young, 2016*]. It can be expected that spalling will happen once the strain within the oxide scale reaches a critical one (see Section 5.4.2).

Moreover, the element constituents of the edge region and central region have been investigated respectively, tabulated in Table 6.1, with respect to the regions marked as “I” and “II” in Figure 6.3.

Table 6.1 Element constituents of oxide surface with and without spalling (wt.%)

Element	O	Cr	Fe	Mn	Ni
Region I	22.39	2.69	74.48	0.34	0.09
Region II	12.82	21.59	55.58	2.54	7.47

It can be found that the scale is visually thick in the spalled region (I) which is rich in iron and lack of chromium and manganese; the region without spalling (II) has a similar chemical composition with the ones formed under the same condition (at 800˚C for initial 48 hours in the 8% water containing air) before breakaway oxidation (see Figure 4.21.b). According to XRD phase identification (see Figure 4.31.d and Figure 4.32.b-1), the oxide scale consists of iron-rich $(Cr, Fe)_2O_3$, $(Fe, Mn)_2O_3$, $MnCr_2O_4$, Fe_3O_4 and minor iron-rich $(Mn_xFe_{(1-x)})_3O_4$.

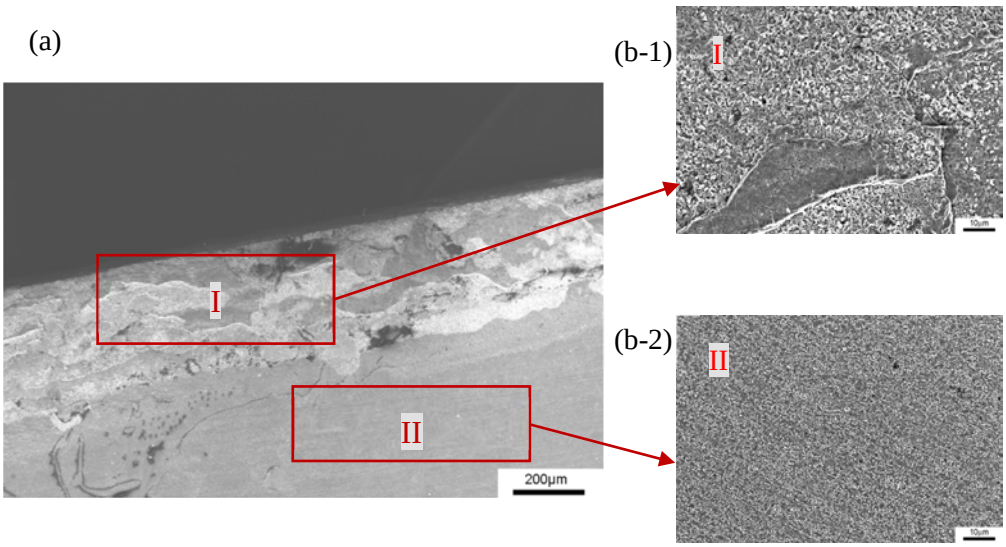

Figure 6.3 SEM images of oxide surface after breakaway oxidation at 800˚C in the air with 8% water vapor for 72 hours

Figure 6.4 illustrates the surface observation of oxide scale formed at 900˚C for 96 hours in the air with 8% water vapor, indicating that breakdown of oxide scale happens in the form of delamination under this condition. The outer oxide layer and inner layer can be observed macroscopically by optical microscopy and microscopically by SEM. The morphology shows that the oxide scale has a complicated multi-layer structure possibly with different oxide constituents and characteristic features respectively. Therefore, elemental analysis has been carried out in regard to the different regions marked with red boxes, the results of which are listed in Table 6.2.

Table 6.2 Elemental analyses corresponding different regions marked in Figure 6.4 (wt.%)

Element	O	Cr	Fe	Mn	Ni
Region I	20.75	28.85	44.56	0.27	5.56
Region II	17.95	4.06	66.65	2.14	9.20
Region III	17.05	1.60	80.38	0.49	0.48
Region IV	19.91	9.20	68.46	0.6	1.84

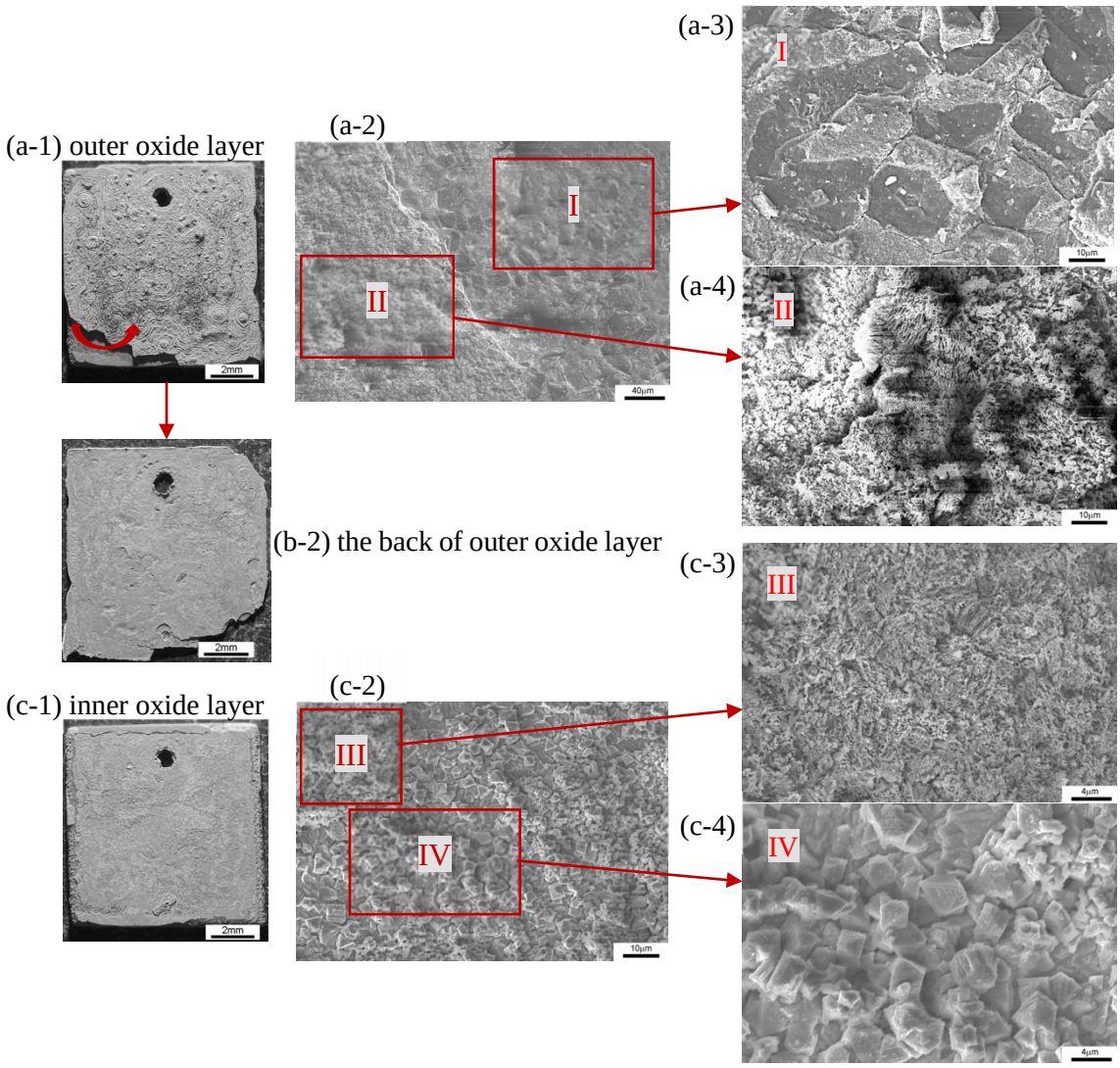

Figure 6.4 Optical observations (a-1, b-1, b-2 and c-1) and SEM images (a-2, 3, 4 and c-2, 3, 4) of oxide surface after breakaway oxidation at 900˚C in the air with 8% water vapor for 96 hours

For the specimen investigated, it can be qualitatively thought that the outer oxide scale has two regions composed by Cr rich oxides (I) and Fe-Ni-Mn (II) rich oxides respectively; the inner oxide scale also has two regions enriched in Fe oxides (III) and Fe-Cr oxides (IV). It has been

suggested that the severe oxidized zone usually includes an oxide island made of Fe-rich corundum oxides and an oxide crater constituted of Ni-rich or Ni-poor Cr-Fe spinel oxides and probably Ni-Fe metallic compounds [*Halvarsson et al., 2006*]. Different local Fe-Cr-Ni-O equilibrium systems are present in the inner reaction zones with respect to oxygen partial pressures [*Jonsson et al., 2016, Jonsson et al., 2017*], and particularly for Fe-Cr spinel oxides, a miscibility gaps exists. This can be used to interpret the presence of Ni in Fe-Cr spinel oxides at higher oxygen partial pressures while absence at lower ones [*Jonsson et al., 2016, Jonsson et al., 2017*]. Unfortunately, XRD phase identification has not been conducted for this serious spalled specimen. However, it can be considered that the connection is present between Region I and Region IV, and between Region II and Region III based on the morphology and chemical compositions. The difference between this oxide scale with the one formed at 800˚C for 72 hours in the air with 8% water vapor (with breakaway oxidation) is the content of nickel in the outer oxide scale, indicating that in this work the oxide scale formed at higher temperature (900˚C) with breakaway oxidation contains more nickel in the outer oxide scale.

Figure 6.5 shows the cross-section microstructure and elemental distribution of oxide scale grown at 900˚C for 24 hours in the air with 8% water vapor. No spalling is observed on this specimen so that the intact oxide scale can be observed. It is clear that the thick oxide scale has a two-layer structure. The outer thicker one consists of iron, nickel and few chromium containing oxides while the inner thin one of chromium and manganese containing oxides.

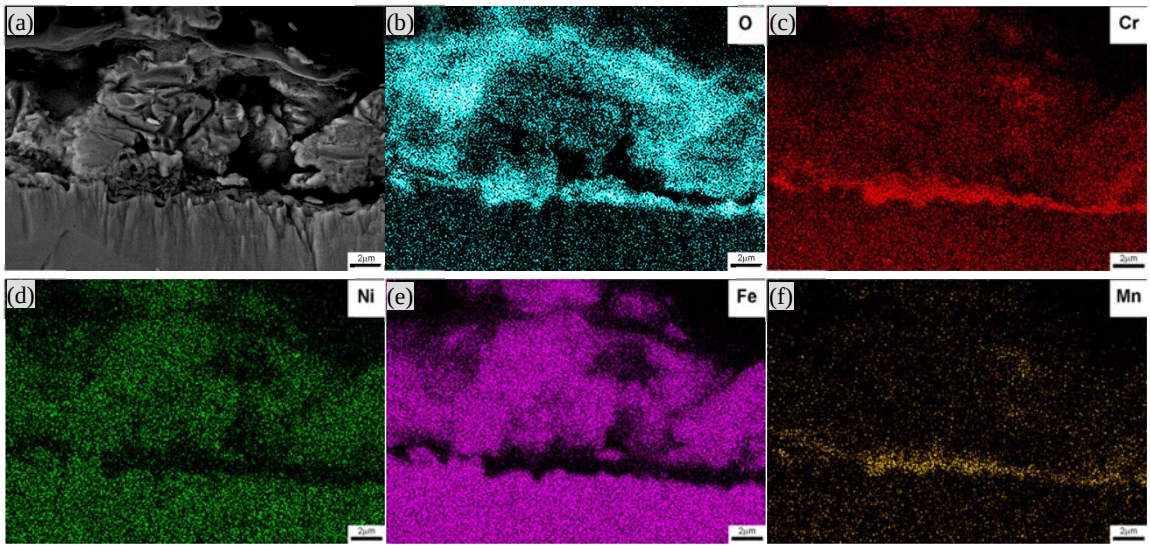

Figure 6.5 SEM image and EDS mapping of oxide scale grown at 900˚C for 24 hours in 8% water vapor containing air: cross-section (a); O mapping (b); Cr mapping (c); Ni mapping (d); Fe mapping (e); Mn mapping (f)

6.4.2 Internal stresses

The investigation of internal stress has also been done for these conditions (at 800˚C in the air with 8% water vapor after 72 hours, at 900˚C in the air with 1% water vapor after 24 hours and with 8% water vapor after 6 hours) where breakaway oxidation is present.

The deflection test shows that the stresses developed during the oxidation are all tensile in these cases (see Figure 5.2.b-c). It should be noted that growth stresses during the oxidation at 800˚C are mostly tensile but the one with a final breakaway oxidation in the oxide scale has the maximum level (see Table 5.2).

From the results of residual stress (Figure 5.7 - Figure 5.10), stresses relax with spalling happened (Local spalling is observed after 72-hour oxidation at 800˚C in the 8% water containing air, shown in Figure 6.3; delamination and local spalling are observed after 96-hour oxidation at 900˚C in the 8% water containing air, shown in Figure 6.4; local spalling is visually observed after 72-hour oxidation at 900˚C in the 8% water containing air). It can also be observed that compressive stresses have not relaxed rapidly as breakaway oxidation happens at 900˚C (see red and sky-blue points in Figure 5.9 and Figure 5.10).

In addition, the average residual stress gradient within the corundum-type oxide scales has been studied for the oxidation of AISI 316L SS at 900˚C for 96 hours in dry air (without breakaway oxidation), at 900˚C for 72 hours in the 1% water containing air (with breakaway oxidation but without spalling) and at 900˚C for 72 hours in the 8% water containing air (with breakaway oxidation as well as spalling). The correlated stress profiles are illustrated in Figure 6.6.

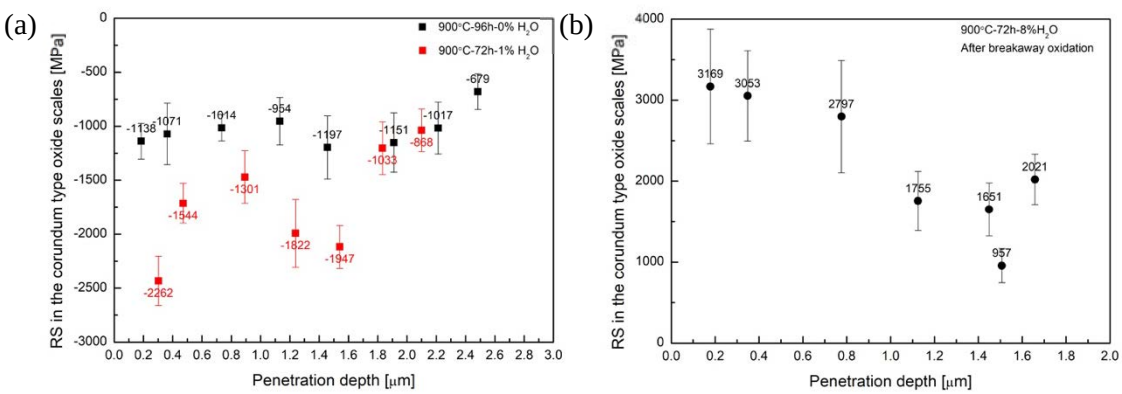

Figure 6.6 Gradient of residual stresses in the corundum-type oxide scales formed at 900˚C in the air with different water contents: 96-hour and 72-hour oxidation in the air with 0% and 1% water vapor (a); 72-hour oxidation in the air with 8% water vapor

In Figure 6.6.a, the two curves represent the stress profiling in the oxide scales formed in dry air without breakaway oxidation (black) and in humid air with breakaway oxidation (red). It

shows that the stress distribution along the thickness is similar for the oxide scales formed in dry and humid air, but the average stress level is relatively large in the latter case. According to the corresponding cross-section observations of these two examples (see Figure 4.10 and Figure 4.28), the main constituents of oxide scales formed in these two cases can be assumed combining the quantitative phase analysis (see Figure 4.32.c), i.e., the outer Cr-Mn spinel-type oxide layer and inner Cr-rich corundum-type oxide layer. (It should be noted here that Figure 4.28 shows the oxide scale formed at 900˚C for 96 hours in the air with 1% water vapor, which can be regarded as the reference for the oxide scale formed at 900˚C for 72 hours in the air with 1% water vapor, since their thicknesses are comparable according to Table App. 1.1.) Moreover, the thicknesses of these two oxide scales are around 1.9 μm and 1.7 μm respectively (see Table App. 1.1). According to Figure 6.6.a, the observations and corresponding mechanisms are proposed as the following:

1. Near the surface, chromia can be observed in the outer layer mainly consisting of spinel-type oxides (see Figure 4.13.d and Figure 4.32.c-1), in the form of grain clusters (see Figure 4.10.a and Figure 4.20.i), resulting in compressive stresses accumulation as the grain generate and grow [*Chason et al., 2002*]. The compressive stresses further release with the formation of chromia layer. In the presence of water vapor, grain growth can be impeded and larger compressive stresses are thus present [*Young, 2008*].

2. In the inner layer, compressive residual stresses increase towards the substrate because the chromia layer near the substrate may be more likely impacted by the substrate especially during the cooling process since thermal stresses (-4250 MPa for 96-hour oxidation without water; -3942 MPa for 72-hour oxidation with 1% water) are of importance to the residual stress determination for AISI 316L SS oxidized at 900˚C (see Section 5.5). With water vapor introduced, oxygen inward diffusion can be motivated [*Setiawan et al., 2010*], resulting in more chromia forming in the inner layer (see Figure 4.32.c-2) where lateral growth strains may probably form within the oxide scale, leading to compressive stresses [*Clarke, 2003*]; this may explain that the average compressive residual stress level developed in the inner layer of the oxide scale formed at 900˚C in the air with 1% water vapor is larger than that in the inner layer of the oxide scale formed at 900˚C in dry air.

3. Residual stresses relax around the interface in these two cases. The plastic deformation of both the substrate and oxide scale at 900˚C [*A. G. Evans, 1983*] may account for this result, which can be verified by the wavy interface (see Figure 4.10 and Figure 4.28). Moreover, voids at the interface may also contribute to stress relaxation possibly through void annihilation under stress. In the presence of water vapor, increased porosity promotes the

creep of oxides by increasing the diffusion [*Schütze, 1997*], and enhanced outward cation diffusion motivates more voids formation at the interface [*Othman et al., 2009*]; so, these two effects may suggest that for AISI 316L SS oxidized at 900˚C in the 1% water containing air, more stresses may relax either within the oxide scale through creep of oxides or near the MO/M interface through interfacial voids. Stress relaxation through interfacial voids or even cracks along the M/M interface (take Figure 6.5 as a reference) may be considerably more important for AISI 316L SS oxidized at 900˚C in the 1% water containing air, because a pronounced stress relief (-1947 MPa to 1038 MPa in Figure 6.6.a) can be observed in the inner oxide layer in this case.

Therefore, based on the result of average residual stress profiling in the oxide scales formed in these two cases where breakaway is present in the 1% water containing air while absent in dry air (see Figure 6.6.a), possibilities which may lead to breakaway oxidation in the first case rather than the second can be suggested:

1. At the oxide surface, according to the larger compressive residual stress in the case with 1% water vapor, it can be deduced that chromia prefers being present in the form of grain clusters in this case rather than a continuous layer in dry air, indicating the less protective oxide scale formed in the external layer for AISI 316L SS oxidized at 900˚C in the 1% water containing air.
2. In the inner layer near the MO/M interface, according to the pronounced stress relief in the case with 1% water vapor, it can be assumed that condensation of interfacial voids as the result of the promoted vacancy formation in the 1% water containing air may further motivate the separation of the inner oxide layer and the substrate, which possibly causes that the insufficient supply of protective metallic element for the outer layer to form a protective layer.

In Figure 6.6.b, the curve represents the stress distribution within the outer part of oxide scale formed at 900˚C for 72 hours in the air with 8% water vapor. Note that local spalling is present in this case. It shows that the oxide scale is subject to tensile stresses, probably implying that the oxide scale is possible to be broken at any time due to the tensile stress. Moreover, tensile stress state within the oxide scale is beneficial for the inward diffusion of oxygen [*Kilner, 2008, Fluri et al., 2016*] (see Section 6.1), which may accelerate the growth of iron-rich oxides (hematite which relies on oxygen inward diffusion) and thus further promotes breakaway oxidation.

6.4.3 Breakaway oxidation of AISI 316L in humid air

It has been accepted that the onset of breakaway oxidation for steels is that the fast growth of non-protective iron-rich oxides substitutes the previous slow growth of protective chromium oxides. Initially researchers thought that the onset of breakaway oxidation is sensitive to water vapor content, such as [*Shen Jianjian, 1997*]. It has been accepted now that it depends on the ratio H_2O/O_2 in fact [*Nickel et al., 1998*]. Ehlers has given a criterion for breakaway oxidation [*Ehlers et al., 2006*], i.e., $(p_{H_2O})/(p_{O_2}) > 1$.

The factors affecting the onset of breakaway oxidation can be summarized as two aspects: chemical attacks and mechanical attacks [*Caplan et al., 1952*]. At higher temperatures (>1170˚C), only chemical attacks contribute to the final breakaway oxidation [*Evans et al., 1999, Saeki et al., 2012*]. The temperature investigated in this work is between 700˚C and 900˚C, hence be deduced that both chemical and mechanical attacks bring into play. This deduction has already been supported by many observations in this work, e.g., chemical attack: relatively high content of iron oxides can be observed before breakaway oxidation for AISI 316L SS oxidized at 900˚C in the air with 1% and 8% water vapor (see Figure 4.32.c); mechanical attack: local spalling is present in the oxide scale where iron oxides form instead of protective chromium oxides for AISI 316L SS oxidized at 800˚C for 72 hours in the air with 8% water vapor (see Figure 6.3 and Table 6.1).

For AISI 316L SS oxidized between 700˚C and 900˚C in humid air for 6 hours to 96 hours, breakaway oxidation is determined by the synergistic thermo-chemo-mechanical conditions. In this work, this is reflected from that breakaway oxidation is only observed in the oxide scales which are subject to tensile stresses and grow in the presence of water vapor. On one hand, the oxide scale is subject to tensile stress, which may promote inward diffusion of oxygen [*Kilner, 2008, Fluri et al., 2016*] and thus facilitate the growth of iron oxides [*Saunders et al., 2008*] especially after breakaway oxidation happens. On the other hand, in the presence of water vapor, the defect structure of oxides can be modified (the concentration of chromium vacancies increases with water introduced, see Figure 2.11) and oxidation mechanism is thus influenced (Dissociation mechanism is proposed [*Fujii et al., 1964*]). Considering theses effects, the process of breakaway oxidation can be explained accordingly, where the oxidation of AISI 316L SS at 900˚C in the air with 8% is taken as an example:

The overlapped countercurrent diffusion of cations and anions can be enhanced owning to the two aspects above (the positive effect of tensile stresses on the inward diffusion of oxygen and the water enhanced formation of cation vacancies within the oxide scale). Consequently, an inner layer consisting of chromium oxides quickly forms, which may contain relatively high

content of iron compared with other conditions without final breakaway oxidation (see Figure 4.32). Simultaneously, an outer layer consisting of Cr-Mn spinel oxides also forms rapidly (see Figure 4.32.c-1). During this stage, the formation of oxides relying on the inward diffusion usually causes compressive stresses [*Srolovitz et al., 1984, Clarke, 2003*], which may release through the creep of substrate. Moreover, the enhanced outward diffusion further leaves more thermal vacancies behind in the substrate, which may accelerate the plastic deformation of substrate. Furthermore, water promoted voids can also stimulate the creep of oxide scale [*Schütze, 1997*]. Due to the double effects of evaporation and enhanced cation outward diffusion, the outer layer becomes rich in iron rich spinel oxides and iron-rich corundum oxides (see Figure 4.32.c-1). But the inner layer, on the contrary, is able to form chromium oxides and Cr-Mn spinel oxides in a short period. The inner layer contains more iron gradually as the result of the depletion zone formation in the substrate beneath the interface (see Figure 4.32.c-3). Since stresses have not relaxed as soon as breakaway oxidation happens (see Figure 5.9), which can be concluded according to Section 5.4.2 that spalling may occur when the stress level reaches a critical level and self-healing cannot be sustained due to the insufficient supply of protective metallic elements.

6.5 Summary

This chapter has studied some interesting observations occurring during the oxidation of AISI 316L SS at 700˚C, 800˚C and 900˚C for 6 hours to 96 hours in the air with 0%, 1%, 2%, 4% and 8% water vapor. The effects of tensile stress, self-healing process and chemical component have been discussed. Based on the studies above, breakaway oxidation has been mainly investigated. In general, the synergistic thermo-chemo-mechanical effects on AISI 316L SS oxidized in the conditions investigated in this work is embodied in the combined influence of water vapor and stress. This will be first summarized. Then the oxidation mechanism with consideration of thermo-chemo-mechanical conditions will be proposed.

6.5.1 Combined actions of water vapor and stress

1. Tensile stresses lower the activation energy of oxygen ions, and inward diffusion is thus enhanced; water vapor also enhances oxygen inward diffusion through dissociation mechanism (see Section 6.1).

2. Tensile stresses usually lead to cracks within the oxide scales, and these cracks can propagate into the substrate if outward cation is insufficient to heal them (see Figure 4.23); water vapor promotes the formation of vacancy and vacancy cluster, which are likely to form cracks under tension (see Section 6.2);

3. Water usually dissolves into protons and hydroxide which may penetrate towards the interface (see Figure 4.36) and even into the substrate, motivating the void condensation near the MO/M interface or in the substrate whereby internal oxidation may occur (see Figure 4.23, Figure 4.26 and Figure 4.28).
4. Water vapor increases the porosity in the oxide scale and motivates cation outward diffusion, which can affect the plasticity of the oxide scale and modify the plasticity of the substrate respectively. Thus, stress state can be accordingly influenced (see Section 5.3.2);
5. Water vapor causes volatilization and thus changes the oxide constituents at the oxide surface, which may affect the mechanical behavior of the surface oxide scale (see Section 5.4.3); plasticity of oxide scale can be modified due to metal deficit iron oxide (wüstite and magnetite) formation (see Section 5.3.2).

6.5.2 Proposed oxidation mechanism

Considering the summary mentioned above, the oxidation mechanism for AISI 316L SS oxidized between 700˚C and 900˚C in humid air for 6 hours to 96 hours can be suggested.

6.5.2.1 In dry air

At 700˚C, a single layer consisting of corundum-type oxides forms mainly through oxygen inward diffusion, generating compressive stresses in the oxide scale. Stresses probably relax through microcracks or plastic deformation of the substrate during oxidation; Stresses may accumulate by new oxide formation within the oxide scale through oxygen inward diffusion.

At 800˚C, the oxide scale is composed by an outer grain-like oxide layer of spinel-type oxides and an inner layer of corundum-type oxides. The plastic deformation of substrate accounts for the stress relaxation. The effects of growth stress on the residual stresses are few since it approaches zero.

At 900˚C, a two-layer oxide scale consisting of the outer spinel-type oxides and inner corundum-type oxides forms quickly owing to fast cation outward diffusion. Growth stresses have little effects on the determination of final residual stresses due to its small value.

6.5.2.2 In humid air

Water vapor has a complicated effect on the oxidation mechanism of AISI 316L SS under the conditions investigated in this work.

At 700˚C, a single layer of corundum-type oxide form in all humidity. For the oxide scales under tensile stresses, through-scale cracks and self-healing repeat continuously during the oxidation, leading to a final decohesion or serious internal oxidation. For the oxide scale under

compressive stresses, a complex oxide scale with three regions enriched in different oxide components forms. During oxidation, buckling, crack and self-repair all present of which the intermediate part consisting of iron-rich mixed oxides and metallic compounds as well as large amounts of cracks gradually develops.

At 800˚C, the oxide scales grown in humid air are similar with those grown in dry air. For the oxide scales under larger tensile stresses, the double enhanced effects of inward oxygen diffusion and cation outward diffusion lead to serious internal oxidation or a final breakaway oxidation. Simultaneously, the formation of wavy interface ascribes to the enhanced creep.

At 900˚C, the oxide scales grown in humid air are similar to those grown in dry air, especially for the oxide scale under compressive stresses. For the oxide scales under tensile stresses, a final breakaway oxidation happens. For the oxide scale formed in the air with 1% water vapor, no spallation is present but a serious internal oxidation. For the oxide formed in the air with 8% water vapor, breakaway oxidation appears after 6-hour oxidation.

6.6 Reference

[A. G. Evans, 1983] A. G. EVANS, G. B. C. A. R. E. D. 1983. A.G.Evans On the mechanical behavior of brittle coatings and layers. *Oxidation of Metals,* 20**,** 193-216.

[A. V. Roshchin, 2003] A. V. ROSHCHIN, V. E. R. 2003. Diffusion of anions and cations in oxide crystal lattices during the reduction and oxidation of metals. *RUSSIAN METALLURGY METALLY C/C OF IZVESTIIA-AKADEMIIA NAUK SSSR METALLY 1,* 2003**,** 1-5.

[Caplan et al., 1952] CAPLAN, D. & COHEN, M. 1952. High temperature oxidation of some iron-chromium alloys. *JOM,* 4**,** 1057-1057.

[Chason et al., 2002] CHASON, E., SHELDON, B. W., FREUND, L. B., FLORO, J. A. & HEARNE, S. J. 2002. Origin of compressive residual stress in polycrystalline thin films. *Phys Rev Lett,* 88**,** 156103.

[Clarke, 2003] CLARKE, D. R. 2003. The lateral growth strain accompanying the formation of a thermally grown oxide. *Acta Materialia,* 51**,** 1393-1407.

[Dieckmann, 2005] DIECKMANN, R. 2005. Solution and transport of water in oxides. *Materials at High Temperatures,* 22**,** 93-103.

[Dorcheh et al., 2018] DORCHEH, A. S., SCHÜTZE, M. & GALETZ, M. C. 2018. Factors affecting isothermal oxidation of pure chromium in air. *Corrosion Science,* 130**,** 261-269.

[Ehlers et al., 2006] EHLERS, J., YOUNG, D. J., SMAARDIJK, E. J., TYAGI, A. K., PENKALLA, H. J., SINGHEISER, L. & QUADAKKERS, W. J. 2006. Enhanced oxidation of the 9%Cr steel P91 in water vapour containing environments. *Corrosion Science,* 48**,** 3428-3454.

[Evans et al., 1999] EVANS, H., DONALDSON, A. & GILMOUR, T. 1999. Mechanisms of breakaway oxidation and application to a chromia-forming steel. *Oxidation of Metals,* 52**,** 379-402.

[Fluri et al., 2016] FLURI, A., PERGOLESI, D., RODDATIS, V., WOKAUN, A. & LIPPERT, T. 2016. In situ stress observation in oxide films and how tensile stress influences oxygen ion conduction. *Nat Commun,* 7**,** 10692.

[Fujii et al., 1964] FUJII, C. & MEUSSNER, R. 1964. The Mechanism of the High-Temperature Oxidation of Iron-Chromium Alloys in Water Vapor. *Journal of the Electrochemical Society,* 111**,** 1215-1221.

[Halvarsson et al., 2006] HALVARSSON, M., TANG, J. E., ASTEMAN, H., SVENSSON, J. E. & JOHANSSON, L. G. 2006. Microstructural investigation of the breakdown of the protective oxide scale on a 304 steel in the presence of oxygen and water vapour at 600°C. *Corrosion Science,* 48**,** 2014-2035.

[Hazen et al., 1984] HAZEN, R. M. & JEANLOZ, R. 1984. Wüstite (Fe1-x O): A review of its defect structure and physical properties. *Reviews of Geophysics,* 22**,** 37-46.

[Huang et al., 2018] HUANG, C.-L., WENG, W.-L., LIAO, C.-N. & TU, K. 2018. Suppression of interdiffusion-induced voiding in oxidation of copper nanowires with twin-modified surface. *Nature communications,* 9**,** 340.

[Jonsson et al., 2016] JONSSON, T., KARLSSON, S., HOOSHYAR, H., SATTARI, M., LISKE, J., SVENSSON, J.-E. & JOHANSSON, L.-G. 2016. Oxidation after breakdown of the chromium-rich scale on stainless steels at high temperature: internal oxidation. *Oxidation of Metals,* 85**,** 509-536.

[Jonsson et al., 2017] JONSSON, T., LARSSON, H., KARLSSON, S., HOOSHYAR, H., SATTARI, M., LISKE, J., SVENSSON, J.-E. & JOHANSSON, L.-G. 2017. High-temperature oxidation of FeCr (Ni) alloys: the behaviour after breakaway. *Oxidation of Metals,* 87**,** 333-341.

[Kilner, 2008] KILNER, J. A. 2008. Ionic conductors: Feel the strain. *Nature Materials,* 7**,** 838.

[Kofstad, 1988] KOFSTAD, P. 1988. High temperature corrosion. *Elsevier Applied Science Publishers, Crown House, Linton Road, Barking, Essex IG 11 8 JU, UK, 1988.*

[Krishnamurthy et al., 2003] KRISHNAMURTHY, R. & SROLOVITZ, D. J. 2003. Stress distributions in growing oxide films. *Acta Materialia,* 51**,** 2171-2190.

[Luo et al., 2018] LUO, L., SU, M., YAN, P., ZOU, L., SCHREIBER, D. K., BAER, D. R., ZHU, Z., ZHOU, G., WANG, Y., BRUEMMER, S. M., XU, Z. & WANG, C. 2018. Atomic origins of water-vapour-promoted alloy oxidation. *Nat Mater,* 17**,** 514-518.

[Nickel et al., 1998] NICKEL, H., WOUTERS, Y., THIELE, M. & QUADAKKERS, W. 1998. The effect of water vapor on the oxidation behavior of 9% Cr steels in simulated combustion gases. *Fresenius' journal of analytical chemistry,* 361**,** 540-544.

[Othman et al., 2009] OTHMAN, N. K., OTHMAN, N., ZHANG, J. & YOUNG, D. J. 2009. Effects of water vapour on isothermal oxidation of chromia-forming alloys in Ar/O2 and Ar/H2 atmospheres. *Corrosion Science,* 51**,** 3039-3049.

[Petrowsky et al., 2009] PETROWSKY, M. & FRECH, R. 2009. Temperature dependence of ion transport: the compensated Arrhenius equation. *The Journal of Physical Chemistry B,* 113**,** 5996-6000.

[Reppich, 1967] REPPICH, B. 1967. PLASTIC DEFORMATION OF FERROUS OXIDE. *PHYS STATUS SOLIDI,* 20**,** 69-82.

[Saeki et al., 2012] SAEKI, I., SUGIYAMA, Y., HAYASHI, S., YAMAUCHI, A., DOI, T., NISHIYAMA, Y., KYO, S., SUZUKI, S., SATO, M. & FUJIMOTO, S. 2012. In situ X-ray diffraction of surface oxide on type 430 stainless steel in breakaway condition using synchrotron radiation. *Corrosion Science,* 55**,** 219-225.

[Saunders et al., 2008] SAUNDERS, S. R. J., MONTEIRO, M. & RIZZO, F. 2008. The oxidation behaviour of metals and alloys at high temperatures in atmospheres containing water vapour: A review. *Progress in Materials Science,* 53**,** 775-837.

[Schütze, 1997] SCHÜTZE, M. 1997. *Protective oxide scales and their breakdown,* Wiley.

[Schütze, 2016] SCHÜTZE, M. 2016. Stress effects in high temperature oxidation.

[Setiawan et al., 2010] SETIAWAN, A. R., ANI, M. H. B., UEDA, M., KAWAMURA, K. & MARUYAMA, T. 2010. Oxygen permeability through internal oxidation zone in Fe–Cr alloys under dry and humid conditions at 973 and 1 073 K. *ISIJ international,* 50**,** 259-263.

[Shen Jianjian, 1997] SHEN JIANJIAN, Z. L., AND LI TIEFAN 1997. High-temperature oxidation of Fe-Cr alloys in wet oxygen. *Oxidation of Metals,* 48**,** 347-356.

[Srolovitz et al., 1984] SROLOVITZ, D. & RAMANARAYANAN, T. A. 1984. An elastic analysis of growth stresses during oxidation. *Oxidation of metals,* 22**,** 133-146.

[Terachi et al., 2008] TERACHI, T., YAMADA, T., MIYAMOTO, T., ARIOKA, K. & FUKUYA, K. 2008. Corrosion Behavior of Stainless Steels in Simulated PWR Primary Water—Effect of Chromium Content in Alloys and Dissolved Hydrogen—. *Journal of Nuclear Science and Technology,* 45**,** 975-984.

[Timoshenko, 1936] TIMOSHENKO, S. 1936. Theory of elastic stability.

[Tuck et al., 1969] TUCK, C., ODGERS, M. & SACHS, K. 1969. The oxidation of iron at 950 C in oxygen/water vapour mixtures. *Corrosion Science,* 9**,** 271-285.

[Wang et al., 2014] WANG, C.-M., GENC, A., CHENG, H., PULLAN, L., BAER, D. R. & BRUEMMER, S. M. 2014. In-Situ TEM visualization of vacancy injection and chemical partition during oxidation of Ni-Cr nanoparticles. *Scientific reports,* 4**,** 3683.

[Young, 2008] YOUNG, D. J. 2008. Effects of Water Vapour on the Oxidation of Chromia Formers. *Materials Science Forum,* 595-598**,** 1189-1197.

[Young, 2016] YOUNG, D. J. 2016. *High temperature oxidation and corrosion of metals,* Elsevier.

CHAPTER

7

Conclusions and Perspectives

Contents

CHAPTER 7 CONCLUSIONS AND PERSPECTIVES **215**

7.1 *CONCLUSIONS* 215

7.2 *PERSPECTIVES* 216

Chapter 7 Conclusions and perspectives

7.1 Conclusions

As a good choice for high temperature applications, the oxidation resistance of AISI 316L SS is of significance. A chromium rich oxide scale usually plays a protective role in the service environment which often contains mixed corrosive atmosphere such as oxygen and water. During the oxidation of AISI 316L SS in this work, both chemical and mechanical attacks impact the oxide growth process so as to determine the lifetime of metallic component. This thesis mainly investigates the oxidation behaviors of AISI 316L SS at 700˚C, 800˚C, and 900˚C in the air with 0%, 1%, 2%, 4% and 8% water vapor considering the thermo-chemo-mechanical conditions.

Firstly, the oxidation kinetics has been studied. It was confirmed that during the stage before breakaway oxidation, the oxidation rate between 700˚C and 900˚C in both dry and humid air follows the parabolic rate law.

Secondly, the morphology, microstructure and constituent of oxide scales have been observed. The oxide scale formed at 700˚C show a single layer structure consisting of corundum-type oxides (Cr_2O_3, $(Fe, Cr)_2O_3$). The oxide scales grown at 800˚C and 900˚C comprise a two-layer structure composed by the inner corundum-type oxides (Cr_2O_3) and outer spinel-type oxides ($MnCr_2O_4$).

Thirdly, the growth stress, thermal stress and residual stress have been studied respectively.

- Growth stress: In dry air, the growth stress developed at 700˚C is of significance for the final stress state. In humid air, either compressive or tensile growth stresses can act on the oxide scales formed at 700˚C and 900˚C, while only tensile stresses act on the oxide scales formed at 800˚C. During isotheral oxidation, plastic deformation, microcracks/through-scale cracks (at 700˚C in the air with 1% and 2% water vapor), buckling (oxidation at 700˚C for 48 hours in the air with 4% water vapor) are the main forms of stress relaxation. Self-healing is able to protect the damaged oxide scale which probably induces stresses.
- Thermal stress: Compressive thermal stresses are present for the outer spinel-type oxide scale. The outer spinel layer acts on the corundum-type oxide scale with a relatively small tensile stress. The corundum-type oxide scale undergoes compressive stress during the cooling process. The thermal stress of corundum-type oxide scales shows sensitivity to the oxidation temperature, i.e., it increases with increasing the temperature. During the cooling process, creep of both the substrate and oxide leading to a wavy interface (after oxidation

at 900˚C), wedging (after oxidation at 700˚C in the air with 1% water vapor), buckling (after 48-hour oxidation at 700˚C in the air with 4% water vapor) and spalling (after 72-hour oxidation at 800˚C in the air with 8% water vapor; after 96-hour oxidation at 900˚C in the air with 1% water vapor; after 72-hour oxidation at 900˚C in the air with 8% water vapor) are the main forms of stress relief.

- Residual stress: Residual stresses in the corundum-type oxide scales show the temperature dependence in dry air. Water vapor has a complex effect on the residual stress evolution in the oxide scales, usually through evaporation process, enhanced void formation, enhanced inward diffusion and component modification.

Fourthly, based on the results above, comprehensive analyses in regard to some key points have been done. In general, the thermo-chemo-mechanical coupling effects on AISI 316L SS oxidized in the conditions investigated in this work is embodied in the combined influence of water vapor and stress.

1. Tensile stresses promote oxygen inward diffusion by lowering the activation energy of diffusion; water has the similar effect according to the dissociation mechanism.
2. Tensile stresses facilitate cracking within the oxide scale; water vapor promotes the formation of vacancy and vacancy cluster, which may promote cracks formation under tension;
3. Dissolved protons and hydroxide ions may penetrate towards the MO/M interface and even into the substrate, leading to void condensation or even internal oxidation;
4. Water vapor may modify plasticity of the oxide scale through increasing porosity within the oxide scale; water vapor may impact the plasticity of the substrate to some extent by promoting the formation of vacancies in the substrate.
5. The evaporation of chromium oxides caused by water vapor may affect the mechanical behavior of the surface oxide scale; water vapor may influence the plasticity of oxide scale by motivating the formation of metal deficit iron oxide (wüstite and magnetite).

In this work, breakaway oxidation happens when oxide scales are subject to tensile growth stresses in the presence of water vapor, the onset of which is determined by the synergistic thermo-chemo-mechanical effects. In the end, oxidation mechanism of AISI 316L SS is proposed with consideration of those mentioned above.

7.2 Perspectives

The future work will primarily focus on three aspects:

- Further characterization

This work has used FESEM/EDX to observe the microstructure of oxide scales, but this method can only solve the up to the micrometer scale. It is difficult to make clear the accurate component and structure of oxides through only the results of SEM or XRD. Therefore, TEM will be used to further investigate more detailed information of oxides. For instance, to better understand the microstructure of oxide scale formed at 900˚C for 24 hours in the air with 8% water vapor (with breakaway oxidation), TEM characterization will be carried out for the cross-section of this specimen, from which the distinction of chemical composition between the inner layer and the thick outer layer should be clear. This will benefit to further analyze the growth mechanism of oxide scale in this condition whereby the cause of breakaway oxidation of AISI 316L SS in this work might be confirmed.

Moreover, with the obtained data from XPS, the component refinement will be done to further observe the phase distribution along the oxide depth profile. This is better to profoundly understand the important diffusion process. For instance, XPS component refinement will be performed for the oxide scales formed under the following conditions, i.e., oxidation at 700˚C for 24 hours in the air with 0% (compressive growth stresses), 2% (tensile growth stresses) and 8% (tensile growth stresses) water vapor; oxidation at 800˚C for 24 hours in the air with 0% (small tensile growth stresses), 2% (large tensile growth stresses) and 8% (large tensile growth stresses) water vapor; oxidation at 900˚C for 6 hours in the air with 0% (small tensile growth stresses), 2% (compressive growth stress) and 8% water vapor (large tensile growth stresses). This work will facilitate to understand the growth mechanisms of AISI 316L SS under the selected conditions by considering the effects of temperature, humidity and growth stresses.

- To analyze growth stresses using creep model

It has been mentioned in Chapter 5 that the creep model suggested by Evans etc. is no more appropriate to the grow stress analysis in this work. So, in the future, a new creep model based on the one proposed by Evans will be established with consideration of real situations in this work. Initially, a natural bending where the protective oxide scale is on the convex side will be assumed; subsequently the strains of both the new-forming oxide scale and the substrate will be expressed with respect to the assumed positions of neutral axes; then according to Norton's equation, the relationship between the stress and strain rate will be established whereby the balanced equations of force and force moment around the MO/M interface can be built; finally these equations will be treated using the MATLAB software.

- Numerical methods

With consideration of thermo-chemo-mechanical conditions, the high temperature oxidation issue becomes quite complex. It has been found in this thesis that many possible mechanisms may account for one phenomenon, and they may take place at the same time. Therefore, a strong analytical model has to be taken into account to deeply understand the oxidation process of AISI 316L SS in this work. Considering the synergistic thermo-chemo-mechanical effects, phase field method may be a good choice since both diffusion process and mechanical behaviors can be concerned.

Appendices

Contents

APPENDIX 1 AN APPROXIMATE CALCULATION OF OXIDE SCALE THICKNESS **221**

APPENDIX 2 RELEVANT PARAMETERS CALCULATIONS FOR XRD **225**

APP. 2.1 X-RAY LINEAR ABSORPTION COEFFICIENT CALCULATION 225

App. 2.1.1 For a compound *225*

App. 2.1.2 For an oxide scale *225*

APP. 2.2 X-RAY PENETRATION DEPTH CALCULATION 225

App. 2.2.1 For phase analysis *225*

App. 2.2.2 For stress analysis *227*

APP. 2.3 DETERMINATION OF X-RAY IRRADIATED AREA 229

REFERENCE 230

APPENDIX 3 QUANTITATIVE COMPOSITIONAL DEPTH PROFILING OF XPS **231**

APP. 3.1 DEFINITION OF DEPTH RESOLUTION IN THIS WORK 231

APP. 3.2 APPROXIMATIVE CONVERSION OF SPUTTERING TIME TO SPUTTERED DEPTH 232

REFERENCE 233

APPENDIX 4 RIETVELD REFINEMENT **235**

APPENDIX 5 ELASTIC MODULI CALCULATION OF SOLID SOLUTION CONFIRMED BY DFT SIMULATION **239**

REFERENCE 240

Appendix 1 An approximate calculation of oxide scale thickness

In this thesis, the equations used to estimate the oxide scale thickness is proposed based on the relationship between the mass gain and the corresponding oxide thickness. Assuming that oxides are homogeneously distributed, the oxide scale thickness d can be evaluated using the following formula:

$$d = [(\Delta m/S) \times \bar{M}_{\mathrm{ox}}]/(M_{\mathrm{O}} \times \bar{n} \times \bar{\rho}_{\mathrm{ox}} \times F), \tag{A1.1}$$

where Δm is the mass gain obtained from thermogravimetric analysis; S the surface area of specimen measured repeatedly with the vernier calipers; M_{O} the relative atomic weight of oxygen ($M_{\mathrm{O}} = 16$ g/mol); $\bar{M}_{\mathrm{ox}}$ the average relative molecular weight of oxide; $\bar{n}$ the average mole number of oxygen atom corresponding to per mole oxide; $\bar{\rho}_{\mathrm{ox}}$ the average true density of oxide; F a structural factor.

The average relative molecular weight of oxide $\bar{M}_{\mathrm{ox}}$ is given by:

$$\bar{M}_{\mathrm{ox}} = \sum_{i=1}^{n} w_i M_{\mathrm{ox}_i}, \tag{A1.2}$$

where w_i is the weight percentage of oxide i , which can be determined by Rietveld refinement based on the results of XRD; M_{ox_i} is the relative molecular weight of oxide i.

Similarly, the average true density of oxide can be obtained by:

$$\bar{\rho}_{\mathrm{ox}} = \sum_{i=1}^{n} w_i \rho_{\mathrm{ox}_i}, \tag{A1.3}$$

where ρ_{ox_i} is the true density of oxide i, derived from literature.

In this thesis, three types of oxides are mainly considered, i.e., the corundum-type (M_2O_3), spinel-type (AB_2O_4) and halite type (MO). Obviously, 1 mole of M_2O_3, AB_2O_4 and MO contains 3 mol, 4 mol and 1 mole oxygen atoms respectively. Therefore, assuming there are x kinds of corundum-type oxides, (e.g., Cr_2O_3, Fe_2O_3. In addition, ABO_3 is simply classified into this group during calculations), y kinds of spinel-type oxides (e.g., $MnCr_2O_4$, Fe_3O_4 etc.) and z kinds of halite type oxides (e.g., FeO) in the oxide scales, $\bar{n}$ can be estimated through:

$$\bar{n} = 3\sum_{i=1}^{x} n_{\mathrm{c}_i} + 4\sum_{j=1}^{y} n_{\mathrm{s}_j} + \sum_{k=1}^{z} n_{\mathrm{m}_k}, \tag{A1.4}$$

where n_{c_i}, n_{s_j} and $n_{\mathrm{m}_k}$are the mole percentages of corundum-type oxide i, spinel-type oxide j and rock salt type oxide k respectively, which can be converted from the weight percentage of each oxide in the oxide scales.

Generally, the porosity and void ratio should be considered for the thickness evaluation. But due to the structural complexity of oxide scales formed under different conditions, the structure

factor F needs to be imported, considering not only the above two but also others related to the microstructure. In this thesis, F can be regarded as a ratio ($0 < F < 1$), given by:

$$F = d_{\mathrm{cal}}/d_{\mathrm{det}}, \tag{A1.5}$$

where d_{cal} is calculated through Equation (A1.1) with $F = 1$; d_{det} the thickness determined from the cross-section image of oxide scale formed at a given temperature and humidity.

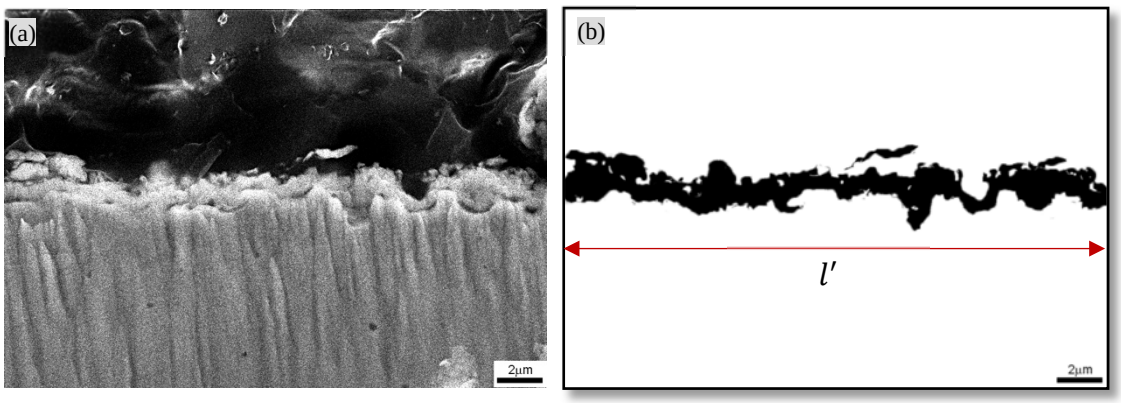

Figure App. 1.1 Thickness determination of oxide scale: SEM image of oxide scale after 96-hour oxidation at 900˚C in the 2% H_2O containing air (a); corresponding oxide scale contour extracted (b)

In fact, d_{det} is an average thickness, decided by:

$$d_{\mathrm{det}} = A'/l', \tag{A1.6}$$

where A' and l' are the area of oxide scale contour and corresponding length, which can be measured using ImageJ.

Based on this method, the thicknesses of oxide scales formed in this work have been determined, as listed in Table App. 4.1. Moreover, the accuracy has also been examined. For instance, the thickness of oxide scale after 96-hour oxidation at 700˚C in the 4% H_2O containing air is around 8.8 μm, which is directly determined through the SEM cross section image. With F obtained, the thickness of oxide scale after 48-hour oxidation at the same temperature and humidity is calculated, around 8.3 μm, which is in a good agreement with the one measured directly from the corresponding SEM image.

Table App. 1.1 Thicknesses of oxide scales formed under different conditions

Humidity (vol. %)	Duration (h)	Thickness (nm)		
		700˚C	800 ˚C	900 ˚C
0	6	634	166	359
	24	751	435	956
	48	1042	604	1497
	72	1578	877	1774
	96	1833	996	1879
1	6	540	75	352
	24	900	194	837
	48	1321	265	1132
	72	1499	400	1758
	96	1449	334	1566
2	6	962	114	246
	24	2601	193	649
	48	2487	410	915
	72	2694	404	1126
	96	3380	405	1425
4	6	5257	96	282
	24	7947	180	628
	48	8320	222	865
	72	6643	227	1131
	96	8823	263	1400
8	6	5637	352	307
	24	10457	641	5811
	48	10421	749	3013
	72	7354	41339	66299
	96	5693	147152	149278

Appendix 2 Relevant parameters calculations for XRD

App. 2.1 X-ray linear absorption coefficient calculation

App. 2.1.1 For a compound

The X-ray linear absorption coefficient (LAC) of a compound μ_{com} is calculated based on:

$$\mu_{com} / \rho_{compound} = \sum_{i=1}^{n} [w_i \times (\mu_i / \rho_i)], \quad \text{(A2.1)}$$

where (μ_i / ρ_i) is the mass absorption coefficient (MAC) of atom i; w_i the atomic weight fraction of atom i.

*Table App. 2.1 MACs of atoms correlated in this thesis [*Bryan, 1993*]*

Atom	O	Cr	Fe	Mn	Ni
MAC (Cu Kα) (cm^2/g)	11	253	311	278	49

Table App. 2.2 MACs of compounds calculated

Compound	Cr_2O_3	Fe_2O_3	$FeMnO_3$	FeO	$FeNi_3$
MAC (Cu Kα) (cm^2/g)	175	221	209	227	111
Compound	$MnCr_2O_4$	$Fe_{1.5}Mn_{1.5}O_4$	$NiFe_2O_4$	Fe_3O_4	
MAC (Cu Kα) (cm^2/g)	190	132	164	227	

App. 2.1.2 For an oxide scale

The oxide scale is an oxide mixture, the mass absorption coefficient of which can be calculated in the same way:

$$\mu_{ox} / \bar{\rho}_{ox} = \sum_{j=1}^{n} [w_j \times (\mu_j / \rho_j)], \quad \text{(A2.2)}$$

where (μ_j / ρ_j) is the mass absorption coefficient of compound j; w_j the weight fraction of compound j in the oxide scale. The linear absorption coefficient of oxide scale μ_{ox} can thus be obtained.

App. 2.2 X-ray penetration depth calculation

App. 2.2.1 For phase analysis

The penetration depth for phase identification is calculated using the plugin of the analysis software HighScore Plus (version 3.0e). The parameters needed are the MAC of oxide scale and corresponding "density". The value of "density" ρ'_{ox} concerns a packing factor (PF), given by:

$$\rho'_{\mathrm{ox}} = PF \times \bar{\rho}_{\mathrm{ox}}, \tag{A2.3}$$

where $PF = 0.5$ in this thesis.

The path length L_{p} is first calculated, which refers to the length the X-rays travel through a material with the given characteristics, until 99% of the intensity is absorbed and only 1% of the initial intensity I_0 is transmitted. Assuming the oxides are mixed homogenously, it can be evaluated through:

$$I_{L_{\mathrm{p}}} = I_0 \times \exp^{-(\mu_{\mathrm{ox}}/\bar{\rho}_{\mathrm{ox}})\bar{\rho}_{\mathrm{ox}} L_{\mathrm{p}}}, \tag{A2.4}$$

The penetration depth d can be accordingly estimated by:

$$d = 0.5 \times L_{\mathrm{p}} \times \sin(\omega), \tag{A2.5}$$

where ω is the grazing incidence angle for phase identification of oxide thin films. In fact, this is the thickness of the specimen contributing 99% of the diffracted intensity at a given ω.

Table App. 2.3 X-ray penetration depths (μm) for phase identification

Humidity (%)	**Duration (h)**	**700˚C**			**800 ˚C**		**900 ˚C**		
		0.5˚	**2˚**	**5˚**	**0.5˚**	**2˚**	**0.5˚**	**2˚**	**5˚**
0	6	0.315	0.963	2.004	0.343	0.972	0.371	1.327	2.175
	24	0.356	0.91	1.655	0.323	1.191	0.366	1.545	3.461
	48	0.312	1.064	1.944	0.398	1.165	0.359	1.48	3.505
	72	0.362	1.185	1.654	0.408	1.616	0.379	1.549	3.572
	96	0.316	1.039	1.785	0.422	1.218	0.396	1.613	3.556
1	6	0.321	1.001	1.842	0.339	1.021	0.376	1.482	2.327
	24	0.308	1.116	2.11	0.363	1.171	0.388	1.513	2.855
	48	0.306	1.046	1.78	0.348	1.396	0.399	1.587	3.01
	72	0.275	0.963	1.893	0.415	1.166	0.402	1.512	3.214
	96	0.32	1.22	2.653	0.401	1.598	0.394	1.561	3.306
2	6	0.318	0.91	1.829	0.321	1.161	0.387	1.518	2.619
	24	0.338	0.962	1.879	0.348	0.956	0.405	1.347	2.668
	48	0.342	1.061	2.22	0.385	1.298	0.393	1.513	2.954
	72	0.339	0.929	1.728	0.383	1.388	0.401	1.467	2.993
	96	0.326	1.144	1.826	0.386	1.065	0.399	1.413	2.955
4	6	0.324	1.035	1.702	0.307	1.148	0.408	1.165	2.306
	24	0.311	1.042	1.813	0.403	1.457	0.349	1.397	2.476
	48	0.33	0.935	1.841	0.371	0.852	0.4	1.438	2.94

	72	0.313	1.274	1.987	0.401	0.737	0.379	1.46	2.937
	96	0.289	0.917	1.722	0.414	0.898	0.37	1.571	2.821
8	6	0.327	0.989	1.7	0.342	1.128	0.39	1.266	2.195
	24	0.269	0.974	1.669	0.403	1.146	0.372	1.447	2.778
	48	0.308	1.114	1.855	0.403	0.967	0.391	1.477	2.93
	72	0.283	1.018	1.702	0.391	1.542	0.394	1.618	3.634
	96	0.312	1.14	1.96	--	--	--	--	--

App. 2.2.2 For stress analysis

For a given specimen, the penetration depth of X-ray varies with changing the three instrumental angles (ω, χ, ϕ). As shown in Figure App. 0.1, α and β represent the angles between the incident and exit X-rays and the specimen surface respectively; S3 and L3 are the normal directions of the specimen surface and diffraction lattice planes {hkl}. During the measurement, the instrument coordinate (I) keeps fixed, while the specimen coordinate (S) rotates around the axis I_1 (the instrumental angle χ), the axis I_2 (the instrumental angle ω) and the axis I_3 (the instrumental angle ϕ). In this thesis, the X-ray penetration depth d for stress analysis refers to the average information depth for an infinitely thick sample, i.e., the so-called $1/e$ penetration depth. It is confined in a volume with a thickness of d, just beneath the specimen surface, from which 63% of diffracted intensity originates. Hence, the penetration depth d is expressed as [*Welzel et al., 2005*]:

$$d = [\sin\alpha \sin\beta]/[\mu_{\mathrm{ox}}(\sin\alpha + \sin\beta)], \tag{A2.6}$$

which can be rewritten using the instrumental angles [*Chen et al., 2011*], as:

$$d = \{\cos\chi\,[\sin^2\theta - \sin^2(\theta-\omega)]\}/[2\mu_{\mathrm{ox}}\sin\theta\cos(\theta-\omega)]. \tag{A2.7}$$

In this work, two diffracted lattice planes {104} and {113} are chosen to determine the residual stresses in the corundum and spinel oxide scales respectively. The corresponding diffracted angles θ are accordingly 16.75˚ and 17.75˚ respectively. The angle χ varies from -35˚ to +35˚. The grazing incidence angle ω is set at 0.5˚ and 2˚.

Table App. 2.4 lists the X-ray penetration depths during the residual stress measurements of corundum-type oxides. The “average” here refers to the average value of the results calculated at a set of χ angles. It should also be noted that these results can be approximatively used for the stress determination of spinel-type oxides because their diffracted angles are quite close.

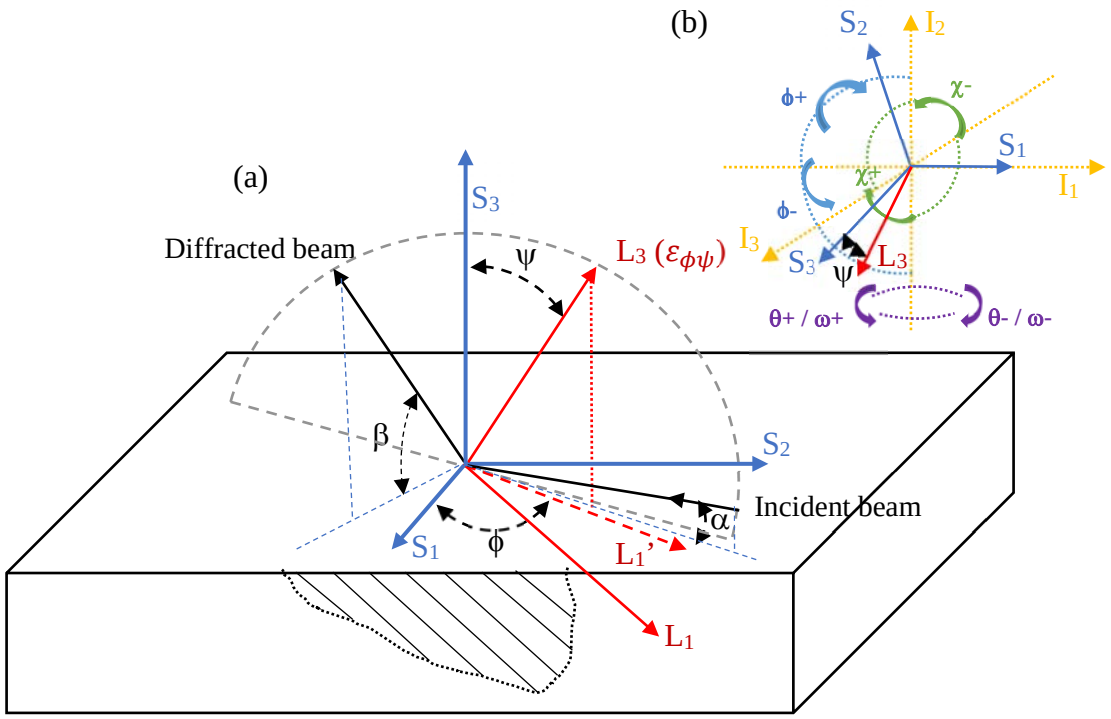

Figure App. 2.1 Residual stress measurement geometry showing the related angles in the systems of specimen (S), laboratory (L) and instrument (I) for constant penetration depth determination: the relation between the sample and instrument coordinate systems (a); the relation between the specimen surface and diffracted plane coordinate systems

Table App. 2.4 Average X-ray penetration depths (μm) for stress determination in corundum-type oxide scales

Humidity	**Duration**	**700˚C**		**800 ˚C**		**900 ˚C**	
(%)	(h)	**0.5˚**	**2˚**	**0.5˚**	**2˚**	**0.5˚**	**2˚**
0	6	0.264	0.638	0.246	0.759	0.197	0.734
	24	0.273	0.681	0.250	0.915	0.151	0.729
	48	0.194	0.741	0.228	0.784	0.146	0.868
	72	0.275	0.643	0.206	0.902	0.183	0.761
	96	0.267	0.627	0.240	0.746	0.185	0.779
1	6	0.227	0.714	0.239	0.741	0.206	0.819
	24	0.188	0.778	0.186	0.790	0.170	0.817
	48	0.161	0.923	0.207	0.731	0.178	0.790
	72	0.175	0.728	0.243	0.920	0.176	0.767
	96	0.192	0.816	0.217	0.897	0.181	0.718
	6	0.244	0.814	0.184	1.069	0.179	0.929

2	24	0.256	0.699	0.206	1.011	0.205	0.806
	48	0.229	0.599	0.219	0.852	0.184	0.754
	72	0.279	0.842	0.212	0.755	0.190	0.725
	96	0.205	0.668	0.224	0.858	0.192	0.722
4	6	0.226	0.608	0.228	0.704	0.206	0.682
	24	0.183	0.670	0.227	0.864	0.177	0.710
	48	0.221	0.698	0.225	1.080	0.187	0.764
	72	0.239	0.692	0.211	0.943	0.174	0.732
	96	0.238	0.619	0.232	1.169	0.167	0.787
8	6	0.191	0.796	0.211	0.673	0.185	0.760
	24	0.201	0.782	0.220	0.894	0.158	0.728
	48	0.207	0.649	0.206	0.763	0.170	0.751
	72	0.226	0.565	0.175	0.621	0.178	0.776
	96	0.259	0.817	-	-	-	-

App. 2.3 Determination of X-ray irradiated area

The optical paths for phase identification and residual stress determination have been introduced in Section 3.5. Therefore, the X-ray irradiated area can be estimated in regard to the given configuration and parameters.

For phase analysis, the irradiated length $L_{\mathrm{irr}}^{\mathrm{p}}$ and width $W_{\mathrm{irr}}^{\mathrm{p}}$ are given respectively by:

$$L_{\mathrm{irr}}^{\mathrm{p}} = 0.12 + 0.3/\sin\omega \text{ (mm)}, \tag{A2.8}$$

$$W_{\mathrm{irr}}^{\mathrm{p}} = M - 3 \text{ (mm)}, \tag{A2.9}$$

where M is the mask's marking ($M = 5$ mm in this work).

For stress analysis, the irradiated length $L_{\mathrm{irr}}^{\mathrm{s}}$ and width $W_{\mathrm{irr}}^{\mathrm{s}}$ are given respectively by:

$$L_{\mathrm{irr}}^{\mathrm{s}} = [h + \delta(R - f)]/\sin\omega + W_{\mathrm{irr}}^{\mathrm{s}}\sin\psi\cot\omega \text{ (mm)}, \tag{A2.10}$$

$$W_{\mathrm{irr}}^{\mathrm{s}} = [w + \delta(R - f)]/\cos\psi \text{ (mm)}, \tag{A2.11}$$

where R is the radius of the goniometer ($R = 320$ mm); f the distance from the focus of the X-ray tube to the crossed slits ($f = 145$ mm); δ the divergence of the X-ray beam emerging from the X-ray lens ($\delta = 0.00523$ rad); h the height of the incident X-ray beam ($h = 1$ mm); w the width of the incident X-ray beam ($w = 5$ mm).

Reference

[Bryan, 1993] BRYAN, R. 1993. International tables for crystallography. Vol. C. Mathematical, physical and chemical tables edited by AJC Wilson. International Union of Crystallography.

[Chen et al., 2011] CHEN, Z., PRUD'HOMME, N., WANG, B. & JI, V. 2011. Residual stress gradient analysis with GIXRD on ZrO2 thin films deposited by MOCVD. *Surface and Coatings Technology,* 206**,** 405-410.

[Welzel et al., 2005] WELZEL, U., LIGOT, J., LAMPARTER, P., VERMEULEN, A. & MITTEMEIJER, E. 2005. Stress analysis of polycrystalline thin films and surface regions by X-ray diffraction. *Journal of Applied Crystallography,* 38**,** 1-29.

Appendix 3 Quantitative compositional depth profiling of XPS

X-ray photoelectron spectroscopy with ion etching is a formidable technique for depth profiling of the compounds with varied chemical states to acquire information about covered regions beneath surfaces. Generally during data analysis, four primary problems need to be considered, i.e., how to convert the measured signal intensities to concentrations, how to define the interfacial transition zone (ITZ), i.e. depth resolution, between two layers, how to covert the experimental sputtering time to sputtered depth, and how to judge the goodness of fitting.

CasaXPS processing software is widely used for XPS spectra analysis, which not only owns the accuracy and reliability to some extent, but also offers a friendly operation interface for users. Thanks to the strong function of CasaXPS, the above first problem regarding to quantification can be solved basically by creating region and component fittings, which is not of interest here. However, it is necessary to mention the depth resolution definition in this thesis, coupled with conversion between sputtering time and sputtered depth. Besides, some factors brought by samples are discussed for better evaluating the results.

App. 3.1 Definition of depth resolution in this work

Depth resolution is usually described by a characteristic length Δz within which the in-depth compositional distribution is not so clear due to the deviation of the measured profile shape from the real shape of the original in-depth distribution. The smaller value of Δz means higher resolution. This kind of deviation which affects the result accuracy is the consequence of compositional or topographical changes in the surface zone during ion beam etching simultaneously interacted with the sample. ASTM E42 states that "Depth resolution is the depth range over which a signal increases (or decreases) by a specified amount when profiling an ideally sharp interface between two media. By convention, the depth resolution corresponds to the distance over which a 16-84% (or 84-16%) change in signal is measured." [*Hofmann, 2012*]

Inspired by the above foundation, the interface between AISI 316L SS and its oxide scale can be presented by the specific Δz width zone, which is defined in this work by calculating the distance over which a 20-80% change in signal of Fe. An interesting phenomenon occurred that Δz increased along with temperature elevated, reflecting that sharper M/O interface formed at higher temperature. It is because that internal oxidation happens more easily at higher temperatures, causing fluctuated M/O interface formation.

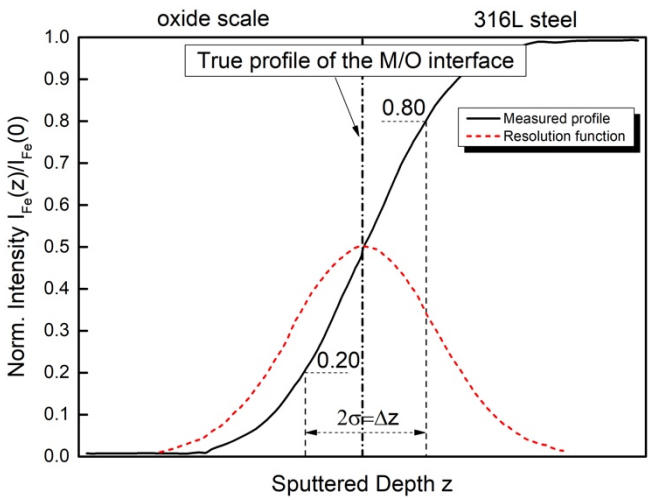

Figure App. 3.1 Schematic broadening of the iron profile at a sharp interface and definition of the depth resolution, Δz (20-80%) in this thesis. For a Gaussian resolution function, Δz=2σ, with σ=the standard deviation.

App. 3.2 Approximative conversion of sputtering time to sputtered depth

The raw data of a depth profiling is a sputtering timescale rather than the intuitionistic depth scale, since it is hard to obtain the instantaneous sputtering rate. Frequently an average rate can be an alternative for calculating the sputtering depth. Supposing that the primary ion current density is a constant, the sputtered depth at sputtering time t_1 is determined by:

$$z(t_1) = \int_0^{t_1} \dot{z}(t)dt, \tag{A3.1}$$

where the sputtering rate $\dot{z}$ given by:

$$\dot{z} = j_I Y_M / eN, \tag{A3.2}$$

with the primary ion current density j_I (A/m^2), the elementary charge e (1.6×10^{-19}A s), the total sputtering yield Y_M (atoms/ion), and the atomic density N (atoms/m^3). Assuming constant Y_M and N, with measurement of j_I, the sputtering rate is constant, and sputtered depth can be obtained by:

$$z = \dot{z}t. \tag{A3.3}$$

In this work, the sputtering rate of oxide scale $\dot{z}_{(\text{oxide})}$, can be estimated by:

$$\dot{z}_{(\text{oxide})} = z_{(\text{oxide})} / t_{(\text{center of interface})}, \tag{A3.4}$$

where the oxide scale thickness $z_{(\text{oxide})}$, which can be acquired from 0 and the corresponding sputtering time $t_{(\text{center of interface})}$ (s).

Consequently, the sputtered depth of oxide scale z is determined by

$$z = \dot{z}_{(\mathrm{oxide})} t. \tag{A3.5}$$

Reference

[Hofmann, 2012] HOFMANN, S. 2012. *Auger-and X-ray photoelectron spectroscopy in materials science: a user-oriented guide*, Springer Science & Business Media.

Appendix 4 Rietveld refinement

Rietveld refinement is carried out using the software HighScore Plus. The Rietveld method is based on:

$$y_{ic} = y_{ib} + \sum_{\mathrm{p}} \sum_{k=k_1^{\mathrm{p}}}^{k_2^{\mathrm{p}}} G_{ik}^{\mathrm{p}} I_k, \tag{A4.1}$$

where y_{ic} and y_{ib} are the net intensity calculated and background intensity at point i in the pattern respectively; $G_{\mathrm{ik}}^{\mathrm{p}}$ a normalized peak profile function; k_1^{p} to k_1^{p} the reflections contributing at point i in the pattern with the possible phases in the sample; I_{k} the intensity of the No. k Bragg reflection.

In this thesis, three parameters were used to evaluate the quality of the refinement is, i.e., R_{wp}, R_{exp} and GOF. Y o

- R_{wp} compares the calculated pattern to the data, as given by:

$$R_{\mathrm{wp}} = \{[\sum w_i (y_{io} - y_{ic})^2]/(\sum w_i y_{io}^2)\}^{1/2}. \tag{A4.2}$$

where y_{io} is the net intensity obtained at point i in the pattern. R_{wp} weights the residual so that higher intensity data points are more important than low intensity data points. It is usually less than 10%.

- R_{exp} evaluates the quality of the data, which is expressed as:

$$R_{\mathrm{exp}} = [(N - P)/(\sum w_i y_{io}^2)]^{1/2}, \tag{A4.3}$$

where N is the number of observations and P the number of least-squares parameters being estimated. R_{exp} evaluates the quality of the data. Normally, data with more noise or low peak intensities has a larger R_{exp}.

- GOF is the goodness of fit, by comparing R_{wp} to R_{exp}, as expressed as:

$$\mathrm{GOF} = \left(R_{\mathrm{wp}}/R_{\mathrm{exp}}\right)^2 \tag{A4.4}$$

Those three parameters for each refinement in this thesis are tabulated in Table App. 0.1.

Table App.4.1 Summary of refinement goodness for the oxide scales formed at 700˚C

700˚C		**0.5˚**			**2˚**			**5˚**		
Humidity (%)	**Duration** (h)	**R_{exp}** (%)	**R_{wp}** (%)	GOF	**R_{exp}** (%)	**R_{wp}** (%)	GOF	**R_{exp}** (%)	**R_{wp}** (%)	GOF
0	6	1.4232	2.3493	2.7248	1.0974	1.4505	1.7472	1.4042	1.5496	1.2178
	24	1.5359	2.4213	2.4852	1.1799	1.2895	1.1943	1.4282	1.6831	1.3889
	48	2.4094	3.3200	1.8988	1.7549	2.0521	1.3674	2.2496	2.2974	1.0430
	72	1.5580	1.9012	1.4890	1.2031	1.4381	1.4288	1.4621	1.8728	1.6407
	96	2.1034	2.8448	1.8291	1.4692	1.9875	1.8301	1.8032	2.2071	1.4982
1	6	1.7074	1.8746	1.2055	1.3205	1.4909	1.2748	1.7024	1.9985	1.3781
	24	2.2299	2.3284	1.0903	1.6371	1.6548	1.0218	2.0402	1.9732	0.9354
	48	1.8118	2.6033	2.0646	1.3450	1.7160	1.6277	1.6751	1.8449	1.2129
	72	1.8492	2.8068	2.3039	1.3640	1.6998	1.5528	1.7112	1.6848	0.9694
	96	2.4119	3.2993	1.8712	1.7279	1.9669	1.2956	2.0493	1.9941	0.9468
2	6	2.0924	2.5497	1.4849	1.7104	2.3430	1.8766	2.0990	2.4026	1.3102
	24	2.3020	2.9996	1.6979	2.0134	2.4797	1.5169	2.5876	3.4817	1.8106
	48	2.2143	2.9177	1.7363	1.6757	1.9625	1.3716	2.0428	2.0650	1.0219
	72	1.2362	1.6948	1.8797	0.8841	1.2969	2.1520	1.0652	1.2562	1.3910
	96	2.1228	2.4861	1.3715	1.5204	1.6996	1.2495	1.4655	1.6777	1.3105
4	6	2.0676	2.7429	1.7599	1.4738	1.5693	1.1338	1.8207	2.0449	1.2614
	24	2.0912	2.9553	1.9972	1.4837	1.5575	1.1019	1.8222	1.7505	0.9229
	48	2.5312	2.8882	1.3020	1.6331	1.7265	1.1176	2.0257	2.1107	1.0857
	72	2.2551	3.3668	2.2289	1.5175	1.9113	1.5864	1.8485	1.9225	1.0818
	96	2.0323	3.7629	3.4281	1.4644	2.4882	2.8869	1.8179	2.1874	1.4479
8	6	1.6351	2.4590	2.2617	1.2604	1.7306	1.8852	1.6161	1.7745	1.7745
	24	1.7136	2.8871	2.8386	1.2703	1.6855	1.7605	1.5996	2.0673	1.6701
	48	1.8501	2.3944	1.6750	1.3231	1.6000	1.4624	1.6494	1.6640	1.0178
	72	1.1791	2.0185	2.9308	0.9043	1.4988	2.7469	1.0705	1.7265	2.6008
	96	2.2307	2.6914	1.4557	1.7684	1.8692	1.1174	2.0184	1.9779	0.9603

Table App. 4.2 Summary of refinement goodness for the oxide scales formed at 800˚C

800˚C		0.5˚			2˚		
Humidity (%)	**Duration (h)**	**R_{exp} (%)**	**R_{wp} (%)**	**GOF**	**R_{exp} (%)**	**R_{wp} (%)**	**GOF**
0	6	1.7481	2.8086	2.5812	1.3580	1.9347	2.0298
	24	1.6417	3.6784	5.0204	1.2428	2.6004	4.3778
	48	1.9243	3.1335	2.6516	1.3958	2.2774	2.6622
	72	1.8036	3.1781	3.1050	1.3469	2.5372	3.5486
	96	1.8669	4.1715	4.9930	1.4151	3.2726	5.3484
1	6	2.2827	3.5825	2.4631	1.7303	2.2687	1.7192
	24	2.4491	3.0052	1.5057	1.8481	2.5864	1.9585
	48	2.6220	4.5426	3.0015	1.9594	3.5488	3.2802
	72	2.7260	4.5296	2.7610	1.9813	3.1424	2.5155
	96	1.9429	3.7116	3.6496	1.3602	3.4445	6.4127
2	6	1.6049	2.5631	2.5506	1.1489	1.4404	1.5719
	24	1.6915	2.4830	2.1548	1.2277	1.9666	2.5660
	48	1.6391	3.9477	5.8005	1.2164	2.4276	3.9829
	72	1.7743	3.2579	3.3714	1.2469	1.9133	2.3545
	96	1.8941	2.5036	1.7472	1.3042	2.5989	3.9712
4	6	2.3272	3.4330	2.1761	1.8711	2.1991	1.3814
	24	2.3344	4.1707	3.1921	1.8863	2.6915	2.0361
	48	2.3163	3.2125	1.9236	1.8047	2.5773	2.0394
	72	1.7751	3.2741	3.2741	1.9642	3.9518	4.0478
	96	2.8957	2.8075	0.9400	2.5219	3.5266	1.9554
8	6	1.6296	1.9175	1.3846	1.1394	1.4027	1.5156
	24	2.1629	3.1405	2.1082	1.2868	2.4038	3.4896
	48	1.7199	3.0060	3.0548	1.2405	2.2725	3.3557
	72	1.4951	1.8342	1.5050	1.1821	1.7652	2.2296
	96	-	-	-	-	-	-

Table App. 4.3 Summary of refinement goodness for the oxide scales formed at 900˚C

900˚C		0.5˚			2˚			5˚		
Humidity (%)	**Duration (h)**	**R_{exp} (%)**	**R_{wp} (%)**	**GOF**	**R_{exp} (%)**	**R_{wp} (%)**	**GOF**	**R_{exp} (%)**	**R_{wp} (%)**	**GOF**
0	6	1.6613	1.9548	1.3846	1.2068	1.4925	1.5296	1.4364	1.6719	1.3549
	24	3.2230	4.3614	1.8312	2.4805	2.9412	1.4060	2.8899	2.8020	0.9401
	48	3.2121	3.8419	1.4306	2.7825	2.8920	1.0803	3.1286	3.0451	0.9474
	72	3.6213	3.9170	1.1700	2.8650	2.9536	1.0629	3.2610	3.1789	0.9503
	96	3.3774	3.3810	1.0021	2.9118	3.3347	1.3115	3.3345	3.0733	0.8495
1	6	2.4556	2.8580	1.3546	1.8937	2.1911	1.3388	2.1862	2.3127	1.1190
	24	2.6711	2.8271	1.1202	2.0696	2.2469	1.1787	2.3222	2.4072	1.0745
	48	2.8820	2.8524	0.9796	2.7227	2.8469	1.0933	2.3504	2.2996	0.9573
	72	2.7129	2.6608	0.9620	2.5862	2.4819	0.9210	2.3172	2.2739	0.9630
	96	2.5371	2.9917	1.3905	2.2803	2.5376	1.2384	2.4638	2.6669	1.1717
2	6	2.9380	3.0969	1.1111	2.1990	2.2346	1.0326	2.4651	2.3386	0.9000
	24	3.0566	3.0932	1.0240	2.5283	2.7820	1.2108	2.7068	2.8324	1.0949
	48	3.1454	3.0144	0.9184	2.7121	2.5686	0.8970	2.8747	3.0000	1.0890
	72	3.2090	3.0676	0.9138	2.7256	2.6770	0.9647	2.8747	3.0000	1.0890
	96	2.9517	3.2565	1.2172	2.4712	2.9825	1.4567	2.7366	3.4020	1.5454
4	6	3.1172	3.1544	1.0240	2.3585	2.8777	1.4887	2.5814	3.2923	1.6266
	24	3.0420	3.0260	0.9895	2.4468	2.6304	1.1557	2.6699	2.8478	1.1377
	48	3.0036	3.2406	1.1640	2.5525	2.3752	0.8659	2.7872	2.7580	0.9792
	72	3.2011	3.2085	1.0046	2.7774	2.7370	0.9711	3.0014	2.8754	0.9178
	96	2.8557	3.5550	1.5497	2.3140	2.6172	1.2793	2.7323	3.1251	1.3081
8	6	2.9277	3.6149	1.5245	2.1589	2.8726	1.7705	2.6988	2.8235	1.0945
	24	2.2427	2.8872	1.6573	1.8630	2.0419	1.2013	2.0725	2.0143	0.9447
	48	2.5425	2.5625	1.0158	1.9305	1.9821	1.0542	2.1785	2.1613	0.9842
	72	1.8253	2.3105	1.6024	1.7312	1.6627	0.9225	2.0843	2.1183	1.0330
	96	-	-	-	-	-	-	-	-	-

Appendix 5 Elastic moduli calculation of solid solution confirmed by DFT simulation

The full range mixing enthalpy for Cr_2O_3 and Fe_2O_3 has been calculated by the cluster expansion method. It is found that the lowest mixing enthalpy (red line in Figure App. 0.1) is always negative, suggesting a tendency to form solid solution for the mixture of Cr_2O_3 and Fe_2O_3. Moreover, the minimum of the mixing enthalpy locates at $0.33Fe_2O_3 \bullet 0.67Cr_2O_3$.

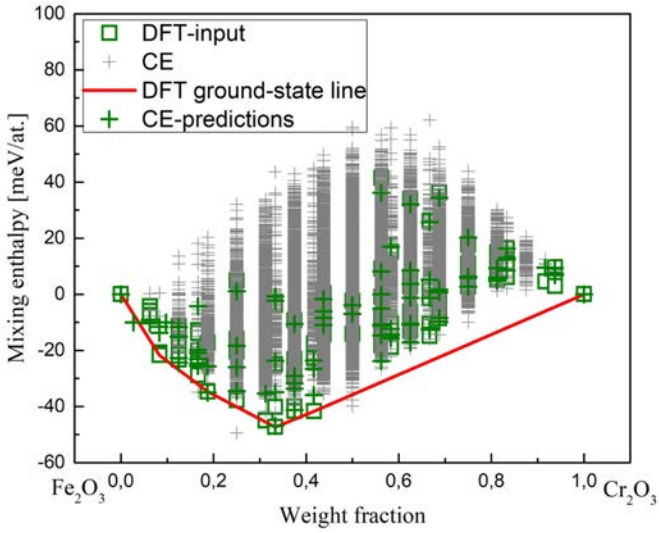

Figure App. 5.1 Mixing enthalpy of ternary (Fe, Cr)$_2O_3$ calculated by cluster expansion

The spin-polarized magnetic calculations based on density functional theory (DFT) [*Hohenberg et al., 1964*] have employed the GGA-PBE [*Perdew et al., 1992*] exchange-correlation functional for describing the interactions. As a correction for localized (strongly correlated) electrons, the Rotationally invariant LSDA+U [*Dudarev et al., 1998*] approach has been used with the correction U =4.3, J =0 for Fe d electrons and U =4.5, J =1.3 for Cr d electrons. The calculations have been done with a planewave cutoff energy of 520eV and a k-spacing of 0.2 per Å. The atomic configurations have been built with the special quasi-random structures (SQS) [*Zunger et al., 1990*], considering the random distribution of Cr and Fe atoms at the metallic lattice site of the corundum-type structure.

First, the single crystal elastic constants have been calculated for the solid solution (Fe, Cr)$_2O_3$ with various weight fractions respectively. Further average of single crystal elastic constants has been carried out using Voigt-Reuss-Hill (VRH) method for isotropic polycrystals. It is found that the Young's modulus (E) and shear modulus (G) increase almost linearly with Cr_2O_3 content while the Poisson's ratio (ν) decreases. It should also be noted that the elastic modulus of solid solution (Fe, Cr)$_2O_3$ at a given weight fraction can be obtained through the linear

combination of elastic moduli of pure Cr_2O_3 and pure Fe_2O_3 with the corresponding weight fraction.

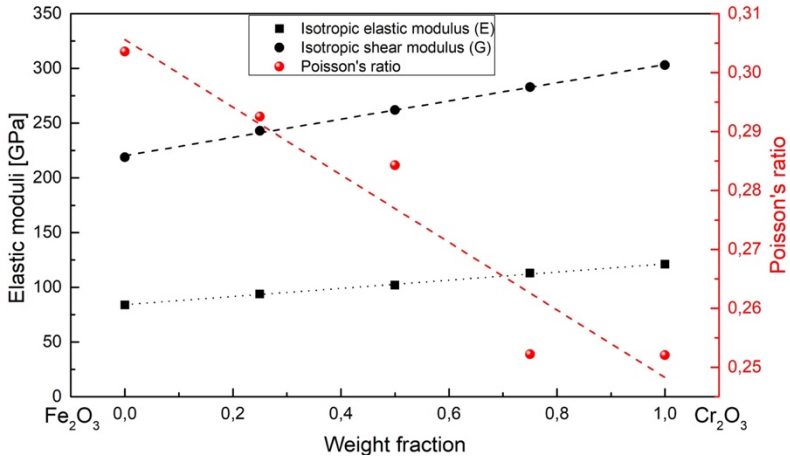

Figure App. 5.2 Voigt-Reuss-Hill average of (Fe, Cr)$_2$O$_3$ solid solution elastic moduli (E, G & ν), calculated by density functional theory

Reference

[Dudarev et al., 1998] DUDAREV, S., BOTTON, G., SAVRASOV, S., HUMPHREYS, C. & SUTTON, A. 1998. Electron-energy-loss spectra and the structural stability of nickel oxide: An LSDA+ U study. *Physical Review B,* 57**,** 1505.

[Hohenberg et al., 1964] HOHENBERG, P. & KOHN, W. 1964. Inhomogeneous electron gas. *Physical review,* 136**,** B864.

[Perdew et al., 1992] PERDEW, J. P. & WANG, Y. 1992. Accurate and simple analytic representation of the electron-gas correlation energy. *Physical Review B,* 45**,** 13244.

[Zunger et al., 1990] ZUNGER, A., WEI, S.-H., FERREIRA, L. & BERNARD, J. E. 1990. Special quasirandom structures. *Physical Review Letters,* 65**,** 353.